The anatectic history of Archaean metasedimentary granulites from the Ancient Gneiss Complex, Swaziland

by

Jeanne Taylor

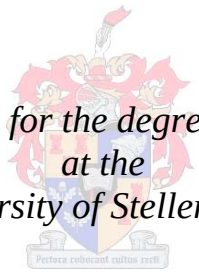

Dissertation presented for the degree of Doctor of Geology
at the
University of Stellenbosch

Promoter: Prof. Gary Stevens
Faculty of Science
Department of Earth Sciences

March 2012

Declaration

By submitting this dissertation electronically, I declare that the entirety of the work contained therein is my own, original work, that I am the sole author thereof (save to the extent explicitly otherwise stated), that reproduction and publication thereof by Stellenbosch University will not infringe any third party rights and that I have not previously in its entirety or in part submitted it for obtaining any qualification.

Signed . . . . . .
(Jeanne Taylor)

November 2011

Dedication

This thesis is dedicated to my grandfather, Roy Oosthuizen, whose remarkable achievements in palaeontology and interest in geology has been a source of inspiration.

The Road Not Taken

By Robert Frost

Two roads diverged in a yellow wood,
And sorry I could not travel both
And be one traveller, long I stood
And looked down one as far as I could
To where it bent in the undergrowth.

Then took the other, as just as fair,
And having perhaps the better claim,
Because it was grassy and wanted wear;
Though as for that the passing there
Had worn them really about the same.

And both that morning equally lay
In leaves no step had trodden black.
Oh, I kept the first for another day!
Yet knowing how way leads on to way,
I doubted if I should ever come back.

I shall be telling this with a sigh
Somewhere ages and ages hence:
Two roads diverged in a wood, and I--
I took the one less travelled by,
And that has made all the difference.

Abstract

This study is an investigation of the anatectic history of high-grade paragneisses from the Ancient Gneiss Complex (AGC) in Swaziland. The work involved an integrated field, metamorphic, geochemical, geochronological and structural study of metasedimentary granulites from three separate, but spatially related areas of outcrop in south-central Swaziland, which were subjected to multiple high-grade partial melting events throughout the Meso- to Neoarchaean. The project has aimed to constrain the age(s) and conditions of metamorphism, so as to contribute to the understanding of geodynamic processes in the Barberton and AGC granite-greenstone terranes, as well as to investigate certain physical and chemical aspects of anatexis in the migmatites. The metamorphic record retained in these rocks, constrained by phase equilibria modelling as well as zircon and monazite SHRIMP and LA-ICP-MS geochronology, informs on the state of the mid- to lower-crust of the southeastern Kaapvaal Craton during key events associated with early lithosphere assembly and crustal differentiation. It also suggests that the region is comprised of more than one high-grade terrane. Two of the areas investigated experienced high-temperature metamorphism at ca. 3.23-3.21 Ga, in addition to a major 830-875º C, 6.5-7.6 kbar anatectic event at ca. 3.11-3.07 Ga. Intermediate and younger high-temperature events are recorded at ca. 3.18 Ga, ca. 3.16 Ga and 2.99 Ga. The timing of these metamorphic events coincided with the amalgamation of the eastern domain of the proto-Craton via subduction and accretion of micro-continental fragments at ca. 3.23 Ga, including the Barberton Greenstone Belt (BGB) and AGC terranes, as well as discrete episodes of crustal differentiation and potassic granitic magmatism between ca. 3.23 and 3.10 Ga. The third area investigated holds no record of Mesoarchaean metamorphism, but instead experienced a 830-855 ºC, 4.4-6.4 kbar partial melting episode at ca. 2.73 Ga. This broadly coincided with the formation of a large continental flood basalt province, the ca. 2.71 Ga Ventersdorp LIP, and widespread intracratonic granitic magmatism on the Craton towards the end of the Neoarchaean. An explanation for the contrast in metamorphic record in the two terranes may be that the 2.71 Ga granulites represent a much younger sedimentary succession, and that granulites from the older terrane were left too restitic, after substantial partial melting during the Mesoarchaean, to record subsequent high-grade events. Finally, this study documents the details of S-type granitic magma production and extraction from a typical metapelitic source. Using the 2.73 Ga granulites from the AGC as a natural field laboratory, a case is made for the selective entrainment of peritectic garnet to the magma as a mechanism for generating relatively mafic, peraluminous S-type granite compositions. The work demonstrates the evolution of entrained peritectic garnet in such magmas, and is in strong support of a ‘peritectic phase entrainment’ process by which relatively mafic granite magmas are produced from melts which, in theory, should be highly leucocratic.

Opsomming

Hierdie studie ondersoek die anatektiese geskiedenis van hoëgraadse metasedimentêre gneise uit die Ancient Gneiss Complex (AGC) in Swaziland. Die werk behels 'n geïntegreerde veld, metamorfiese, geochemiese, geochronologiese en strukturele studie van metasedimentêre granuliete van drie afsonderlike, maar ruimtelik verwante gebiede in suid-sentraal Swaziland, wat aan verskeie hoëgraadse anatektiese gebeure onderworpe was gedurende die Meso-tot Neoargeïese tydsperiode. Die studie is daarop gemik om die ouderdomme en die kondisies van metamorfose vas te stel, om sodoende by te dra tot die begrip van die geodinamiese prosesse in die Barberton en AGC graniet-groensteen terrein, asook om sekere fisiese en chemiese aspekte van die anatektiese proses te ondersoek. Die metamorfe rekord, bepaal deur mineraal ewewigsmodellering sowel as sirkoon en monasiet SHRIMP en LA-ICP-MS geochronologie, belig die toestand van die middel-tot laer-kors van die suidoostelike Kaapvaal Kraton tydens vroeë litosfeer samesmelting en differensiasie. Dit stel ook voor dat die streek uit meer as een hoëgraadse terrein bestaan. Twee van die gebiede het hoë-temperatuur metamorfose by 3.23-3.21 Ga ervaar, asook 'n hoof 830-875 ° C, 6.5-7.6 kbar anatektiese gebeurtenis by 3.11-3.07 Ga. Intermediêre en jonger hoë-temperatuur gebeure was ook by 3.18 Ga, 3.16 Ga en 2.99 Ga geregistreer. Die metamorfose van die gebied stem ooreen met die samesmelting van die oos Kaapvaal Kraton domein deur subduksie en aanwas van mikro-kontinente by 3.23 Ga, insluitend die Barberton en AGC terreine, asook diskrete episodes van kors differensiasie en kalium-ryke graniet magmatisme tussen 3.23 en 3.10 Ga. Die derde gebied hou geen rekord van Mesoargeïkum metamorfose nie. In plaas daarvan het dit 'n 830-855 ° C, 4.4-6.4 kbar anatektiese episode by 2.73 Ga ervaar, wat ooreenstem met die vorming van 'n groot kontinentale vloedbasalt provinsie, die 2.71 Ga Ventersdorp Supergroep, en wydverspreide intrakratoniese graniet magmatisme teen die einde van die Neoargeïkum. 'n Moontlike verduideliking vir die kontras in metamorfe rekord in die twee terreine mag wees dat die 2.71 Ga granuliete 'n jonger sedimentêre afsetting verteenwoordig, en dat granuliete van die ouer terrein te restieties gelaat was na aansienlike anateksis in die Mesoargeïkum, om daaropvolgende hoëgraadse gebeure te registreer. Ten slotte, hierdie studie dokumenteer die besonderhede van S-tipe graniet magma produksie en ontginning van 'n tipiese metasedimentêre bron. Die 2.73 Ga granuliete word gebruik as 'n natuurlike veld laboratorium om die selektiewe optel-en-meevoering van peritektiese granaat tot die magma te ondersoek. Die werk toon die evolusie van peritektiese granate in sulke magmas aan, en ondersteun lewering van relatiewe mafiese graniet magmas deur 'n ‘peritektiese fase optel-en-meevoerings’ proses.

Acknowledgements

Firstly I would like to convey my immense gratitude to my supervisor, Gary Stevens, who has supported me in many ways since I arrived at Stellenbosch, and to whom I am greatly indebted. Thank you for seeing potential in me, for encouraging me and for setting the bar high so that I could reach my potential. Mostly, thank you for the years of patients, energy and friendship.

I wish to thank all the past and current members of staff in the department who assisted me in different ways, and who have played an important role in my education: Riana Van der Berg, Alex Kisters, Ian Buick, Cristiano Lana, John Clemens, Jeff Moyen, Abraham Rozendaal, Jodie Miller, Riana Rossouw, Madelaine Frazenburg, Dave Glenister, Esmê Spicer, George Olivier and Faizel Timmey. Thank you for making my time at Stellenbosch such a rewarding experience. Thanks also to Cathy, Roy, and René for their support. I'd like to particularly thank Loxie Conradie, my geology Mom – thank you for taking care of me and for all the times you came to my rescue. Thanks to my fellow inmates in 'Postgradcatraz' who made my stay more bearable, namely Rob, Arnaud, Federico, Byron, Kathryn, Angelique, Luhan, Corne and Risa. Importantly, thank you to my office mate, Cynthia – we've walked a long road together and without you I would not have managed. Thank you for always being ready to lend me your ear and for being my rock!

I wish to thank the Geological Survey and Mines Department of Swaziland for their friendly assistance and support of my research, with special thanks to Dr. Noah Nhleko. I also extend my appreciation to the Surveyor General's Department for their generosity in providing me with the necessary aerial photographs, and the Kubuta Sisa Cattle Ranch for granting me access to their land.

Thank you to my friends, family and parents for their many years of physical and emotional support. Mom – thanks for being there over the past few months and for taking charge when I was too tired or overwhelmed to cope; and Dad – thank you for always being my sounding board and star technical support!

Most of all, thank you Konrad for suggesting in 2002 that I study geology, and for standing behind me every step of the way. Thank you for being an ocean of calmness, for your wit and humour and for bringing me back to my senses; for staying up with me when I had to work late; for proofreading manuscripts of which you understand nothing save the words "Ancient g-neises"; for holding my hand when things got really rough, and for celebrating my every success.

This research was supported by South African National Research Foundation (NRF) funding to Gary Stevens via the SARChI programme, as well as a PhD bursary granted to me for the duration of my studies.

Table of Contents

List of Figures

List of Tables

Chapter 1

GENERAL INTRODUCTION

CHAPTER 1

The nature of the geological processes that controlled initial crustal growth and evolution during the early stages of Earth's history remains the subject of intense scientific debate (e.g. De Wit, 1998; Hamilton, 1998; Collins et al., 1998; Marshak, 1999; Collins and Van Kranendonk, 1999; Kisters et al., 2003; Stern, 2005; Moyen et al., 2006; Bédard, 2006; Condie and Pease, 2008). Given the limited record of such ancient crust worldwide, excellent exposure of Paleo- to Neoarchaean (i.e. ca. 3.7-2.7 Ga) rocks from the Barberton and Ancient Gneiss Complex granite-greenstone terranes in South Africa and Swaziland are invaluable to understanding these processes. Together they record events related to the formation and stabilisation of an early continental nucleus, the Kaapvaal Cratonic shield, which spans a period of almost 1 Ga. Hence, there are few other places in the world where such a continuous record of crustal evolution can be chronicled in rocks that are as well preserved.

There is no general consensus on whether the early Earth was characterised by magmatic and tectonic processes very different, or analogous to those of today. Notable differences between Archaean and post-Archaean terranes are that the former tend to be dominated by trondhjemite-tonalite-granodiorite (TTG) suite granitoids and mafic-ultramafic (e.g. high MgO komatiite) volcanic rocks compositionally unique to the Archaean. In addition, some investigators have argued that many of the distinctive features diagnostic of Phanerozoic-style plate-tectonics, e.g. ophiolites, rifted margin successions, accretionary wedges, magmatic arcs, high-pressure low-temperature subduction-zone metamorphic signatures, are absent from the Archaean rock record and hence, modern plate-tectonic processes could not have been operational in the Archaean (Hamilton, 1998). Central to the debate on early Earth processes are speculations on the potential consequences of an Archaean crust and mantle 100-300 ºC hotter than today, arising from primordial heat retention by the young Earth and a greater concentration of the radioactive elements U, Th and K in the mantle (e.g. Lambert, 1976; Thompson, 1984; Richter, 1985; Percival, 1994). Some of the proposed consequences include: a more vigorously convecting mantle; more abundant mantle plumes; higher degrees of partial melting in the mantle; faster spreading rates and plate motions; thicker and more buoyant oceanic lithosphere which was difficult to subduct, resulting in shallower subduction angles or failed subduction; higher geothermal gradients; rheologically weaker lithosphere; and density stratification of the crust (e.g. Hamilton, 1998; Marshak, 1999, Bédard, 2006, Condie and Pease, 2008 and references therein for discussion). On the other hand, De Wit (1998) has pointed out that there are no constraints on the rate and efficiency of heat-loss by the Archaean Earth, and that the high MgO komatiites, which seemingly require an extremely hot mantle source, could have

been derived from a hydrous Archaean mantle <100 ºC hotter than today. Hence, subduction-accretion processes may have been viable on Earth as early as the Paleoarchaean (De Wit, 1998). This is supported by a wealth of recent geochronological, geochemical, palaeomagnetic, stratigraphic, structural, and metamorphic data from Archaean cratons around the world including Yilgarn, Pilbara, Superior, North China, Slave, and Southern Africa, which point towards a modern-style of plate tectonics by lateral accretion since at least the Mesoarchaean (e.g. Cawood et al., 2009, Condie and Pease, 2008 and references therein).

The well-studied and characterised Barberton Greenstone Belt (BGB) in South Africa and Swaziland is divided into three main lithostratigraphic units (Fig. 1.1): the lower mafic-ultramafic volcanic and mafic-silicic volcanoclastic, ca. 3.55-3.30 Ga Onverwacht Group, which is overlain by clastic marine sediments and felsic volcanic rocks of the ca. 3.26-3.22 Ma Fig Tree Group and coarse-grained sandstones and conglomerates of the < ca. 3.22 Ga Moodies Group. The greenstone belt is bordered on all sides by ca. 3.5 to 3.2 Ga TTG gneisses, as well as granitoids belonging to the ca. 3.14-3.10 Ga granodiorite-monzogranite-syenogranite (GMS) suite which is extensively developed throughout South Africa and Swaziland. Investigations into the tectono-metamorphic evolution of the BGB has revealed that it is made up of discrete, fault-bounded tectonic blocks that have experienced complex, polyphase deformational and metamorphic histories (e.g. De Wit et al., 1992; De Ronde and De Wit, 1994; Kamo and Davis, 1994; Lowe, 1994; Lowe et al., 1999; De Ronde and Kamo, 2000; Dziggel et al., 2002; Kisters et al., 2003; Diener et al., 2005; Moyen et al., 2006; Lowe and Byerly, 2007; Schoene et al., 2008; Schoene et al., 2009). Two well-documented deformational events, D_1 at ca. 3.45 Ga and D_2 at ca. 3.23 Ga, coincided with periods of TTG magmatism and greenschist- to amphibolite-facies metamorphism. Thrusting and recumbent folding associated with D_1 deformation mainly affected lower units of the Onverwacht Group and is documented in the southern domain of the belt (De Ronde and De Wit, 1994). D_1 was accompanied by upper-greenschist-facies metamorphism, interpreted to have resulted from both seafloor and burial metamorphism associated with this event (Cloete, 1991; Lopez-Martinez et al., 1984).

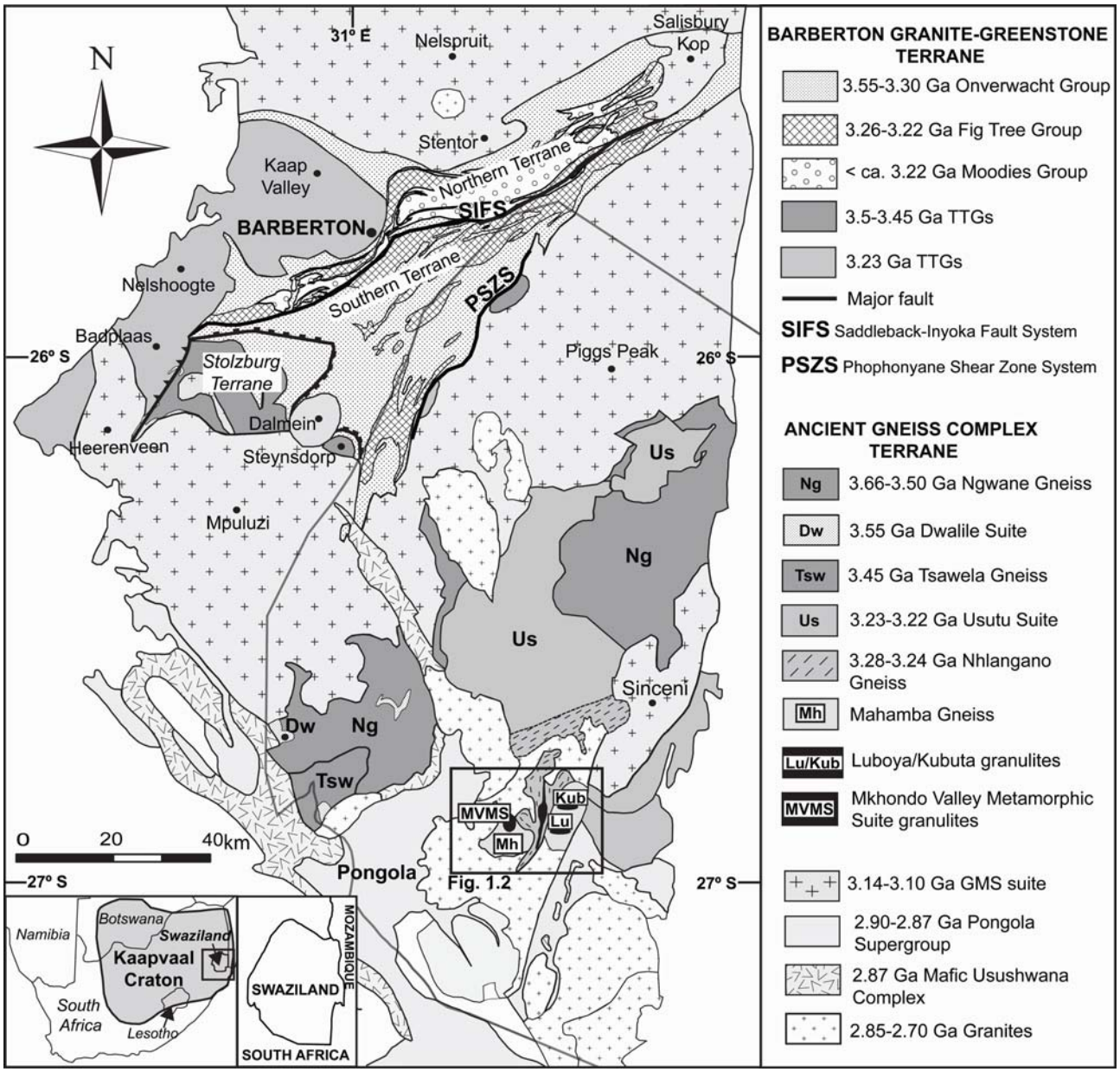

Figure 1.1 *Simplified geological map of the eastern Kaapvaal Craton, modified after Wilson (1982) and Schoene and Bowring (2010). The map depicts important components of the Barberton granite-greenstone terrane, the Ancient Gneiss Complex and the granodiorite-monzogranite-syenogranite (GMS) suite. The black box indicates the study area and the location of the metasedimentary granulites referred to in the text (see Fig. 1.2 for a detailed map of the Mkhondo, Ngudwane-Luboya and Matsanjeni River outcrops).*

Although alternative interpretations of the D_2 structural and metamorphic elements in the BGB exist (e.g. density-driven, partial convective overturn of a stratified crust at ca. 3.23 Ga; Van Kranendonk et al., 2009), the m ajority of studies which have docum ented the regional tectono-m etamorphic event D_2, are in strong support of a subduction -accretion model for the main assembly phase of the BGB and surrounding orthogneiss terrane at ca. 3.23 Ga in a collisional arc setting (e.g. De Ronde

and De Wit, 1994; Kamo and Davis, 1994; Lowe 1994; Lowe et al., 1999; De Ronde and Kamo, 2000; Dziggel et al., 2002; Kisters et al., 2003; Diener et al., 2005; Moyen et al., 2006; Schoene and Bowring, 2010; Lana et al., 2010b). This is proposed to have resulted from the juxtaposition of microcontinental fragments with distinct tectono-stratigraphic and geochronological characteristics, namely suturing of the ca. 3.33 Ga Northern and ca. 3.45 Ga Southern Barberton terranes along the Saddleback-Inyoka Fault System, partial subduction followed by post collisional exhumation of the ca. 3.50-3.45 Ga Stolzburg block to the south of the belt (e.g. Kisters et al., 2010; Lana et al. 2010b), as well as accretion of the ca. 3.66 Ga Ancient Gneiss Complex (AGC) terrane to the southeast of the greenstone belt along the Phophonyane Shear Zone System (e.g. Lana et al., 2011) (Fig. 1.1). The combined stratigraphic, magmatic, structural and metamorphic evidence from these studies suggests the presence of a northwest-dipping subduction-zone at ca. 3.30-3.23 Ga (Kamo and Davis, 1994; Dziggel et al., 2002; Diener et al., 2005; Moyen et al., 2006; Lana et al., 2011; Kisters et al., 2010). This is seen, for example, in the deposition of upward coarsening, volcanic-arc like Fig Tree and terrigenous Moodies Group sedimentary successions in fault-bounded basins, consistent with ocean basin closure; synchronous syn- to late-tectonic TTG magmatism to the north of the belt (Kamo and Davis, 1994; Schoene et al., 2008; Kisters et al., 2010); regional shortening, thrusting and recumbent folding in the core of the belt (De Ronde and De Wit, 1994); and anomalously low geothermal gradients to the south (Dziggel et al., 2002; Diener et al., 2005; Moyen et al., 2006; Lana et al., 2011). Recently, Schoene and Bowring (2010) revised the subduction-accretion model by proposing a doubly vergent subduction zone, which dipped NW beneath the Northern Barberton terrane and SE beneath the southern Stolzburg and AGC terranes, to account for a comparable magmatic and deformational history in the AGC.

D_2 deformation and metamorphism in the BGB was followed by a protracted period of intracrustal differentiation and calc-alkaline granitoid magmatism, which gave rise to the voluminous 3.14-3.10 Ga GMS suite plutons (e.g. Schoene and Bowring, 2007; Kamo and Davis, 1994) (Fig. 1.1). Recent Sm-Nd and Lu-Hf isotopic studies by Schoene et al. (2009) and Zeh et al. (2011) show that after ca. 3.23 Ga, the eastern Kaapvaal Craton behaved as a coherent lithospheric block dominated by intense crustal recycling. This played an important role in consolidating, and increasing the strength and preservation potential of the newly-assembled cratonic lithosphere, by cutting across pre-existing structural breaks and transporting heat-producing elements to the upper crust, leaving behind a large volume of refractory granulite-facies rocks in the lower crust (Schoene et al., 2008). Crustal differentiation was accompanied by continued regional shortening on the Craton (D_3 of De

Ronde and De Wit, 1994), and diachronous and differential orogen-parallel exhumation and cooling of the various crustal blocks, along all m argins of the BGB and AGC, between 3.23 and 3.10 Ga (De Ronde and De W it, 1994; Kisters et al., 2003; W estraat et al., 2005; Belcher and Kisters, 2006a; Schoene and Bowring, 2007; Schoene et al., 2008; Lana et al., 2010b; Lana et al., 2011).

After 3.10 Ga, the evolution of th e Kaapvaal Craton was marked by periods of convergence along the western and northern m argins of the prot o-continent (i.e. form ation of the 3.08-2.93 Ga Kraaipan and associated greenst one belts in the Kim berley te rrain, e.g. Robb et al., 1991 and Schmitz et al., 2004; and the 3.09-2.97 Ga Murchis on and associated greenstone belts in the Pietersburg terrain, e.g. see Poujol et al., 2003). By this tim e the sufficiently stable lithosphere w as able to support extensive intracratonic sedim entary basins in both the central (3.07-2.71 Ga Dominion and Witwatersrand Basins, e.g. Armstrong et al., 1991) and south-eastern domains of the Craton (2.98-2.83 Ga Pongola Basi n, e.g. Hegner et al., 1994 a nd G utzmer et al., 1999). The development of both of these basins seem s to have b een characterised b y an initial s tage of riftin g, indicated by the volcano-sedim entary successi ons of the lower Dom inion and Nsuze Groups, followed by a therm al subsidence stage that coinci ded with deposition of the siliciclastic W est-Central Rand and Mozaan Groups. By 2.7 Ga, se dimentation in the W itwatersrand and Pongola basins had ceased, and a num ber of discrete t ectono-magmatic events m arked the end of the Archaean d evelopment of the Kaap vaal Craton. Th is includ es th e well docum ented ca. 2.70 Ga Limpopo Orogeny along the northern m argin of the Craton (e.g. Smit and Van Reenen, 1997; Kreissig et al., 2001), an d a period of regional crustal m elting seen in th e extensive outpourings of the ca. 2.71 Ga Vent ersdorp Supergroup flood basalts (Arm strong et al., 1991), as well as widespread 2.7 Ga granitic magmatism (Poujol et al., 2003).

Compared to the BGB, the AGC is dom inated by a struc turally com plex interm ixture of TTG gneisses, i.e. the 3.66-3.50 Ga Ngwane, 3.45-3.43 Ga Tsawela, 3.28-3.24 Ga Nhlangano and 3.23-3.22 Ga Usutu Suite gneisses (e.g. Kröner et al., 1989; Schoene a nd B owring, 2010), with m inor supracrustal units (Fig. 1.1). The latter include s the ca. 3.55 Ga volcano -sedimentary Dwalile Suite in western Swaziland (Kröner and Tegtmeyer, 1994), and metasediments of unknown age in south-central Swaziland, namely the Mkhondo Valley Metamorphic Suite (Wilson, 1980, 1982; Condie et al., 1996) and paragneisses form erly known as the Bloemendal/Shiselweni gneisses (Kröner et al., 1993) but referred to here (for the sake of distinguishing between different outcrop localities) as the

Luboya and Kubuta gneisses (Fig. 1.1). At present, our understanding of the geological history of the AGC, and its context within the regional framework of the evolution of the Craton is limited. Importantly, building a comprehensive metamorphic framework for the AGC is essential to understanding the geodynamic history of this ancient crustal remnant. However, prior to the current work, no published, detailed metamorphic studies had been conducted on any of the rock units comprising the AGC. This largely stems from the fact that the AGC is an orthogneiss-dominated terrane, containing very little of the supracrustal 'greenstone' material that is typically more useful for recording pressure-temperature (P-T) change. The existence of rare metasedimentary units within the AGC therefore provides excellent opportunities for conducting metamorphic studies of this kind. The most extensively preserved of these units occur in the form of high-grade, migmatitic paragneisses developed along a number of river sections in south-central Swaziland, i.e. the Mkhondo, Ngudwane-Luboya and Matsanjeni Rivers (Fig. 1.2).

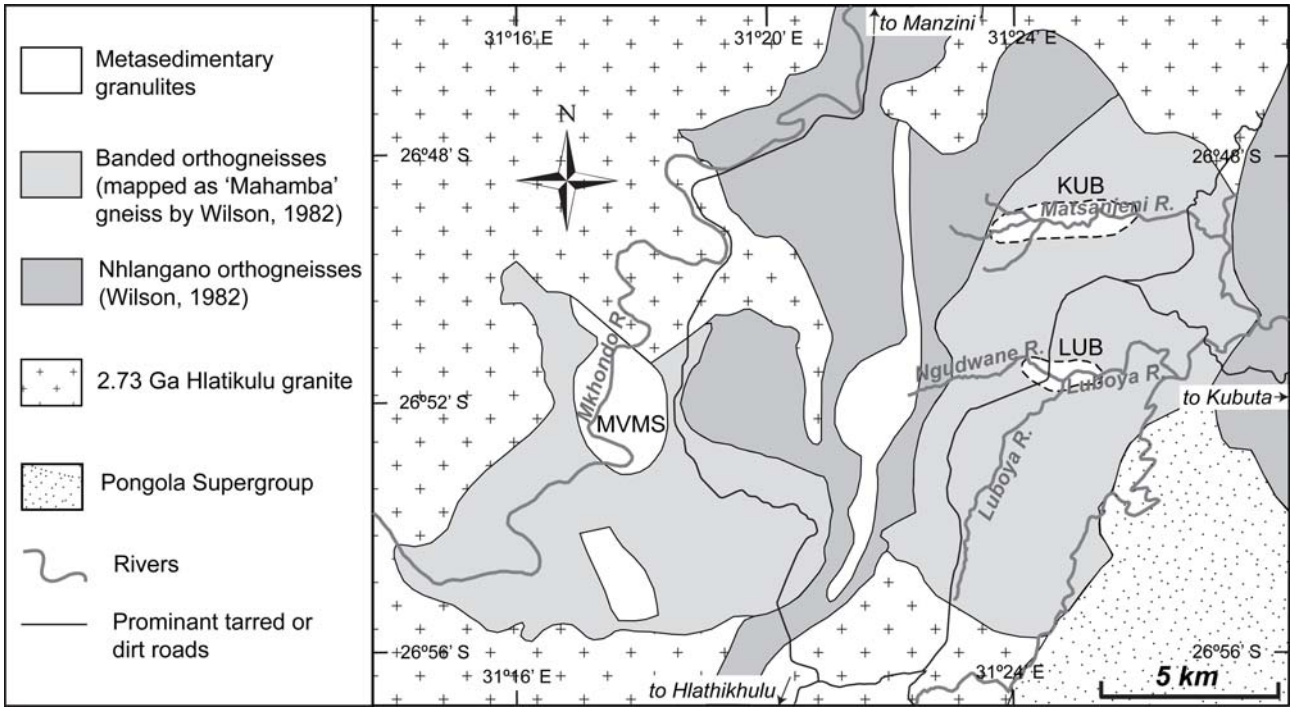

Figure 1.2 *Detailed map indicating the location of the Mkhondo, Ngudwane-Luboya and Matsanjeni Rivers in south-central Swaziland, and the Mkhondo Valley Metamorphic Suite (MVMS), Luboya (LUB) and Kubuta (KUB) metasedimentary granulites.*

The apparent granulite-facies metamorphism recorded by these gneisses contrasts with the typical greenschist- and, less commonly, amphibolite-facies metamorphism in the BGB and the Dwalile greenstone remnant in western Swaziland (e.g. Dziggel et al., 2002; Diener et al., 2005; Tegtmeyer,

1989). The granulites may therefore potentially inform on a multitude of processes associated with cratonic assembly, crustal differentiation and S-type granite (*senso stricto*) production during the Archaean. However, in order to fully understand the geological context within which these units occur, better constraints on both the conditions and ages of metamorphism are required. To date, ill-constrained P-T estimates for the gneisses were primarily based on the unpublished data of Milisenda (1986) (e.g. Kröner et al., 1993; Condie et al., 1996). In addition, there has been no consensus on the age(s) of metamorphism, and whether the granulites record more than one high-grade event. For example Condie et al. (1996) employed a mean Pb-Pb zircon evaporation method to date an *in situ* leucosome from the Mkhondo River, and obtained an age of 2745 ± 2 Ma for the partial melting event. Whole-rock Sm-Nd (isotope dilution) dating of pelitic gneiss samples by the same authors yielded an age of 2739 ± 154 Ma, and garnet separates from two metapelitic samples yielded Sm-Nd ages of 2653 ± 73 Ma and 2706 ± 61 Ma. In contrast, proposed metamorphic zircon grains from the Matsanjeni River granulites have yielded an unpublished Pb-Pb zircon evaporation age of ca. 3.30 Ga for the metamorphism (Kröner et al., 1993).

Differentiation of the crust through partial melting of sedimentary material is integral to the recycling of Earth's continental lithosphere. Partial melting of sedimentary detritus gives rise to a geochemically distinct class of granitoid (i.e. 'S-type') which typically displays a range in composition from leucogranitic through monzogranitic to granodioritic. A characteristic chemical feature of these granites is their tendency to closely reflect certain aspects of their source-rock chemistry, e.g. the aluminous character of S-type granite sources (Chappell and White, 1974; Clemens, 2003). One dominant theory of how this imaging occurs involves the entire unmelted fraction of the source becoming entrained in the melt during granitic magma segregation, known as the 'restite entrainment model' of Chappell and White (1974) (further developed by White and Chappell, 1977; Chappell et al., 1987; Chappell, 1997; and Chappell et al., 2000). A recently-proposed alternative hypothesis is that only the solid peritectic products of melting can realistically become entrained in the melt, termed 'selective peritectic phase entrainment' by Stevens et al. (2007) and Villaros et al. (2009a & b) (see also Villaros et al., 2011, and Clemens et al., 2011). The latter model adequately explains the variability of certain chemical parameters observed in S-type granites, such as K_2O and Na_2O, whilst accounting for a consistently close correlation between other components such as FeO + MgO and TiO_2 in the same rocks. Although the 'restite entrainment model' of Chappell and White (1974) has come to be regarded by some as a non-viable process for large-scale S-type magma generation and segregation (e.g. Clemens, 1989; 2003), the

physical mechanisms by which 'peritectic phase entrainment' takes place in the source as an alternative mechanism (Stevens et al., 2007), and the behaviour of such entrained phases during magma segregation, is not yet fully understood.

In light of this, in this thesis I attempt to contribute to the state of knowledge on both the evolution of the Barberton-AGC early cratonic crust and S-type magma production in general, by investigating the metamorphism and anatexis of these poorly understood metasedimentary granulites from south-central Swaziland (Fig. 1.2). I present the work as a compilation of three published and accepted manuscripts which were generated during the course of the PhD, and which can be summarised as follows.

(1) In the first manuscript I document granulite-facies metamorphism in metapelites from the Mkhondo Valley Metamorphic Suite which crop out along the Mkhondo River (Fig. 1.2). Here, a mid- to shallow-crustal, 830 – 850 °C partial melting event at ca. 2.73 Ga coincided with a period of regional crustal anatexis on the Craton. The metamorphism, and its implications for the evolution of the Kaapvaal Craton towards the end of the Neoarchaean, is consequently explored.

(2) The second manuscript is an investigation into the anatectic process in the Mkhondo Valley Metamorphic Suite, where unique insight into the details of S-type magma production and extraction from its source can be gained. In this paper I critically evaluate the generally accepted models for restite entrainment to account for the chemical connection that exists between granitic magmas and their sources. Specific features in the Mkhondo Valley Metamorphic Suite migmatites make a strong textural and mineral chemical case for the selective entrainment of peritectic garnet in the magma. This mechanism may account for the more mafic character of some natural peraluminous S-type granites when compared to typical compositions of natural and experimental melts.

(3) In the third manuscript I present a combination of metamorphic, structural and U-Pb zircon and monazite age constraints for the Luboya and Kubuta metapelitic and metapsammitic granulites which crop out along the Ngudwane-Luboya and Matsanjeni Rivers (Fig. 1.2). Remarkably these migmatites, located a mere 20 km E to NE of the Mkhondo Valley Metamorphic Suite, record hitherto undocumented episodes of Mesoarchaean, high-grade polymetamorphism and deformation.

In this paper I explore the regional implications of the metamorphism, which coincided with terrane assembly at 3.23 Ga and consolidation of the Kaapvaal Craton between 3.23 Ga and 3.10 Ga.

References

Armstrong, R.A., Compston, W ., Retief, E.A., W illiams, I.S., and W elke, H.J., 1991, Zircon Ion Microprobe studies bearing on the age and evol ution of the W itwatersrand Triad: Precam brian Research, v. 53, p. 243-266.

Bédard, J.H., 2006, A cataly tic delam ination-driven m odel for coupled genesis of Archaean crust and sub-continental lithospheric mantle: Geochimica et Cosmochimica Acta, v. 70, p. 1188-1214

Belcher, R.W., and Ki sters, A.F.M., 2006a, Synt ectonic em placement and deform ation of the Heerenveen batholith: conjectures on the structural setting of the 3.1 Ga granite magmatism in the Barberton granite-greenstone terrain, South Africa: Geological Society of America, Special Paper, v. 405, p. 211-231.

Cawood, P.A., Kröner, A., Collins, W.J., Kusky, T.M., Mooney, W .D., and W indley, B.F., 2009, Accretionary orogens through Earth history: Geological Society, London, Special Publications, v. 318; p. 1-36.

Chappell, B.W ., 1997, Com positional variatio n within granite suites o f the Lachlan Fold Belt: its causes and im plications f or the physica l state of granitic m agma: Transac tions of the Royal Society of Edinburgh, Earth Science, v. 88, p. 159-170

Chappell, B.W., and W hite, A.J.R., 1974, Two contra sting granite types: Pacific Geology, v. 8, p. 173-174.

Chappell, B.W., W hite, A.J.R., and Wyborn, D., 1987, The importance of residual source m aterial in granite petrogenesis: Journal of Petrology, v. 28, p. 1111-1138.

Chappell, B.W., White, A.J.R., Williams, I.S., Wyborn, D., and Wyborn, L.A.I., 2000, Lachlan Fold Belt granites revised: high- and low-temperature granites and their implications: Australian Journal of Earth Science, v. 47, p. 123-138

Clemens, J.D., 1989, The importance of residual source material (restite) in granite petrogenesis: a comment: Journal of Petrology, v. 30, p. 1313-1316.

Clemens, J.D., 2003, S-type granitic magmas-petrogenetic issues, models and evidence: Earth-Science Reviews, v. 61, p. 1-18.

Clemens, J.D., Stevens, G., and Farina, R., 2011, The enigmatic sources of I-type granites: the peritectic connexion: Lithos, *in press*
DOI 10.1016/j.lithos.2011.07.004

Cloete, M., 1991, An overview of metamorphism in the Barberton greenstone belt, *in* Ashwal, L.D., ed., Two Cratons and an Orogen - Excursion Guidebook and Review Articles for a Field Workshop through Selected Archean Terranes of Swaziland, South Africa and Zimbabwe: Johannesburg, IGCP project 280, Department of Geology, University of the Witwatersrand, p. 84-98.

Collins, W.J. and Van Kradendonk, M.J., 1999, Model for the development of kyanite during partial convective overturn of Archaean granite-greenstone terranes: the Pilbara Craton, Australia: Journal of Metamorphic Geology, v. 17, p. 145-156.

Collins, W.J., Van Kradendonk, M.J., and Teyssier, C., 1998, Partial convective overturn of the Archaean crust in the eastern part of the Pilbara Craton, Western Australia: 2. Driving mechanisms and tectonic implications: Journal of Structural Geology, v. 20, p. 1405–1424.

Condie, K.C., Kröner, A., and Milisenda, C. C., 1996, Geochemistry and geochronology of the Mkhondo suite, Swaziland: Evidence for passive-margin deposition and granulite-facies metamorphism in the late Archaean of southern Africa: Journal of African Earth Sciences, v. 22, p. 483-506.

Condie, K.C., and Pease, V., 2008, When did plate tectonic begin on planet Earth?: The Geological society of America, Special Paper, v.440, p. 294

De Ronde, C.E.J., and De Wit, M.J., 1994, Tectonic history of the Barberton greenstone belt, South Africa: 490 million years of Archean crustal evolution: Tectonics, v. 13, p. 983-1005.

De Ronde, C.E.J., and Kamo, S.L., 2000, An Archean arc-arc collisional event: A short-lived (ca. 3Myr) episode, Weltevreden area, Barberton greenstone belt, South Africa: Journal of African Earth Sciences, v. 30, p. 219-248.

De Wit, M.J., 1998, On Archaean granites, greenstones, cratons and tectonics: does the evidence demand a verdict?: Precambrian Research, v. 91, p. 181–226.

De Wit, M.J., Roering, C., Hart, R.J., Armstrong, R.A., De Ronde, C.E.J., Green, R.W.E, Tredoux, M., Peberdy, E., and Hart, R.A., 1992, Formation of an Archaean continent: Nature, v. 357, p. 553-562.

Diener, J.F.A, Stevens, G., Kisters, A.F.M., and Poujol, M., 2005, Geotectonic evolution of the Tjakastad Schist belt, Barberton greenstone belt, South Africa: a record of mid-Archaean metamorphism and terrain exhumation: Precambrian Research, v. 143, p. 87-112.

Dziggel, A., Stevens, G., Poujol, M., Anhaeusser, C.R., and Armstrong, R.A., 2002, Metamorphism of the granite-greenstone terrane south of the Barberton Greenstone Belt, South Africa: An insight into the tectono-thermal evolution of the 'lower' portions of the Onverwacht Group: Precambrian Research, v. 114, p. 221-247.

Gutzmer, J., Nhleko, N., Beukes, N.J., Pickard, A., and Barley, M.E., 1999, Geochemistry and ion microprobe (SHRIMP) age of a quartz porphyry sill in the Mozaan Group of the Pongola Supergoup: implications for the Pongola and Witwatersrand Supergroups: South African Journal of Geology, v. 102, p. 139–146.

Hamilton, W.B., 1998, Archaean magmatism and deformation were not products of plate tectonics: Precambrian Research, v. 91, p. 143–179.

Hegner, E., Kröner, A., and Hunt, P ., 1994, A preci se U–Pb zircon age for the Archaean Pongola Supergroup volcanics in Swaziland: Journal of African Earth Sciences, v. 18, p. 339–341.

Kamo, S.L., and Davis, D.W ., 1994, Reassessm ent of Archaean crustal developm ent in the Barberton Mountain Land, South-Africa, based on U-Pb dating: Tectonics, v. 13, p. 167-192.

Kisters, A.F.M., Belcher, R.W ., Poujol, M., and Dziggel, A., 2010, Continental growth and convergence-related arc plutonism in the Mesoar chaean: Evidence from the Barberto n granitoid-greenstone terrain, South Africa: Precambrian Research, v. 178, p. 15-26.

Kisters, A.F.M., Stevens, G., Dziggel, A., and Arm strong, R.A., 2003, Extensional detachm ent faulting and core-com plex form ation in the sout hern Barberton granite-g reenstone terrain, South Africa: evidence for a 3.2 Ga orogenic collapse: Precambrian Research, v. 127, p. 355-378.

Kreissig, K. , Holzer, L., Frei, R., Villa, I.M., Kr amers, J.D., Kröner, A., Sm it, C.A., and Van Reenen, D., 2001, Geochronology of the Hout River Shear Zone and the m etamorphism in the Southern Marginal Zone of the Limpopo Belt, S outhern Africa: Precam brian Research, v. 109, p. 145-173.

Kröner, A., Compston, W., and Williams, I.S., 1989, Growth of early Archaean crust in the Ancient Gneiss Complex of Swaziland as revealed by single zircon dating: Tectonophysics, v. 161, p. 271-298.

Kröner, A., and Tegtm eyer, A., 1994, Gneiss-greens tone relationships in the Ancient Gneiss Complex of southwestern Swaziland, southern Africa, and im plications for early crustal evolution: Precambrian Research, v. 67, p. 109-139.

Kröner, A., W endt, J.I., Milis enda, C.C., Compston, W ., and Maphalala, R., 1993, Zirco n geochronology and Nd isotopic system atic of the Ancient Gneiss Com plex, Swaziland, and implications for crustal evolution, *in* Kröner, A., ed., The Ancient Gneiss Com plex: Overview papers and guidebook for excursion: Swaziland Geological Survey and Mines Departm ent., Bulletin 11, p. 15-37.

Lambert, R.St.-J., 1976, Archaean therm al regimes, crustal and upper m antle temperatures, and a progressive evolutionary m odel for t he Earth. In : W indley, B.F. (Ed.), The Early History of the Earth. J.Wiley, London, p. 363–373.

Lana, C., Buick, I., Stevens, G., Rossouw, R., and De Wet, W., 2011, 3230-3200 Ma post-orogenic extension and mid-crustal magmatism along the southeastern margin of the Barberton Greenstone Belt, South Africa: Journal of Structural Geology, *in press*

Lana, C., Kisters, A.F.M., and Stevens, G., 2010b, Exhumation of Mesoarchean TTG gneisses from the mid-crust: Insights from the Steynsdorp core complex, Barberton granitoid-greenstone terrain, South Africa: Geological Society of American Bulletin, v. 122, p. 183-197.

Lopez-Martinez, M., York, D., Hall, C.M., and Hanes, J.A., 1984, Oldest reliable $^{40}Ar/^{39}Ar$ ages for terrestrial rocks: Barberton Mountain komatiites: Nature, v. 307, p. 352–354.

Lowe, D.R., 1994, Accretionary history of the Ar chean Barberton greenst one belt (3.55-3.22 Ga), Southern Africa: Geology, v. 22, p. 1099-1102.

Lowe, D.R., and Byerly, G.R., 2007, An overview of the geology of the Barberton greenstone belt and vicinity: Implications for early crustal development: *in* Van Kranendonk, M.J., Sm ithies, H., and Bennett, V., ed., Earth's Oldest Rocks, Elsevier, Amsterdam, p. 481-526.

Lowe, D.R., Byerly, G.R., and Heubeck, C., 1999, St ructural divisions and developm ent of the west-central part of the Barberton Greenstone Belt: *in* L owe, D.R., and Byerly, G.R., ed., Geologic evolution of the Barberton Greenstone Belt, South Africa: Geological Society of America, Special Paper, v. 329, p. 37-82.

Marshak, S ., 1999, Defor mation style way back when: thoughts on the contrasts between Archaean/Paleoproterozoic and contemporary oroge ns: Journ al of Structural Geolog y, v. 21, p. 1175–1182.

Milisenda, C.C., 1986, Petrographie und geochem ie archaischer granulite und gneise des Ancient Gneiss Complex in Swaziland, südliches Afrika. Unpublished Diplom a Thesis, University of Mainz, Germany, p. 137.

Moyen, J.F., Stevens, G., and Kisters, A., 2 006, Record of m id-Archaean subduction from metamorphism in the Barberton terrain, South Africa: Nature, v. 442, p. 559-562.

Percival, J. A., and Hel mstaedt, H., 2004, Insight s on Archean continent–ocean assem bly, western Superior P rovince, from ne w structural, geochemical and geochronological observations: Introduction and summary: Precambrian Research, v. 132, p. 209–212.

Poujol, M., Robb, L.J., Anhaeusser, C.R., and Geri cke, B., 2003, A review of the geochronological constraints on the evolution of the Kaapvaal Craton, South Africa: Precambrian Research, v. 127, p. 181-213.

Richter, F.M., 1985. Models for the Archean therm al regime: Earth and Planetary Science Letters, v. 73, p. 350–360.

Robb, L.J., Davis, D.W ., and Kam o, S.L., 1991, Ch ronological fram ework for the W itwatersrand Basin and environs: towards a time constrained depositional m odel: S outh African Journal of Geology, v. 94, p. 86-95

Schmitz, M. D., Bowring, S. A., De W it, M. J., and Gartz, V., 2004, Subduction and terrane collision stabilized the western Kaapvaal craton tectosphere 2.9 billion years ago: Earth and Planetary Science Letters, v. 222, p. 363-376.

Schoene, B., and Bowring, S.A., 2007, Determ ining accurate tem perature-time paths in U-Pb thermochronology: An exam ple from the SE Kaa pvaal craton, southern Af rica: Geochim ica et Cosmochimica Acta, v. 71, p. 165-185.

Schoene, B., and Bowring, S.A., 2010, Rates and mechanisms of Mesoarchean m agmatic arc construction, eastern Kaapvaal crato n, Swazila nd: Geological Society of Am erican Bulletin, v. 122, p. 408-429.

Schoene, B., De W it, M.J., and B owring, S.A., 2008, Mesoarchean assem bly and stabilization of the eastern Kaapvaal cr aton: a structural-therm ochronological perspectiv e: Tectonics, v. 27, doi:10.1029/2008TC002267, TC5010.

Schoene, B., Dudas, F.O.L., Bo wring, S.A., and De W it, M.J., 2009, Sm-Nd isotopic m apping of lithospheric growth and stabiliz ation in the eastern Kaapvaal craton: Terra Nova, v. 21, p. 219-228.

Smit, C.A., and Van Reenen, D., 1997, Deep crus tal shear zones, high- grade tectonics, and associated metasomatic alteration in the Limpopo Belt, South Africa: implications for deep crustal processes: Journal of Geology, v. 105, p. 37-57.

Stern, R. J., 2005, Evidence from ophiolites, blue schists and ultrahigh- pressure m etamorphic terranes that the modern episode of subduction tectonics began in the Neoproterozoic: Geology, v. 33, p. 557–560.

Stevens, G., Villaros, A ., and Moy en, J.F., 20 07, Se lective peritectic garn et entrainm ent as the origin of geochemical diversity in S-type granites: Geology, v. 35, p. 9-12.

Tegtmeyer, A.R., 1989, Geochr onologie und geochem ie im Präka mbrian des südlichen Afrika. Unpublished Dissertation, University of Mainz, Germany, p. 270.

Thompson, A.B., 1984, Geotherm al gradients through time. In: Holland, H.D., Trendall, A.F (Ed.), Patterns of Change in Earth Evolution. Springer-Verlag, Berlin, p. 345-355.

Villaros, A., Buick, I.S., and Stevens, G., 2011, Isotopic variations in S-type granites: an inheritance from a heterogeneous source?: Contributions to Mineralogy and Petrology, *in press* DOI 10.1007/s00410-011-0673-9

Villaros, A., Stevens, G., and Buick, I.S., 2009a, Tracking S-type granite from source to emplacement: clues from garnet in the Cape Granite Suite: Lithos, v. 112, p. 217-235.

Villaros, A., Stevens, G., Moyen, J.F., and Buick, I.S., 2009b, The trace element compositions of S-type granites: evidence for disequilibrium melting and accessory phase entrainment in the source: Contributions to Mineralogy and Petrology, v. 158, p. 543-561.

Westraat, J. D., Kisters, A.F.M., Poujol, M., and Stevens, G. , 2005, Transcurrent shearing, granite sheeting and the increm ental construction of th e tabular 3.1 Ga Mpuluzi batholith, Barberton granite-greenstone terrain, South Africa: Geological Society of London, v. 162, p. 373-388.

White, A.J.R., and Chappell, B.W ., 1977, U ltrametamorphism and granitoid genesis: Tectonophysics, v. 43, p. 7-22.

Wilson, A.C., 1980, 1:50 000 Geological Map of Swaz iland, with explanatory notes. Swaziland Geological Survey and Mines Department, Mbabane.

Wilson, A.C., 1982, 1:250 000 Geologi cal Map of Swaziland, with e xplanatory notes. Swaziland Geological Survey and Mines Department, Mbabane.

Zeh, A., Gerdes, A., and Millonig, L., 2011, Hafn ium isotope record of the Ancient Gneiss Complex, Swaziland, southern Africa: evid ence for Archaean crust–m antle form ation and crust reworking between 3.66 and 2.73 Ga. Geological Society of London, v.168, p. 953-964.

Chapter 2

GRANULITE FACIES ANATEXIS IN THE ANCIENT GNEISS COMPLEX, SWAZILAND, AT 2.73 GA: MID-CRUSTAL METAMORPHIC EVIDENCE FOR MANTLE HEATING OF THE KAAPVAAL CRATON DURING VENTERSDORP MAGMATISM

CHAPTER 2

Presentation of the publication

This paper [*], first authored by Jeanne Taylor, was accepted for publication in the journal Precambrian Research. The following aspects of the research was done independently by Jeanne Taylor while receiving standard supervision by her supervisor Gary Stevens: (i) fieldwork and sampling; (ii) zircon separation, and preparation of zircon separates for SHRIMP dating; (iii) mineral equilibria modelling in Thermocalc; (iv) acquisition of mineral chemical data on the SEM, and zircon U-Pb data on the SHRIMP; (v) writing of the manuscript. Zircon U-Pb SHRIMP data reduction was done by Richard Armstrong. Alex Kisters guided the development of the debate around 2.7 Ga tectonic processes on the Kaapvaal Craton.

Jeanne Taylor[a]

Gary Stevens[a]

Richard Armstrong[b]

Alexander F.M. Kisters[a]

a: Centre for Crustal Petrology, Department of Earth Sciences, Stellenbosch University, Private Bag X1, Matieland 7602, South Africa

b: Research School of Earth Sciences, Australian National University, Canberra, Australia

---

Reference[*]: Taylor, J., Stevens, G., Armstrong, R., and Kisters, A. F.M., 2010, Granulite facies anatexis in the Ancient Gneiss Complex, Swaziland, at 2.73 Ga: Mid-crustal metamorphic evidence for mantle heating of the Kaapvaal craton during Ventersdorp magmatism: *Precambrian Research*, v. 177, p. 88–102. doi:10.1016/j.precamres.2009.11.005

Precambrian Research 177 (2010) 88–102

Contents lists available at ScienceDirect

Precambrian Research

journal homepage: www.elsevier.com/locate/precamres

Granulite facies anatexis in the Ancient Gneiss Complex, Swaziland, at 2.73 Ga: Mid-crustal metamorphic evidence for mantle heating of the Kaapvaal craton during Ventersdorp magmatism

Jeanne Taylor[a,*], Gary Stevens[a], Richard Armstrong[b], Alexander F.M. Kisters[a]

[a] Centre for Crustal Petrology, Department of Earth Sciences, Stellenbosch University, Private Bag X1, Matieland 7602, South Africa
[b] Research School of Earth Sciences, Australian National University, Canberra, Australia

ARTICLE INFO

Article history:
Received 21 July 2009
Received in revised form
18 November 2009
Accepted 18 November 2009

Keywords:
Ancient Gneiss Complex
Archaean
Metamorphism
Geochronology
Kaapvaal craton
Neoarchaean crustal evolution

ABSTRACT

The 3.7–3.2 Ga Ancient Gneiss Complex (AGC) of Swaziland, located S and SE of the Barberton Greenstone Belt (BGB), is a complex geological terrane where few studies have focussed on the timing and conditions of deformation and metamorphism, despite the fact that minor metasedimentary units within the AGC provide excellent opportunities for constraining metamorphic evolution. One of these, the Mkhondo Valley Metamorphic Suite consists of migmatitic metapelitic granulites, within which the peak metamorphic assemblage garnet + cordierite + biotite + plagioclase + quartz ± K-feldspar + melt is dominant. NCKFMASHTO pseudosection modelling of this anatectic assemblage constrains peak metamorphic conditions to 850–830 °C and 4.4 kbars, followed by near isobaric cooling of the terrane to 680 °C and 3.9 kbars. These conditions indicate a period of anomalously high heat flow within the crust due to the direct addition of mantle heat. U–Pb SHRIMP dating of zircons from an in situ leucosome indicates an age of ca. 2.73 Ga for peak granulite facies metamorphism, approximating the age of Ventersdorp Supergroup flood basalt volcanism on the craton and widespread intracratonic granitic magmatism. The current study suggests that substantial heat input to the Kaapvaal cratonic crust during underplating by Ventersdorp related magmas, possibly related to the presence of a ~2.7 Ga mantle plume marginal to the craton, was responsible for high-grade metamorphism in the AGC and a period associated with regional crustal anatexis. The resultant mid-crustal ductility and weakening may have initiated mobilisation of the mid-crust as gneissic domes, producing basement uplift and sedimentary recycling of auriferous reefs of the Central Rand Group of the Witwatersrand Supergroup.

1. Introduction

The Ancient Gneiss Complex (AGC) of Swaziland, located south and southeast of the Barberton Greenstone Belt (Fig. 1), is a complex Archaean terrane comprised of tonalite-trondhjemite-granodiorite (TTG) suite rocks and minor greenstone remnants which are cross-cut by numerous younger granite intrusives (Hunter, 1968, 1970, 1974; Jackson, 1984). Due to its early development at ~3.68–3.55 Ga (Compston and Kröner, 1988) the AGC, in combination with the Southern and Northern Barberton Terranes, has been proposed to form the oldest portion of the core to the early Kaapvaal cratonic shield around which continental growth via discrete crust forming tectono-magmatic events took place, from 3.7 to 2.6 Ga (De Wit et al., 1992). Despite the potential of the AGC to inform on the processes of cratonic assembly, surprisingly few studies have focussed on the timing and conditions of deformation and metamorphism in these rocks. Metasedimentary units make up a small fraction of the exposed geology, but are disproportionately useful in their potential to record metamorphic change during crustal recycling and growth. One of these units, in particular, migmatitic paragneisses from the Mkhondo Valley Metamorphic Suite (MVMS), preserves evidence for a period of high-grade metamorphism in south-central Swaziland that was accompanied by abundant in situ crustal anatexis (Hunter, 1970, 1974; Hunter et al., 1978, 1984, 1993; Milisenda, 1986; Wilson and Jackson, 1988; Kröner et al., 1993; Condie et al., 1996). Although the timing of the migmatite formation has recently been constrained to 2745 ± 2 Ma, the zircon evaporation age of an in situ anatectic leucosome (Condie et al., 1996), the geodynamic context for the high-grade metamorphism and partial melting remains poorly understood. Ill-constrained pressure–temperature (*P*–*T*) estimates for the MVMS range anywhere from >600 °C at 3 kbars (Hunter, 1970) to 700–900 °C at 5–8 kbars, and are primarily based on the unpublished metamor-

* Corresponding author. Tel.: +27 848760163.
E-mail addresses: jtaylor@sun.ac.za (J. Taylor), gs@sun.ac.za (G. Stevens), richard.armstrong@anu.edu.au (R. Armstrong), akisters@exchange.sun.ac.za (A.F.M. Kisters).

0301-9268/$ – see front matter © 2009 Elsevier B.V. All rights reserved.
doi:10.1016/j.precamres.2009.11.005

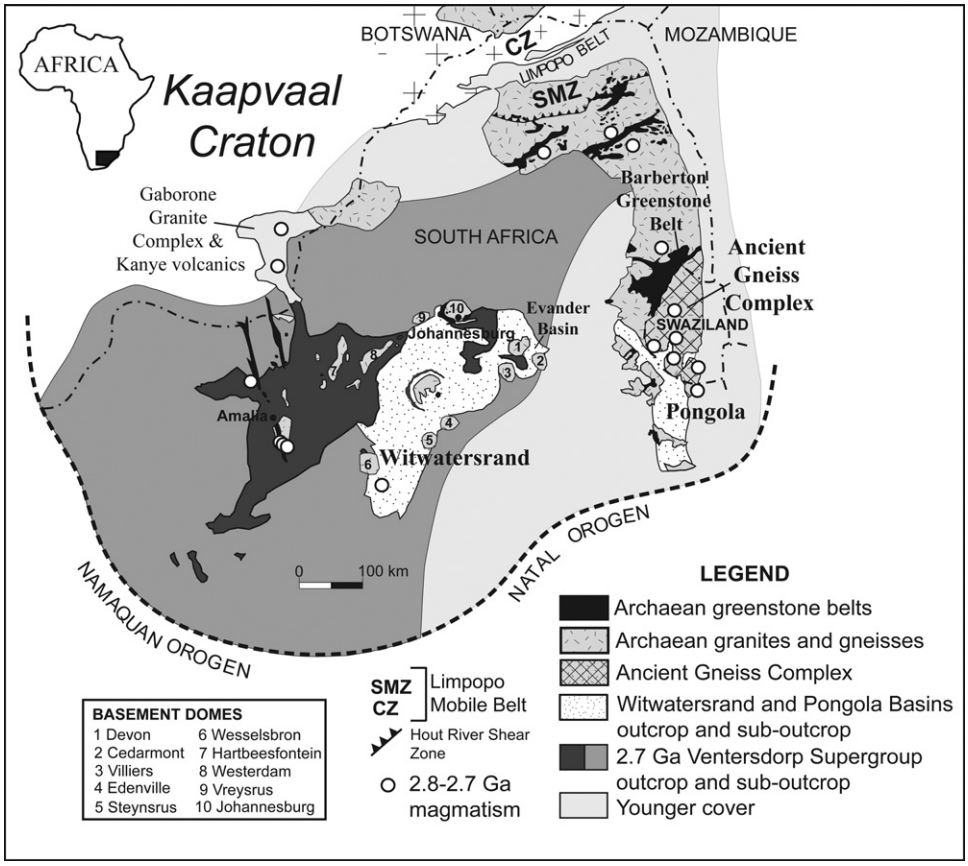

Fig. 1. Schematic diagram showing the various components of the Archaean Kaapvaal craton referred to in the text and widespread 2.8–2.7 Ga magmatism on the craton (white circles on the map), including the ~2.7 Ga Ventersdorp LIP outcrop and sub-outcrop (for more information on the various magmatic units see Hunter and Wilson, 1988; Layer et al., 1989; Hunter et al., 1992; Meyer et al., 1994; Maphalala and Kröner, 1993; Reimold et al., 1993; Robb et al., 1992, 1993; Kamo and Davis, 1994; Henderson et al., 2000; Kröner et al., 2000; Poujol et al., 1996, 2002, 2003; Poujol, 2001; Gericke, 2001; Anhaeusser and Walraven, 1999; Moore et al., 1993; Grobler and Walraven, 1993).

phic data of Milisenda (1986) (e.g. Kröner et al., 1993; Condie et al., 1996).

Assuming the above age of 2745 ± 2 Ma for peak metamorphism in the MVMS is correct, the timing of the high-grade metamorphism matches that proposed for continental collision and granulite facies metamorphism in the Southern Marginal Zone of the Limpopo Belt at ca. 2.7–2.6 Ga (Fig. 1) (Stevens and Van Reenen, 1992; Van Reenen et al., 1995; Smit and Van Reenen, 1997; Kreissig et al., 2001), as well as the timing of major ~2.71 Ga flood basalt volcanism on the craton during the formation of the Ventersdorp Supergroup Large Igneous Province (LIP) (Armstrong et al., 1991; Burke et al., 1985), and it coincides broadly with sedimentation of auriferous reefs within the 2.89–2.71 Ga Central Witwatersrand basin (Coward et al., 1995). Given the wide range in the existing *P–T* constraints for peak metamorphism and the lack of information on the *P–T* path followed by these rocks, the appropriate geological setting for high-grade metamorphism in the AGC and its broad regional significance cannot be resolved. For example, the lowest *P–T* estimates (700 °C at 3–5 kbars) are indicative of fluid-present melting and may have resulted from high levels of radiogenic heat production, and/or direct transfer of magmatic heat to the crust (Sandiford and Hand, 1998; Vernon et al., 1990; Wickham and Oxburgh, 1985); in contrast, the highest *P–T* estimates (900 °C at 8 kbars) are consistent with metamorphic conditions in the Southern Marginal Zone (SMZ) of the Limpopo Belt associated with crustal thickening (Van Reenen, 1983; Stevens and Van Reenen, 1992), and indicative of fluid-absent melting conditions.

Consequently, the current study aims to better constrain peak metamorphism and partial melting in the MVMS in order to understand the regional context for high-grade metamorphism and anatexis at a significant time in the evolution of the craton. In addition, a U–Pb SHRIMP zircon dating technique will be applied in an attempt to verify the single zircon evaporation age of Condie et al. (1996) as the age of high-grade metamorphism, given the known limitations of the evaporation method to correct for common Pb, judge the discordance of data and investigate the potential for inheritance in the zircons.

2. General geology of the Mkhondo Valley Metamorphic Suite

The current study focuses on the MVMS where it is best exposed as a 4.5 km × 2.5 km inlier along the Mkhondo River in south-central Swaziland (Fig. 2). Here the MVMS is characterised by a thick succession of migmatitic, metapelitic garnet–cordierite–biotite–feldspar ± opx bearing gneisses, metapsammitic cordierite–biotite–feldspar gneisses, metaquartzites, BIF, biotite–diopside–hornblende and cummingtonite–anthopyllite–cordierite gneisses (Milisenda, 1986; Wilson and Jackson, 1988; Kröner et al., 1993). In order to simplify the terminology the prefix 'meta' will be omitted from our description of these units, as all the MVMS rocks have been subjected to high-grades of metamorphism.

Wilson (1982) and Wilson and Jackson (1988) have in the past considered the MVMS paragneisses to be high-grade equivalents of the 2.97–2.87 Ga siliciclastic Mozaan Group of the Pongola Supergroup, a correlative of the Witwatersrand Supergroup (Nelson et al., 1995; Hegner et al., 1984). However, limited available geochronological data on the age of detrital zircons from the MVMS have indicated ages in excess of 3.36 Ga in the case of a garnet–biotite gneiss investigated by Kröner et al. (1993), and 3.43 Ga for a

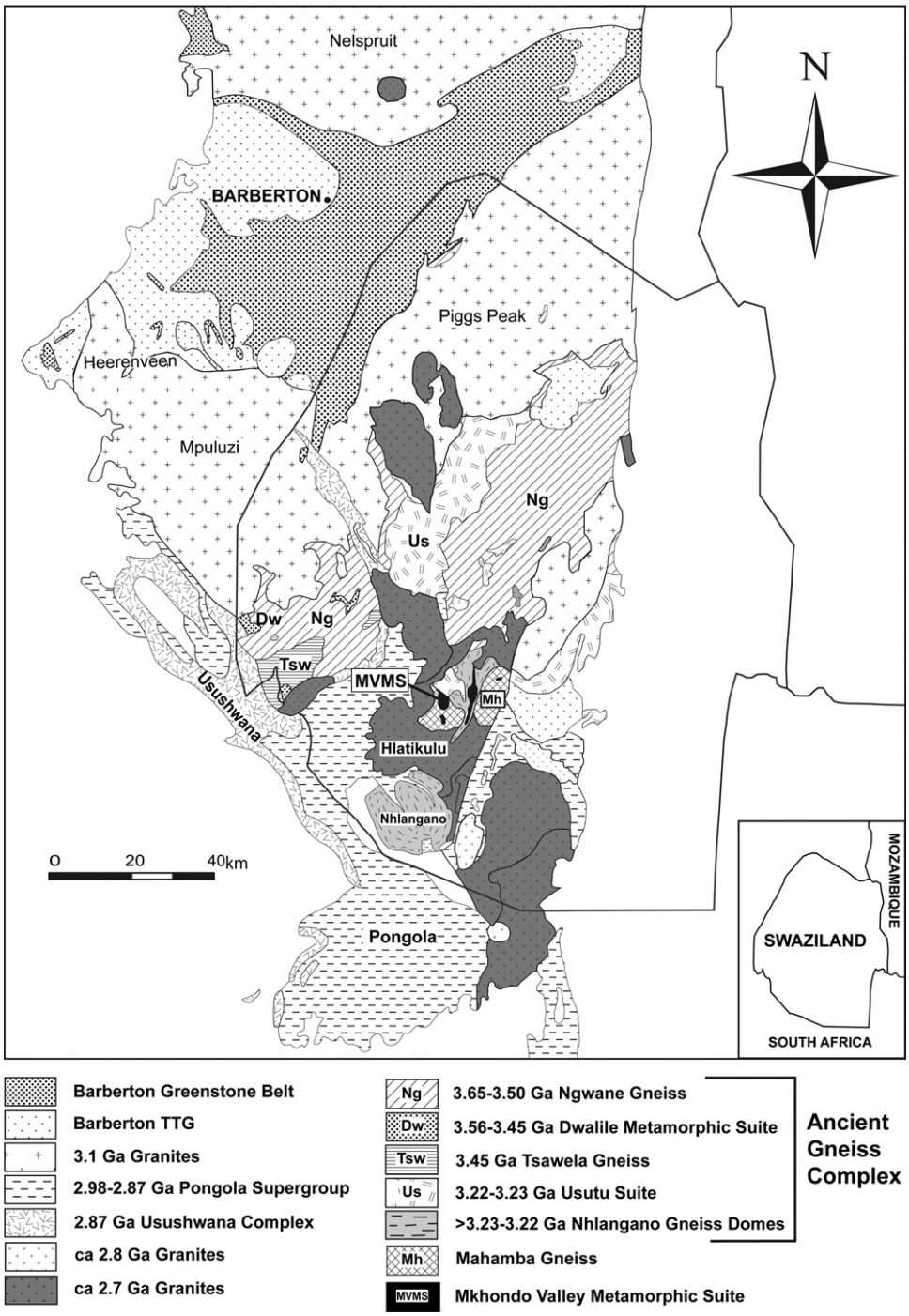

Fig. 2. Schematic geological map of Swaziland modified after Wilson (1982). Components of the Ancient Gneiss Complex include the Archaean TTGs, namely the Ngwane Gneiss, Tsawela Gneiss, Usutu Suite and Nhlangano Gneiss Domes, as well as the supracrustal Dwalile and Mkhondo Valley Metamorphic Suite. Also shown is the Barberton Greenstone Belt (BGB) and its associated TTGs, the ~2.98–2.87 Ga Pongola Supergroup, the ~2.87 Ga mafic Usushwana Complex intruding the northern margins of the Pongola Basin, and numerous ~2.7 Ga granites in Swaziland.

biotite–quartzite investigated by Condie et al. (1996). Detailed mapping has shown that the Mkhondo Valley inlier represents the preserved hinge zone of a doubly plunging synformal syncline (Wilson, 1982; Wilson and Jackson, 1988; Condie et al., 1996). Because of the deformation, age relations between the MVMS supracrustals and surrounding gneisses are mostly obscured (Condie et al., 1996). However, locally the MVMS is closely associated with the >3.2 Ga Nhlangano Granite Gneiss Dome (Schoene and Bowring, in press; Wilson and Jackson, 1988), and is intruded by the undeformed ca. 2.72 Ga Hlatikulu granite (Maphalala and Kröner, 1993) (Fig. 2).

3. Anatectic features of the Mkhondo Valley Metamorphic Suite

Both pelitic and psammitic layers preserve evidence for in situ anatexis, however, large variations in the degree of partial melting between rocks of different composition exists. Partial melting within highly fertile pelites has produced large peritectic garnet porphyroblasts that are composite in character. These are hosted in isolated, lensoid-shaped leucosome pockets (Fig. 3b), or are linked by thin, stromatic, foliation-parallel leucosomes. In areas of outcrop where the degree of partial melting was high, fossil melt-filled

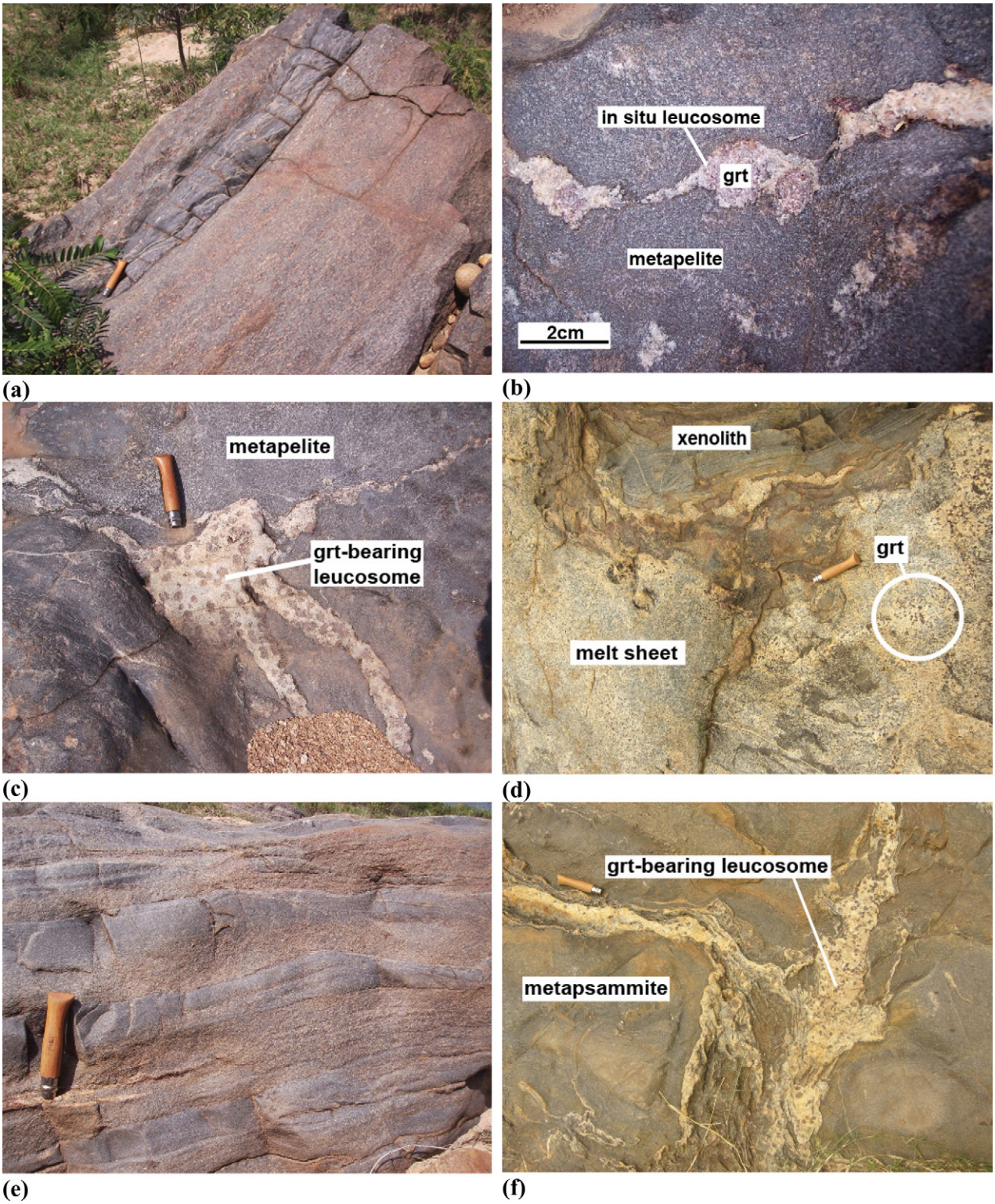

Fig. 3. Anatectic features of the Mkhondo Valley Metamorphic Suite. In the field photographs a pocket-knife of 10 cm is used for scale: (a) sedimentary layering in the pelites and psammites; (b) garnet-bearing leucosomes that have developed in situ during partial melting of the highly fertile pelites; (c) cross-cutting, garnet-bearing leucosomes marking the sights of melt accumulation; (d) a garnet-bearing melt sheet intruding adjacent psammites, and carrying xenoliths of the more competent material; (e) sedimentary structures preserved in undeformed psammites, such as graded and trough-cross beds; (f) garnet-bearing leucosomes intruding and brecciating the psammites, prior to melt drainage from these sites.

channels feed into one another to form an interconnected melt drainage network of 2–20 cm, concordant or cross-cutting leucosomes that are largely undeformed (Fig. 3c). These coalesce further into granitic melt sheets or small intrusive bodies of garnet-bearing granite. Thus melt segregation appears to have been efficient, and migmatites are predominantly metatexitic in character.

Cross-cutting leucosomes and melt sheets are generally discordant to the compositional layering within less fertile psammites,

and typically carry rafts of the more competent material (Fig. 3d). Psammites that preserve original sedimentary structures such as graded bedding and trough-cross beds (Fig. 3e), have contributed clasts to large melt-filled breccias. Within the breccias, meter-scale psammitic clasts are rotated relative to one another, separated by leucosome layers ≤10 cm thick (Fig. 3f). These structures are interpreted to reflect zones of considerable melt accumulation, within which clasts of unmelted rock rotated prior to collapse during melt extraction. The common occurrence of more competent psammitic clasts within these breccias may indicate that deformation of competent layers was important in creating space at the sites of melt accumulation (Kisters et al., 1998).

The above field evidence indicates that high-grade metamorphism and partial melting within the MVMS was responsible for the production of significant volumes of S-type granitic melt. As large garnet crystals developed in conjunction with leucosomes at the sites of melting, incongruent melting of biotite via the reaction biotite + quartz + plagioclase = garnet + cordierite + K-feldspar + melt was likely responsible for the bulk of the melt and for the development of the dominant peak metamorphic assemblage. For the purposes of this study, representative samples of MVMS pelites and leucosomes were collected along the banks of the Mkhondo River (26°52′S and 31°17′E).

4. Petrography and mineral chemistry

4.1. Pelites

In the pelites, 5–20 mm poikiloblastic garnet aggregates and 0.3–2 mm cordierite poikiloblasts are hosted in a fine- to medium-grained matrix consisting of platy red-brown biotite, quartz, plagioclase ± perthitic K-feldspar with minor apatite, monazite, zir-

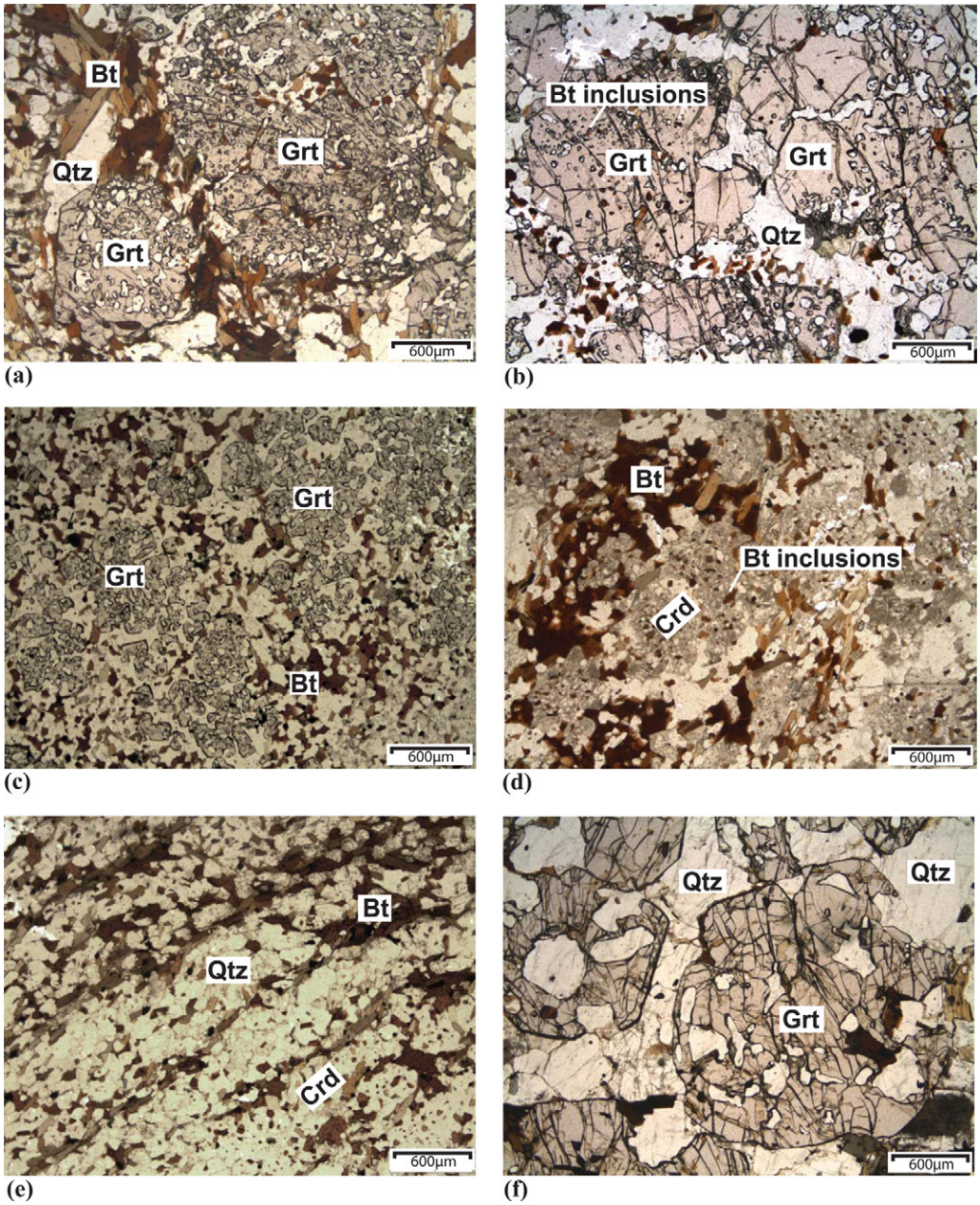

Fig. 4. Photomicrographs: (a and b) subhedral garnet poikiloblasts, and (c) interlocking networks of poikilitic garnet fragments in the pelites. The garnets contain numerous lobate, rounded quartz and rounded biotite inclusions; (d) cordierite poikiloblasts in the pelites contain flaky or rounded biotite, rounded quartz as well as minor plagioclase and K-feldspar inclusions; (e) cordierites are occasionally aligned in the foliation where the weak to moderate fabric is defined by bands of matrix biotite, quartz, and feldspar; (f) subhedral to euhedral, coarse-grained garnet in the leucosomes is hosted in a matrix dominated by quartz and plagioclase, with minor biotite and perthitic K-feldspar.

Table 1
Major element compositions and structural formulae of representative garnets, biotites, feldspars and cordierites from MVMS metapelites Mk2-2a and Mk2-2b, and leucosome Mk3.

	Garnet							Biotite					Feldspar						Cordierite
	Mk2-2a		Mk2-2b		Mk3			Mk2-2a			Mk3		Mk2-2a			Mk3			Mk2-2a
	Gt r	Gt c	Gt r	Gt c	Gt r	Gt c		Bt m	Bt rGt	Bt iGt	Bt m		Ksp	Plag r	Plag c	Ksp	Plag		Crd
SiO_2	37.76	38.06	37.31	37.49	36.28	37.05	SiO_2	36.00	35.62	36.98	35.13	SiO_2	65.97	69.09	64.49	65.26	63.07	SiO_2	50.56
Al_2O_3	21.49	21.76	21.24	21.53	20.83	21.10	TiO_2	4.06	2.76	3.67	3.20	Al_2O_3	18.72	19.51	22.74	18.33	23.21	Al_2O_3	31.52
Cr_2O_3	0.00	0.00	0.00	0.00	0.00	0.00	Al_2O_3	17.49	17.81	18.33	17.27	FeO	0.00	0.00	0.00	0.00	0.00	FeO	8.72
Fe_2O_3	0.57	1.83	1.62	1.94	3.25	2.44	Cr_2O_3	0.27	0.15	0.22	0.00	CaO	0.06	0.43	3.27	0.00	4.55	MnO	0.00
FeO	34.82	33.55	36.05	33.25	34.08	33.62	FeO	20.45	19.13	14.21	20.84	Na_2O	5.72	11.50	9.69	3.57	8.97	MgO	8.53
MnO	0.47	0.39	0.34	0.46	1.43	1.01	MnO	0.00	0.00	0.00	0.00	K_2O	8.27	0.11	0.31	11.40	0.21	CaO	0.00
MgO	5.00	6.06	4.08	5.74	3.82	4.82	MgO	9.27	11.10	13.31	9.15	BaO	0.54	0.00	0.00	0.37	0.00	Na_2O	0.26
CaO	0.74	0.61	0.74	0.71	0.83	0.85	Na_2O	0.32	0.25	0.66	0.31	Totals	99.34	100.70	100.78	98.93	100.08	K_2O	0.00
Na_2O	0.00	0.00	0.00	0.00	0.00	0.00	K_2O	9.68	8.97	9.06	9.21	Si	3.00	3.00	2.83	3.00	2.79	Totals	99.59
K_2O	0.00	0.00	0.00	0.00	0.00	0.00	Totals	97.54	95.79	96.44	95.10	Al	1.00	1.00	1.17	0.99	1.21	Si	5.14
Totals	100.84	102.26	101.39	101.11	100.53	100.88	Si	5.40	5.38	5.41	5.41	Fe^{2+}	0.00	0.00	0.00	0.00	0.00	Al	3.78
Si	2.98	2.95	2.96	2.95	2.91	2.94	Ti	0.46	0.31	0.40	0.37	Ca	0.00	0.02	0.15	0.00	0.22	Fe^{2+}	0.74
Al	2.00	1.99	1.99	1.99	1.97	1.97	Al^{IV}	2.60	2.62	2.59	2.59	Na	0.50	0.97	0.82	0.32	0.77	Mn	0.00
Cr	0.00	0.00	0.00	0.00	0.00	0.00	Al^{IV}	0.49	0.56	0.58	0.55	K	0.48	0.01	0.02	0.67	0.01	Mg	1.29
Fe^{3+}	0.03	0.11	0.10	0.11	0.20	0.15	Cr	0.03	0.02	0.03	0.00	Ba	0.01	0.00	0.00	0.01	0.00	Ca	0.00
Fe^{2+}	2.30	2.18	2.39	2.18	2.29	2.23	Fe^{2+}	2.56	2.42	1.74	2.68	Totals	4.99	4.99	4.99	4.99	5.00	Na	0.05
Mn	0.03	0.03	0.02	0.03	0.10	0.07	Mn	0.00	0.00	0.00	0.00	X_{Ab}	0.51	0.97	0.83	0.32	0.77	K	0.00
Mg	0.59	0.70	0.48	0.67	0.46	0.57	Mg	2.07	2.50	2.90	2.10	X_{An}	0.00	0.02	0.15	0.00	0.22	Totals	11.00
Ca	0.06	0.05	0.06	0.06	0.07	0.07	Na	0.09	0.07	0.19	0.09	X_{San}	0.49	0.01	0.02	0.68	0.01	X_{FeCrd}	0.36
Na	0.00	0.00	0.00	0.00	0.00	0.00	K	1.85	1.73	1.69	1.81							X_{MgCrd}	0.64
K	0.00	0.00	0.00	0.00	0.00	0.00	Totals	15.56	15.61	15.53	15.60							Mg#	63.54
Totals	8.00	8.00	8.00	8.00	8.00	8.00	Mg#	44.69	50.84	62.54	43.89								
X_{Alm}	0.77	0.74	0.81	0.74	0.79	0.76													
X_{Spss}	0.01	0.01	0.01	0.01	0.03	0.02													
X_{Py}	0.20	0.24	0.16	0.23	0.16	0.19													
X_{Grs}	0.02	0.02	0.02	0.02	0.02	0.02													
Mg#	20.38	24.34	16.79	23.51	16.66	20.34													

Number of ions calculated on the basis of 12 oxygens for garnet, 22 oxygens for biotite, 8 oxygens for feldspar, and 18 oxygens for cordierite. $X_{Alm} = Fe^{2+}/(Fe^{2+} + Mn + Mg + Ca)$, $X_{Spss} = Mn/(Fe^{2+} + Mn + Mg + Ca)$, $X_{Py} = Mg/(Fe^{2+} + Mn + Mg + Ca)$, $X_{Grs} = Ca/(Fe^{2+} + Mn + Mg + Ca)$, $Mg\# = 100 \times Mg/(Mg + Fe^{2+})$, $X_{Ab} = Na/(Ca + Na + K)$, $X_{An} = Ca/(Ca + Na + K)$, $X_{San} = K/(Ca + Na + K)$, $X_{FeCrd} = Fe^{2+} = (Fe^{2+} + Mg)$, $X_{MgCrd} = Mg/(Fe^{2+} + Mg)$. Gt = garnet; Bt = biotite; Ksp = perthitic K-feldspar; Plag = plagioclase; Crd = cordierite; c = core; r = rim; m = matrix; rGt = rimming garnet; iGt = inclusion in garnet.

con, pyrite and ilmenite as accessory phases. Garnet aggregates are made up of an interlocking network of crystals consisting of 1–3 mm subhedral garnet poikiloblasts (Fig. 4a and b), or 50–600 μm anhedral poikilitic garnet fragments (Fig. 4c). Garnets in the pelites are characterised by numerous, lobate 10–300 μm quartz inclusions and rounded, 10–50 μm biotite inclusions (Fig. 4a and b). Garnets with embayed margins are commonly surrounded by moats of coarse crystalline quartz and feldspar (Fig. 4b). Compositionally, the garnet is an Fe-rich, almandine-pyrope solid-solution with minor grossular and spessertine components (Table 1). Garnet core compositions between samples vary from X_{Alm} ($Fe^{2+}/(Fe^{2+} + Mg + Ca + Mn)$) = 0.71–0.76, X_{Py} ($Mg/(Fe^{2+} + Mg + Ca + Mn)$) = 0.20–0.26, X_{Spss} ($Mn/(Fe^{2+} + Mg + Ca + Mn)$) = 0.01–0.02 and Mg# ($100 \times Mg/(Mg + Fe^{2+})$) = 20–27. Garnets are largely unzoned in terms of their major element chemistry, with broad homogenous cores surrounded by thin 5–20 μm retrograde rims displaying slightly lower Mg# and higher X_{Spss}.

Anhedral cordierite poikiloblasts contain abundant rounded biotite, rounded quartz as well as minor plagioclase and K-feldspar inclusions (Fig. 4d). Cordierite is unzoned, ranges in composition from Mg# 63–70 between samples (Table 1), and is highly pinitized in places. Cordierite poikiloblasts are occasionally aligned in the foliation (Fig. 4e), the weak to moderate fabric in the rocks defined by bands of matrix biotite, quartz, and feldspar. In at least one of the samples, large perthitic K-feldspar crystals are aligned in the foliation, demonstrating that K-feldspar formed part of the original peak assemblage and did not grow entirely as a result of melt crystallisation. Na-rich matrix plagioclase typically displays slight zonation with X_{Ab} = Na/(Ca + Na + K) = 0.78–0.83 in the cores and X_{Ab} = 0.94–0.98 in the rims (Table 1). Perthitic K-feldspar contains X_{San} = K/(Ca + Na + K) = 0.5–0.7 and X_{Ab} = 0.3–0.5, and is only present in certain samples (Table 1). Patchy sericitization of both plagioclase and K-feldspar is common.

Three textural and compositional varieties of biotite are present (Table 1). These include small, rounded high Ti^{4+}, high Mg# biotites included in garnet, interpreted to be remnants of the high-temperature biotite that underwent incongruent melting during peritectic garnet growth; foliated matrix biotite of intermediate composition, also occurring as inclusions in cordierite; and lastly, minor, coarse-grained, low Ti^{4+}, low Mg# retrograde biotite rimming and replacing garnet.

4.2. Leucosomes

Leucosomes and melt sheets contain coarse-grained aggregates of subhedral to euhedral garnets hosted in a matrix dominated by quartz and plagioclase, with minor interstitial biotite and perthitic K-feldspar (Fig. 4f). Compared to the peritectic garnets in the pelites, leucosome garnets are less poikilitic with uniform, inclusion-free zones separated by abundant mica-filled joins and fractures. However, they do occasionally contain the same rounded, high Ti^{4+}, high Mg# biotite inclusions that characterise the peritectic garnets in the pelites, and since leucosome and pelitic garnet compositions and their inclusion suites are identical (Table 1), the garnets in the leucosomes are interpreted to be peritectic in origin. These garnets also contain large (700–1000 μm), complex quartz ± plagioclase inclusions with low angle terminations (Fig. 4f), interpreted as melt inclusions (Holness, 2006).

5. Mineral equilibria modelling

A powerful approach to constraining metamorphic conditions in rocks of this kind involves the use of equilibrium phase diagrams constructed within the confines of a specific bulk-rock composition, i.e. pseudosections (Powell et al., 1998). Pseudosections have been successfully applied to evaluate phase relations and mineral assemblage stability, through the use of an internally consistent thermodynamic dataset (Powell and Holland, 1985, 1988) and the software program Thermocalc. This dataset presently includes a broad range of end-members of phases, allowing for modelling in large and complex chemical systems like $MnO–Na_2O–CaO–K_2O–FeO–MgO–Al_2O_3–SiO_2–H_2O–TiO_2–O_2$ (MnNCKFMASHTO), thereby including all the main components that control metamorphic assemblages in metapelites (Holland and Powell, 1990, 1998; White et al., 2001; Johnson et al., 2003; Johnson and Brown, 2004). An additional refinement has been the development of a thermodynamic model for silicate melt, so as to constrain melt-bearing equilibria in high-grade pelites (Holland and Powell, 2001).

Pseudosections were calculated for metapelite sample Mk2-2a (Table 2), and the equilibrium assemblage stable at peak metamorphic conditions, i.e. grt + bt + crd + plag + kspar + ilm + qrtz + melt, located in *P–T* space. The low variance of this assemblage makes it an ideal candidate for constraining metamorphism, given the typically restricted nature of low variance fields in *P–T–X* space. Modelling was undertaken using Thermocalc 3.30 (Powell and Holland, 1988) and the internally consistent dataset of Holland and Powell (1998, and subsequent upgrades), in the chemical system NCKFMASHTO. XRF data converted to molar percent of the oxide was used as an effective bulk-rock constraint (SiO_2 = 63.75, Al_2O_3 = 11.3, CaO = 0.54, MgO = 9.84, FeO = 11.9, K_2O = 1.87, Na_2O = 0.064, TiO_2 = 0.734, 0 = 0.297 molar%), quartz was treated as a saturated phase and the ferric iron content of the rock was estimated at ±5% of total iron.

Table 2
Representative whole-rock compositions of metapelites and a garnet-bearing leucosome from the MVMS.

Wt% Oxide	Metapelites (Grt + Crd + Bt + Plag + Qtz ± Kspar)					Leucosome
	Mk 2-1	Mk 2-2a	Mk 2-2b	Mk4	Mk 5	Mk 3
SiO_2	57.00	57.50	70.31	57.17	57.98	70.93
TiO_2	0.86	0.88	0.46	0.69	0.88	0.47
Cr_2O_3	0.35	0.25	0.09	0.27	0.33	0.05
Al_2O_3	19.54	17.30	12.19	16.98	20.36	15.02
Fe_2O_3	13.47	14.27	10.45	14.83	9.16	3.57
MnO	0.07	0.06	0.04	0.07	0.04	0.03
MgO	5.29	5.95	4.08	7.51	4.09	1.20
CaO	0.26	0.45	0.48	0.19	0.31	1.74
Na_2O	0.84	0.06	0.65	0.19	1.52	3.58
K_2O	3.49	2.65	1.32	1.99	5.80	3.45
P_2O_5	0.04	0.05	0.04	0.02	0.03	0.10
NiO	0.03	0.06	0.06	0.06	0.03	0.02
Total	101.26	99.48	100.17	100.01	100.55	100.02
Mg#	44	45	44	50	47	40

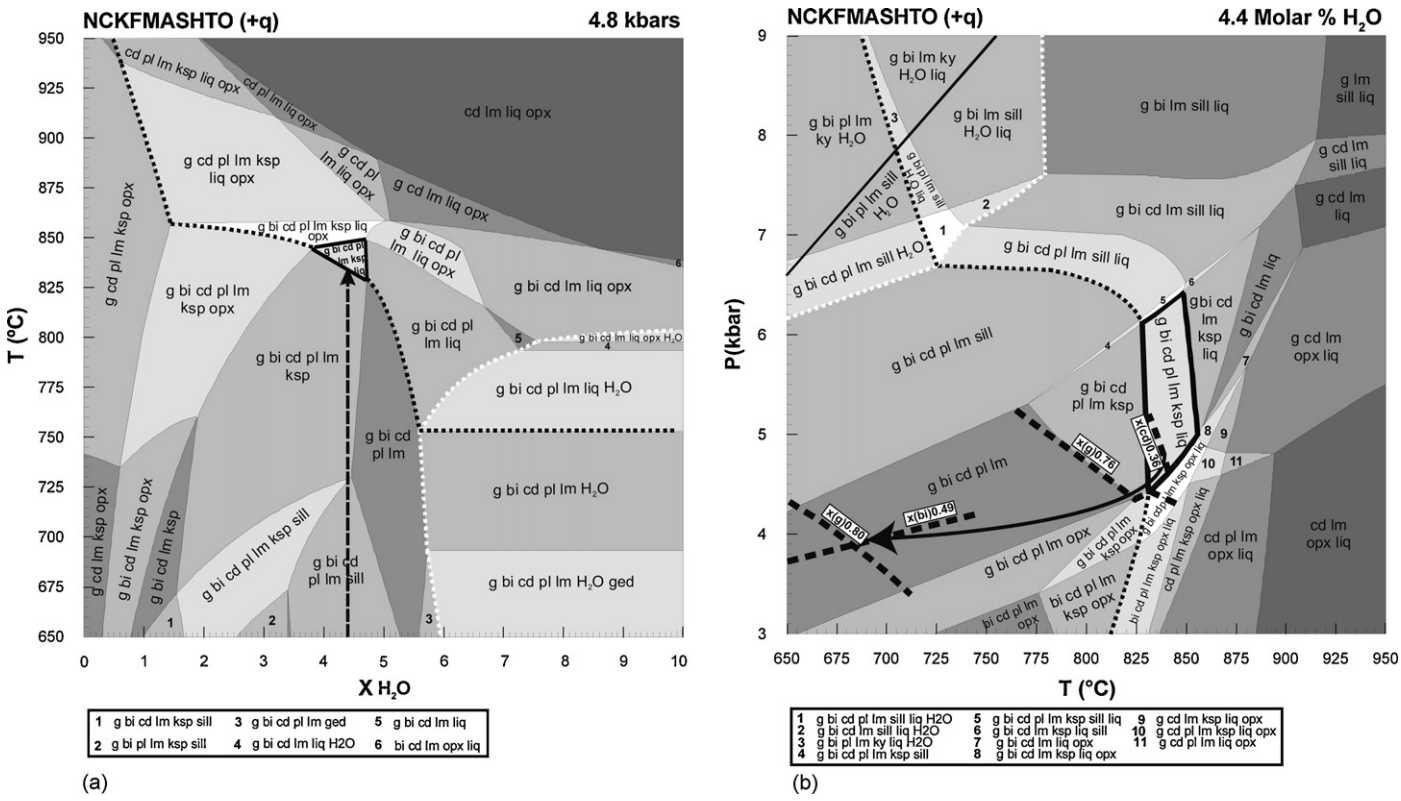

Fig. 5. Symbols: g = garnet; bi = biotite; cd = cordierite; pl = plagioclase; ksp = K-feldspar; lm = ilmenite; liq = melt; opx = orthopyroxene; sill = sillimanite; ky = kyanite; ged = gedrite. (a) NCKFMASHTO (+qtz in excess) $T - X_{H_2O}$ pseudosection for metapelite Mk2-2a (SiO_2 = 63.75, Al_2O_3 = 11.3, CaO = 0.54, MgO = 9.84, FeO = 11.9, K_2O = 1.87, Na_2O = 0.064, TiO_2 = 0.734, O = 0.297 molar%) at a fixed pressure of 4.8 kbars, with variation in bulk water content from 0 to 10 molar% (±0–3 wt% H_2O). The stippled black line represents the solidus, and the stippled white line those fields with free H_2O as part of the assemblage. At 4.8 kbars, the peak assemblage g + bi + cd + pl + ksp + lm + liq is stable and plots in a small triangular field between 830 and 850 °C and 3.9–4.7 molar% H_2O, consistent with a fluid-absent metamorphic evolution. (b) NCKFMASHTO (+qtz in excess) *P–T* pseudosection for Mk2-2a at a fixed H_2O content of 4.4 molar%. The stippled black line represents the solidus. The peak metamorphic assemblage, g + bi + cd + pl + ksp + lm + liq occupies a narrow field to the right of the centre of the diagram (highlighted in black), constraining peak metamorphism in the MVMS to 830–855 °C and 4.4–6.4 kbars. The $x(g)$, $x(cd)$ and $x(bi) = Fe^{2+}/(Fe^{2+} + Mg)$ mineral compositional isopleths, shown as dark dashed lines in the figure, constrains peak metamorphism further and defines a relatively flat cooling path followed during the retrograde evolution of the rocks.

5.1. Constraining H_2O in the bulk composition: $T - X_{H_2O}$ pseudosection

Pseudosections represent a two-dimensional slice through *P–T–X* space, where *X* can be a variety of variables including bulk-rock composition, bulk Mg#, or water activity (aH_2O). This allows for the investigation of the dependence of mineral equilibria on two of the variables (*P*, *T* or *X*), with the third variable fixed (Kelsey et al., 2003). As water controls the kinetics and rates of metamorphic reactions, as well as the *P–T* conditions and degree of partial melting, the choice of water content in the bulk composition is crucial when modelling anatexis. Consequently, a $T - X_{H_2O}$ section, investigating the dependence of the mineral equilibria on bulk-H_2O content, was used to constrain the maximum rock H_2O content to values consistent with the formation of the observed peak assemblage (Fig. 5a). This approach differs slightly from the convention of assuming the lowest possible bulk-H_2O content to fully hydrate the assemblage below the wet solidus (White et al., 2001).

Fig. 5a is a $T - X_{H_2O}$ section for the bulk composition of metapelite Mk2-2a at a fixed pressure of 4.8 kbars, with the *x*-axis representing variation in bulk water content from 0 to 10 molar% (±0–3 wt% H_2O). The diagram demonstrates that at this pressure, the relevant assemblage grt + bt + crd + plag + kspar + ilm + qrtz + melt is stable, and plots in a small triangular field between 3.9 and 4.7 molar% H_2O and 830–850 °C. The solidus is shown as a stippled black line in Fig. 5a. The stability field of the peak assemblage is constrained by two univariant reaction lines and the solidus. Up temperature, opx comes into the assemblage, at slightly higher H_2O contents K-feldspar leaves the assemblage, and immediately down temperature the solidus is crossed. The isochemical heating path, admittedly ignoring the inevitable concurrent pressure increase, is consistent with a fluid-absent metamorphic evolution. Investigation of the pressure stability of this field through a $P - X_{H_2O}$ section reveals that it is elongated in the pressure direction and remains stable over a narrow range in H_2O contents (4.2–5.0 molar%), between 4.5 and 6.2 kbars. Therefore, given the restricted nature of the relevant field in $P - T - X_{H_2O}$ space, a water content of 4.4 molar% H_2O was chosen to model the *P–T* stability of this assemblage in more detail.

5.2. P–T pseudosection

A *P–T* pseudosection for Mk2-2a is presented in Fig. 5b. The diagram illustrates that the peak mineral assemblage occupies a narrow field between 830 and 855 °C and 4.4–6.4 kbars. Fairly rigid pressure limits are provided by the sillimanite-in univariant reaction line up pressure, the opx-in univariant reaction line down pressure, the solidus to the left (stippled black line in Fig. 5b) and the plagioclase-out univariant reaction line up temperature. As temperature increases and melting proceeds, mole proportions of plagioclase and biotite rapidly decrease until first plagioclase, and then biotite, leaves the assemblage. This is consistent with a plagioclase and biotite-consuming, garnet producing melting reaction. Since field and petrographic evidence suggest that garnet is produced at the sites of melting, and that there is no textural or min-

eral chemical evidence for an earlier generation of garnet growth, the bulk of the garnet is interpreted to be peritectic.

Peak conditions for granulite facies metamorphism and anatexis in this sample is therefore constrained to 830–855 °C and 4.4–6.4 kbars, consistent with experiments that have investigated fluid-absent partial melting in rocks of similar composition (Vielzeuf and Holloway, 1988; Patiño Douce and Beard, 1995; Stevens et al., 1997). Field evidence describing the metatexitic character of the MVMS migmatites presented in earlier sections of the paper, indicates that efficient melt segregation and extraction took place at or near to the conditions of peak metamorphism. In addition, the restitic character of the metapelites and well-preserved granulite facies mineral assemblage is consistent with substantial melt-loss during peak metamorphism. When modelling anatexis, it is important to consider the role that melt-loss plays in modifying the rock's original bulk composition, and upon cooling preventing prograde reactions from being reversed (White et al., 2001; White and Powell, 2002). Thus, where considerable melt-loss has occurred, only the peak and post-peak metamorphic evolution of a rock can be reliably modelled. In addition, no record of the prograde history (e.g. inclusion suites, replacement textures or different generations of mineral growth) prior to peak metamorphism and melt-loss from the MVMS metapelites is preserved. Therefore, in order to more accurately constrain peak metamorphism and the retrograde path followed by the rocks during cooling, Fig. 5b was contoured for garnet compositional isopleths and compared to measured garnet core $x(g) = Fe^{2+}/(Fe^{2+} + Mg) = 0.76$ and rim $x(g) = Fe^{2+}/(Fe^{2+} + Mg) = 0.80$ compositions in Mk2-2a. Fig. 5b shows the $x(g) = 0.76$ core compositional isopleth intersecting the peak assemblage at 830 °C and 4.4 kbars. Similarly, the relevant matrix cordierite $x(cd) = Fe^{2+}/(Fe^{2+} + Mg) = 0.36$ compositional isopleth intersects the peak assemblage close to the $x(g)$ isopleth, indicating that the *P–T* conditions of peak metamorphism lie in the lower pressure part of the peak assemblage stability field. In contrast, pressure constraints on the rock during its retrograde evolution are provided by the sillimanite-bearing and opx bearing fields at high- and low-pressure, respectively, which bound the grt + bt + crd + plag + ilm + qrtz field through which the rock must have cooled. Fig. 5b shows the $x(g) = 0.80$ rim compositional isopleth intersecting the appropriate field at low temperature, indicating equilibration of the garnet rims between 710 and 650 °C and 4.2–3.4 kbars. This garnet rim composition also intersects the average retrograde biotite composition in the rock, i.e. biotite rimming and replacing garnet with a composition $x(bi) = Fe^{2+}/(Fe^{2+} + Mg) = 0.49$, at ±680 °C and 3.9 kbars (Fig. 5b). Therefore, the best constrained retrograde path followed by the rocks indicates substantial cooling following peak metamorphism from ±850–830 to 680 °C, with only slight concurrent decompression.

6. Zircon U–Pb geochronology

Zircon grains extracted from an in situ garnet-bearing leucosome Mk3 are short, prismatic and subhedral to euhedral. They are generally red-brown to dark-brown in transmitted light, and range in size from 80 to 200 μm. Some grains have slightly rounded edges towards their apex, giving them a spheroidal shape, and others are more elongate in form. They are translucent to extremely cloudy or opaque (high-U metamict grains), with rare transparent cores. Most grains are fractured, with radial cracks stemming from their cores, and contain abundant biotite and other unidentified inclusions. CL imaging reveals that the zircons commonly display unzoned central areas surrounded by fine-scale magmatic oscillatory zoning of varying intensity and width, typical of magmatic zircon crystallised in the presence of a melt. However, this zonation pattern is truncated at sites of embayment by uniform grey over-

Table 3
Summary of SHRIMP U–Pb zircon data for leucosome Mk3.

Grain spot	% $^{206}Pb_c$	U (ppm)	Th (ppm)	$^{232}Th/^{238}U$	$^{206}Pb^*$ (ppm)	(1) $^{206}Pb/^{238}U$ age (Ma)	(1) $^{207}Pb/^{206}Pb$ age (Ma)	% Disc.	(1) $^{207}Pb^*/^{206}Pb^*$	± (%)	(1) $^{207}Pb^*/^{235}U$	± (%)	(1) $^{206}Pb^*/^{238}U$	± (%)	Err. Corr.
1	0.16	299	70	0.24	131	2658	2725.2 ±6.4	2	0.18805	0.39	13.23	1.3	0.5102	1.2	0.954
2	–	71	90	1.30	32	2719	2737.8 ±9.4	1	0.1895	0.57	13.71	1.8	0.5248	1.7	0.946
3	–	107	82	0.80	44.8	2572	2727.3 ±8.1	6	0.18829	0.49	12.73	1.4	0.4902	1.3	0.933
4	0.08	327	24	0.07	149	2735	2736.0 ±5.4	0	0.18929	0.33	13.79	1.2	0.5284	1.2	0.965
5	0.03	396	27	0.07	176	2686	2731.7 ±5.1	2	0.18879	0.31	13.46	1.2	0.517	1.2	0.968
6	0.11	383	24	0.06	172	2705	2722.0 ±5.5	1	0.18768	0.33	13.49	1.2	0.5214	1.2	0.964

Note: Errors are 1-sigma; Pbc and Pb* indicate the common and radiogenic portions, respectively. Error in Standard calibration was 0.32% (not included in above errors but required when comparing data from different mounts).
(1) Common Pb corrected using measured ^{204}Pb.

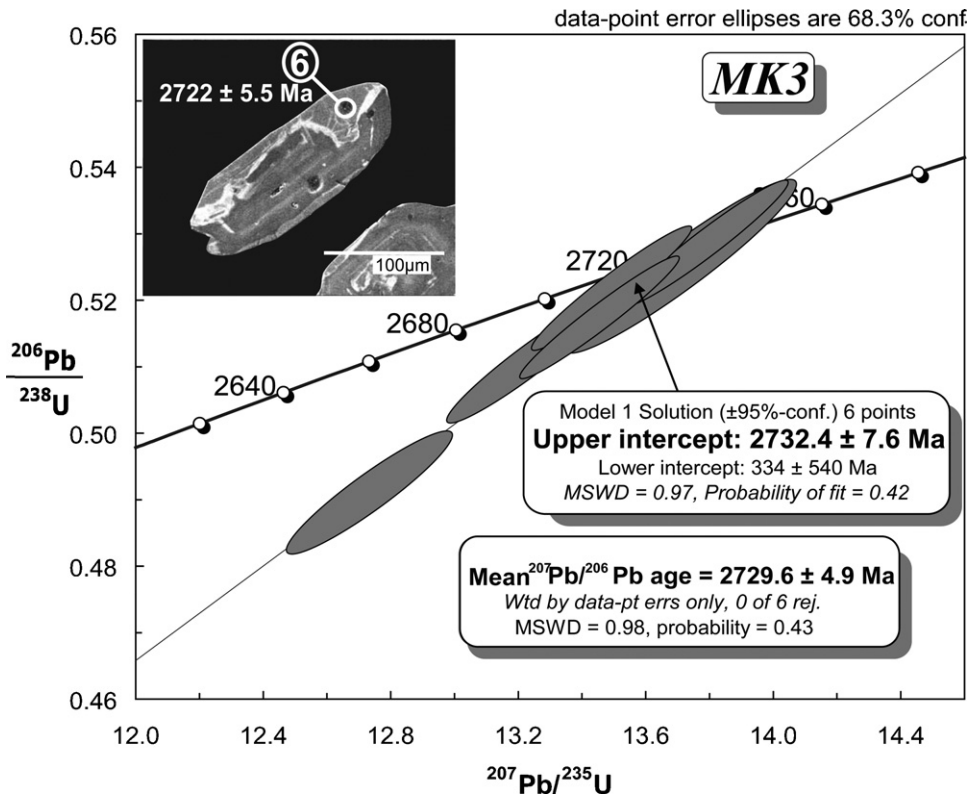

Fig. 6. Concordia diagram showing the SHRIMP U–Pb analyses and $^{207}Pb/^{206}Pb$ age of an in situ anatectic leucosome, Mk3. Cathodoluminescence (CL) imaging of the zircons reveals unzoned central areas surrounded by fine-scale magmatic oscillatory zoning of varying intensity and width, truncated at sites of embayment by uniform grey overgrowths or distinctly bright rims. There is no geochronological evidence to suggest an age difference between the various structural domains, and any record of a magmatic to metamorphic history falls within the uncertainty limits of the age calculations.

growths or distinctly bright rims. For the analysis of these zircons, SHRIMP spots were targeted in the unzoned central portions, the zoned domains interpreted to reflect magmatic crystallisation, as well as in the rim overgrowths. SHRIMP U–Pb analyses reveal cores are typically characterised by low-U concentrations; areas which displayed oscillatory zonation contain high-U concentrations; and grey embayments or rims of bright recrystallised zircon have relatively low Th/U ratios (~0.07), consistent with a metamorphic origin.

Most of the SHRIMP U–Pb analyses, especially of the high-U zircon domains, are extremely discordant and offer limited geochronological information. High common Pb in the zircons correlates with elevated U contents, confirming a relationship between metamictisation, alteration and Pb-loss. A small set of concordant/near-concordant data from leucosome Mk3 (Table 3) plots as a linear cluster near Concordia (Fig. 6), where an upper intercept age of 2732.4 ± 7.6 Ma (n = 6; MSWD [mean square of weighted deviates] = 0.97) can be calculated, as well as a weighted mean $^{207}Pb/^{206}Pb$ age of 2729.6 ± 4.9 Ma (MSWD = 0.98). Some of these concordant analyses were derived from zircon cores and others from embayments or rims, and if there is a magmatic to metamorphic history recorded in the structure of the zircons, then the age of the metamorphic rims are within error of the magmatic age.

7. Discussion

7.1. The age of high-grade metamorphism

Although zircons from the MVMS leucosome appear complex in terms of their internal structure and Th/U content, there is no geochronological evidence to suggest a significant difference in age between the various structural domains. All the concordant or near-concordant data (≥94% concordant), whether produced from rim or core domains indicate, within error, the same age. Thus, although there is clear textural and mineral chemical evidence for metamorphic growth/recrystallisation on zoned, magmatic grains, as well as textural evidence for the existence of older cores, none of the zircon domains have discernibly different ages. As the MVMS leucosomes were derived from the partial melting of metasediment, it is logical to expect the zircons to carry some record of inheritance. The fact that they do not, may be interpreted in one of two ways given our current understanding of metamorphism and partial melting in the MVMS. The first possibility involves complete resetting of the U–Pb isotope system during peak granulite facies metamorphism. However, this seems unlikely since volume diffusion of Pb in zircon is generally considered insignificant for most conditions realised in the earth's crust (Mezger and Krogstad, 1997). Calculated closure temperatures for the diffusion of Pb in average sized zircons, using the traditional Dodson (1973) equation, are high (Lee et al., 1997; Cherniak and Watson, 2000). Field based studies also indicate closure temperatures in excess of 950–1000 °C for Pb in zircon (e.g. Claoué-Long et al., 1991; Williams, 1992), much higher than peak metamorphic conditions reached in the MVMS. A more plausible explanation involves the solubility of zircon and monazite within silicate melt, relative to their abundance in the source (Kelsey et al., 2008). We suggest that zircon cores represent magmatic zircon crystallised from in situ melts, early in the rock's cooling history, at a time when most of the monazite and therefore available Th was completely dissolved in the melt. This may explain the high Th/U character of the core domains. Upon further cooling, late-stage growth or recrystallisation of zircon on zoned, magmatic grains may have occurred concurrent with monazite crystallisation, either via a pro-

cess of dissolution-precipitation following melt extraction, or via subsolidus recrystallisation similar to that described by Pidgeon (1992) and Pidgeon et al. (1998), producing rims with a relatively low Th/U signature.

The very small cluster of concordant to near-concordant rim and core ages, however, allows for their combined age of 2732.4 ± 7.6 Ma and weighted mean age of 2729.6 ± 4.9 Ma to be interpreted as the best current estimate of the age of high-grade metamorphism and partial melting in the MVMS. The U–Pb SHRIMP age comes close to being within error of Condie et al.'s 2745 ± 2 Ma zircon evaporation age, and the current data therefore confirms and extends this age. The fact that the zircon evaporation age is slightly older may be attributed to the bulk sampling technique employed by Condie et al., and the inclusion of some small fraction of inherited material in the analysis. We interpret our age to be more accurate due to the inability of the evaporation method to correct for common Pb and to judge the discordance of data.

7.2. Origin of the metamorphism

The relatively tightly constrained conditions for peak metamorphism and anatexis indicate that the MVMS sediments underwent granulite facies (850–830 °C) metamorphism at a crustal depth of approximately 15 km. This translates to an elevated apparent metamorphic field gradient of ±55 °C/km. Furthermore, pseudosection modelling shows that the garnet preserved in the rocks equilibrated at 830 °C and 4.4 kbars, followed by near isobaric cooling to 680 °C and 3.9 kbars. Although the granulites are not amenable to constraining their prograde evolution (for reasons already discussed) and therefore the overall shape of the *P–T* path, some inferences can be made using the current peak and post-peak *P–T* constraints, which is in itself diagnostic of tectonic environment. The MVMS underwent granulite facies metamorphism involving extensive biotite fluid-absent melting at moderate- to shallow-crustal depths, followed by substantial cooling without significant decompression during or after peak metamorphism. This is unlike metamorphic rocks typical of continental collision belts which are buried and metamorphosed at depth and commonly undergo isothermal decompression following peak metamorphism (England and Thompson, 1984; Thompson and England, 1984). In contrast, models to explain regional terranes with comparable low-medium *P*, high-*T* metamorphism, isobaric cooling and flat *P–T* paths, typically involve extension of hot over-thickened crust, either during convective thinning or delamination of the lower lithosphere (e.g. Damara Belt, Jung, 2000; Namaqualand Metamorphic Complex, Waters, 1990 and Gibson et al., 1996; Mount Stafford, Loosveld and Etheridge, 1990, Vernon et al., 1990 and Greenfield et al., 1998; Napier Complex, Harley, 1988), or alternatively, extension and thinning of normal thickness crust associated with intra-continental rifts (Sandiford and Powell, 1986; Wickham and Oxburgh, 1985) or continental mantle plumes (Zhao et al., 1998, 1999, 2001). Here, metamorphism may be enhanced by the introduction of felsic magmas into the upper crust as a local source of heat superimposed on a regional thermal pulse (Lux et al., 1986; Collins et al., 1991). A common feature of all of these models, however, is the amount of advected mantle heat that is required for mid- to shallow-crustal, granulite facies metamorphism to occur. The metamorphic conditions in the MVMS are therefore interpreted to reflect a period of anomalously high heat flow within the crust, although the specific setting most applicable to the MVMS can be determined only once metamorphism is considered within a more regional context.

Orogenic collapse and extension of over-thickened crust seems plausible at first, in light of the inferred timing of continental collision in the Southern Marginal Zone (SMZ) of the Limpopo Belt (Van Reenen et al., 1995; Smit and Van Reenen, 1997) (Fig. 1), where recent data has indicated an age of 2691 ± 7 Ma for peak metamorphism (Kreissig et al., 2001). However, significant thickening of the crust during the ~2.7 Ga Limpopo Orogeny seems unlikely considering the lack of extensive regional deformation, metamorphism and uplift that one would expect in areas such as the Barberton Greenstone Belt (BGB) and AGC. In fact, late D3 deformation in the BGB and the emplacement of sheet-like potassic granites at ~3.10–3.07 Ga (Mpuluzi, Pigg's Peak, Nelspruit, and Heerenveen batholiths), during a period of late-stage crustal convergence following D2 deformation (De Ronde and De Wit, 1994; Belcher and Kisters, 2006), is the last penetrative deformation event recorded in the belt (Schoene et al., 2008). In addition, thermochronology suggests that the BGB has not experienced temperatures in excess of 300 °C since ~3.10 Ga (Toulkeridis et al., 1994).

A regionally significant event that was broadly coeval with high-grade metamorphism in the MVMS was the voluminous outpourings of the Ventersdorp Supergroup flood basalts at 2714 ± 8 Ma (Klipriviersberg Group) and at 2709 ± 4 Ma (Platberg Group), in major NE–SW trending grabens and extensional basins (Fig. 1) (Armstrong et al., 1991; Burke et al., 1985; Stanistreet and McCarthy, 1991). The Ventersdorp magmas are comprised of mafic/ultramafic lavas with geochemistries indicative of both a lithospheric and asthenospheric mantle source (Nelson et al., 1992; Marsh et al., 1992), and were directly derived from extensive partial melting in the mantle. This period in the Neoarchaean evolution of the Kaapvaal craton is also associated with widespread crustal anatexis and post-tectonic granitic magmatism (Fig. 1) (Poujol et al., 2003). A significant proportion of these granites intruded the Barberton and AGC terranes, and areas surrounding the Pongola Basin between 2.74 and 2.69 Ga, with a definite peak at ~2.72 Ga (Fig. 2), as numerous small, I-type bodies with geochemical characteristics of modern, within-plate granites (Hunter and Wilson, 1988; Layer et al., 1989; Hunter et al., 1992; Meyer et al., 1994; Maphalala and Kröner, 1993; Reimold et al., 1993; Robb et al., 1993; Kamo and Davis, 1994). Further evidence of a regional anatectic event is found within xenoliths from central Kaapvaal craton kimberlites, which indicate a period of ultra-high-temperature metamorphism and partial melting in the lower crust, concurrent with Ventersdorp magmatism, at ca. 2720–2715 Ma (Schmitz and Bowring, 2003). Schmitz and Bowring (2003) have constrained the precise onset of partial melting in the deep crust to ca. 2743–2730 Ma, by dating the oldest, oscillatory zoned zircon growth phases, an age which is directly comparable to high-grade metamorphism in the MVMS.

Thus, mid-crustal granulite facies metamorphism and anatexis in the AGC at ca. 2.73 Ga, and widespread melting of an anomalously hot crust, appear to have been broadly coeval with Ventersdorp magmatism resulting from extensive partial melting in the mantle, under- or intra-plating of mantle-derived melts, and major heating of the Kaapvaal craton crust.

7.3. Evidence of a mantle plume?

Mantle plumes have commonly been proposed to account for a globally recognised magmatic event at ~2.7 Ga (Nelson, 1998; Condie, 1998, 2001a; Isley and Abbott, 1999), an event which was widely associated with crustal extension and flood basalt volcanism. Record of this is found on the Superior craton (Uchi and Hemlo granite-greenstone belts), the Slave Province (Yellowknife Supergroup), the Pilbara craton (Nullagine and Mount Jope Supersequences, the Fortescue Group), Southern India, the Eastern Block of the North China Craton, and, the Kaapvaal craton (Calvert et al., 2004; Beakhouse and Davis, 2005; Blake, 1993; Jayananda et al., 2000; Zhao et al., 1998, 1999, 2001; Eriksson et al., 2002). Condie (1998, 2001a) and Eriksson et al. (2002) have suggested that Ventersdorp magmatism and extension were related to the rapid ascent of ponded plume magma beneath thinned sub-Witwatersrand

lithosphere (Sleep, 1997), transported laterally from a plume head situated marginally to the craton during the late Archaean. The marginal location of the plume is invoked to explain the apparent lack of km-scale, regional uplift typically associated with a plume. This is compatible with the presence of 3.2–2.9 Ga aged diamonds beneath the craton (Richardson et al., 2001) and the apparent existence of a thick, intact, lithospheric mantle keel since these times. If there was indeed a Ventersdorp aged plume, underplating and ponding of magma beneath thinned lithosphere in areas such as the Witwatersrand and Pongola basins would have induced high-grade metamorphism and initiated partial melting of the overlying crust.

7.4. Implications for the Kaapvaal cratonic crust: basement doming during Upper Central Rand deposition

The MVMS granulites offer an unique opportunity to peer into the mid-crust of the Kaapvaal craton during the Neoarchaean. A striking implication is that high-grade metamorphism and partial melting at depths of only 15–20 km suggest the brittle–ductile transition in the crust was situated at a rather shallow level. This may have resulted in significant rheological weakening of the crust, and has implications for basement structure by promoting ductile flow at mid- and upper crustal levels. The activation of basement domes within the vicinity of the MVMS, i.e. the Nhlangano Gneiss Domes (Fig. 2) (Wilson, 1982; Wilson and Jackson, 1988), may be evidence of this. Based on the relationship between metamorphic grade and the position of supracrustals around the domes, Wilson and Jackson (1988) suggested a causal link between doming and high-grade metamorphism, however, the precise timing of dome activation is unknown. Recent ion microprobe zircon dating has indicated a crystallisation age of >3.23–3.22 Ga for the Nhlangano Gneiss, placing it within the category of AGC basement (Schoene and Bowring, in press). We suggest crustal weakening at the time of the proposed high-grade metamorphism, and the resulting instability, to have been the true cause of the doming. This would not only serve as a mechanism for bringing rocks metamorphosed at a depth of 15 km to surface, but may explain the observed deformation and folding within the MVMS.

The final stages of Upper Central Rand Group deposition within the economically important 2.89–2.71 Ga Central Rand basin (Fig. 1), 300 km east of the MVMS, may therefore also have taken place upon rheologically weakened crust. This period of Witwatersrand development and the concentration of placer gold within the basin coincides with the timing of high-grade metamorphism in the MVMS, ending abruptly at 2714 Ma with Ventersdorp volcanism. Several Wits-based studies have described syn-sedimentary basement uplift and the effects of changing basement topography on facies changes within the basin. A number of basement domes flanking the basin margins have been identified (Fig. 1), namely the Johannesburg, Devon, Cedarmont, Westerdam, Vreysrus (Rand Anticline), Villiers, Hartebeesfontein, Edenville, Steynsrus and Wesselsbron Domes (Minter et al., 1986; Anhaeusser, 1973, 1992; Robb and Meyer, 1987; Poujol and Anhaeusser, 2001). For example, Tweedie (1986) concluded that the concentration of gold within the Evander Basin (Fig. 1), a subsidiary to the main Central Rand basin and host to the Kimberley Reef deposit, took place during successive transgressive and regressive phases directly related to activation and uplift of the nearby Devon Dome, which was terminated by the Ventersdorp lavas. Stanistreet and McCarthy (1991) suggested that the active tectonics associated with Central Rand basin development was largely controlled by NE–SW directed compression and regional shortening, resulting in the syn-sedimentary folds and strike-slip block faulting that is so characteristic of the Central Rand basin. Hence, both the shallow location of the brittle–ductile transition, and, coupling of the ductile portion of the crust to the brittle upper crust, are likely to have found their manifestation in the active syn-sedimentary tectonics and highly dynamic basement topography.

8. Conclusions

The findings of this study allow for the following important conclusions to be made concerning granulite facies metamorphism in the MVMS:

1. Peak metamorphism and partial melting in the MVMS, constrained to 850–830 °C at 4.4 kbars, occurred at ca. 2.73 Ga. This was followed by near isobaric cooling of the terrane to 680 °C and 3.9 kbars.
2. High-*T*, mid- to shallow-crustal metamorphism in the MVMS was coeval with widespread, regional crustal anatexis towards the end of the Archaean, including the formation of the Ventersdorp LIP (Large Igneous Province).
3. Metamorphism in the MVMS is interpreted to reflect a period of anomalously high heat flow within the Kaapvaal craton crust. An increase in the heat input from the mantle via magmatic under- or intra-plating is proposed to explain the observed thermal anomaly, with the Ventersdorp lavas being the eruptive manifestation of these mantle-derived melts.
4. We suggest the formation of a Ventersdorp aged plume marginal to the craton, which coincided with a globally recognized ~2.7 Ga mantle plume event. This is compatible with underplating and ponding of mantle-derived magmas beneath thinned sub-Witwatersrand/Pongola lithosphere, initiating high-grade metamorphism and anatexis of the overlying crust.
5. High-*T* metamorphism in the MVMS has provided evidence for significant mid-crustal heating, anatexis and, thus, rheological weakening of the Kaapvaal crust. Mobilisation of the mid-crust as gneissic domes and syn-sedimentary basement uplift was concurrent with sedimentation of auriferous reefs of the Upper Central Rand Group of the Witwatersrand Supergroup, and may have played a role in the recycling of gold-rich horizons within the Central Rand Basin.

Acknowledgements

This work forms part of a PhD study by Jeanne Taylor. We gratefully acknowledge South African National Research Foundation (NRF) grant funding to Professor Gary Stevens, as well as a PhD Bursary to Jeanne Taylor by the NRF.

Appendix A. Analytical techniques

A.1. Whole-rock chemistry

Samples were crushed to a fine powder using a jaw crusher and swing mill, and glass disks prepared for XRF analysis using 1.5 g of high purity trace element and REE element free flux ($LiBO_2$ = 80%, $Li_2B_4O_7$ = 20%) mixed with 0.28 g of the rock sample. Whole-rock major element compositions (Table A.1) were determined by XRF spectrometry on a Philips 1404Wavelength Dispersive spectrometer at the Department of Earth Sciences, Stellenbosch University, South Africa. The spectrometer is fitted with an Rh tube, analysing crystals LIF200, LIF220, LIF420, PE, TLAP and PX1. The instrument is fitted with a gas-flow proportional counter and a scintillation detector. The gas-flow proportional counter uses a 90% Argon, 10% methane gas mixture. Major elements were analyzed on a fused glass disk at 50 kV and 50 mA tube operating conditions. Matrix effects in the samples were corrected for by applying theoretical alpha factors and measured line overlap factors to the raw intensi-

Table A.1
A comparison of the measured and actual major element compositions of control standards used, as a reflection of the accuracy of the XRF analytical technique.

	SiO_2	Al_2O_3	Fe_2O_3	MnO	MgO	CaO	Na_2O	K_2O	TiO_2	P_2O_5	Cr_2O_3	NiO
Andesite												
AGV	58.292	17.012	6.783	0.100	1.276	4.905	4.158	2.920	1.094	0.501	0.000	0.005
Certified	58.790	17.140	6.760	0.092	1.530	4.940	4.260	2.910	1.050	0.490	0.000	0.002
Dev.	0.498	0.128	−0.023	−0.008	0.254	0.035	0.102	−0.010	−0.044	−0.011	0.000	−0.003
Dev. %	0.847	0.747	−0.340	−8.696	16.601	0.709	2.394	−0.344	−4.190	−2.245	100.000	−212.500
Granite												
NIM-G	75.869	12.641	2.035	0.022	0.045	0.752	3.516	5.027	0.095	0.007	0.000	0.000
Certified	75.700	12.080	2.020	0.021	0.060	0.780	3.360	4.990	0.090	0.010	0.001	0.000
Dev.	−0.169	−0.561	−0.015	−0.001	0.015	0.028	−0.156	−0.037	−0.005	0.003	0.001	0.000
Dev. %	−0.223	−4.644	−0.743	−4.762	25.000	3.590	−4.643	−0.741	−5.556	30.000	100.000	100.000
Basalt												
BHVO-1	49.945	13.408	12.770	0.163	7.051	11.852	2.128	0.554	2.784	0.288	0.003	0.015
Certified	49.940	13.800	12.230	0.168	7.230	11.400	2.260	0.520	2.710	0.273	0.029	0.012
Dev.	−0.005	0.392	−0.540	0.005	0.179	−0.452	0.132	−0.034	−0.074	−0.015	0.026	−0.003
Dev. %	−0.010	2.841	−4.415	2.976	2.476	−3.965	5.841	−6.538	−2.731	−5.495	89.619	−23.967

All values are given in wt% of the oxide.

ties measured with the SuperQ Philips software. Control standards that were used in the calibration procedures for major element analyses were AGV (Andesite from the United States Geological Survey, Reston), NIM-G (Granite from the Council for Mineral Technology, South Africa) and BHVO-1 (Basalt from the United States Geological Survey, Reston). A comparison of the measured and accepted major element compositions of the control standards used, as a reflection of the accuracy of the analytical technique, is presented in Table A.1.

A.2. Mineral chemistry

Mineral compositional analysis was performed using a Leo® 1430VP scanning electron microscope at Stellenbosch University. Prior to imaging and analysis the samples were sputter-coated with carbon. Textures were studied in backscattered electron (BSE) mode and phase compositions quantified by EDS analysis using an Oxford Instruments® 133 keV ED detector and Oxford INCA software. Beam conditions during the quantitative analyses were 20 kV and approximately1.5 nA, with a working distance of 13 mm and a specimen beam current of −4.0 nA. X-ray counts with the set-up used were typically ~7000 cps. The counting time was 50 s live-time. Analyses were quantified using natural mineral standards, and mineral chemical compositions were recalculated to mineral stoichiometries to obtain resultant mineral structural formulae. Comparisons between measured and accepted compositions of control standard, as a reflection of the accuracy of the analytical technique, have been published by Diener et al. (2005) and Moyen et al. (2006).

A.3. Zircon separation and sensitive high resolution ion microprobe (SHRIMP) U–Pb zircon dating

Samples were crushed and pulverised to a fine-medium grained powder using a large and small jaw crusher and separated into different size fractions using 350, 180, and 60 μm sized sieves at Stellenbosch University. Heavy minerals were concentrated using water and a panner, and zircons hand picked under a binocular microscope. SHRIMP II and SHRIMP RG U–Th–Pb analyses were performed at the Research School of Earth Sciences at the Australian National University, Canberra. Zircons were mounted in Pb-free epoxy, together with the Research School of Earth Sciences zircon standards FC1 and SL13. All grains were subsequently polished to half their thickness to expose internal structures. Transmitted and reflected light microphotography, as well as SEM (scanning electron microscope), cathodoluminescence (CL) imaging, was used to investigate internal structures and growth complexities in the zircon grains, before single spot U–Th–Pb SHRIMP analyses were performed.

For the zircon age calibration, the Pb/U ratios were normalized relative to a value of 0.1859 for the $^{206}Pb^*/^{238}U$ ratio of the FC1 reference standard, equivalent to an age of 1099 Ma (Paces and Miller, 1993). Uranium and thorium concentrations were determined relative to the SL13 standard. SHRIMP analyses comprised 6 repeated scans through the species $^{196}Zr_2O$, ^{204}Pb (common Pb), background ^{206}Pb, ^{207}Pb, ^{208}Pb, ^{238}U, ^{248}ThO, and ^{254}UO. The data were reduced in a manner similar to that described by Williams (1998, and references therein), using the SQUID Excel Macro of Ludwig (2000a). Corrections for common Pb were made using the appropriate model values of Stacey and Kramers (1975). Uncertainties given for individual analyses (ratios and ages) are at the 1σ level unless stated otherwise, and uncertainties in the calculated weighted mean, intercept, or Concordia ages are reported at 95% confidence limits. Concordia plots and age calculations were carried out using Isoplot/Ex (Ludwig, 2000b) or SQUID.

References

Anhaeusser, C.R., 1973. The geology and geochemistry of the Archaean granites and gneisses of the Johannesburg–Pretoria dome. Spec. Publ. Geol. Soc. S. Afr. 3, 361–385.

Anhaeusser, C.R., 1992. An overview of the Archaean granite-greenstone basement in the Witwatersrand hinterland. A Short Course Reviewing Recent Developments in the Understanding of the Witwatersrand Basin, vol. I. Economic Geology Research Institute, University of the Witwatersrand, pp. 23–34.

Anhaeusser, C.R., Walraven, F., 1999. Episodic granitoid emplacement in the western Kaapvaal craton: evidence from the Archaean Kraaipan granite-greenstone terrane, South Africa. J. Afr. Earth Sci. 28 (2), 289–309.

Armstrong, R.A., Compston, W., Retief, E.A., Williams, I.S., Welke, H.J., 1991. Zircon ion microprobe studies bearing on the age and evolution of the Witwatersrand Triad. Precambrian Res. 53 (3–4), 243–266.

Beakhouse, G.P., Davis, D.W., 2005. Evolution and tectonic significance of intermediate to felsic plutonism associated with the Hemlo greenstone belt, Superior Province, Canada. Precambrian Res. 137 (1–2), 61–92.

Belcher, R.W., Kisters, A.F.M., 2006. Progressive adjustments of ascent and emplacement controls during incremental construction of the 3.1 Ga Heerenveen batholith, South Africa. J. Struct. Geol. 28 (8), 1406–1421.

Blake, T.S., 1993. Late Archaean crustal extension, sedimentary basin formation, flood-basalt volcanism and continental rifting—the Nullagine and Mount Jope Supersequences, western-Australia. Precambrian Res. 60 (1–4), 185–241.

Burke, K., Kidd, W.S.F., Kusky, T., 1985. Is the Ventersdorp rift system of southern-Africa related to a continental collision between the Kaapvaal and Zimbabwe Cratons at 2.64 Ga ago? Tectonophysics 115 (1–2), 1–24.

Calvert, A.J., Cruden, A.R., Hynes, A., 2004. Seismic evidence for preservation of the Archaean Uchi granite-greenstone belt by crustal-scale extension. Tectonophysics 388 (1–4), 135–143.

Cherniak, D.J., Watson, E.B., 2000. Pb diffusion in zircon. Chem. Geol. 172, 5–24.

Claoué-Long, J.C., Sobolev, N.N., Shatsky, V.S., Sobolev, A.V., 1991. Zircon response to diamond-pressure metamorphism in the Kokchetav Massif, USSR. Geology 95, 87–105.

Collins, W.J., Vernon, R.H., Clarke, G.L., 1991. Discrete proterozoic structural terranes associated with low-*P*, high-*T* metamorphism, Anmatjira Range, Arunta Inlier, Central Australia—tectonic implications. J. Struct. Geol. 13 (10), 1157–1171.

Compston, W., Kröner, A., 1988. Multiple zircon growth within early Archaean tonalitic gneiss from the Ancient Gneiss Complex, Swaziland. Earth Planet. Sci. Lett. 87 (1–2), 13–28.

Condie, K.C., 1998. Episodic continental growth and supercontinents: a mantle avalanche connection? Earth Planet. Sci. Lett. 163 (1–4), 97–108.

Condie, K.C., 2001a. Mantle Plumes and Their Record in Earth History. Cambridge University Press, Cambridge.

Condie, K.C., Kröner, A., Milisenda, C.C., 1996. Geochemistry and geochronology of the Mkhondo suite, Swaziland: evidence for passive-margin deposition and granulite facies metamorphism in the late Archaean of southern Africa. J. Afr. Earth Sci. 22 (4), 483–506.

Coward, M.P., Spencer, R.M., Spencer, C.E., 1995. Development of the Witwatersrand Basin, South Africa. In: Coward, M.P., Ries, A.C. (Eds.). Early Precambrian Processes, Geol. Soc., London, 243–269 (Spec. Publ. 95).

De Ronde, C.E.J., De Wit, M.J., 1994. Tectonic history of the Barberton Greenstone Belt, South Africa: 490 million years of Archaean crustal evolution. Tectonics 13, 983–1005.

De Wit, M.J., Roering, C., Hart, R.J., Armstrong, R.A., De Ronde, C.E.J., Green, R.W.E., Tredoux, M., Peberdy, E., Hart, R.A., 1992. Formation of an Archaean continent. Nature 357, 553–562.

Diener, J.F.A., Stevens, G., Kisters, A.F.M., Poujol, M., 2005. Geotectonic evolution of the Tjakastad Schist belt, Barberton Greenstone Belt, South Africa: a record of mid-Archaean metamorphism and terrane exhumation. Precambrian Res. 143, 87–112.

Dodson, M.H., 1973. Closure temperature in cooling geochronological and petrological systems. Contrib. Miner. Petrol. 40, 259–274.

England, P.C., Thompson, A.B., 1984. Pressure–temperature–time paths of regional metamorphism. I. Heat transfer during the evolution of regions of thickened continental crust. J. Petrol. 25, 894–928.

Eriksson, P.G., Condie, K.C., van der Westhuizen, W., van der Merwe, R., De Bruiyn, H., Nelson, D.R., Altermann, W., Catuneanu, O., Bumby, A.J., Lindsay, J., Cunningham, M., 2002. Late Archaean superplume events: a Kaapvaal-Pilbara perspective. J. Geodyn. 34 (2), 207–247.

Gericke, B., 2001. New single zircon U–Pb age constraints on the Kraaipan and Amalia granite-greensrtone terrane, South Africa: implications for the evolution of the western Kaapvaal Craton. B.Sc. (Hons.) dissertation (Unpubl.), University of Witwatersrand, Johannesburg, 91 pp.

Gibson, R.L., Robb, L.J., Kisters, A.F.M., Cawthorn, R.G., 1996. Regional setting and geological evolution of the Okiep Copper District, Namaqualand, South Africa. S. Afr. J. Geol. 99 (2), 107–120.

Greenfield, J.E., Clarke, G.L., White, R.W., 1998. A sequence of partial melting reactions at Mt Stafford, central Australia. J. Met. Geol. 16 (3), 363–378.

Grobler, D.F., Walraven, F., 1993. Geochronology of Gaborone Granite Complex extensions in the area north of Mafikeng, South-Africa. Chem. Geol. 105 (4), 319–337.

Harley, S.L., 1988. Ultra-high temperature granulite metamorphism (1050 °C, 12 kbar) and decompression in garnet (Mg70)-orthopyroxene-sillimanite gneisses from Rauer Group, East Antarctica. J. Met. Geol. 16, 541–562.

Hegner, E., Kröner, A., Hofmann, A.W., 1984. Age and isotope geochemistry of the Archaean Pongola and Usushwana Suites in Swaziland, Southern-Africa—a case for crustal contamination of mantle-derived magma. Earth Planet. Sci. Lett. 70 (2), 267–279.

Henderson, D.R., Long, L.E., Barton, J.M., 2000. Isotopic ages and chemical and isotopic composition of the Archaean Turfloop Batholith, Pietersburg granite-greenstone terrane, Kaapvaal craton, South Africa. S. Afr. J. Geol. 103 (1), 38–46.

Holland, T.J.B., Powell, R., 1990. An enlarged and updated internally consistent thermodynamic dataset with uncertainties and correlations—the system K_2O–Na_2O–Cao–Mgo–Mno–Feo–Fe_2O_3–Al_2O_3–TiO_2–SiO_2–C–H_2–O_2. J. Met. Geol. 8 (1), 89–124.

Holland, T.J.B., Powell, R., 1998. An internally consistent thermodynamic data set for phases of petrological interest. J. Met. Geol. 16 (3), 309–343.

Holland, T.J.B., Powell, R., 2001. Calculation of phase relations involving haplogranitic melts using an internally consistent thermodynamic dataset. J. Petrol. 42 (4), 673–683.

Holness, M.B., 2006. Melt-solid dihedral angles of common minerals in natural rocks. J. Petrol. 47 (4), 791–800.

Hunter, D.R., 1968. The Precambrian terrane in Swaziland with particular reference to the granitic rocks. Unpubl. Ph.D. Thesis. University of the Witwatersrand, 273 pp.

Hunter, D.R., 1970. The Ancient Gneiss Complex in Swaziland. Trans. Geol. Soc. S. Afr. 73, 107–150.

Hunter, D.R., 1974. Crustal development in the Kaapvaal Craton. I. The Archaean. Precambrian Res. 1, 259–294.

Hunter, D.R., Barker, F., Millard, H.T., 1978. Geochemical nature of the Archaean Ancient Gneiss Complex and Granodiorite Suite, Swaziland—preliminary-study. Precambrian Res. 7 (2), 105–127.

Hunter, D.R., Barker, F., Millard, H.T., 1984. Geochemical investigation of Archaean Bimodal and Dwalile Metamorphic Suites, Ancient Gneiss Complex, Swaziland. Precambrian Res. 24 (2), 131–155.

Hunter, D.R., Kröner, A., Maphalala, R., Milisenda, C.C., 1993. The Ancient Gneiss Complex. In: Kröner, A. (Ed.), The Ancient Gneiss Complex: Overview Papers and Guidebook for Excursion, Bull. 11. Geol. Surv. Mines Dept., Swaziland, 62 pp.

Hunter, D.R., Smith, R.G., Sleigh, D.W.W., 1992. Geochemical studies of Archaean granitoid rocks in the southeastern Kaapvaal Province—implications for crustal development. J. Afr. Earth Sci. 15 (1), 127–151.

Hunter, D.R., Wilson, A.H., 1988. A continuous record of Archaean evolution from 3.5 Ga to 2.6 Ga in Swaziland and northern Natal. S. Afr. J. Geol. 91 (1), 57–74.

Isley, A.E., Abbott, D.H., 1999. Plume-related mafic volcanism and the deposition of banded iron formation. J. Geophys. Res. Solid Earth 104 (B7), 15461–15477.

Jackson, M.P.A., 1984. Archaean structural styles in the Ancient Gneiss Complex of Swaziland, southern Africa. In: Kröner, A., Greiling, R. (Eds.), Precambrian Tectonics Illustrated. Schweizerbart'sche Verlagsbuchhandlung, Stuttgart, pp. 1–18.

Jayananda, M., Moyen, J.F., Martin, H., Peucat, J.J., Auvray, B., Mahabaleswar, B., 2000. Late Archaean (2550–2520 Ma) juvenile magmatism in the Eastern Dharwar craton, southern India: constraints from geochronology, Nd–Sr isotopes and whole rock geochemistry. Precambrian Res. 99, 225–254.

Johnson, T., Brown, M., 2004. Quantitative constraints on metamorphism in the variscides of southern Brittany—a complementary pseudosection approach. J. Petrol. 45 (6), 1237–1259.

Johnson, T., Brown, M., Solar, G.S., 2003. Low-pressure subsolidus and suprasolidus phase equilibria in the MnNCKFMASH system: constraints on conditions of regional metamorphism in western Maine, northern Appalachians. Am. Miner. 88 (4), 624–638.

Jung, S., 2000. High-temperature, low/medium-pressure clockwise *P*–*T* paths and melting in the development of regional migmatites: the role of crustal thickening and repeated plutonism. Geol. J. 35, 345–359.

Kamo, S.L., Davis, D.W., 1994. Reassessment of Archaean crustal development in the Barberton Mountain Land, South-Africa, based on U–Pb dating. Tectonics 13 (1), 167–192.

Kelsey, D.E., Clark, C., Hand, M., 2008. Thermobarometric modelling of zircon and monazite growth in melt-bearing systems: examples using model metapelitic and metapsammitic granulites. J. Met. Geol. 26, 199–212.

Kelsey, D.E., White, R.W., Powell, R., 2003. Orthopyroxene–sillimanite–quartz assemblages: distribution, petrology, quantitative *P*–*T*–*X* constraints and *P*–*T* paths. J. Met. Geol. 21 (5), 439–453.

Kisters, A.F.M., Gibson, R.L., Charlesworth, E.G., Anhaeusser, C.R., 1998. The role of strain localization in the segregation and ascent of anatectic melts, Namaqualand, South Africa. J. Struct. Geol. 20, 229–242.

Kreissig, K., Holzer, L., Frei, R., Villa, I.M., Kramers, J.D., Kröner, A., Smit, C.A., Van Reenen, D., 2001. Geochronology of the Hout River Shear Zone and the metamorphism in the Southern Marginal Zone of the Limpopo Belt, Southern Africa. Precambrian Res. 109 (1–2), 145–173.

Kröner, A., Jaeckel, P., Brandl, G., 2000. Single zircon ages for felsic to intermediate rocks from the Pietersburg and Giyani greenstone belts and bordering granitoid orthogneisses, northern Kaapvaal Craton, South Africa. J. Afr. Earth Sci. 30 (4), 773–793.

Kröner, A., Wendt, J.I., Milisenda, C.C., Compston, W., Maphalala, R., 1993. Zircon geochronology and Nd isotopic systematic of the Ancient Gneiss Complex, Swaziland, and implications for crustal evolution. In: Kröner, A. (Ed.), The Ancient Gneiss Complex: Overview Papers and Guidebook for Excursion, Bull. 11. Geol. Surv. Mines Dept, Swaziland, 62 pp.

Layer, P.W., Kröner, A., Mc Williams, M., York, D., 1989. Elements of the Archaean thermal history and apparent polar wander of the eastern Kaapvaal Craton, Swaziland, from single grain dating and paleomagnetism. Earth Planet. Sci. Lett. 93 (1), 23–34.

Lee, J.K.W., Williams, I.S., Ellis, D.J., 1997. Pb, U and Th diffusion in natural zircon. Nature 390, 159–162.

Loosveld, R.J.H., Etheridge, M.A., 1990. A model for low-pressure facies metamorphism during crustal thickening. J. Met. Geol. 8 (3), 257–267.

Ludwig, K.R., 2000a. SQUID:1.00, A User's Manual, Berkeley Geochronology Center, Berkeley, CA, 17 pp. (Spec. Publ. 2).

Ludwig, K.R., 2000b. Isoplot/Ex: A Geochronological Toolkit for Microsoft Excel. Berkeley Geochronology Center, Berkeley, CA, 53 pp. (Spec. Publ. 1a).

Lux, D.R., Deyoreo, J.J., Guldotti, C.V., Decker, E.R., 1986. Role of plutonism in low-pressure metamorphic belt formation. Nature 323, 794–797.

Maphalala, R., Kröner, A., 1993. Pb–Pb single zircon ages for the younger Archaean granitoids of Swaziland, southern Africa. In: Ext. Abstr.16th International Colloquium on African Geology, Mbabane, Swaziland, pp. 201–206.

Marsh, J.S., Bowen, M.P., Rogers, N.W., Bowen, T.B., 1992. Petrogenesis of Late Archaean flood-type basic lavas from the Klipriviersberg Group, Ventersdorp Supergroup, South Africa. J. Petrol. 33, 817–847.

Meyer, F.M., Robb, L.J., Reimold, W.U., Debruiyn, H., 1994. Contrasting low-Ca and high-Ca granites in the Archaean Barberton Mountain Land, southern Africa. Lithos 32 (1–2), 63–76.

Mezger, K., Krogstad, E.J., 1997. Interpretation of discordant U–Pb zircon ages: an evaluation. J. Met. Geol. 15, 127–140.

Milisenda, C.C., 1986. Petrographie und geochemie archaischer granulite und gneise des Ancient Gneiss Complex in Swaziland, südliches Afrika. Unpubl. Diploma Thesis. University of Mainz, Germany, 137 pp.

Minter, W.E.L., Hill, W.C.N., Kidger, R.J., Kingsley, C.S., Snowden, P.A., 1986. The Welkom Goldfield. In: Anhaeusser, C.R., Maske, S. (Eds.), Mineral Deposits of Southern Africa. Geol. Soc. S. Afr. I, 497–539.

Moore, M., Davis, D.W., Robb, L.J., Jackson, M.C., Grobler, D.F., 1993. Archaean rapakivi granite anorthosite rhyolite complex in the Witwatersrand Basin hinterland, southern Africa. Geology 21 (11), 1031–1034.

Moyen, J.F., Stevens, G., Kisters, A.F.M., 2006. Record of mid-Archaean subduction from metamorphism in the Barberton terrane, South Africa. Nature 442, 559–562.
Nelson, J.P., Beukes, N.J., Cairncross, B., 1995. Tectono-stratigraphic setting of the ~2.9 Ga Mozaan Group of the Pongola Supergroup and correlation with the Witwatersrand Supergroup. In: Ext. Abstr. Centennial Geocongress, Geol. Soc. S. Afr., Rand Afrikaans University, vol. 1, Johannesburg, South Africa, pp. 838–840.
Nelson, D.R., 1998. Granite-greenstone crust formation on the Archaean Earth: a consequence of two superimposed processes. Earth Planet. Sci. Lett. 158 (3–4), 109–119.
Nelson, D.R., Trendall, A.F., de Laeter, J.R., Grobler, N.J., Fletcher, I.R., 1992. A comparative study of the geochemical and isotopic systematics of late Archaean flood basalts from the Pilbara and Kaapvaal Cratons. Precambrian Res. 54, 231–256.
Paces, J.B., Miller, J.D., 1993. Precise U–Pb ages of Duluth Complex and related mafic intrusions, northeastern Minnesota—geochronological insights to physical, petrogenetic, paleomagnetic, and tectonomagmatic processes associated with the 1.1 Ga Midcontinent Rift System. J. Geophys. Res. Solid Earth 98 (B8), 13997–14013.
Patiño Douce, A.E., Beard, J.S., 1995. Dehydration-melting of biotite gneiss and quartz amphibolite from 3 to 15 kbar. J. Petrol. 36, 707–738.
Pidgeon, R.T., 1992. Recrystallisation of oscillatory zoned zircon: some geochronological and petrological implications. Contrib. Miner. Petrol. 110, 463–472.
Pidgeon, R.T., Nemchin, A.A., Hitchen, G.J., 1998. Internal structures of zircons from Archaean granites from the Darling Range batholith: implications for zircon stability and the interpretation of zircon U–Pb ages. Contrib. Miner. Petrol. 132, 288–299.
Poujol, M., 2001. U–Pb isotopic evidence for episodic granitoid emplacement in the Murchison greenstone belt, South Africa. J. Afr. Earth Sci. 33 (1), 155–163.
Poujol, M., Anhaeusser, C.R., 2001. The Johannesburg Dome, South Africa: new single zircon U–Pb isotopic evidence for early Archaean granite-greenstone development within the central Kaapvaal Craton. Precambrian Res. 108, 139–157.
Poujol, M., Anhaeusser, C.R., Armstrong, R.A., 2002. Episodic granitoid emplacement in the Archaean Amalia-Kraaipan terrane, South Africa: confirmation from single zircon U–Pb geochronology. J. Afr. Earth Sci. 35 (1), 147–161.
Poujol, M., Robb, L.J., Anhaeusser, C.R., Gericke, B., 2003. A review of the geochronological constraints on the evolution of the Kaapvaal Craton, South Africa. Precambrian Res. 127 (1–3), 181–213.
Poujol, M., Robb, L.J., Respaut, J.P., Anhaeusser, C.R., 1996. 3.07–2.97 Ga Greenstone Belt formation in the northeastern Kaapvaal Craton: implications for the origin of the Witwatersrand Basin. Econ. Geol. 91, 1455–1461.
Powell, R., Holland, T.J.B., 1985. An internally consistent thermodynamic dataset with uncertainties and correlations. 1. Methods and a worked example. J. Met. Geol. 3 (4), 327–342.
Powell, R., Holland, T.J.B., 1988. An internally consistent dataset with uncertainties and correlations. 3. Applications to geobarometry, worked examples and a computer-program. J. Met. Geol. 6 (2), 173–204.
Powell, R., Holland, T.J.B., Worley, B., 1998. Calculating phase diagrams involving solid solutions via non-linear equations, with examples using THERMOCALC. J. Met. Geol. 16 (4), 577–588.
Reimold, W.U., Meyer, F.M., Walraven, F., Matthews, P.E., 1993. Geochemistry and chronology of pre- and post-Pongola granitoids from northeastern Natal. In: Ext. Abstr.16th International Colloquium on African Geology, vol. 2, Mbabane, Swaziland, pp. 294–296.
Richardson, S.H., Shirey, S.B., Harris, J.W., Carlson, R.W., 2001. Archaean subduction recorded by Re-Os isotopes in eclogitic sulfide inclusions in Kimberley diamonds. Earth Planet. Sci. Lett. 191, 257–266.
Robb, L.J., Davis, D.W., Kamo, S.L., Meyer, F.M., 1992. Ages of altered granites adjoining the Witwatersrand Basin with implications for the origin of gold and uranium. Nature 357, 677–680.
Robb, L.J., Meyer, F.M., 1987. The nature of the Archaean basement in the hinterland of the Witwatersrand Basin. I. The Rand anticline between Randfontein and Rysmierbult. S. Afr. J. Geol. 90 (1), 44–63.
Robb, L.J., Meyer, F.M., Kröner, A., Trumbull, R.B., Reimold, W.U., De Bruiyn, H., Walraven, F., Toulkeridis, T., 1993. Late-stage granite plutons in the Barberton region and Swaziland: an update. In: Ext. Abstr.16th International Colloquium on African Geology, Mbabane, Swaziland, pp. 299–301.
Sandiford, M., Hand, M., 1998. Controls on the locus of intra-plate deformation in central Australia. Earth Planet. Sci. Lett. 162 (1–4), 97–110.
Sandiford, M., Powell, R., 1986. Pyroxene exsolution in granulites from Fyfe Hills, Enderby Land, Antarctica: evidence for 1000 °C metamorphic temperatures in Archaean continental crust. Am. Miner. 7 (1), 946–954.
Schmitz, M.D., Bowring, S.A., 2003. Ultrahigh-temperature metamorphism in the lower crust during Neoarchaean Ventersdorp rifting and magmatism, Kaapvaal Craton, southern Africa. Geol. Soc. Am. Bull. 115 (5), 533–548.
Schoene, B., De Wit, M.J., Bowring, S.A., 2008. Mesoarchaean assembly and stabilization of the eastern Kaapvaal craton: a structural-thermochronological perspective. Tectonics, 27.
Schoene, B., Bowring, S.A., in press. Rates and mechanisms of Mesoarchaean magmatic arc construction, eastern Kaapvaal craton, Swaziland, Geol. Soc. Am. Bull.
Sleep, N.H., 1997. Lateral flow and ponding of starting plume material. J. Geophys. Res. Solid Earth 102 (B5), 10001–10012.
Smit, C.A., Van Reenen, D., 1997. Deep crustal shear zones, high-grade tectonics, and associated metasomatic alteration in the Limpopo Belt, South Africa: implications for deep crustal processes. J. Geol. 105, 37–57.
Stacey, J.S., Kramers, J.D., 1975. Approximation of terrestrial lead isotope evolution by a 2-stage model. Earth Planet. Sci. Lett. 26 (2), 207–221.
Stanistreet, I.G., McCarthy, T.S., 1991. Changing tectono-sedimentary scenarios relevant to the development of the Late Archaean Witwatersrand Basin. J. Afr. Earth Sci. 13 (1), 65–81.
Stevens, G., Clemens, J.D., Droop, G.T.R., 1997. Melt production during granulite-facies anatexis: experimental data from "primitive" sedimentary protoliths. Contrib. Miner. Petrol. 128, 352–370.
Stevens, G., Van Reenen, D., 1992. Constraints on the form of the P–T loop in the Southern Marginal Zone of the Limpopo Belt, South-Africa. Precambrian Res. 55 (1–4), 279–296.
Thompson, A.B., England, P.C., 1984. Pressure–temperature–time paths of regional metamorphism. II. Their inference and interpretation using mineral assemblages in metamorphic rocks. J. Petrol. 25, 929–955.
Toulkeridis, T., Goldstein, S.L., Clauer, N., Kröner, A., Lowe, D.R., 1994. Sm–Nd dating of Fig Tree clay minerals of the Barberton Greenstone Belt, South Africa. Geology 22, 199–202.
Tweedie, E.B., 1986. The Evander Goldfield. In: Anhaeusser, C.R., Maske, S. (Eds.), Mineral Deposits of Southern Africa. Geol. Soc. S. Afr. I, 705–730.
Van Reenen, D., 1983. Cordierite + garnet + hypersthene + biotite-bearing assemblages as a function of changing metamorphic conditions in the Southern Marginal Zone of the Limpopo metamorphic complex, South Africa. In: Van Biljon, W.J., Legg, J.H. (Eds.), Geol. Soc. S. Afr., Spec. Publ. 8, 143–167.
Van Reenen, D., McCourt, S., Smit, C.A., 1995. Are the Southern and Northern Marginal Zones of the Limpopo Belt related to a single continental collision event? S. Afr. J. Geol. 98 (4), 498–504.
Vernon, R.H., Clarke, G.L., Collins, W.J., 1990. Mid-crustal granulite facies metamorphism: low-pressure metamorphism and melting, Mount Stafford, central Australia. In: Ashworth, J.R., Brown, M. (Eds.), High-Temperature Metamorphism and Crustal Anatexis, Spec. Publ. Miner. Soc. 2, 272–319.
Vielzeuf, D., Holloway, J.R., 1988. Experimental determination of the fluid-absent melting reactions in the pelitic system: consequences for crustal differentiation. Contrib. Miner. Petrol. 98, 257–276.
Waters, D.J., 1990. Thermal history and tectonic setting of the Namaqualand granulites, southern Africa: clues to Proterozoic crustal development. In: Vielzeuf, D., Vidal, Ph. (Eds.), Granulites and Crustal Evolution. Kluwer Academic, Dordrecht, pp. 243–256.
White, R.W., Powell, R., Holland, T.J.B., 2001. Calculation of partial melting equilibria in the system Na_2O–CaO–K_2O–FeO–MgO–Al_2O_3–SiO_2–H_2O (NCKFMASH). J. Met. Geol. 19 (2), 139–153.
White, R.W., Powell, R., 2002. Melt loss and the preservation of granulite facies mineral assemblages. J. Met. Geol. 20, 621–632.
Wickham, S.M., Oxburgh, E.R., 1985. Continental rifts as a setting for regional metamorphism. Nature 318, 330–333.
Williams, I.S., 1992. Some observations on the use of zircon U–Pb geochronology on the study of granitic rocks. Trans. R. Soc. Edinburgh: Earth Sci. 83, 447–458.
Williams, I.S., 1998. U–Th–Pb geochronology by ion microprobe. In: McKibben, M.A., Shanks III, W.C., Ridley, W.I. (Eds.), Applications of microanalytical techniques to understanding mineralization processes. Reviews in Economic Geology 7, 1–35.
Wilson, A.C., 1982. 1:250 000 Geological Map of Swaziland, with Explanatory Notes. Geological Survey of Swaziland.
Wilson, A.C., Jackson, M.P.A., 1988. Mantled gneiss domes in southern Swaziland and the concept of 'stable' Pongola cratonic cover. S. Afr. J. Geol. 91 (3), 404–414.
Zhao, G.C., Wilde, S.A., Cawood, P.A., Lu, L.Z., 1998. Thermal evolution of the Archaean basement rocks from the eastern part of the North China Craton and its bearing on tectonic setting. Int. Geol. Rev. 40, 706–721.
Zhao, G.C., Wilde, S.A., Cawood, P.A., Lu, L.Z., 1999. Thermal evolution of two types of mafic granulites from the North China craton: implications for both mantle plume and collisional tectonics. Geol. Mag. 136, 223–240.
Zhao, G.C., Wilde, S.A., Cawood, P.A., Sun, M., 2001. Archaean blocks and their boundaries in the North China Craton: lithological, geochemical, structural and *P–T* path constraints and tectonic evolution. Precambrian Res. 107, 45–73.

Chapter 3

SELECTIVE ENTRAINMENT OF PERITECTIC GARNET INTO S-TYPE GRANITIC MAGMAS: EVIDENCE FROM ARCHAEAN MID-CRUSTAL ANATECTITES

CHAPTER 3

Presentation of the publication

This paper*, first authored by Jeanne Taylor, was accepted for publication in the journal Lithos. The following aspects of the research was done independently by Jeanne Taylor while receiving standard supervision by her supervisor Gary Stevens: (i) fieldwork and sampling; (ii) acquisition of mineral chemical data on the SEM; (iii) acquisition of LA-ICP-MS garnet trace element data; (iv) writing of the manuscript.

Jeanne Taylor[a]

Gary Stevens[a]

a: Centre for Crustal Petrology, Department of Earth Sciences, Stellenbosch University, Private Bag X1, Matieland 7602, South Africa

---

Reference*: Taylor, J., and Stevens, G., 2010, Selective entrainment of peritectic garnet into S-type granitic magmas: Evidence from Archaean mid-crustal anatectites: *Lithos*, v. 120, p. 277–292. doi:10.1016/j.lithos.2010.08.015

Lithos 120 (2010) 277–292

Contents lists available at ScienceDirect

Lithos

journal homepage: www.elsevier.com/locate/lithos

Selective entrainment of peritectic garnet into S-type granitic magmas: Evidence from Archaean mid-crustal anatectites

Jeanne Taylor *, Gary Stevens

Centre for Crustal Petrology, Department of Earth Sciences, Stellenbosch University, Private Bag X1, Matieland 7602, South Africa

ARTICLE INFO

Article history:
Received 16 March 2010
Accepted 10 August 2010
Available online 15 August 2010

Keywords:
Peritectic garnet entrainment
Anatexis
Granite geochemistry
Granite petrogenesis

ABSTRACT

Entrainment of restite is commonly invoked to explain both the origin of relatively mafic granites and granodiorites, as well as the chemical connection between granite magmas and their sources. This concept has become linked to models for magma migration out of the source, as restite entrainment is considered to take place when diatexitic sources mobilise *en masse*. This is at odds with the common occurrence of relatively mafic granites as high level intrusions in the crust or their eruptive equivalents that must have formed from markedly water-undersaturated magmas that ascended through narrow conduits. We investigate pelitic migmatites from the Mkhondo Valley Metamorphic Suite (MVMS) in Swaziland, where a mid-crustal heating event produced metatexitic migmatites with minimal post-anatectic recrystallisation. In these rocks all the garnet is peritectic, having arisen through biotite fluid-absent melting, which produced garnet poikiloblasts characterised by inclusions of melt, quartz and biotite. Leucosomes that represent sites of melt transfer carry similar, smaller (typically <1 mm), entrained garnet poikiloblasts, which were capable of amalgamating to form larger composite grains. In anatectic structures where melt was present for longer, entrained garnet was extensively recrystallised, via a dissolution-precipitation process, to adopt a more magmatic character. The peritectic garnet in the pelitic source appears to have grown out of equilibrium with feldspar and HREE-rich accessory phases, while the recrystallised garnet in the larger melt-filled structures became progressively better equilibrated with these minerals. Thus, peritectic garnet in the source grew sufficiently rapidly to prevent trace element equilibrium with the bulk-rock composition, and, concurrent rapid magma segregation prevented the development of diatexitic source conditions. The segregated magma consisted of melt, the peritectic assemblage (principally garnet) and the accessory minerals monazite and zircon. These rocks illustrate that mafic granites may arise purely as mixtures of melt and the peritectic assemblage produced by the incongruent melting reaction. Importantly, under the circumstances which produced the MVMS anatectites, peritectic garnet is entrained as <1 mm poikiloblasts, demonstrating how mafic granitic magmas can migrate out of the source without the source becoming diatexitic.

1. Introduction

Several studies have highlighted the fact that relevant experimental melt compositions are typically more leucocratic than most granites and granodiorites (e.g. Montel and Vielzeuf, 1997; Stevens et al., 2007). Additionally, relatively mafic granites and granodiorites appear to faithfully image the composition of their sources, as evidenced by the applicability of the S- and I-type classification scheme (Chappell and White, 1974) in certain areas of the world, such as the Lachlan Fold Belt (LFB) of south-eastern Australia and the Cape Granite Suite of South Africa. This chemical memory of the source has been interpreted to reflect the entrainment of solid source material to the melt (e.g. Chappell and White, 1974; Stevens et al., 2007). Our current understanding of how this process might occur in the anatectic crust is strongly linked to the 'restite entrainment' model of Chappell and White (1974) and the 'restite unmixing' model of White and Chappell (1977), Chappell et al. (1987), Chappell (1997), and Chappell et al. (2000). In combination these models propose that restitic fractions of the source are entrained to the melt and that the subsequent fractionation of this entrained material accounts for the systematic compositional variations observed within granitoid suites of the Lachlan Fold Belt (LFB). Thus the term 'restite' in these models includes a variety of different source components, i.e. minerals not involved in the melting reactions (e.g. the pre-anatectic anhydrous ferromagnesian and oxide minerals), the remains of the minerals partially consumed by anatexis (e.g. plagioclase), the solid products of the typically incongruent melt-generating reactions (e.g. peritectic garnet, cordierite, orthopyroxene, K-feldspar), as well as unmelted or less melted fragments of rock. The latter category commonly manifests as amphibolite facies enclaves in granites, which has led

* Corresponding author. Tel./fax: +27 21 808 3129.
E-mail addresses: jtaylor@sun.ac.za (J. Taylor), gs@sun.ac.za (G. Stevens).

0024-4937/$ – see front matter © 2010 Elsevier B.V. All rights reserved.
doi:10.1016/j.lithos.2010.08.015

to the suggestion that such granites arise by relatively low-temperature melting involving elevated water activity in the source (Chappell et al., 2000). Restite entrainment is proposed to occur once melt fractions in the source are sufficiently high to break down the rigid rock framework (i.e. once the Critical Melt Fraction of van der Molen and Paterson, 1979 is reached) and the crystal/rock fragment-rich magma can move *en masse*, systematically freeing itself of restite as it ascends to higher levels in the crust (White and Chappell, 1977; Chappell, 1997).

Further coupling between the restite models for granite petrogenesis and source processes has been achieved by models for melt segregation developed by Sawyer (1994, 1996, 1998, 2001), which consider the contamination of melt by residual phases, the possibility of entrainment of a whole-source component in the melt and the progressive separation of these entrained components during magma flow. Sawyer (1996) suggested that efficient melt-residuum segregation is mainly restricted to metatexitic migmatites where melt fractions are low and where segregation is generally deformation-assisted. Under such conditions there is sufficient melt present to form an interconnected network through which melt can move, i.e. $\leq$10% (First Percolation Threshold of Vigneresse et al., 1996), but insufficient to mobilise the solid fraction in the source. Magma mobility on the other hand, defined as the movement of melt plus entrained source material, is only considered to take place with the development of a pervasive melt fraction throughout the whole rock volume, i.e. in diatexitic migmatites. The solid matrix framework then looses cohesion and bulk flow of the melt plus the entire residue may occur, producing the residuum enriched granites described by White and Chappell (1977) and Chappell et al. (1987).

Mobilisation of a diatexitic source prior to magma segregation from entrained restite is at odds with several important lines of evidence concerning the conditions of anatexis in granite source areas and the mechanisms by which granite magmas ascend. Firstly, some granite magmas can be demonstrated to have left their source areas rapidly enough that trace element equilibrium between the melt and residuum is not attained (Ayres and Harris, 1997; Bea et al., 2006; Villaros et al., 2009b). Secondly, granite magmas which intrude at high-levels in the crust and/or erupt, very likely ascend through dykes and narrow conduits propagated by magma buoyancy (Clemens and Mawer, 1992; Petford et al., 1993). Such magmas must be markedly water-undersaturated, and arise through high-temperature, fluid-absent melting reactions (e.g. Clemens, 1992). The plutons and eruptive products that these magmas produce typically display a wide range in chemistry from leucogranites to mafic granodiorites, thus necessitating a mechanism for mafic granite production by fluid-absent melting.

Recently, 'selective peritectic phase entrainment' has been proposed as an alternative model to explain the petrogenesis of mafic, peraluminous granites (Stevens et al., 2007; Villaros et al., 2009a,b). The process involves the entrainment of only the solid peritectic products of the melting reaction to the melt. Specifically, the entrainment of garnet and ilmenite arising through high-temperature, incongruent, fluid-absent melting of biotite in metapelites is suggested to control the chemistry of the strongly peraluminous, mafic granites studied by Stevens et al. (2007). Thus, the admixture to melt is controlled by the stoichiometry of the melting reaction and this is proposed to explain the very tight inter-element correlations displayed by some granites as a function of increasing maficity (Fe + Mg), namely an increase in A/CNK, Mg# and Ca, a decrease in Si and K, as well as the very focused positive correlation of Ti with maficity (Stevens et al., 2007). Selective entrainment of the peritectic assemblage to the melt therefore appears to be a viable mechanism for producing hot, water-undersaturated, mafic granitic magmas. Consequently, we follow Sawyers lead and investigate appropriate

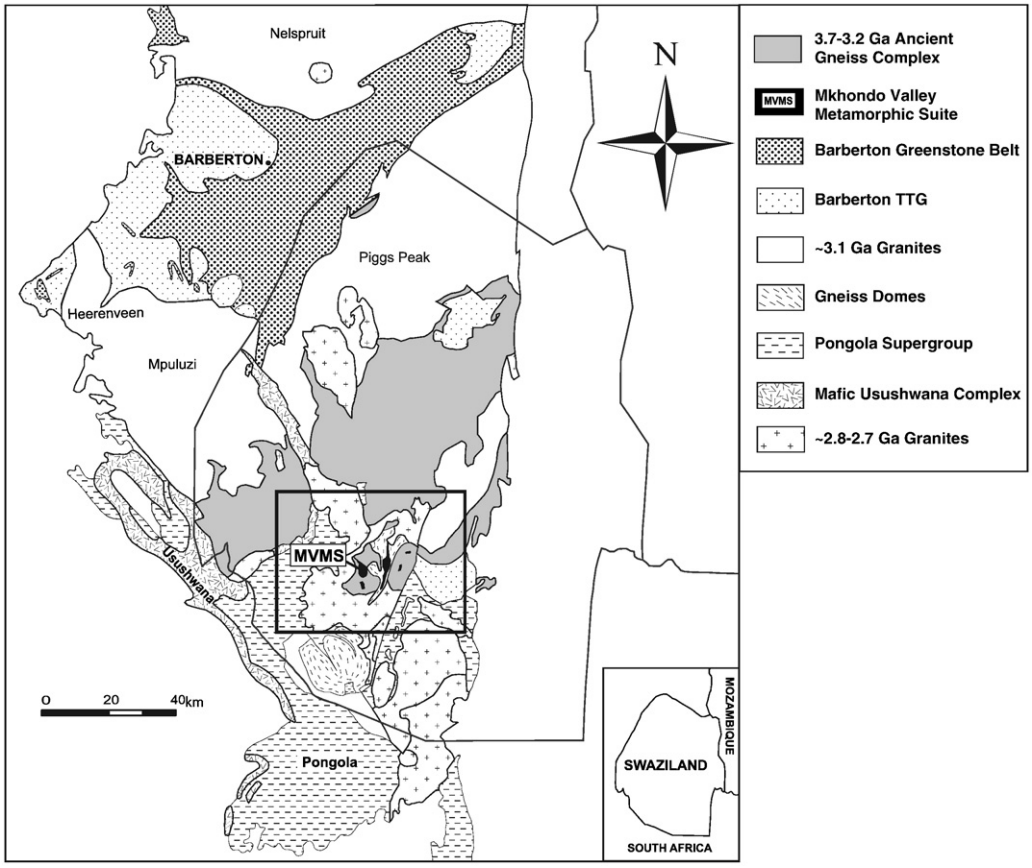

Fig. 1. Schematic geological map of Swaziland modified after Wilson (1982), showing the AGC and location of the Mkhondo Valley Metamorphic Suite (MVMS) study area.

metasedimentary migmatites with the aim of gaining insight into the details of this process in the source.

2. Geological setting

The current study focuses on the Mkhondo Valley Metamorphic Suite (MVMS) in the 3.7–3.2 Ga Ancient Gneiss Complex (AGC) of Swaziland. The MVMS is a diverse suite of high-grade paragneisses preserved as small supracrustal keels which are infolded within surrounding TTG basement (Fig. 1). One of these supracrustal keels is a 4.5 km × 2.5 km inlier along the Mkhondo River in south-central Swaziland (26°52'S and 31°17′E), which is dominated by a thick succession of metapelitic garnet–cordierite–biotite–feldspar–quartz ± opx bearing gneisses and metapsammitic cordierite–biotite–feldspar–quartz gneisses (Hunter,

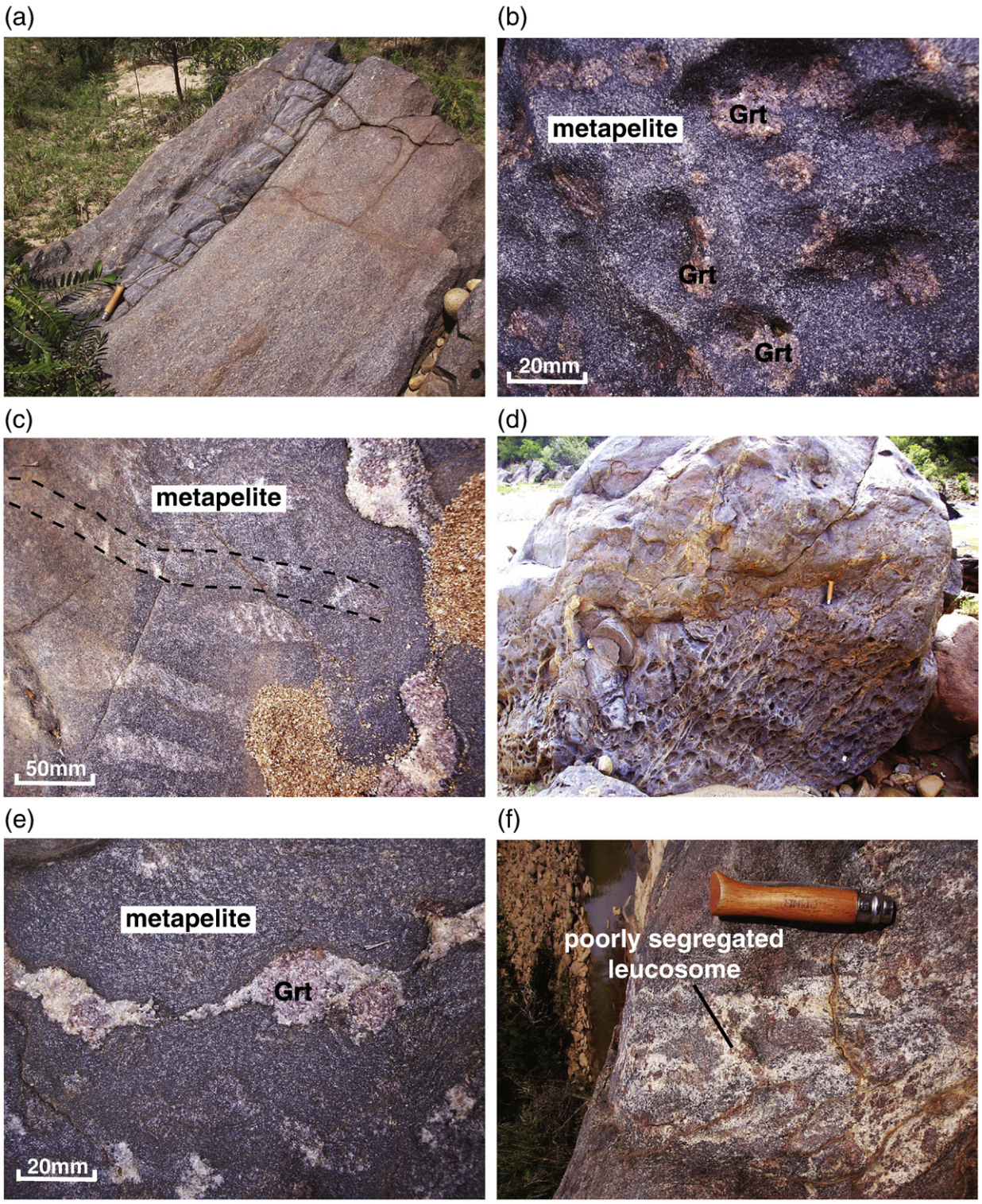

Fig. 2. Anatectic features of the MVMS: (a) sedimentary layering and bedding preserved in the metapelites and metapsammites from the MVMS; (b) restitic metapelites containing large porphyroblastic aggregates of garnet; (c) remnant leucotraces in the metapelites which track the movement of melt from the residuum enriched pelitic source to discrete leucosomes; (d) stromatic leucosome veins in the metapelites; (e) in situ leucosomes in the metapelites containing rounded aggregates of garnet; and (f) a poorly segregated leucosome from the MVMS.

1974; Kröner et al., 1993; Condie et al., 1996). Peak granulite facies metamorphism and partial melting in the MVMS at ca 2.73 Ga has been constrained to 830–850 °C at pressures of 4.4–6.4 kbars (Taylor et al., 2010). The low to medium pressure, high-temperature event coincided with widespread flood basalt volcanism on the craton and intra-plate granitic magmatism in Swaziland (Fig. 1). Taylor et al. (2010) proposed that this period of regional crustal anatexis likely arose from extensive partial melting in the mantle and under/intraplating of the crust.

Migmatites are commonly considered to represent the initial stages of granitic magma generation during high-grade, regional

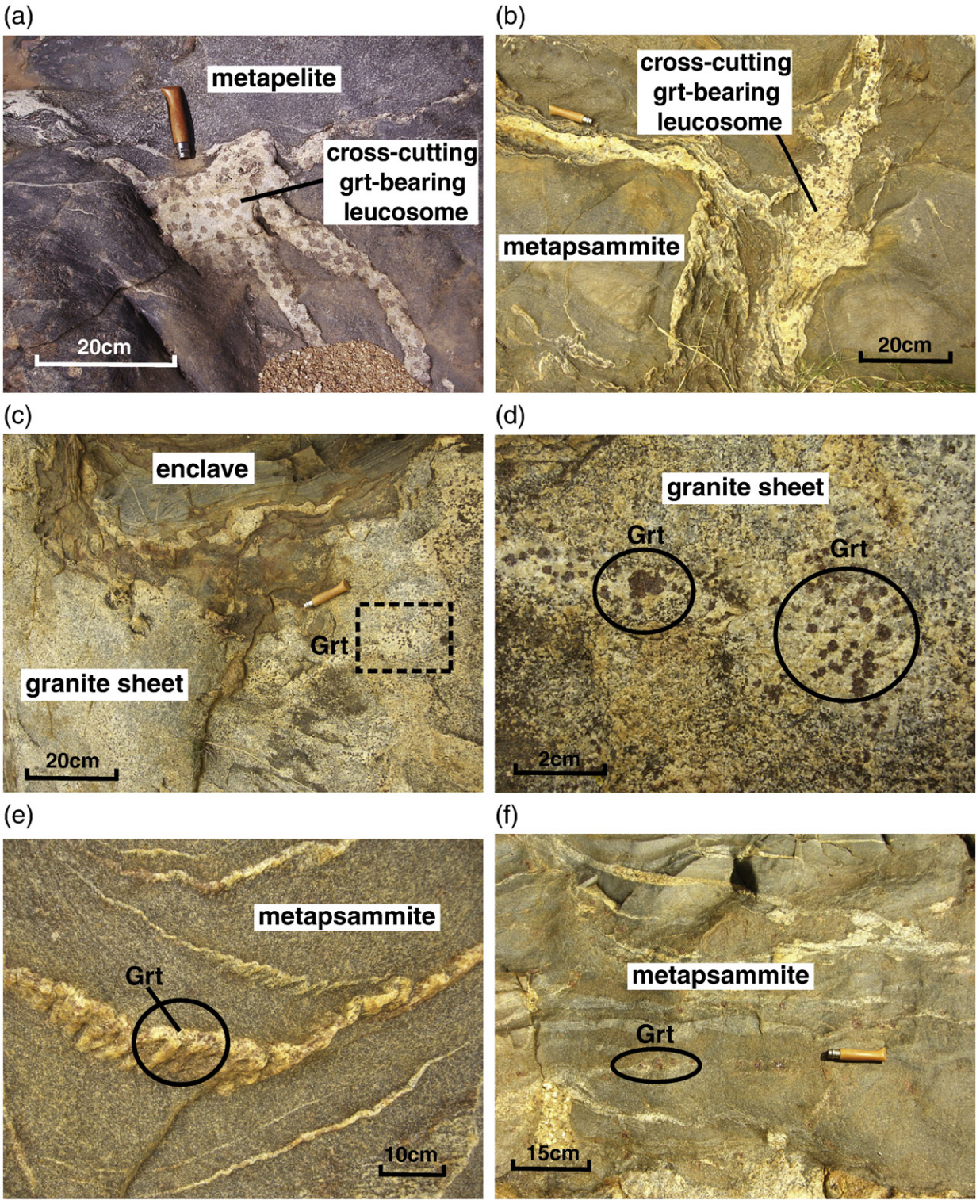

Fig. 3. Anatectic features of the MVMS continued: (a) discordant leucosomes developed in the metapelites containing rounded, porphyroblastic aggregates of garnet; (b) garnet-bearing leucosomes intruding and brecciating metapsammite layers; (c) a granite sheet containing patchy distributions of 1–5 mm, individual, rounded to euhedral garnets; (d) an enlargement of the garnets in the granite sheet; (e) discordant leucosome veins carrying small (<1 mm), individual, rounded to euhedral garnet crystals; and (f) rare ± 50 mm garnet porphyroblasts in the metapsammites, interspaced along remnant leucotraces, as the only evidence for limited in situ melting in the metapsammites.

metamorphism, though in general migmatites have limitations in terms of their use as natural laboratories for studying the origins of granites. This is because they may undergo protracted periods of post-anatectic metamorphic evolution involving recrystallisation, deformation, diffusion and ultimately retrogression (White and Powell, 2002). Due to the nature of the heat source for the MVMS anatectic event, however, the migmatites are largely free of penetrative deformation and post-anatectic recrystallisation, rendering them good candidates for studying the details of S-type magma generation in the source.

3. Anatectic features of the Mkhondo Valley Metamorphic Suite

Metapelites from the MVMS have undergone substantially higher degrees of melting relative to less fertile metapsammites. Layers within the metapelites which are parallel to the primary compositional banding are characterised by large (5–20 mm) porphyroblastic aggregates of garnet (Fig. 2b). These layers retain indications of the paths of melt migration in the form of remnant leucotraces, where movement of melt can be traced from the residuum enriched source to discrete leucosomes (Fig. 2c). Three main varieties of leucosome are preserved: (1) sets of thin, stromatic, foliation-parallel leucosome veins within metapelites, specifically in domains most enriched in garnet (Fig. 2d); (2) small, in situ lensoid shaped leucosomes within metapelites that terminate in the foliation and contain rounded aggregates of garnet (Fig. 2e). These are interpreted to be the vestiges of melt transfer zones through which melt flowed from the metapelites into the leucosomes. Occasionally these leucosomes are relatively rich in residuum and carry small schlieren defining disrupted foliation, and we refer to these as 'poorly segregated leucosomes' (Fig. 2f); (3) Thirdly, discrete 2–20 cm, layer-parallel or cross-cutting garnet-bearing leucosomes are developed in the metapelites (Fig. 3a), but more commonly within unmelted metapsammites (Fig. 3b). These discordant leucosomes coalesce and feed into meter-sized garnet-bearing granite sheets, or small intrusive bodies of garnet-bearing granite, which contain rafts of the more competent wall-rock material (Fig. 3c and d). The host gneisses and xenoliths carry a fabric that developed pre- to syn the high-grade metamorphism, whereas the garnet-bearing granite sheets and granites are undeformed, and were clearly anatectic magmas during or following peak metamorphism. Thus the larger magmatic structures were fed by discordant leucosomes associated with melt extraction from the source, and are interpreted to represent sites of considerable melt accumulation. Where leucosomes cross-cut the metapsammitic gneisses, they typically occur as the matrix within breccias (Fig. 3b) where meter-scale metapsammitic clasts are rotated relative to one another, yet are separated by garnet-bearing leucosomes $\leq$20 cm thick. These structures are interpreted to reflect zones inflated by melt, within which clasts of unmelted material rotated prior to collapse during melt extraction. The occurrence of more competent metapsammitic clasts within these breccias may indicate that deformation of competent layers was important in creating space for melt to accumulate (e.g. Kisters et al., 1998). Thinner, typically $\leq$5 cm thick, discordant leucosome veins also intrude the metapsammites and carry small (1–2 mm), individual, rounded to euhedral garnets (Fig. 3e). Within the metapsammitic gneisses, evidence for incongruent melting is restricted to rare $\pm$50 mm garnet porphyroblasts surrounded by diffuse leucocratic halos, interspaced along thin leucosome veins and remnant leucotraces (Fig. 3f). These may be interpreted as evidence for limited in situ melting; alternatively they may represent melt transfer zones through which garnet-bearing melts, derived from metapelites, have passed. Importantly, all garnet in the MVMS is associated with anatectic features and likely formed via the incongruent melting reaction bt + qtz + plag = grt + melt. Field evidence suggests that partial melting in the MVMS was responsible for the production of significant volumes of S-type granitic melt. Despite this, metapelites and metapsammites retain their original compositional banding and bedding (Fig. 2a); within coarser-grained, quartz-rich layers, fine-scale cross-bedding and graded bedding is preserved; and the pre- to syn high-grade foliation and fabric in the migmatitic gneisses has generally not been disrupted by the presence of melt. Thus, efficient melt segregation and extraction left basic pre-migmatite structures intact, and the MVMS migmatites are metatexitic.

All structures associated with melt segregation contain high proportions of garnet. Discordant leucosomes contain rounded aggregates of garnet which texturally resemble those in the pelitic residua (Fig. 3a and b); and granite sheets or small granitic bodies contain patchy distributions of individual, 1–5 mm rounded to euhedral garnets (Fig. 3d). The garnets in these structures have one of two possible origins: i.e. either they crystallised directly from the magma during cooling, or they formed with the magma as the solid peritectic product of the incongruent melting reaction at the sites of in situ anatexis, prior to being entrained. Irrespective of the mode of garnet formation, melt compositions in this system are known from experiments to be strongly leucocratic under conditions where quartz + biotite assemblages persist (e.g. Stevens et al., 2007). Therefore the high proportions of garnet indicate significant melt loss from these structures. This is in agreement with the absence of retrogression of the garnet in the leucosomes (White and Powell, 2002), as well as whole-rock geochemical data which reveals that the MVMS leucosome compositions depart from the compositions expected of typical experimental melts generated by incongruent, fluid-absent melting of biotite. Besides for being more mafic, the leucosomes are enriched in CaO and depleted in K_2O relative to experimental melt compositions (Fig. 4). This is interpreted as indicative of melt loss from these structures, following the crystallisation of Ca-rich plagioclase. The remainder of this work presents a detailed comparison of garnet texture and chemistry in the metapelitic residue with that of garnets hosted in the structures associated with melt segregation, with important implications for S-type granite petrogenesis.

4. Analytical techniques

4.1. Whole-rock geochemistry

Samples were crushed to a fine powder using a jaw crusher and tungsten swing mill at the Department of Earth Sciences, Stellenbosch University, South Africa. Whole-rock compositions were determined at Acme Analytical Laboratories in Vancouver, Canada, following a Lithium metaborate/tetrabortate fusion and dilute nitric digestion on 0.2 g of powdered rock. Major oxide abundances were determined by Inductively Coupled Plasma (ICP)-emission spectrometry. Trace element concentrations were determined by ICP-mass spectrometry (MS). Loss on ignition (LOI) is by weight difference after ignition at 1000 °C. For each element analysed, the reproducibility of replicate analyses and the deviation from the certified values of the secondary standards are less than 5% relative.

4.2. Mineral chemistry

Garnet and biotite major element compositions were analysed using a Leo® 1430VP Scanning Electron Microscope at the Department of Earth Sciences, Stellenbosch University, South Africa. Textures were studied in backscattered electron (BSE) mode and mineral compositions quantified by EDX (Energy Dispersive X-ray) analysis using an Oxford Instruments ® 133 keV ED X-ray detector and Oxford INCA software. Beam conditions during the quantitative analyses were 20 kV accelerating voltage and 1.5 nA probe current, with a working distance of 13 mm and a specimen beam current of −4.0 nA. X-ray counts were typically ~7000 cps, and the counting time was 50 s live-time. Analyses were quantified using natural mineral standards,

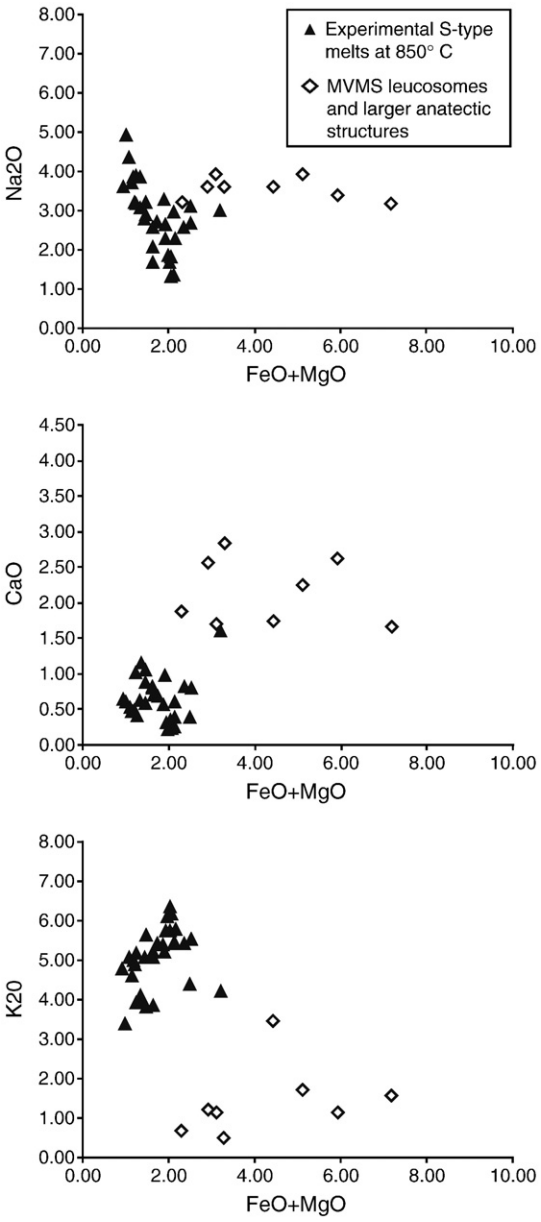

Fig. 4. A comparison of the major element compositions of experimental S-type melts at ± 850 °C (Vielzeuf and Holloway, 1988; Patiño Douce and Johnston, 1991; Stevens et al., 1997; Pickering and Johnston, 1998; Patiño Douce and Harris, 1998) with the compositions of MVMS leucosomes and larger anatectic structures as a function of increasing maficity.

and mineral chemical compositions were recalculated to mineral stoichiometries to obtain resultant mineral structural formulae. Comparisons between measured and accepted compositions of control standards within this laboratory, as a reflection of the accuracy of the analytical technique, have been published by Diener et al. (2005) and Moyen et al. (2006).

Garnet trace element compositions were analysed using a Laser Ablation ICP-MS at Department of Earth Sciences, Stellenbosch University, South Africa. In situ sampling on polished thin sections was performed using a 40 μm diameter ablation spot generated by a New Wave 213 nm Nd-YAG Laser coupled to an Agilent 7500ce ICP-MS mixture of Ar–He as carrier gas. Operating conditions for the laser were 6 Hz frequency and 10.5 kJ energy. Data was acquired in time resolved mode (Longerich et al., 1996), which allowed potential contamination from mineral inclusions or fractures to be identified and excluded from the analysis. NIST-612 glass was used as a control standard and measured garnet (via EDS) SiO_2 contents were used as an internal standard. Accuracy and reproducibility of multiple analyses was established from the analysis of the secondary standard BHVO 2G, a USGS natural basaltic glass standard. Results were better than 5% relative for most elements. Data was processed using Glitter (v 4.4.2) software and σ1 errors as well as chondrite-normalised trace element values are reported as defined by the software.

For the construction of garnet major and trace element maps, Mg^{2+} and Y compositional zoning in garnet was determined using a Zeiss EVO® MA15VP Scanning Electron Microscope at the Department of Earth Sciences, Stellenbosch University. Major and trace element compositions were quantified by EDX and WD (Wavelength-Dispersive) X-ray analysis respectively, using an Oxford Instruments® 133 keV detector and Oxford INCA software. Beam conditions during the quantitative analyses were 20 kV with a working distance of 8.5 mm and a specimen beam current of −20 nA. The counting time was 10 s live-time for the ED detector and 60 s on-peak, with symmetrical 30 s background measurement for the WD detector. Internal Astimex Scientific mineral standards were used for standardization and verification of the analyses. Pure Co was used periodically to correct for detector drift.

5. Petrography and major element chemistry

5.1. Metapelites

Peritectic garnets in the metapelites are characterised by numerous 10–300 μm, rounded to lobate quartz inclusions, polymineralic inclusions with low angle terminations interpreted to be melt inclusions (Holness, 2006), as well as 10–50 μm, round, high Ti^{4+} and high Mg# [Mg/(Mg + Fe)]*100 = 59–69 biotite inclusions (Fig. 5a and b). The high Ti^{4+} and high Mg# biotite inclusions are interpreted to be remnants of the high-temperature biotite that underwent incongruent melting during peritectic garnet growth (Table 1b), whereas the abundant quartz inclusions in the garnets may be the remnants of reactant quartz, or were produced by the peritectic reaction itself (Barbey, 2007). Compositionally, the garnet is an Fe-rich almandine-pyrope solid-solution with minor grossular and spessartine components (Table 1a). Peritectic garnets from different metapelites vary between Mg# [Mg/ (Mg + Fe)] *100 = 20–27, but have uniform X_{Spss} [Mn/(Fe + Mg + Ca + Mn)] = 0.01. Garnets are unzoned in terms of their major element chemistry, with homogeneous interiors surrounded by occasional 5–20 μm wide, retrograde rims that display slightly lower Mg# and higher Mn contents. Different textural varieties of garnet in the metapelites appear to record various stages of garnet growth, from small (50–500 μm) interlocking, poikilitic crystal-fragment networks (Fig. 5a) to larger (1–3 mm) subhedral poikiloblasts (Fig. 5b). The latter appear to have grown from the aggregation of smaller poikilitic fragments, and are

Fig. 5. Photomicrographs: (a) peritectic garnets in the metapelites forming networks of poikilitic crystals; (b) subhedral, composite garnet poikiloblasts in the metapelites; (c and d) rounded to euhedral garnet poikiloblasts in the poorly segregated leucosome displaying amalgamation features (the arrows in the figure indicate grains which would have amalgamated, had the rock continued to equilibrate further in the magmatic state); (e) highly fragmented, coarse-grained garnet in the leucosomes; (f) fine-grained, rounded poikiloblasts in the granite sheet displaying amalgamation features; (g) coarse-grained, inclusion-free garnets in the granite sheet displaying amalgamation features; and (h) garnet in the granite.

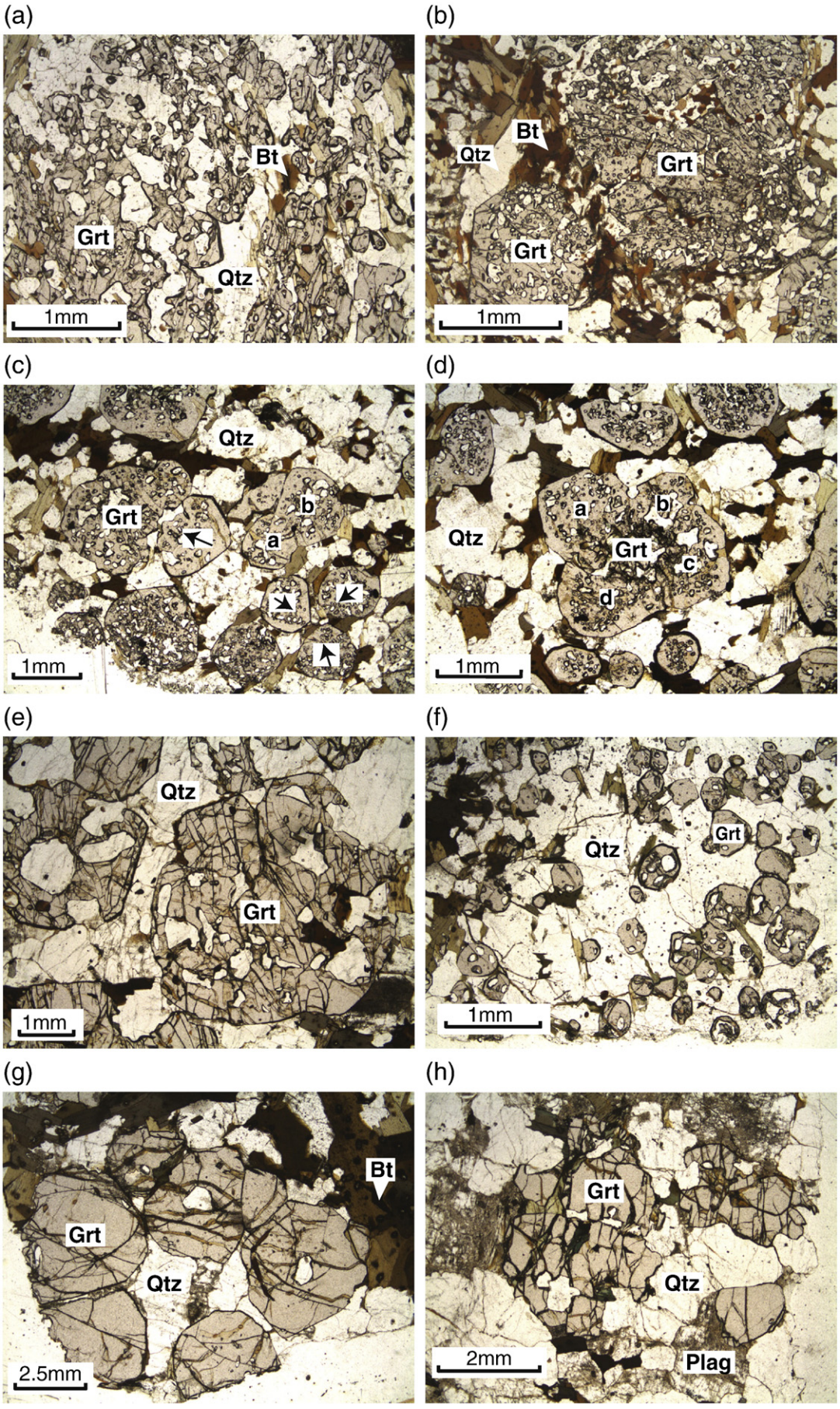

Table 1a
Major element compositions and structural formulae of representative garnets from metapelites, a poorly segregated leucosome, concordant and discordant leucosomes, a granite sheet and garnet-bearing granite from the MVMS.

	Mk2-2a		Mk4		Mk11		Mk10		Mk29		Mk32b				Mk28	
	Metapelite		Metapelite		Poorly segr. Leuco.		Leucosome concordant		Leucosome discordant		Granite sheet big		Granite sheet small		Granite	
	Grt r	Grt c	Grt r	Grt c	Grt r	Grt c	Grt r	Grt c	Grt r	Grt c	Grt r	Grt c	Grt r	Grt c	Grt r	Grt c
SiO_2	38.55	38.45	38.35	38.79	36.88	37.27	37.14	37.35	37.49	37.51	37.05	37.66	36.64	37.44	36.09	36.77
Al_2O_3	21.69	21.57	21.77	21.78	20.54	20.67	21.10	20.94	20.93	21.01	20.85	20.91	20.42	20.99	20.46	20.93
Fe_2O_3	0.52	1.02	0.44	0.55	1.36	1.28	1.29	1.53	1.22	1.05	1.03	0.83	1.46	1.21	0.69	1.81
FeO	35.44	34.32	32.64	33.03	34.57	34.13	32.72	32.86	34.64	34.42	35.52	34.24	37.09	37.07	34.62	34.46
MnO	0.45	0.48	0.43	0.56	0.44	0.48	0.63	0.63	1.01	0.94	1.37	1.13	2.22	1.60	6.77	1.20
MgO	5.26	5.86	6.62	6.69	4.41	4.98	5.80	5.89	4.57	4.74	3.43	4.58	1.87	2.93	0.96	4.14
CaO	0.70	0.64	0.83	0.75	1.02	0.92	0.66	0.62	0.94	0.95	1.21	1.32	1.22	0.91	0.97	0.89
Totals	102.63	102.33	101.09	102.15	99.21	99.72	99.33	99.81	100.81	100.61	100.45	100.67	100.90	102.15	100.55	100.20
Si	2.99	2.98	2.99	2.99	2.98	2.99	2.97	2.97	2.98	2.98	2.98	3.00	2.98	2.98	2.98	2.95
^{IV}Al	0.01	0.02	0.01	0.01	0.02	0.01	0.03	0.03	0.02	0.02	0.02	0.00	0.02	0.02	0.02	0.05
^{VI}Al	1.98	1.96	1.99	1.97	1.94	1.94	1.95	1.94	1.94	1.95	1.96	1.95	1.93	1.95	1.98	1.94
Fe^{3+}	0.03	0.06	0.03	0.03	0.08	0.08	0.08	0.09	0.07	0.06	0.06	0.05	0.09	0.07	0.04	0.11
$\sum 3^+$	2.01	2.02	2.01	2.01	2.02	2.01	2.03	2.03	2.02	2.02	2.02	2.00	2.02	2.02	2.02	2.05
Fe^{2+}	2.30	2.23	2.13	2.13	2.34	2.29	2.19	2.19	2.30	2.29	2.39	2.28	2.52	2.47	2.39	2.32
Mn	0.02	0.03	0.02	0.03	0.02	0.03	0.03	0.03	0.06	0.05	0.08	0.06	0.12	0.09	0.39	0.07
Mg	0.61	0.68	0.77	0.77	0.53	0.59	0.69	0.70	0.54	0.56	0.41	0.54	0.23	0.35	0.12	0.50
Ca	0.06	0.05	0.07	0.06	0.09	0.08	0.06	0.05	0.08	0.08	0.10	0.11	0.11	0.08	0.09	0.08
$\sum 2^+$	2.99	2.98	2.99	2.99	2.98	2.99	2.97	2.97	2.98	2.98	2.98	3.00	2.98	2.98	2.98	2.95
Tot	8.00	8.00	8.00	8.00	8.00	8.00	8.00	8.00	8.00	8.00	8.00	8.00	8.00	8.00	8.00	8.00
XAlm	0.77	0.75	0.71	0.71	0.78	0.77	0.74	0.74	0.77	0.77	0.80	0.76	0.85	0.83	0.80	0.78
XSpss	0.01	0.01	0.01	0.01	0.01	0.01	0.01	0.01	0.02	0.02	0.03	0.02	0.04	0.03	0.13	0.02
XPy	0.20	0.23	0.26	0.26	0.18	0.20	0.23	0.24	0.18	0.19	0.14	0.18	0.08	0.12	0.04	0.17
XGrs	0.02	0.02	0.02	0.02	0.03	0.03	0.02	0.02	0.03	0.03	0.03	0.04	0.04	0.03	0.03	0.03
Mg#	21	23	27	27	19	21	24	24	19	20	15	19	8	12	5	18

Number of ions calculated on the basis of 12 oxygens for garnet. XAlm = $Fe^{2+}/(Fe^{2+}+Mn+Mg+Ca)$, XSpss = $Mn/(Fe^{2+}+Mn+Mg+Ca)$, XPy = $Mg/(Fe^{2+}+Mn+Mg+Ca)$, XGrs = $Ca/(Fe^{2+}+Mn+Mg+Ca)$, Mg# = $100\times Mg/(Mg+Fe^{2+})$; Grt = garnet, r = rim, c = core.

therefore composite. More detailed petrographic and mineral compositional information on the metamorphic assemblages in the MVMS metapelites are reported in Taylor et al. (2010).

Table 1b
Major element compositions and structural formulae of representative biotite inclusions in garnet from a metapelite, poorly segregated leucosome, concordant and discordant leucosomes, a granite sheet and garnet-bearing granite from the MVMS.

	Mk2-2a	Mk11	Mk10	Mk29	Mk32b	Mk28
	Metapelite	Poorly segr. Leuco.	Leucosome concordant	Leucosome discordant	Granite sheet	Granite
	Bt inclusion	Bt inclusion	Bt inclusion	Bt inclusion	Bt inclusion	Bt inclusion
SiO_2	36.98	36.74	36.13	35.29	35.15	35.15
TiO_2	3.67	3.51	3.50	4.41	3.84	4.38
Al_2O_3	18.33	17.37	17.71	17.58	17.49	17.74
Cr_2O_3	0.22	0.00	0.16	0.00	0.00	0.00
FeO	14.21	14.82	15.83	13.26	17.77	19.56
MnO	0.00	0.00	0.00	0.00	0.00	0.00
MgO	13.31	13.89	13.31	13.74	11.26	9.77
Na_2O	0.66	0.52	0.72	0.49	0.49	0.59
K2O	9.06	9.26	8.70	9.05	9.08	9.19
Totals	96.44	96.11	96.05	93.82	95.06	96.38
Si	5.41	5.42	5.36	5.31	5.34	5.31
Ti	0.40	0.39	0.39	0.50	0.44	0.50
Al^{IV}	2.59	2.58	2.64	2.69	2.66	2.69
Al^{VI}	0.58	0.45	0.45	0.43	0.47	0.47
Cr	0.03	0.00	0.02	0.00	0.00	0.00
Fe^{2+}	1.74	1.83	1.96	1.67	2.26	2.47
Mn	0.00	0.00	0.00	0.00	0.00	0.00
Mg	2.90	3.06	2.94	3.08	2.55	2.20
Na	0.19	0.15	0.21	0.14	0.14	0.17
K	1.69	1.74	1.65	1.74	1.76	1.77
Totals	15.53	15.62	15.62	15.57	15.61	15.58
Mg#	63	63	60	65	53	47

Number of ions calculated on the basis of 22 oxygens for biotite. Mg# = $100\times Mg/(Mg+Fe^{2+})$; Bt = biotite.

5.2. Poorly segregated leucosomes

Poorly segregated leucosomes are occasionally developed in the metapelites, and represent an intermediate stage of melt–restite segregation (Fig. 2f). The poorly segregated leucosomes contain garnets which are texturally distinct from the composite aggregates in the metapelitic residue. These garnets occur as small (typically ≤1 mm), individual, rounded to euhedral poikiloblasts (Fig. 5c and d). The garnets have inclusion-rich cores with abundant 10–200 μm, round or lobate quartz + polycrystalline 'melt' inclusions, as well as identical high Ti^{4+} and high Mg# (60–63) biotite inclusions to those hosted in peritectic garnets in the metapelites (Table 1b). Furthermore the garnet core compositions Mg# = 20–22 and $X_{Spss} = 0.01$ (Table 1a) are indistinguishable from peritectic garnet compositions in the metapelites, and we therefore interpret the garnets hosted in the poorly segregated leucosome to be peritectic. However, the garnets are also characterised by 100–200 μm inclusion-free rims which imply a different episode of garnet growth, but which are compositionally indistinguishable from the cores. The only major element zonation displayed by the garnets are occasional, 5–20 μm wide rims with lower Mg# and higher Mn contents.

An additional distinguishing feature of these garnets is their apparent involvement in a physical process of amalgamation and textural coarsening within the melt-rich environment. The observed textures appear to indicate encounters between individual garnet grains resulting in the crystals aggregating, amalgamating and fusing to form larger composite poikiloblasts, thereby necessitating magma flow (Fig. 5c and d; the arrows in the figure indicate grains which would have amalgamated, had the rock continued to equilibrate further in the magmatic state). In some cases the outlines of the amalgamated garnets are still visible, indicating where up to four grains have fused into a single large poikiloblast with petal-like lobes (Fig. 5d, garnets 'a', 'b', 'c' and 'd'). In general, where the garnets have joined there are no preserved, pre-amalgamation, garnet-to-garnet grain boundaries and we refer to these as 'fused' grain boundaries

(Fig. 5c garnets 'a' and 'b'). Less frequently, the grain boundaries of the amalgamated grains are still visible and we refer to these as 'preserved pre-amalgamation grain boundaries'. In most cases, growth of the 100–200 μm inclusion-free rim post-dates amalgamation.

5.3. Larger anatectic structures

Within the larger anatectic structures, garnet is commonly hosted in a coarse-grained matrix of quartz, plagioclase, minor perthitic K-feldspar and interstitial biotite or retrograde biotite replacing garnet. Texturally, the garnet differs markedly from peritectic garnet in the metapelites and poorly segregated leucosome. Apart from being coarser grained (1–5 mm), the garnet is less poikilitic with large inclusion-free zones separated by abundant mica-filled fractures (Fig. 5e–h).

5.3.1. Discrete leucosomes

Garnets hosted in both concordant and cross-cutting leucosomes are anhedral to subhedral and highly fragmented (Fig. 5e). The garnets are compositionally similar to peritectic garnets in the metapelites and poorly segregated leucosomes, with large homogenous interiors, Mg# = 20–24 and X_{Spss} = 0.01–0.02, and occasional 5–20 μm wide retrograde rims (Table 1a). Although the garnets are less poikilitic, they do occasionally contain the same rounded, high Ti^{4+} high Mg# (58–65) biotite inclusions that typify peritectic garnets in the metapelites and poorly segregated leucosomes (Table 1b). In addition, garnets hosted in discrete leucosomes contain much larger (700–1000 μm), polycrystalline 'melt' inclusions with low angle terminations.

5.3.2. Granite sheets

Two distinct varieties of garnet characterise the granite sheet, but are closely associated within the same thin section and occur within the same leucocratic domain in the rock. The first is a coarse-grained (0.8–4 mm), inclusion-free garnet that is rounded to euhedral in shape (Fig. 5g) and approximates the composition of peritectic garnet in the metapelites and poorly segregated leucosome, Mg# = 18–21 and X_{Spss} = 0.02 (Table 1a). However the garnets have 100–300 μm wide, distinctly retrograde rims, Mg# = 7–16 and X_{Spss} = 0.03–0.04. The coarse-grained garnets occasionally contain high Ti^{4+}, but slightly lower Mg# (53) biotite inclusions compared to the peritectic garnets (Table 1b). A second variety of garnet occurs as tiny (75–600 μm), rounded to euhedral poikiloblasts containing rounded quartz inclusions (Fig. 5f). Compositionally this garnet differs markedly from peritectic garnet in the metapelites and poorly segregated leucosome with Mg# = 12–14 and X_{Spss} = 0.02–0.03 in the cores, and Mg# = 8–10 and X_{Spss} = 0.04 in the rims (Table 1a). A distinguishing feature of the granite sheet is the presence of a large proportion of coarse-grained, magmatic biotite (Mg# = 36–39) which likely formed from back reaction of garnet with K and H_2O in the melt during crystallisation of the magma (Fig. 5g).

Both varieties of garnet display amalgamation features similar to the textures described for the poorly segregated leucosome. Clusters of garnet in the granite sheet (Fig. 3d; Fig. 5f and g) formed either as a result of the injection of individual batches of magma carrying varying fractions of entrained garnet, or as a result of flow within the magmatic environment which brought garnet crystals together. Within these clusters, both the small garnet poikiloblasts and the larger inclusion-free grains appear to be amalgamating to form increasingly larger, compound crystals (Fig. 5f and g).

5.3.3. Garnet-bearing granite

The granite investigated in this study is a ± 10 m tabular, medium-grained granodiorite containing biotite, quartz, garnet, plagioclase and minor K-feldspar. Rounded, subhedral to euhedral, 1.5–3 mm garnets are highly fragmented with numerous fractures filled by chlorite or retrograde biotite (Fig. 5h). Compositionally, this garnet resembles the coarse-grained garnet in the granite sheet with Mg# = 14–18 and X_{Spss} = 0.02–0.03 in their cores, and 20–150 μm, strongly retrograde rims (Table 1a). The garnets occasionally contain high Ti^{4+}, but markedly lower Mg# (27–47) biotite inclusions (Table 1b). In addition, a large fraction of low Ti^{4+}, low Mg# (33) retrograde biotite replaces garnet. Texturally the garnet resembles the coarse-grained garnet in the granite sheet, and may therefore have grown by the same amalgamation process described above (Fig. 5h).

5.4. Garnet zonation profiles

5.4.1. Mn and Y profiles: evidence for garnet amalgamation

Granulite facies garnets with characteristically flat major element zonation profiles, often retain trace element zonation which helps to constrain the conditions of formation of the garnet (e.g. Hermann and Rubatto, 2003; Schwandt et al., 1996; Clarke et al., 2007). The trace element character of the garnet generations described above were investigated by focusing on the distribution of Y in the crystals for the following main reasons: Y is considered a reasonable proxy for HREE behaviour in garnet; and Y concentrations are high enough in all garnet generations to allow for the use of a small laser spot-size during LA-ICP-MS analysis (± 40 μm), as well as high enough in some of the garnets (e.g. the granite sheet) to allow for e-beam WD electron microprobe analyses. Additionally, as garnet Mn concentrations are low enough to be measured by LA-ICP-MS concurrently with the trace elements, Mn was measured during the trace element profiling of the garnets in order to demonstrate the major element zonation within a single coherent dataset. By using a time resolved mode of analyses on the LA-ICP-MS, and by carefully monitoring the concentrations of elements such as Zr and Ce, we were able to identify potential contamination from small accessory phase inclusions in the garnet, and to exclude those analyses from the dataset.

As expected, the peritectic garnets in the metapelites display flat major element zonation, evidenced by little to no variation in Mn content between garnet core and rim domains (Fig. 6a). However, the garnets do display intra-crystalline zoning with respect to Y, although Y concentrations are low (<100 ppm) and the zonation appears to be irregular. In the poorly segregated leucosome investigated, composite garnets typically consist of 2–4 amalgamated grains where pre-amalgamated grain boundaries are either preserved, or where the grain boundaries are entirely fused such that the positions of the former grain boundaries cannot be determined accurately by optical or SEM imaging techniques. A profile through a 700 μm garnet which textural evidence suggests formed by amalgamation of 2–3, smaller garnets does not show significant rim-to-rim zonation with respect to Mn, except for a very slight inflection in Mn content across the still visible, pre-amalgamated grain boundaries (Fig. 6b). Garnet B to the right in Fig. 6b is slightly more zoned with respect to Mn than garnet A. In contrast, the amalgamated grains retain their individual Y-enriched cores (250 ppm and 140 ppm respectively), with a relatively sharp decrease in Y concentration towards the rims and at the pre-amalgamated grain boundary. The Y concentration at this internal boundary is similar (~50 ppm) to that at the rims. A rim-to-rim profile through a garnet from the poorly segregated leucosome where the crystal shape suggests the presence of two completely fused grains shows slight Mn enrichment towards the rims and at the fused grain boundaries (Fig. 6c). Although Y concentrations in the garnet are extremely variable, a large inflection in Y content in the vicinity of the fused grain boundary allows the amalgamated grains to be distinguished. Garnet A in Fig. 6c consists of a Y-rich core (230 ppm) surrounded by an intermediate zone of relative Y depletion (20–45 ppm) and an outer rim where Y values are similar to that of the core (250–416 ppm). In contrast, garnet B has a more-or-less flat Y profile where concentrations remain below 50 ppm.

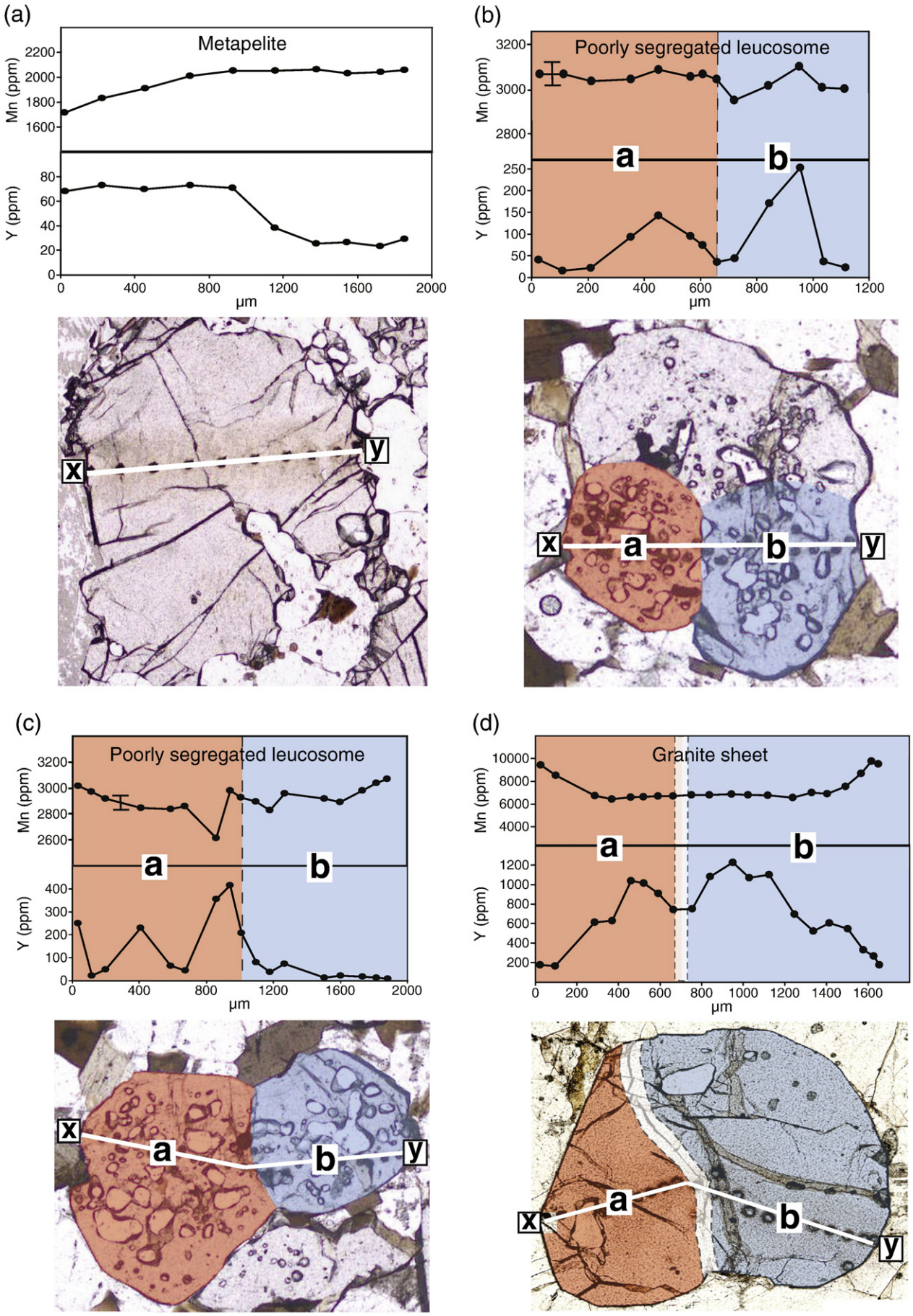

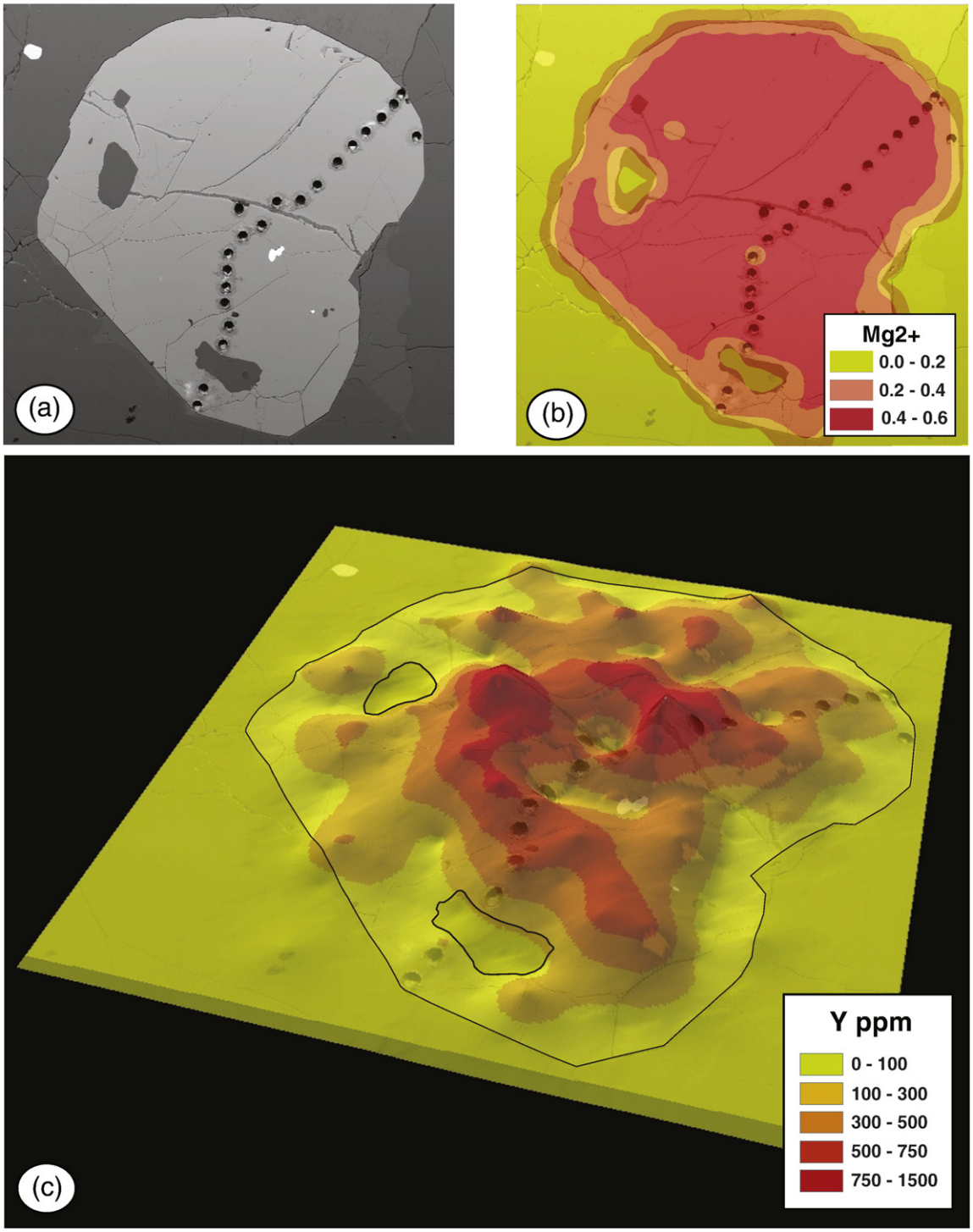

Fig. 7. Major and trace element contour maps of amalgamated garnet grains in the granite sheet, which have fused to form a single compound garnet crystal: (a) SEM backscattered electron (BSE) image of the compound garnet; (b) contours of Mg^{2+} in the garnet showing a homogeneous core surrounded by a ± 300 μm Mg-poor rim; and (c) 3D contour map of Y concentration in the garnet showing two Y peaks in the core of the garnet with shapes that are determined by the location of the fused grain boundaries and the outlines of the amalgamated grains.

Within the granite sheet, a large garnet with a crystal shape that suggests the presence of two fused grains has an interior characterised by flat major element zonation, surrounded by a 300 μm wide, Mn and Fe-rich zoned rim (Fig. 6d). The unzoned central domain straddles the position of the suspected fused grain boundaries. In contrast, the two amalgamated grains preserve individual Y-rich cores

Fig. 6. Mn and Y profiles through: (a) peritectic garnet from a metapelite; (b) amalgamated garnets ('a' and 'b') from the poorly segregated leucosome; (c) fused garnets ('a' and 'b') from the poorly segregated leucosome; and (d) fused garnets ('a' and 'b') from the granite sheet. Sigma (σ) 1 errors are typically <50 ppm for Y and <500 ppm for Mn. Where errors are equal to, or smaller than the symbols on the figures they are not indicated. These profiles emphasise the flat major element zonation in the amalgamated and fused garnet grains, while the individual, bell-shaped Y zonation profiles of the pre-amalgamated crystals are preserved.

(1040 ppm and 1230 ppm respectively) with a clear decrease in Y concentration towards the rims (±200 ppm) and in the vicinity of the fused grain boundaries (±750 ppm Y, indicated by the white shaded area in Fig. 6d). The 300 μm lower Mg# rim zone corresponds to a decrease in Y concentration from ±600 ppm to 200 ppm, which suggests that it grew post the amalgamation of the garnets. SEM major and trace element concentration contour maps, obtained by placing a grid of point analyses with a 100×100 μm spacing over the garnet and extrapolating between the points (using krigging as the statistical method in ArcMap 9.2), shows clear differences in the major and trace element zonation patterns of the garnet (Fig. 7). While the distribution of Mg^{2+} is homogenous throughout the core of the garnet (Fig. 7a), two Y-enriched peaks, with shapes that are determined by the location of the fused grain boundaries and the outlines of the amalgamated grains, are preserved (Fig. 7b).

5.4.2. Heavy Rare Earth Element (HREE) patterns

Heavy Rare Earth Element concentrations in garnet were measured in conjunction with Y and Mn (Table 2). As expected, both the garnet core–rim HREE zonation, as well as the differences in HREE abundances between garnets from the different structures, mimic the details for Y described above. Absolute HREE abundances are low in peritectic garnets from the metapelites and poorly segregated leucosome, with ∑HREE (Gd–Lu) = 59 ppm and 142 ppm respectively (σ1 errors ≤ 2.2 ppm). There appears to be no discernable difference in HREE content between the cores and rims of garnets from the metapelite (Fig. 8a), whereas in the poorly segregated leucosome the garnets from Fig. 6a show a small decrease in HREE content towards the rims and at the pre-amalgamated grain boundaries (Fig. 8b). Peritectic garnets from both rocks types have either slightly positive or flat to slightly negative chondrite-normalised Gd–Lu slopes (Lu_N/Gd_N = 0.98–0.16 in garnets from the metapelite; Lu_N/Gd_N = 1.59–0.56 in garnets from the poorly segregated leucosome). Small negative Eu anomalies characterise garnets from the metapelites ($Eu/Eu^*(Eu_N/(Sm_N+Gd_N)/2)$ = 0.50) and moderately negative Eu anomalies garnets from the poorly segregated leucosome (Eu/Eu^* = 0.07).

Strongly contrasting behaviour is observed in the coarse-grained, inclusion-free garnets from the granite sheet. In comparison with the peritectic garnets, absolute HREE abundances are orders of magnitude higher in the cores of these garnets ∑HREE (Gd–Lu) = 677 (1σ errors ≤ 15 ppm). The garnets also display more pronounced HREE zonation (Fig. 8c), with the fused grain boundaries approaching the HREE-enriched nature of the cores, though slightly lower at the boundary, and with significantly lower HREE concentrations towards the rims. Relative to the peritectic garnets, there is a steep increase in the abundance of HREE with increasing atomic number from Gd–Tm in the interior of the granite sheet garnets (Lu_N/Gd_N = 28.38), whereas the HREE profiles flatten out towards the rims (Lu_N/Gd_N = 1.15). Eu anomalies in both the cores and rims of the garnets are strongly negative (Eu/Eu^* = 0.03) and significantly more pronounced than in the peritectic garnets from the metapelites and

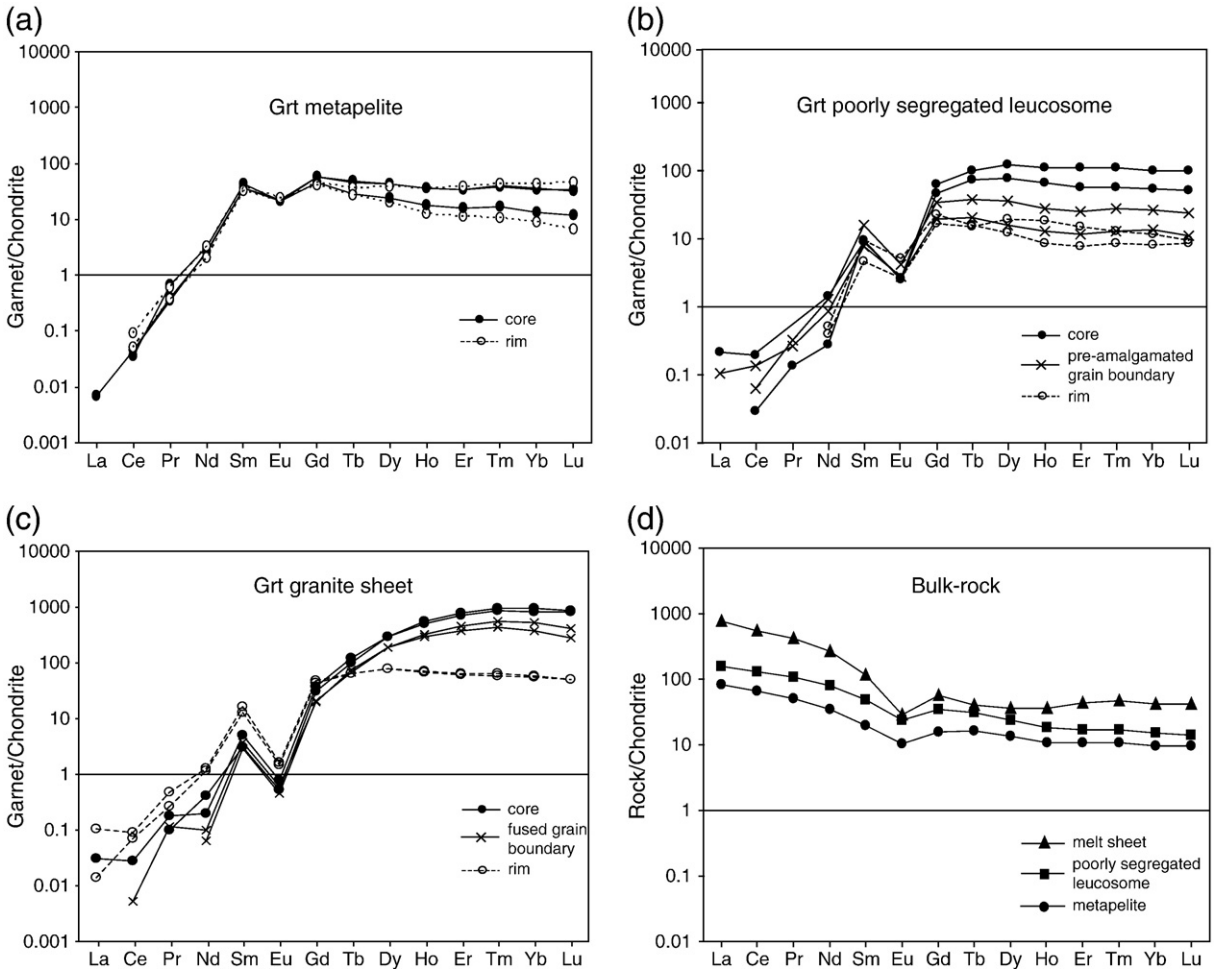

Fig. 8. Chondrite-normalised (Taylor and McLennan, 1985) REE zonation patterns in garnet from: (a) the metapelitic residua; (b) the poorly segregated leucosome; and (c) the granite sheet. Peritectic garnets from the metapelites are unzoned in terms of HREE, have flat HREE patterns and small negative Eu anomalies. In contrast, garnets hosted in the granite sheet are strongly zoned in terms of HREE, enriched in HREE and have pronounced negative Eu anomalies. Peritectic garnets from the poorly segregated leucosome are intermediate between the two. (d) Comparison of bulk-rock HREE patterns in the metapelites, poorly segregated leucosome and granite sheet.

Table 2
Representative trace element compositions of garnets from a metapelite, poorly segregated leucosome and granite sheet from the MVMS.

	Mk4		Mk11		Mk32b	
	Metapelite		Poorly segr. Leuco.		Granite sheet	
	Grt r	Grt c	Grt r	Grt c	Grt r	Grt c
Y	67.94	72.70	40.57	252.54	178.33	1227.59
La	0.00	0.00	0.00	0.08	0.04	0.00
Ce	0.05	0.04	0.05	0.18	0.09	0.03
Pr	0.05	0.05	0.03	0.02	0.07	0.01
Nd	1.45	1.79	0.29	1.01	0.89	0.30
Sm	7.23	8.24	1.10	2.12	3.70	0.73
Eu	1.82	1.93	0.23	0.23	0.15	0.05
Gd	14.26	17.64	5.06	19.63	14.50	9.28
Tb	2.07	2.63	0.86	5.90	3.67	5.80
Dy	14.43	15.94	7.60	47.35	30.52	111.47
Ho	3.05	3.06	1.57	9.35	6.13	46.33
Er	9.25	8.41	3.72	26.97	15.90	199.68
Tm	1.52	1.41	0.46	3.91	2.31	34.21
Yb	10.61	8.98	2.92	24.75	14.56	237.19
Lu	1.74	1.25	0.36	3.89	1.94	32.80

poorly segregated leucosome. The finer-grained garnets from the granite sheet show the same trace element patterns as the coarse-grained garnets, with $\sum$HREE = 530–700 (1σ errors ≤ 20 ppm); bell-shapes zonation profiles, with Y typically 1200 ppm in the cores and ± 500 ppm at the rims; $Lu_N/Gd_N = 30$ in the cores of the garnets and $Lu_N/Gd_N = 2$–5 at the rims; and pronounced negative Eu anomalies ($Eu/Eu^* = 0.003$–0.02).

Comparison of the metapelite, poorly segregated leucosome and granite sheet bulk-rock trace element compositions show that HREE abundances are relatively low and that all three rock types display negative chondrite-normalised Gd–Lu slopes ($Lu_N/Gd_N = 0.61$, 0.4 and 0.75 respectively) (Fig. 8d, Table 3). Europium anomalies are negative, moderate, and vary between $Eu/Eu^* = 0.57$ in the metapelite and $Eu/Eu^* = 0.33$ in the granite sheet.

6. Discussion and conclusions

6.1. The origin of the garnet in the anatectic structures

Garnet in the MVMS metapelites is exclusively associated with the development of leucosomes, and where there is no leucosome present the rock is highly restitic and has clearly lost a significant quantity of melt. In addition, rocks that do not contain garnet show little evidence for having melted. Thus the bulk of the garnet in the metapelites is interpreted to be the peritectic product of the incongruent melting reaction. Discrete leucosomes and anatectic structures associated with melt segregation contain large aggregates of garnet. Although these structures are likely to have lost melt, the granulite facies character of the garnet and its limited potential to be accommodated as a dissolved component in the melt (Montel and Vielzeuf, 1997), argue against such large volumes of garnet in relatively small anatectic features having crystallised from the melt. In essence, melts in quartz saturated pelitic compositions at 850 °C have very low maximum values for dissolved FeO + MgO (typically < 2.2 wt.% in the dataset of Stevens et al., 2007), strongly limiting the volume of ferromagnesian minerals that can crystallise from them. Thus we can conclude that peritectic garnet from the pelitic source was entrained to the melt, and segregated with the magma. The likely size and shape of the entrained crystals are demonstrated by the garnet crystals in the thinnest, cross-cutting leucosome veins, which carry < 1 mm, intensely poikiloblastic garnets of the type found in the poorly segregated leucosome (Fig. 6b and c).

6.2. The textural and chemical evolution of garnet in the magma

Careful comparison of garnet texture and chemistry in the anatectic structures with the peritectic garnets in the metapelitic residue shows the following: garnets in the poorly segregated leucosome and more discrete leucosomes contain the same mineral inclusion suites that characterise the peritectic garnets in the metapelites; and in terms of their major element compositions they are identical. However, there is a systematic change in garnet texture, chemistry and zonation details as the scale of the anatectic structure increases. This includes a systematic loss of inclusions; an increase in crystal size; the adoption of more euhedral grain-shapes; a small but step-wise decrease in Mg#; an increase in X_{Spss}; and, the development of a relatively wide rim domain characterised by increasing X_{Spss} and decreasing Mg#. In combination, these features render the garnets in the larger anatectic structures more magmatic in character. In a recent study by Villaros et al. (2009a) of S-type granites from the Cape Granite Suite (CGS), garnet dissolution–precipitation in the melt was invoked as a fast and efficient mechanism to re-equilibrate large quantities of entrained peritectic garnet with the magma during its ascent. This resulted in the garnets, now hosted in the granites, appearing magmatic and having little or no chemical–textural record of their peritectic origin. The garnet amalgamation process described for the MVMS leucosomes, where compound crystals formed from the

Table 3
Major and trace element compositions of a metapelite, poorly segregated leucosome, discrete leucosome, granite sheet and garnet-bearing granite from the MVMS. For the granite sheet and granite, a composition that is representative of the whole structure has been used.

	Metapelite	Poorly segr. leuc.	Discrete leucosome	Granite sheet	Garnet-bearing granite
SiO_2	55.13	63.39	70.72	70.53	69.92
TiO_2	0.72	0.53	0.12	0.22	0.54
Cr_2O_3	0.098	0.086	0.011	0.007	0.012
Al_2O_3	16.86	12.91	14.21	14.52	14.80
FeO	15.33	13.17	5.90	4.70	3.81
MnO	0.09	0.11	0.14	0.09	0.04
MgO	5.36	3.59	1.18	1.14	1.21
CaO	0.23	0.90	1.65	2.58	2.20
Na_2O	0.32	1.32	3.14	3.35	3.86
K_2O	2.49	2.04	1.55	1.13	1.68
P_2O_5	0.07	0.06	0.10	0.09	0.12
Total	99.53	99.60	99.49	99.46	99.41
Ba	414.00	298.00	276.00	244.00	207.00
Cs	3.40	3.30	0.60	2.40	1.60
Ga	20.20	15.10	13.80	12.40	18.60
Hf	3.90	13.30	11.20	17.70	21.70
Nb	18.30	48.10	6.30	6.60	24.20
Rb	137.60	111.60	39.90	45.70	75.40
Sr	49.50	136.90	164.00	387.30	207.10
Ta	1.10	4.80	0.20	0.50	0.90
Th	11.00	10.00	98.60	124.10	185.90
U	1.00	1.30	5.20	5.80	8.60
V	157.00	98.00	13.00	18.00	26.00
W	950.60	743.50	1523.00	1256.00	1273.00
Zr	134.30	568.30	418.90	658.40	862.70
Y	26.40	43.10	209.00	82.80	72.00
La	30.30	57.40	185.20	279.20	314.70
Ce	63.60	125.80	348.60	519.70	586.30
Pr	7.03	15.01	38.85	57.93	65.42
Nd	25.10	57.40	129.80	191.30	219.60
Sm	4.63	11.33	20.32	26.93	33.77
Eu	0.90	2.09	1.83	2.51	2.13
Gd	4.89	10.74	17.81	17.20	24.39
Tb	0.94	1.79	3.44	2.32	3.25
Dy	5.15	9.03	26.92	13.94	14.41
Ho	0.91	1.53	7.56	3.12	2.54
Er	2.64	4.20	25.79	10.77	7.33
Tm	0.39	0.60	4.16	1.70	1.10
Yb	2.37	3.71	24.63	10.60	6.30
Lu	0.37	0.53	3.57	1.60	0.95

fusion of several smaller grains, as well as the tendency of the garnets to evolve into large, rounded to euhedral, inclusion-free crystals in the presence of melt, requires significant recrystallisation. We propose that the most efficient mechanism to achieve this is via dissolution–precipitation driven recrystallisation, where the garnet essentially behaves as an oversaturated solute in the granitic magma solvent (Clarke, 2007), and that this may explain the increasing magmatic character of the garnets in the larger anatectic structures.

In addition, peritectic garnets in the metapelites and the poorly segregated leucosome are characterised by low absolute Y and HREE abundances, flat HREE patterns, weak to moderately negative Eu anomalies and in some cases variable trace element zonation. This is strongly contrasted by the high absolute Y and HREE abundances of the granite sheet garnets, as well as their steeper HREE slopes, strongly negative Eu anomalies and regular, bell-shaped zonation patterns. The increase in chondrite-normalised HREE slope in garnet as the anatectic feature scales up does not simply reflect a bulk-rock control, as indicated in Fig. 8d by the negative bulk-HREE slopes in all three rock types. An alternative explanation is that peritectic garnet in the metapelitic source was initially out of trace element equilibrium with HREE-rich accessory phases zircon and monazite, and became better equilibrated with these minerals subsequent to being entrained. In addition, small negative Eu anomalies in peritectic garnets where feldspar was present throughout the rock's anatectic history is unusual, as equilibrium partitioning should result in Eu strongly partitioning into feldspar (e.g. Acosta-Vigil et al., 2010; Bea and Montero, 1999; Bea, 1996). These findings may have important implications for the rates of melting, namely, that peritectic garnet growth by incongruent reaction was significantly faster than the rate of HREE-rich accessory phase dissolution in the melt, and the rate at which garnet-residual feldspar equilibration could occur. This is in agreement with findings by Villaros et al. (2009b) who demonstrated that the rate of zircon dissolution in a peraluminous granitic melt is relatively slow, and Barbey (2007) who showed that peritectic reactions involving biotite are likely to be strongly diffusion controlled during the initial stages of the reaction. Only once the entrained peritectic garnet recrystallised within the larger anatectic structures and consequently re-equilibrated with the magma could trace element equilibrium between garnet, melt, feldspar and dissolved HREE-rich accessory phases be achieved.

Fig. 9 is a diagram illustrating the garnet dissolution–precipitation and amalgamation process described above. As the garnets within the anatectic structures display flat major element zonation, commonly interpreted to reflect syn to post-peak re-equilibration in granulites, a number of observations can be made about the relative timing of the textural and chemical evolution of the entrained peritectic garnets in the MVMS anatectic structures. (1) Subsequent to being entrained, garnets in the poorly segregated leucosome began to amalgamate at high temperature, prior to major element homogenisation. The fact that the amalgamated grains retain their inclusion-rich cores and individual trace element zonation patterns indicates that the bulk of the garnet did not recrystallise. Growth of the 100–200 μm inclusion-free rims likely occurred after amalgamation of the garnets as a result of minor dissolution–precipitation of garnet in the melt. This was followed much later by diffusional resetting of the 5–20 μm retrograde rims. (2) The lack of inclusions and higher trace element abundances in the cores of the coarse-grained, fused granite sheet garnets demonstrate that the cores were completely reworked by

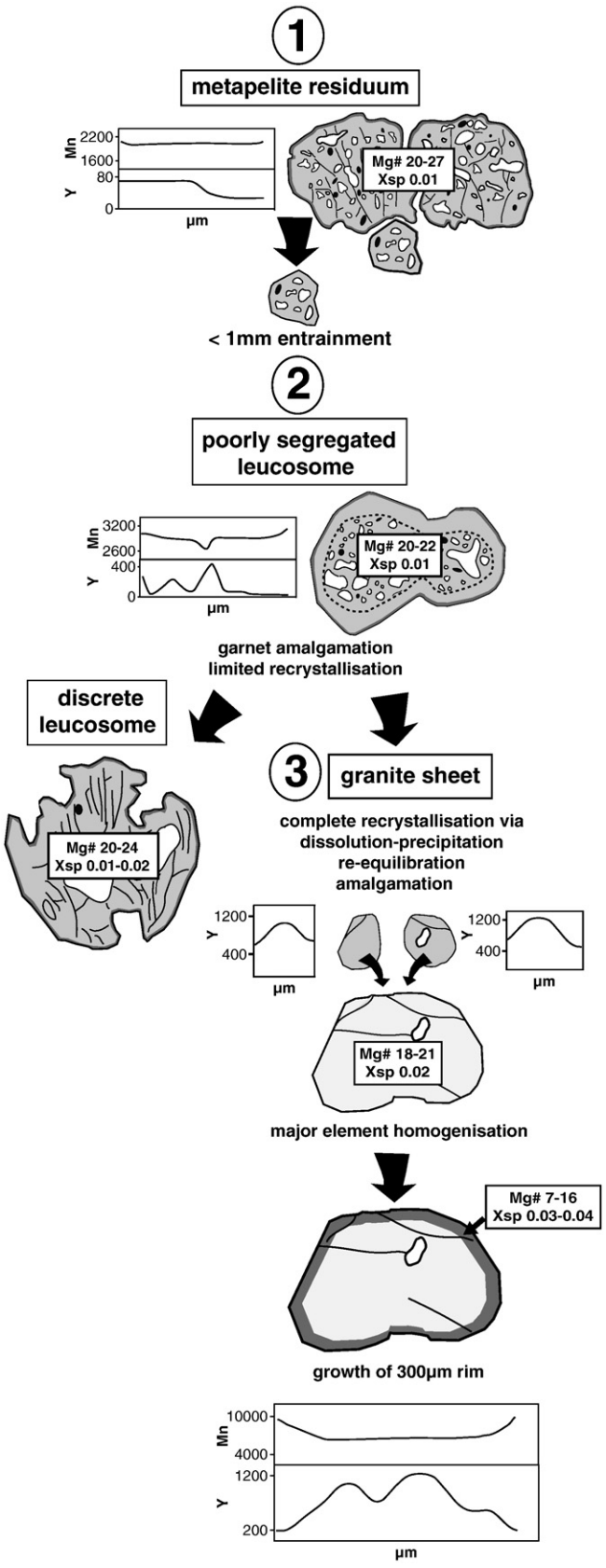

Fig. 9. An illustration of the garnet entrainment process in the MVMS: (1) In the metapelites melting is rapid and produces small (<1 mm) peritectic garnet poikiloblasts rich in biotite, quartz + melt inclusions, which are highly mobile and readily entrained to the melt; (2) entrained peritectic garnet in the poorly segregated leucosome undergoes limited recrystallisation and begins to amalgamate at high temperature, prior to major element homogenisation of the garnet; and (3) in the granite sheet the garnet undergoes rapid dissolution–precipitation, re-equilibration with the magma and amalgamation to form larger compound, rounded to euhedral crystals, prior to major element homogenisation of the garnet. The compound garnets retain the individual, bell-shaped trace element zonation patterns of the fused garnets. This is followed by a period of late-stage garnet growth by dissolution–precipitation and exchange with biotite during cooling, or crystallisation from the melt in equilibrium with biotite, to produce 300 μm wide, compositionally distinct rims.

dissolution–precipitation and re-equilibration with the magma prior to their amalgamation. The trace element patterns of the fine-grained garnets in the granite sheet imply that most crystallised contemporaneously with the HREE and Y-rich cores of the large garnets, and are therefore representative of the original garnets that amalgamated to form the compound grains. This supports the idea that the garnets are small when they are entrained, and that they undergo rapid dissolution–precipitation and amalgamation in the magma to form larger compound, rounded to euhedral crystals. The compound garnets retain the individual, bell-shaped trace element zonation patterns of the fused garnets. Major elements do not mimic this zonation, thus granulite facies homogenisation occurred post amalgamation. The presence of a 300 μm-wide, compositionally distinct Fe-rich rim indicates a period of late-stage garnet growth by dissolution–precipitation and exchange with biotite, or crystallisation from the melt in equilibrium with biotite.

6.3. Physical mechanisms for garnet entrainment and implications for S-type granites

The question of how peritectic garnet leaves the source and is mobilised over substantial distances is important in understanding S-type granite petrogenesis and the apparent chemical memory of the source that these granites display. Firstly the garnet needs to move through the same restricted spaces that the melt moves through during initial magma segregation. Secondly, the higher density garnet must be prevented from fractionating from the magma in the deeper portions of the crust. An important insight into this process gained during this study is the ability of garnet to mobilise as <1 mm (sometimes as small as 75 μm) intensely poikiloblastic grains. The obvious consequence of the finer grain-size of the garnet is its ability to move through narrow spaces and to maximize its surface area contact with the melt. In addition, the presence of quartz + melt inclusions lowers the effective density of the garnet, bringing it closer to that of the melt. These features, combined with the fact that garnet is often the main solid product of the incongruent melting of biotite at high temperature, ultimately enhances its capacity for being selectively entrained and transported in the magma to high-levels in the crust.

As suggested by the magmatic structures in the MVMS, entrained peritectic garnet has the potential to strongly control the FeO + MgO budget of the resulting magma. However, this does not imply that the Mg# of the magmatic products must match the Mg# of the peritectic garnet in a given source rock. This is because the garnets in all the MVMS rocks and anatectic structures have undergone major element, diffusional homogenisation that post-dates anatexis. Thus, the original peritectic garnet compositions may have been similar to the garnet compositions now recorded in the granulites, however their precise major element compositions cannot be measured. Furthermore, for rocks evolving along the same PT trajectory, the Mg# of the peritectic garnets produced will evolve to higher values as melting progresses, and, in addition will be strongly dependant on the bulk-rock composition. Thus, magma accumulations which have received additions of different batches of magma will very likely have received peritectic garnets of different composition. Lastly, although the entrained peritectic garnet contains a significant fraction of the FeO + MgO budget of the more mafic granitoid compositions, FeO + MgO that arrived in the magma as dissolved components in the melt also constitute an appreciable fraction of the maficity of the magma (up to 2.15 wt.% in the experimental melts of Patiño Douce and Johnston, 1991).

The 'restite entrainment model' of White and Chappell (1977), which involves the entrainment of a mineralogically diverse, whole-rock, residual source component in the melt as a mechanism for generating peraluminous, mafic granites is clearly not applicable to magma generation in the MVMS. Experimental evidence (e.g. Montel and Vielzeuf, 1997; Stevens et al., 1997) suggests that between 20–25% melt may be generated by fluid-absent melting of equivalent metapelite compositions at 850 °C, and field evidence is in agreement with a total melt yield in this range. However, despite the fact that this approaches conditions where bulk flow in a diatexitic environment occurs (van der Molen and Paterson, 1979), pre-migmatisation structures are preserved and the MVMS migmatites remained metatexitic. Thus, the full volume of melt was probably never present in the metapelites at once, and melt was continuously drained as it was produced, thereby prohibiting whole-source mobility. The current study therefore emphasises the potential for efficient segregation of garnet-rich magma, and selective entrainment of only the solid peritectic product of the incongruent melting reaction in aluminous sources where metatexitic conditions prevail. In circumstances with a high heat flux, as in the MVMS, the melting reaction is rapid and produces small garnet crystals at the sites of biotite breakdown which are potentially out of trace element equilibrium with their source, and which are readily entrained to the melt. The peritectic garnets are highly mobile and capable of migrating out of the source along thin grain-boundary melt films. Once in a dominantly magmatic environment, the garnets evolve texturally and chemically, rapidly losing their peritectic character via dissolution–precipitation, re-equilibration with the magma and physical amalgamation.

Melting initiated by major mantle heat addition to the crust is considered to be one of the main mechanisms by which voluminous granitic magmas arise. Thus, the processes recorded by the MVMS may be considerably more relevant to the production of such magmas than those which occur in migmatites which underwent slower, and more protracted heating. It is from sources such as these that more mafic, but also hot, water-undersaturated and highly mobile S-type granitic melts may be derived. The physical process for entrainment described here is in agreement with granitic magma ascent through narrow conduits such as fractures and dykes (e.g. Clemens and Mawer, 1992), as opposed to the restite model where whole-source mobility is assumed (Wyborn and Chappell, 1986).

Acknowledgements

This research was supported by South African National Research Foundation (NRF) grant funding to Professor G Stevens via the SARChI programme, as well as a PhD Bursary to J Taylor. F. Bea and P. Barbey are thanked for providing constructive reviews, which led to the substantial improvement of the original version of the manuscript. The authors gratefully acknowledge C. Lana for his assistance with the compilation of garnet major and trace element contour maps, and I. Buick who provided helpful comments on an earlier version of the manuscript.

References

Acosta-Vigil, A., Buick, I., Hermann, J., Cesare, B., Rubatto, D., London, D., Morgan, G.B., 2010. Mechanisms of crustal anatexis: a geochemical study of partially melted metapelitic enclaves and host dacite, SE Spain. Journal of Petrology Advanced Access 1–37p.

Ayres, M., Harris, N., 1997. REE fractionation and Nd-isotope disequilibrium during crustal anatexis: constraints from Himalayan leucogranites. Chemical Geology 139, 249–269.

Barbey, P., 2007. Diffusion-controlled biotite breakdown reaction textures at the solid/liquid transition in the continental crust. Contributions to Mineralogy and Petrology 154, 707–716.

Bea, F., 1996. Residence of REE, Y, Th and U in granites and crustal protoliths; implications for the chemistry of crustal melts. Journal of Petrology 37, 521–552.

Bea, F., Montero, P., Ortega, M., 2006. A LA-ICP-MS evaluation of Zr reservoirs in common crystal rocks: implications for Zr and Hf geochemistry, and zircon-forming processes. Canadian Mineralogist 44, 693–714.

Bea, F., Montero, P., 1999. Behaviour of accessory phases and redistribution of Zr, REE, Y, Th, and U during metamorphism and partial melting of metapelites in the lower crust: an example from the Kinzigite Formation of Ivrea–Verbano, NW Italy. Geochimica et Cosmochimica Acta 63, 1133–1153.

Chappell, B.W., 1997. Compositional variation within granite suites of the Lachlan Fold Belt: its causes and implications for the physical state of granitic magma. Transactions of the Royal Society of Edinburgh, Earth Science 88, 159–170.

Chappell, B.W., White, A.J.R., 1974. Two contrasting granite types. Pacific Geology 8, 173–174.
Chappell, B.W., White, A.J.R., Wyborn, D., 1987. The importance of residual source material in granite petrogenesis. Journal of Petrology 28, 1111–1138.
Chappell, B.W., White, A.J.R., Williams, I.S., Wyborn, D., Wyborn, L.A.I., 2000. Lachlan Fold Belt granites revised: high- and low-temperature granites and their implications. Australian Journal of Earth Science 47, 123–138.
Clarke, G.L., White, R.W., Lui, S., Fitzherbert, J.A., Pearson, N.J., 2007. Contrasting behaviour of rare earth and major elements during partial melting in granulite facies migmatites, Wuluma Hills, Arunta Block, central Australia. Journal of Metamorphic Geology 25, 1–18.
Clarke, D.B., 2007. Assimilation of xenocrysts in granitic magmas: principles, processes, proxies and problems. Canadian Mineralogy 45, 5–30.
Clemens, J.D., 1992. Partial melting and granulite genesis — a partisan overview. Precambrian Research 55, 297–301.
Clemens, J.D., Mawer, C.K., 1992. Granitic magma transport by fracture propagation. Tectonophysics 204, 339–360.
Condie, K.C., Kröner, A., Milisenda, C.C., 1996. Geochemistry and geochronology of the Mkhondo suite, Swaziland: evidence for passive-margin deposition and granulite facies metamorphism in the late Archaean of southern Africa. Journal of African Earth Science 22, 483–506.
Diener, J.F.A., Stevens, G., Kisters, A.F.M., Poujol, M., 2005. Metamorphism and exhumation of the basal parts of the Barberton greenstone belt, South Africa: constraining the rates of Mesoarchaean tectonism. Precambrian Research 143, 87–112.
Hermann, J., Rubatto, D., 2003. Relating zircon and monazite domains to garnet growth zones: age and duration of granulite facies metamorphism in Val Malenco lower crust. Journal of Metamorphic Geology 21, 833–852.
Holness, M.B., 2006. Melt-solid dihedral angles of common minerals in natural rocks. Journal of Petrology 47, 791–800.
Hunter, D.R., 1974. Crustal development in the Kaapvaal Craton, I: The Archaean. Precambrian Research 1, 259–294.
Kisters, A.F.M., Gibson, R.L., Charlesworth, E.G., Anhaeusser, C.R., 1998. The role of strain localization in the segregation and ascent of anatectic melts, Namaqualand, South Africa. Journal of Structural Geology 20, 229–242.
Kröner, A., Wendt, J.I., Milisenda, C.C., Compston, W., Maphalala, R., 1993. Zircon geochronology and Nd isotopic systematics of the Ancient Gneiss Complex, Swaziland, and implications for crustal evolution. In: Kröner, A. (Ed.), The Ancient Gneiss Complex: overview papers and guidebook for excursion. Bull, 11. Swaziland Geological Survey and Mines Department, pp. 15–37.
Longerich, H.P., Jackson, S.E., Gunther, D., 1996. Laser ablation inductively coupled plasma mass spectrometric transient signal data acquisition and analyte concentration calculation. Journal of Analytical Atomic Spectrometry 11, 899–904.
Montel, J.M., Vielzeuf, D., 1997. Partial melting of metagreywackes. Part II. Compositions of minerals and melts. Contributions to Mineralogy and Petrology 128, 176–196.
Moyen, J.F., Stevens, G., Kisters, A., 2006. Record of mid-Archaean subduction from metamorphism in the Barberton terrain, South Africa. Nature 442, 559–562.
Patiño Douce, A.E., Johnston, A.D., 1991. Phase equilibria and melt productivity in the pelitic system: implications for the origin of peraluminous granitoids and aluminous granites. Contributions to Mineralogy and Petrology 107, 202–218.
Patiño Douce, A.E., Harris, N., 1998. Experimental constraints on Himalayan anatexis: Journal of Petrology 39, 689–710.
Petford, N., Kerr, R.C., Lister, J.R., 1993. Dike transport of granitic magmas. Geology 21, 845–847.
Pickering, J.M., Johnston, A.D., 1998. Fluid-absent melting behaviour of a two-mica metapelite: experimental constraints on the origin of the Black Hills granite. Journal of Petrology 39, 1787–1804.
Sawyer, E.W., 1994. Melt segregation in the continental crust. Geology 22, 1019–1022.
Sawyer, E.W., 1996. Melt segregation and magma flow in migmatites: implications for the generation of granite magmas. Transactions of the Royal Society of Edinburgh, Earth Science 87, 85–94.
Sawyer, E.W., 1998. Formation and evolution of granite magmas during crustal reworking: the significance of diatexites. Journal of Petrology 39, 1147–1167.
Sawyer, E.W., 2001. Melt segregation in the continental crust: distribution and movement of melt in anatectic rocks. Journal of Metamorphic Geology 19, 291–309.
Schwandt, C.S., Papike, J.J., Shearer, C.K., 1996. Trace element zoning in pelitic garnet of the Black Hills, South Dakota. American Mineralogist 81, 1195–1207.
Stevens, G., Clemens, J.D., Droop, G.T.R., 1997. Melt production during granulite-facies anatexis: experimental data from “primitive” metasedimentary protoliths. Contributions to Mineralogy and Petrology 128, 352–370.
Stevens, G., Villaros, A., Moyen, J.F., 2007. Selective peritectic garnet entrainment as the origin of geochemical diversity in S-type granites. Geology 35, 9–12.
Taylor, J., Stevens, G., Armstrong, R., Kisters, A.F.M., 2010. Granulite facies anatexis in the Ancient Gneiss Complex, Swaziland, at 2.73 Ga: mid crustal metamorphic evidence for mantle heating of the Kaapvaal craton during Ventersdorp magmatism. Precambrian Research 177, 88–102.
Taylor, S.R., McLennan, S.M., 1985. The continental crust: its composition and evolution. Blackwell, Oxford. 312 pp.
Van der Molen, I., Paterson, M.S., 1979. Experimental deformation of partially melted granite. Contributions to Mineralogy and Petrology 70, 299–318.
Vielzeuf, D., Holloway, J.R., 1988. Experimental determination of the fluid-absent melting relations in the pelitic system. Consequences for crustal differentiation. Contributions to Mineralogy and Petrology 98, 257–276.
Vigneresse, J.L., Barbey, P., Cuney, M., 1996. Rheological transitions during partial melting and crystallisation with application to felsic magma segregation and transfer. Journal of Petrology 37, 1579–1600.
Villaros, A., Stevens, G., Buick, I.S., 2009a. Tracking S-type granite from source to emplacement: clues from garnet in the Cape Granite Suite. Lithos 112, 217–235.
Villaros, A., Stevens, G., Moyen, J.F., Buick, I.S., 2009b. The trace element compositions of S-type granites: evidence for disequilibrium melting and accessory phase entrainment in the source. Contributions to Mineralogy and Petrology 158, 543–561.
White, A.J.R., Chappell, B.W., 1977. Ultrametamorphism and granitoid genesis. Tectonophysics 43, 7–22.
White, R.W., Powell, R., 2002. Melt loss and the preservation of granulite facies mineral assemblages. Journal of Metamorphic Geology 20, 621–632.
Wilson, A.C., 1982. 1:250 000 Geological Map of Swaziland, with explanatory notes. Geological Survey of Swaziland.
Wyborn, D., Chappell, B.W., 1986. The petrogenetic significance of chemically related plutonic and volcanic rocks. Geological Magazine 123, 619–628.

Chapter 4

MID-CRUSTAL, HIGH-GRADE POLYMETAMORPHISM DURING MESOARCHAEAN OROGENY ALONG THE SE MARGIN OF THE PROTO-KAAPVAAL CRATON

CHAPTER 4

Presentation of the publication

This paper [*], first authored by Jeanne Taylor, has been accepted for publication in the journal Geological Society of America (GSA) Bulletin. The following aspects of the research was done independently by Jeanne Taylor while receiving standard supervision by her supervisor Gary Stevens, as well as co-authors Ian Buick and Cristiano Lana: (i) fieldwork and sampling; (ii) structural analysis; (iii) zircon and monazite separation, and preparation of mineral separates for dating by LA-ICP-MS; (iv) mineral equilibria modelling in Thermocalc; (v) acquisition of mineral chemical data on the SEM; (vi) acquisition of LA-ICP-MS zircon and monazite U-Pb data, and U-Pb data reduction; (vii) acquisition of LA-ICP-MS zircon and monazite trace element data; (viii) writing of the manuscript.

Jeanne Taylor[a]

Gary Stevens[a]

Ian S. Buick[a]

Cristiano Lana[a,b]

a: Centre for Crustal Petrology, Department of Earth Sciences, Stellenbosch University, Private Bag X1, Matieland 7602, South Africa

b: Departamento de Geologia (DEGEO), Universidade Federal de Ouro Preto, Morro do Cruzeiro, Ouro preto, Minas Gerais 35400000, Brazil.

Reference[*]: Taylor, J., Stevens, G., Buick, I.S., and Lana, C., 2011, Mid-crustal, high-grade polymetamorphism during Mesoarchaean orogeny along the SE margin of the proto-Kaapvaal Craton: *GSA Bulletin, accepted with minor revision.*

Mid-crustal, high-grade polymetamorphism during Mesoarchaean orogeny along the SE margin of the proto-Kaapvaal Craton

J. Taylor[a*], G. Stevens[a], I.S. Buick[a] and C. Lana[a,b]

[a]Centre for Crustal Petrology, Department of Earth Sciences, Stellenbosch University, Private Bag X1, Matieland 7602, South Africa; jtaylor@sun.ac.za; gs@sun.ac.za; buick@sun.ac.za

[b]Now at: Departamento de Geologia (DEGEO), Universidade Federal de Ouro Preto, Morro do Cruzeiro, Ouro preto, Minas Gerais 35400000, Brazil.

cristianodeclana@gmail.com

Keywords: *Mesoarchaean orogeny; granulite-facies metamorphism; pseudosections; geochronology; Kaapvaal Craton.*

Abstract

In this study we investigate the evolution of continental crust at the Paleo- to Mesoarchaean boundary by documenting granulite-facies metamorphism and partial melting of supracrustal gneisses from the Ancient Gneiss Complex in Swaziland. The polymetamorphic episodes recorded by the granulites between ca. 3.23 and 3.07 Ga coincide, in the first instance, with the timing of subduction-accretion in the adjacent Barberton greenstone belt (BGB), and with discrete pulses of potassic granitic magmatism during differentiation and consolidation of the newly-assembled lithosphere. The trace element signatures of ca. 3.23-3.18 Ga aged zircons and monazites suggest growth at temperatures > ~750 ºC and pressures > 4-5 kbar. Mineral equilibria modeling constrains ca. 3.11-3.07 Ga metamorphism and partial melting in the rocks to ~830-875 ºC at ≥ 6.5-7.6 kbar, translating to 20-25 km burial depth; followed by clockwise decompression and cooling to ~650 ºC and ~4.0 kbar. Hence, the granulites evolved along P–T paths similar to those documented for metamorphism in modern collisional orogens. High-temperature, solid-state deformation of the migmatites during uplift of the terrane is coaxial with the main NE-SW trending structural grain of the BGB, and mirrors the NW-SE shortening and NE-SW orogen-parallel extension exhibited by the younger potassic granites. We reconcile these features with Mesoarchaean terrane assembly in Barberton via two NW-dipping subduction zones. The trace of the first is represented by the main terrane boundary within the BGB; the second resulted in accretion, burial and high-temperature metamorphism along the SE margin of the proto-Kaapvaal Craton, with the granulites providing valuable insight into the mid- to lower-crustal response to what appears to have been a protracted Mesoarchaean orogenic event.

INTRODUCTION

The Barberton granite-greenstone terrane and the Ancient Gneiss Complex (AGC) in the eastern to southeastern Kaapvaal Craton together represent one of the oldest, best-preserved remnants of ancient continental crust on Earth. The excellent Paeleo- to Mesoarchaean rock record in the Barberton greenstone belt (BGB), specifically, has led to detailed investigations into the geodynamic evolution of this ancient crust, the majority of which are in strong support of a subduction-accretion model for the main assembly phase of the greenstone belt and surrounding orthogneiss terrane at ca. 3.23 Ga (BGB-D_2, De Wit et al., 1992; De Ronde and De Wit, 1994; De Ronde and Kamo, 2000; Kamo and Davis, 1994; Lowe, 1994; Dziggel et al., 2002; Diener et al., 2005; Moyen et al., 2006; Kisters et al., 2010; Schoene and Bowring 2010; Lana et al., 2010b). This is believed to have resulted from the collision and amalgamation of various microcontinental fragments, namely suturing of the ca. 3.33 Ga Northern and ca. 3.45 Ga Southern Barberton terranes along the Saddleback-Inyoka Fault System, the post collisional exhumation of the ca. 3.50-3.45 Ga Stolzburg block to the south of the belt (e.g. Kisters et al., 2010; Lana et al. 2010b), as well as accretion of the ca. 3.66 Ga Ancient Gneiss Complex (AGC) terrane to the southeast of the greenstone belt along the Phophonyane Shear Zone System (e.g. Lana et al., 2011) (Fig. 1). Key constraints on the timing and nature of this event (summarized in Fig. 2), is consistent with terrane accretion in an arc-trench setting where a NW-dipping subduction zone is inferred (e.g. Moyen et al., 2006). Recently, Schoene and Bowring (2010) revised this model by proposing a doubly vergent subduction system to account for a comparable magmatic and deformational history in the AGC (discussed in detail later).

The eastern Kaapvaal Craton subsequently experienced a protracted (>120 Ma) period of crustal differentiation and episodic calc-alkaline granitoid magmatism (e.g. the ca. 3.23-3.22 Ga Usutu Suite, ca. 3.20 Ga Dalmein and ca. 3.14-3.10 Ga GMS suite magmatism; Fig. 1; Schoene et al., 2008; Schoene and Bowring, 2010; Lana et al., 2010a), which consolidated and increased the strength and preservation potential of the newly-accreted terranes (e.g. Schoene et al., 2008). This was accompanied by continued NW-SE regional shortening (BGB-D_3, De Ronde and De Wit 1994; Westraat et al., 2005; Belcher and Kisters, 2006a), and concomitant NE-SW transtensional tectonism; resulting in the diachronous and differential orogen-parallel exhumation and cooling of the various crustal blocks along all margins of the BGB and AGC between 3.23 and 3.10 Ga (De Ronde and De Wit, 1994; Kisters et al., 2003; Schoene and Bowring, 2007; Schoene et al., 2008; Lana et al., 2010b; Lana et al., 2011).

The details of crustal evolution following ca. 3.23 Ga terrane assembly remain somewhat controversial, largely because little metamorphic information from appropriate crustal depths is

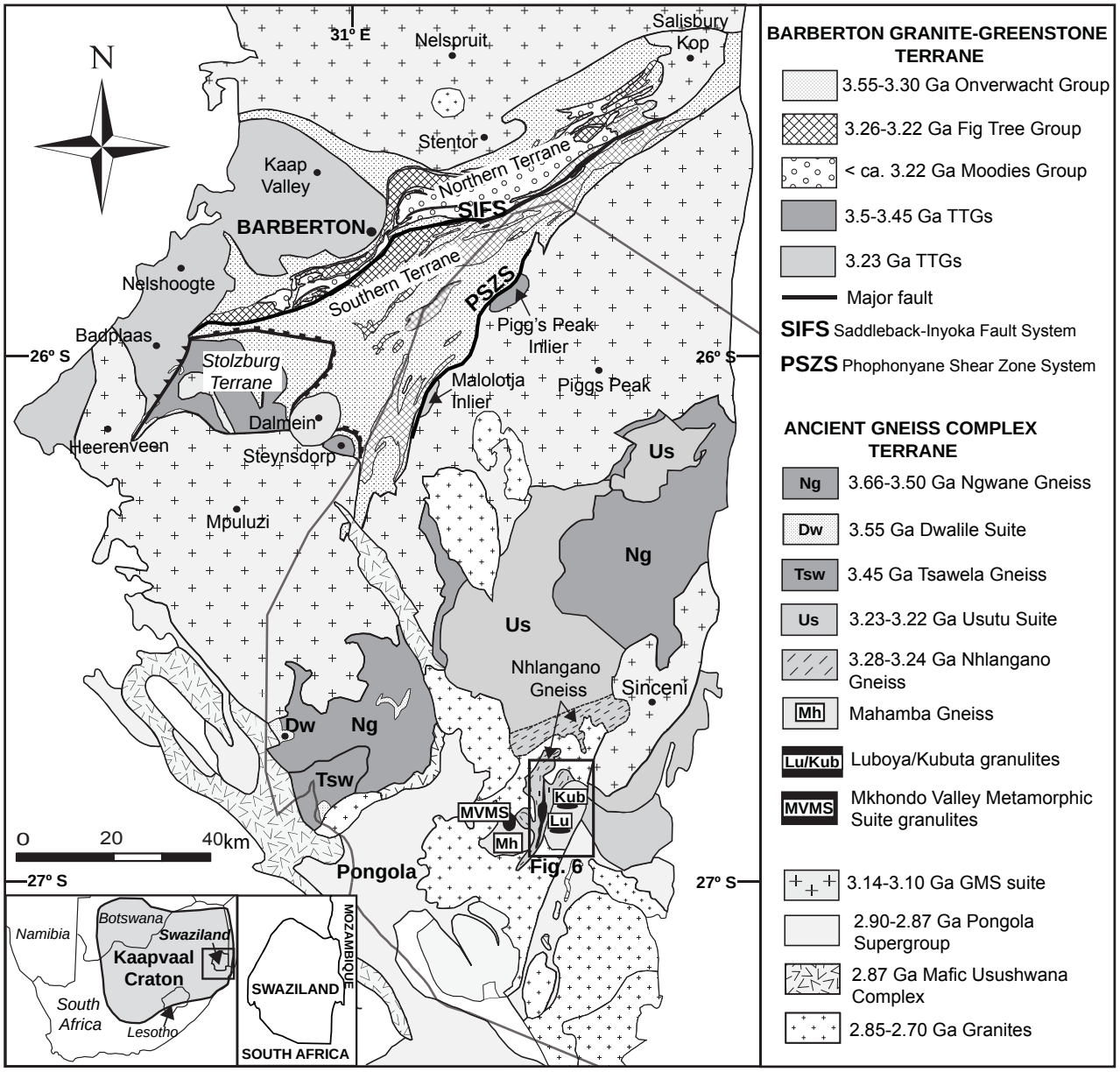

Figure 1. Simplified geological map of the eastern Kaapvaal Craton, modified after Wilson (1982) and Schoene and Bowring (2010). The map depicts important components of the Barberton granite-greenstone terrane, the Ancient Gneiss Complex and the granodiorite-monzogranite-syenogranite (GMS) suite. The black box indicates the study area and the location of the detailed map in Fig. 6.

available for this time period. In comparison to the BGB, the AGC remains highly under-explored. Virtually no published metamorphic studies have to date been conducted on any of the rock units comprising the AGC, with the exception of recent investigations of ca. 2.73 Ga granulites from the Mkhondo Valley Metamorphic Suite (MVMS) (Fig. 1) which formed subsequent to Kaapvaal Craton consolidation (Taylor et al., 2010; Taylor and Stevens, 2010). Rare metasedimentary units within the AGC provide excellent opportunity for constraining the geodynamic evolution of this terrane; in particular, high-grade paragneisses developed in south-central Swaziland (Wilson, 1980, 1982; Kröner et

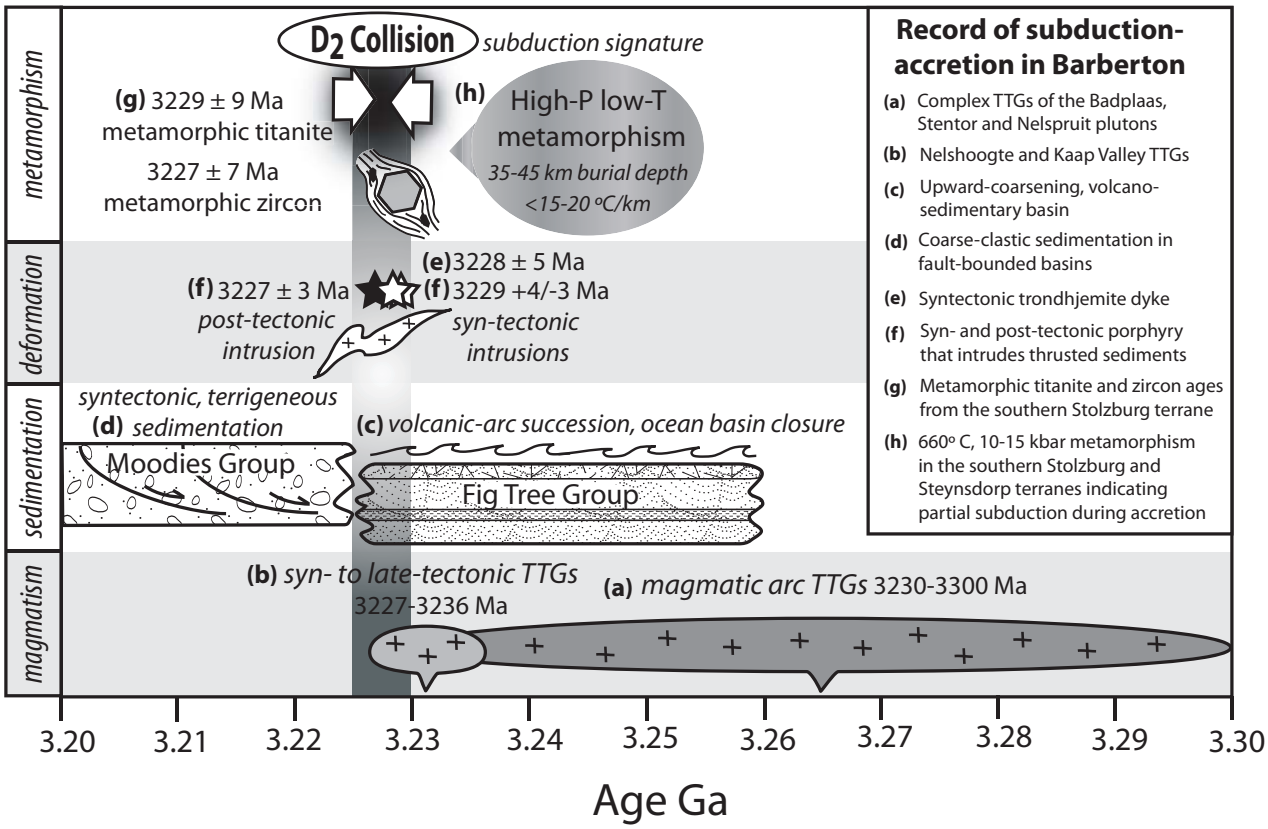

Figure 2. Diagram summarizing the magmatic, sedimentary, tectonic and metamorphic constraints for ca. 3.23 Ga subduction-accretion in Barberton. References: (a & b) Kamo and Davis, 1994; Schoene et al., 2008; Kisters et al., 2010; (c) Lowe and Byerly, 1999; (d) Heubeck and Low, 1994; (e) Dziggel et al., 2002; (f) De Ronde et al., 1991; Kamo and Davis, 1994; (g) Dziggel et al., 2002; (h) Kamo & Davis, 1994; Diener et al., 2005; Moyen et al., 2006; Lana et al., 2010b.

al., 1993; Fig. 1). The granulite-facies grades of metamorphism recorded by theses gneisses are contrasted by the typical lower greenschist-facies grades of metamorphism in the BGB (with the exception of the high-pressure amphibolite-facies southern Barberton terrane, Dziggel et al., 2002; Diener et al., 2005; Moyen et al., 2006), and amphibolite-grade conditions throughout much of the AGC in Swaziland (Jackson, 1984). Consequently, these rocks have the potential to provide insight into the deeper regions of the southeastern Kaapvaal Craton crust, and processes pertaining to early cratonization and crustal differentiation. The current study represents the first detailed investigation into the evolution of this high-grade terrane, with the aim of expanding what is currently known about the development of one of the oldest proposed accretionary cratonic margins on Earth, and our understanding of the nature of Archaean tectonometamorphic processes in general.

GEOLOGICAL SETTING

The AGC in Swaziland is an orthogneiss-dominated terrane comprised of four main lithological units (Fig. 1): finely interlayered and multiply deformed TTGs of the ca. 3.66-3.50 Ga Ngwane gneiss (Kröner et al., 1989); the ca. 3.55 Ga mafic- to felsic, volcano-sedimentary Dwalile Suite (Kröner and Tegtmeyer, 1994); the ca. 3.45-3.43 Ga Tsawela tonalite (Kröner et al., 1989); and ca. 3.23-3.22 Ga tonalites and

granodiorites of the Usutu Suite (Schoene and Bowring, 2010). In addition, metasedimentary units of unknown association occur in south-central Swaziland (Fig. 1). These include the Mkhondo Valley Metamorphic Suite (MVMS) gneisses, as well as high-grade paragneisses to the NE of the MVMS referred to as 'Shiselweni' gneisses by Kröner et al. (1993), but mapped as 'Mahamba' gneisses in the latest geological map of Swaziland (Wilson, 1982). In addition, mafic-felsic banded orthogneiss units mapped as both 'Mahamba' and 'Nhlangano' gneiss (Wilson, 1982) are intimately associated with these metasedimentary units (Fig. 1). The AGC in the southeastern Kaapvaal Craton is overlain by a thick, Late Archaean volcano-sedimentary succession, the < 2.98 Ga Pongola Supergroup (Hegner et al., 1994), and is cross-cut by numerous younger granites (Fig. 1).

Available CA-ID-TIMS U-Pb zircon ages for some components of the orthogneisses mapped as 'Nhlangano' gneiss, indicate that these rocks likely form part of the ca. 3.28-3.24 Ga basement in the area (Schoene and Bowring, 2010). In the model for Kaapvaal Craton assembly proposed by Schoene and Bowring (2010), the ca. 3.28-3.24 Ga Nhlangano orthogneiss and ca. 3.23-3.22 Ga Usutu Suite represent subduction-driven arc magmatism south of Barberton in a NW-SE compressive tectonic regime, which coincided with ca. 3.30-3.23 Ga magmatic arc formation in the Northern Barberton terrane (Badplaas, Nelspruit, Stentor, Nelshoogte and Kaap Valley magmatism, Fig. 1) as well as ca. 3.30-3.22 Ga Fig Tree basin closure (Kamo and Davis, 1994; Schoene et al., 2008; Kisters et al., 2010). In their model, a doubly-vergent subduction zone which dipped NW beneath the Northern Barberton terrane and SE beneath the southern Stolzburg and AGC terranes, is proposed to account for the coeval magmatism.

The high-grade paragneisses investigated in this study crop out along three main river sections in south-central Swaziland: namely at the intersection between the Ngudwane and Luboya Rivers (26º51'43.1''S and 31º24'29.3''E); and the Matsanjeni River on the Kubuta Sisa Cattle Ranch in the area of Kubuta (26º49'11.8''S and 31º25'32.7''E). Due to inconsistencies in the nomenclature used in both the published and unpublished literature (e.g. Wilson, 1982; Kröner et al., 1993), as well as ambiguity in the classification of these gneisses, we have chosen to refer to these units as the 'Luboya' gneisses (supracrustal gneisses exposed near the Ngudwane-Luboya River intersection) and the 'Kubuta' gneisses (supracrustal gneisses exposed along the Matsanjeni River on the Kubuta Sisa Cattle Ranch). No published metamorphic or geochronological constraints exist for the Luboya and Kubuta gneisses, which are dominated by partially melted and deformed metapelites and metagraywackes. An earlier metamorphic investigation (Milisenda, 1986; unpublished Diploma Thesis), suggested equilibration temperatures of 700-900 ºC and pressures of 7-8 kbar for the Luboya and Kubuta assemblages. In the following sections we present a combination of field, metamorphic, structural, and LA-ICP-MS U-Pb zircon and monazite age data for the gneisses from these two localities.

METAMORPHIC ROCK TYPES AND ANATECTIC FEATURES

At the Ngudwane-Luboya River intersection there is limited exposure of interlayered metapelites and metapsammites. The dominant peak metamorphic assemblage in the metapelites is Grt + Crd + Bt + Sil + Kfs + Qtz ± Pl ± gahnite-rich Spl (Fig. 3a) (mineral abbreviations are after Kretz, 1983), while finer-grained metapsammites preserve the assemblage Grt + Bt + Pl + Qtz ± Kfs (Fig. 3b). Most rock types display features that reflect substantial in situ partial melting. Metapelites contain stromatic, foliation-parallel leucosomes that are developed as lenses around cm-scale Grt porphyroblasts (Fig. 3a & i). Layers of the high-grade pelitic host gneiss alternate with mm to cm-wide, concordant, coarse-grained Grt + Qtz + Kfs ± Pl-bearing leucosome segregations (Fig. 3c & d). In places with a high leucosome proportion, host gneiss and leucosome are separated by thin, melanocratic bands rich in Bt + Crd rich (Fig. 3e). Where there is little in situ leucosome present, the pelitic gneisses are restitic containing 30-40 volume % Grt (Fig. 3a). The petrographic features of these garnets, discussed in detail later, suggest that they are peritectic. In contrast, the metapsammites show less evidence for having melted pervasively, containing a significantly lower proportion of peritectic Grt that manifests as small euhedral garnets surrounded by narrow Qtz-feldspar halos, and occasional cm-wide, layer-parallel Grt-bearing leucosomes (Fig. 3b).

Paragneisses on the Kubuta Sisa Cattle Ranch form a > 6 km continuous section of exposure along the Matsanjeni River. The dominant sedimentary rock type here is an aluminous metagraywacke preserving the peak assemblage Grt + Bt + Pl + Qtz ± Kfs ± Opx. Subordinate metagraywackes preserve the assemblage Crd + Bt + Opx + Pl + Qtz. A single thick unit of metagraywacke contains the assemblage Hbl + Bt + Kfs + Pl + Qtz. Rare metapelitic layers preserve the assemblage Crd + Bt + Sil + Kfs + Pl + Ms + Qtz. Metagraywackes typically host mm- to cm-wide stromatic, foliation and/or layer-parallel leucosomes containing coarse-grained Grt/Opx + Qtz + Pl + Kfs ± Ms (Fig. 3h). The stromatic leucosomes feed into cross-cutting segregations that are discordant to the layering and fabric in the host gneiss (Fig. 3h). Opx in the leucosomes is commonly replaced by Hbl, Ep or Chl, and Grt by Chl. In contrast, where there is little in situ leucosome present, metagraywackes appear restitic with high proportions of Grt ± Opx. In some areas of the outcrop, metagraywackes and metapelites are intruded by m-thick, Grt-bearing melt sheets, indicating substantial melt production by the gneisses in this area. The entire Matsanjeni River succession is intruded by granodioritic sheets and dykes, which clearly cross-cut the high-grade layering and fabric.

A detailed description of key petrographic and mineral chemical features in representative metapelites and metagraywackes from the Luboya and Kubuta areas follows.

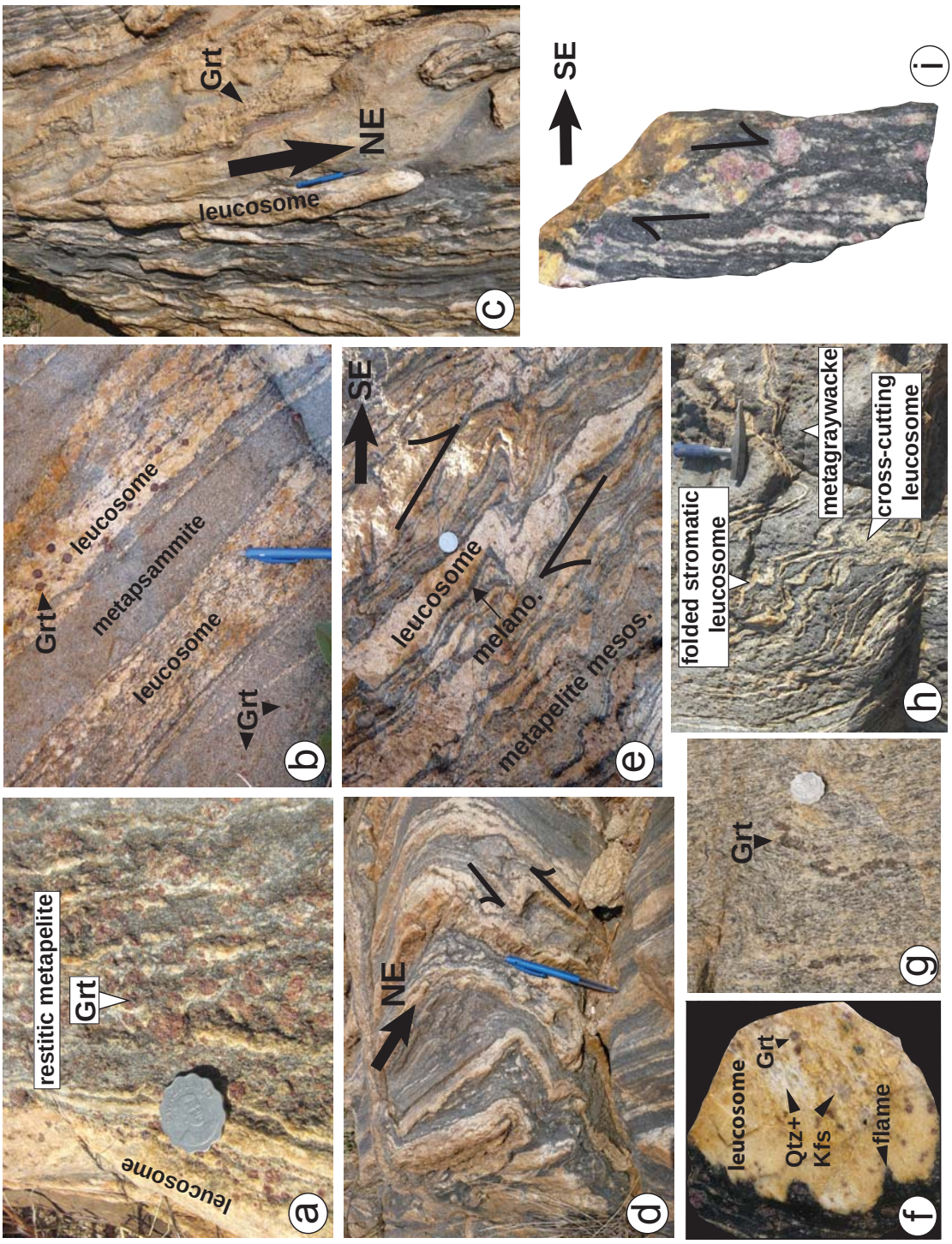

Figure 3. Anatectic and structural features of the Luboya and Kubuta migmatites. (a) Restitic Luboya metapelite. (b) Luboya metapsammite hosting concordant Grt-bearing leucosomes. (c) Prolate leucosome rods hosted by metapelites at Luboya defining the NE-SW aligned L_2 stretching lineation. (d) Layers of metapelitic host gneiss alternating with concordant leucosomes at Luboya, defining the regionally developed, SE-dipping S_2 foliation which is intimately associated with the formation of tube-like asymmetric folds. (e) S_2 layering of pelitic mesosome, melanosome and leucosome at Luboya that has been tightly folded during a period of solid-state D_2 deformation; the fold asymmetry is associated with a normal-sense of shear (SE-side down, NW-side up) along low angle parallel shear planes. (f & g) Stretched and recrystallized Qtz + feldspar lenses, aligned accumulations of peritectic minerals in the leucosomes, as well as cuspate flame structures at the gneiss-leucosome contact is indicative of the D_2 solid-state deformation. (h) Stromatic and cross-cutting leucosomes hosted by a Kubuta metagraywacke, indicating the presence of a syn-peak anatectic S_1 compositional layering in the gneisses. (i) Rotated Grt porphyroblasts in the Luboya metapelites indicate a normal sense of shear.

PETROGRAPHY AND MINERAL CHEMISTRY

Luboya gneisses

Sample Lu2 is a representative Grt + Bt + Crd + Sil + Kfs + Qtz-bearing Luboya metapelite containing accessory minerals Zrn, Mnz, Ap, Ilm, and minor Aln. In this sample, 5-10mm Grt porphyroblasts (locally as large as 20-30mm) are hosted by stromatic leucosomes that form coarse-grained Qtz + Kfs halos around the garnets. The leucosomes and garnets are set in a medium to fine-grained matrix dominated by strongly foliated Bt, Crd, Grt, Sil, Qtz and Kfs, with the foliation typically wrapping around the Grt. The interiors of the Grt porphyroblasts contain large lobate Qtz, or low-dihedral angle, polycrystalline (Qtz + Bt ± Kfs) inclusions, as well as fine Sil needles, less common rounded Bt and Zrn + Mnz inclusions (Fig. 4a). The low-dihedral angle inclusions are interpreted to be crystallized former melt (Holness, 2006). In addition, some Grt porphyroblasts from equivalent pelitic samples contain abundant, fine-grained Ilm inclusion trails in their cores.

A characteristic feature of the Grt porphyroblasts from all the metapelites in this area is the presence of 200-400µm wide, texturally distinct rims, preferentially developed where the Grt is in direct contact with the strongly foliated matrix (Fig. 4b & c). These rims contain large concentrations of rounded Bt, Qtz and Kfs inclusions; Sil needles; Zrn and Mnz inclusions; and polycrystalline former 'melt' inclusions. Some of the Sil inclusions situated along fine cracks in the Grt are partially replaced by phengetic Ms. This likely reflects retrogression of Sil during cooling into the Ms stability field, aided by increasing water and potassium activity as the in situ melts crystallized. In addition to the mm- to cm-sized Grt porphyroblasts, fine-grained (100-300µm) garnets, which texturally resemble the rims on the porphyroblasts, are aligned in the Bt folia in the matrix (Fig. 4d). In combination, the textural evidence indicates growth of the inclusion-rich rims and fine-grained matrix Grt concurrently with, or subsequent to, the development of a high-grade fabric in the rocks.

The Grt porphyroblasts are almandine-rich and are characterized by broad, homogeneous interiors where Mg# [100 x Mg/(Mg + Fe^{2+})] = 24-25, XSpss [Mn/(Fe^{2+} + Mg + Ca + Mn)] = 0.02 and XGrs [Ca/(Fe^{2+} + Mg + Ca + Mn)] = 0.02 (Table 1a; Fig. 5a). Approximately 100-600µm from the rim the Grt grains become strongly zoned. In this region there is a gradual, rimwards decrease in Mg# and increase in XSpss to Mg# = 11, XSpss = 0.03 and XGrs = 0.01 (Fig. 5a). The fine-grained Grt grains in the matrix range in composition from Mg# = 17-20, XSpss = 0.02-0.03 and XGrs = 0.01 in the cores, to Mg# = 11-18 in the rims. All Grt types are extensively replaced by Crd (Mg# = 59), which forms broad, attenuated mantles around the grains (Fig. 4a & b). Large Sil crystals in the matrix are also rimmed and replaced by Crd of the same composition (Fig. 4e). Crd in this sample is extensively pinitized and almost entirely replaced by fine-grained, phengetic Ms (Mg# = 53-65). Three textural and compositional

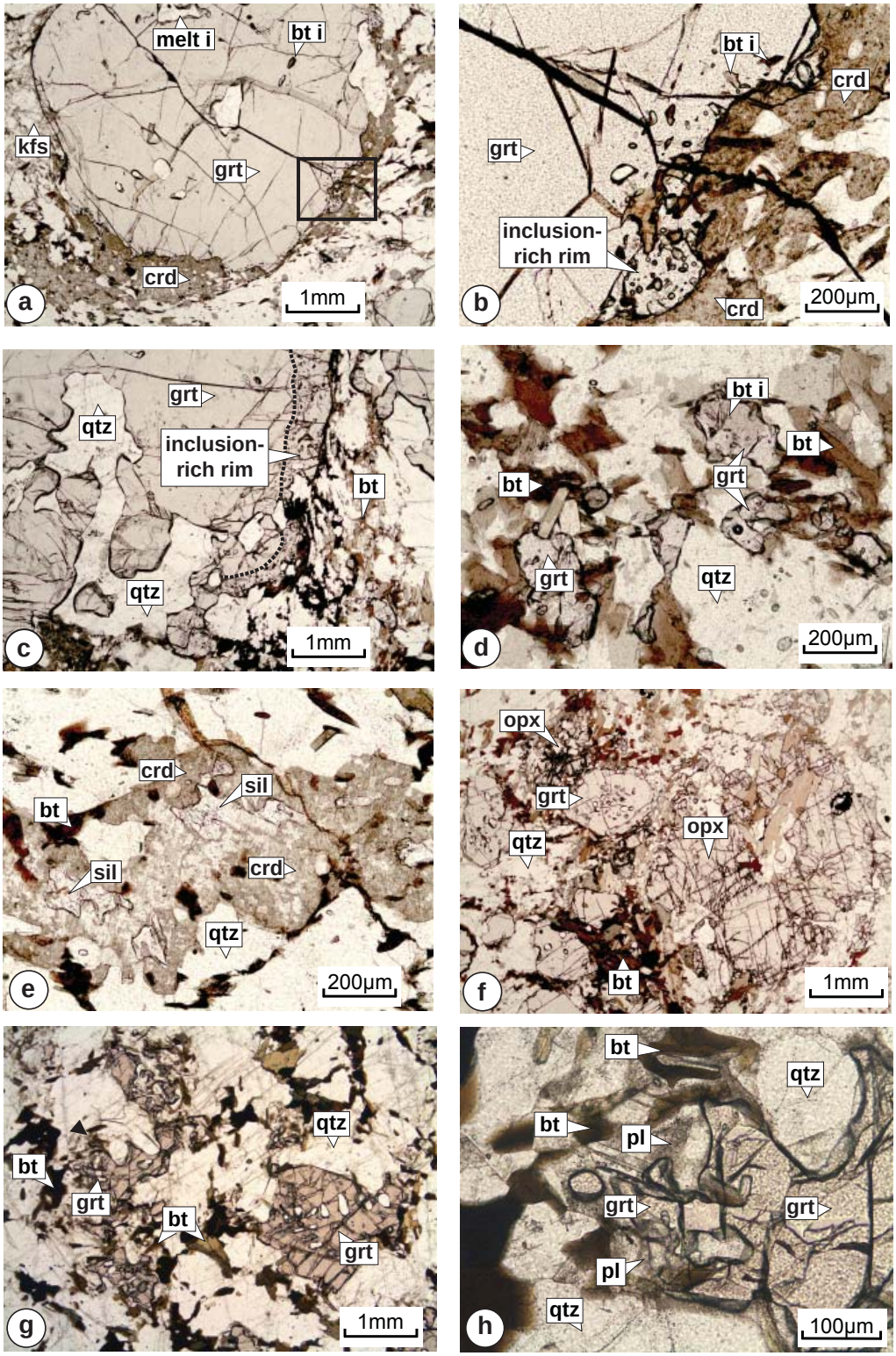

Figure 4. (a) Peritectic Grt porphyroblasts from metapelite sample Lu2, which are mantled and replaced by Crd in the matrix. The black box indicates the location of the inclusion-rich rim domain. (b) An enlargement of the rim domain in Grt from Lu2, showing high concentrations of Bt, Qtz, Kfs, Sil and former 'melt' inclusions. The rim domain is extensively replaced by Crd. (c) A large Grt porphyroblast from a Luboya metapelite showing the presence and absence of an inclusion-rich rim. (d) Fine-grained peritectic Grt in sample Lu2 growing in the Bt folia in the matrix. (e) Replacement of Sil in the matrix by Crd in sample Lu2. (f) Peritectic Grt poikiloblasts and Opx in the Kubuta metagraywacke Kub8. (g & h) The Kubuta metagraywacke Kub23, containing garnets with highly embayed margins where they are extensively replaced by Bt + Pl + Qtz intergrowths, interpreted as crystallization-hydration replacement textures.

varieties of Bt are present (Table 1a). Rounded, high Ti Bt (Mg# = 59-71), included in both the core and rim domains of the Grt, is interpreted to be remnants of the high temperature Bt that underwent incongruent melting during peritectic Grt growth. High Ti Bt (Mg# = 48) is also present in the matrix foliation. Coarser-grained, low Ti Bt (Mg# = 63) preferentially forms in the pressure shadows around Grt where it replaces the Grt. Perthitic Kfs occurs as medium- to coarse-grained crystals in the matrix and around Grt (XSan = K/(Ca + Na + K) = 0.50-0.71), and occasionally as rounded inclusions in Grt (XSan = 0.42-0.92). The 100-600µm compositional rims on the Grt porphyroblasts are not always present, and are neither correlated with the width or presence of an inclusion-rich rim domain. Instead, the intensity of the zoning depends entirely on the presence of Fe-Mg exchange partners replacing Grt. Where there is no Crd/Bt in direct contact with the Grt, the inclusion-rich rims have identical compositions to the broad homogenous cores, and the compositional zoning in the Grt is minor or absent. This demonstrates diffusional resetting of Grt after growth of the inclusion-rich rims.

Kubuta gneisses

Sample Kub8 is a medium-grained metagraywacke preserving the peak assemblage Grt + Bt + Opx + Pl + Kfs + Qtz, and contains accessory minerals Zrn, Mnz, Ap, Ilm, and Py.

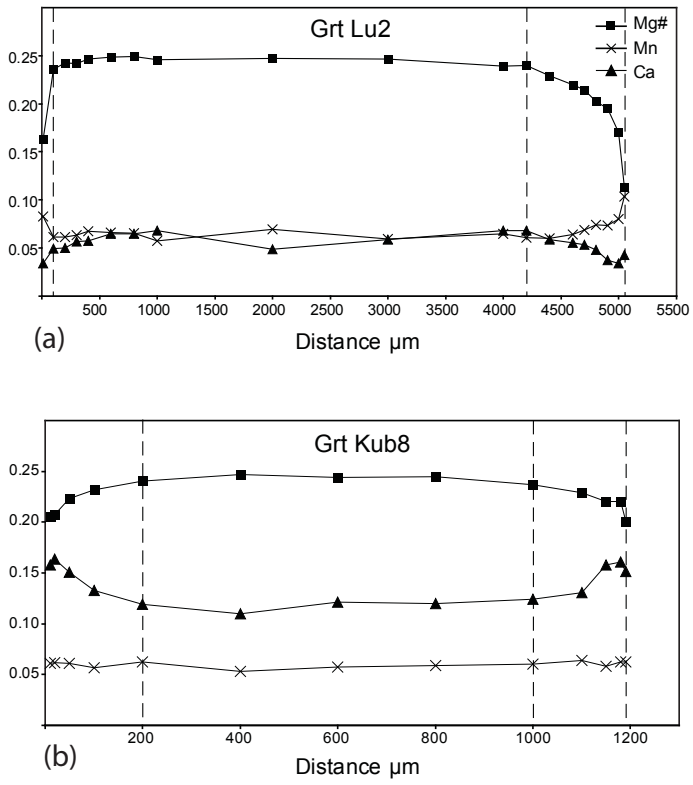

Figure 5. (a) Chemical zonation profiles through peritectic Grt from samples Lu2, and (b) Kub8. The garnets are characterised by broad, compositionally unzoned interiors surrounded by 100-600µm wide retrograde rims (dashed lines), which are neither correlated with the width or presence of inclusion-rich rim domains.

Table 1a Major element compositions and structural formulae of representative mineral compositions from Luboya metapelite sample Lu2. The composition of Perthite was determined via bulk area analysis on the SEM.

Garnet		Biotite				Cordierite		Perthite		Muscovite	
core	rim		matrix	incl. Grt	rimming Grt		matrix & rimming Grt		matrix		matrix & rimming Grt
SiO_2	37.5	37.4	SiO_2	36.9	37.6	37.2	SiO_2	47.6	SiO_2	66.6	SiO_2	46.1
Al_2O_3	21.4	21.2	TiO_2	4.1	4.6	0.8	Al_2O_3	30.2	Al_2O_3	18.3	TiO_2	0.2
Fe_2O_3	0.8	0.8	Al_2O_3	17.2	17.4	17.6	FeO	9.4	FeO	0.1	Al_2O_3	32.0
FeO	32.4	37.7	FeO	20.3	14.4	15.3	MnO	0.0	CaO	0.0	FeO	5.3
MnO	1.0	1.5	MnO	0.0	0.0	0.0	MgO	7.5	Na_2O	3.3	MnO	0.0
MgO	6.0	2.7	MgO	10.5	14.3	14.6	CaO	0.4	K_2O	12.3	MgO	3.9
CaO	0.6	0.5	Na_2O	0.3	0.7	0.2	Na_2O	0.0	BaO	0.2	Na_2O	0.2
Totals	**99.6**	**101.9**	K_2O	9.9	9.7	10.0	K_2O	0.8	**Totals**	**100.8**	K_2O	8.8
Si	2.97	2.98	**Totals**	**99.1**	**98.7**	**95.7**	**Totals**	**95.8**	Si	3.01	BaO	0.0
^{IV}Al	0.03	0.02	Si	5.43	5.41	5.53	Si	5.09	Al	0.98	**Totals**	**96.5**
^{VI}Al	1.98	1.97	Ti	0.46	0.50	0.09	Al	3.80	Fe^{2+}	0.00	Si	6.14
Fe^{3+}	0.05	0.05	^{IV}Al	2.57	2.59	2.47	Fe^{2+}	0.84	Ca	0.00	Ti	0.02
$\sum 3^+$	2.03	2.02	^{VI}Al	0.41	0.35	0.63	Mn	0.00	Na	0.29	^{IV}Al	1.86
Fe^{2+}	2.15	2.51	Fe^{2+}	2.49	1.73	1.90	Mg	1.19	K	0.71	^{VI}Al	3.17
Mn	0.07	0.10	Mn	0.00	0.00	0.00	Ca	0.04	Ba	0.00	Fe^{2+}	0.59
Mg	0.71	0.32	Mg	2.29	3.07	3.24	Na	0.00	**Totals**	**5.00**	Mn	0.00
Ca	0.05	0.04	Na	0.08	0.19	0.07	K	0.11	X_{Ab}	0.29	Mg	0.78
$\sum 2^+$	2.97	2.98	K	1.86	1.78	1.90	**Totals**	**11.07**	X_{An}	0.00	Na	0.05
Totals	**8.00**	**8.00**	**Totals**	**15.60**	**15.61**	**15.81**	**Mg#**	**59**	X_{San}	0.71	K	1.50
X_{Alm}	0.72	0.84	**Mg#**	**48**	**64**	**63**					Ba	0.00
X_{Spss}	0.02	0.03									**Totals**	**14.10**
X_{Py}	0.24	0.11									**Mg#**	**57**
X_{Grs}	0.02	0.01										
Mg#	**25**	**11**										
x(g)	0.75	0.89										

Number of ions calculated on the basis of 12 oxygens for garnet, 22 oxygens for biotite and muscovite, 8 oxygens for feldspar, and 18 oxygens for cordierite. $X_{Alm} = Fe^{2+}/(Fe^{2+}+Mn+Mg+Ca)$, $X_{Spss} = Mn/(Fe^{2+}+Mn+Mg+Ca)$, $X_{Py} = Mg/(Fe^{2+}+Mn+Mg+Ca)$, $X_{Grs} = Ca/(Fe^{2+}+Mn+Mg+Ca)$, $Mg\# = 100 \times Mg/(Mg + Fe^{2+})$, $x(g) = Fe^{2+}/(Fe^{2+}+Mg)$, $X_{Ab} = Na/(Ca+Na+K)$, $X_{An} = Ca/(Ca+Na+K)$, $X_{San} = K/(Ca+Na+K)$.

Table 1b Major element compositions and structural formulae of representative mineral compositions from Kubuta metagraywacke sample Kub8. The composition of Perthite was determined via bulk area analysis on the SEM.

	Garnet			**Biotite**				**Orthopyroxene**		**Perthite**	**Plagioclase**		**Anthophyllite**
	core	rim		matrix; rimming Grt & Opx	incl. Grt	incl. Opx		matrix		matrix	matrix & rimming Grt		rimming Opx
SiO_2	37.5	36.9	SiO_2	36.1	36.2	36.0	SiO_2	50.7	SiO_2	64.7	60.7	SiO_2	63.3
Al_2O_3	20.9	20.7	TiO_2	3.8	4.2	3.8	Al_2O_3	1.6	Al_2O_3	18.6	24.5	TiO_2	0.0
Cr_2O_3	0.0	0.1	Al_2O_3	16.1	16.0	15.4	Fe_2O_3	0.0	FeO	0.2	0.3	Al_2O_3	2.3
Fe_2O_3	1.8	1.3	Cr_2O_3	0.3	0.3	0.4	FeO	32.5	CaO	0.0	6.2	Cr_2O_3	0.0
FeO	31.6	33.3	FeO	20.0	15.4	20.0	MnO	0.3	Na_2O	2.5	8.0	FeO	12.3
MnO	0.9	0.8	MnO	0.0	0.0	0.0	MgO	15.4	K_2O	13.2	0.0	MnO	0.0
MgO	5.8	4.4	MgO	10.7	13.6	11.2	CaO	0.2	BaO	0.7	0.0	MgO	18.3
CaO	1.6	1.8	Na_2O	0.2	0.4	0.4	**Totals**	**100.7**	**Totals**	**99.9**	**99.6**	CaO	0.0
Totals	**100.0**	**99.4**	K_2O	10.0	9.4	9.2	Si	1.96	Si	2.98	2.71	Na_2O	0.2
Si	2.97	2.97	**Totals**	**97.3**	**95.6**	**96.4**	^{IV}Al	0.04	Al	1.01	1.29	K_2O	1.2
^{IV}Al	0.03	0.03	Si	5.44	5.41	5.46	^{VI}Al	0.04	Fe^{2+}	0.01	0.01	**Totals**	**97.5**
^{VI}Al	1.92	1.94	Ti	0.43	0.48	0.44	Fe^{3+}	0.00	Ca	0.00	0.30	Si	8.61
Cr	0.00	0.01	^{IV}Al	2.56	2.59	2.54	Fe^{2+}	1.05	Na	0.23	0.69	Ti	0.00
Fe^{3+}	0.11	0.08	^{VI}Al	0.29	0.24	0.22	Mn	0.01	K	0.78	0.00	^{IV}Al	0.00
$\sum 3^+$	2.03	2.03	Cr	0.04	0.04	0.05	Mg	0.89	Ba	0.01	0.00	^{VI}Al	0.36
Fe^{2+}	2.10	2.24	Fe^{2+}	2.52	1.92	2.53	Ca	0.01	**Totals**	**5.01**	**4.99**	Cr	0.00
Mn	0.06	0.06	Mn	0.00	0.00	0.00	**Totals**	**4.00**	X_{Ab}	0.22	0.70	Fe^{2+}	1.40
Mg	0.68	0.52	Mg	2.40	3.04	2.52	**Mg#**	**46**	X_{An}	0.00	0.30	Mn	0.00
Ca	0.13	0.15	Na	0.05	0.11	0.11	x(opx)	0.54	X_{San}	0.78	0.00	Mg	3.71
$\sum 2^+$	2.97	2.97	K	1.93	1.80	1.78						Ca	0.00
Totals	**8.00**	**8.00**	**Totals**	**15.67**	**15.63**	**15.65**						Na	0.06
X_{Alm}	0.71	0.75	**Mg#**	**49**	**61**	**50**						K	0.20
X_{Spss}	0.02	0.02										**Totals**	**14.34**
X_{Py}	0.23	0.18										**Mg#**	**73**
X_{Grs}	0.05	0.05											
Mg#	**25**	**19**											
x(g)	0.75	0.81											
z(g)	0.05	0.05											

Number of ions calculated on the basis of 12 oxygens for garnet, 22 oxygens for biotite, 6 oxygens for pyroxene, 8 oxygens for feldspar, and 23 oxygens for amphibole. $X_{Alm} = Fe^{2+}/(Fe^{2+}+Mn+Mg+Ca)$, $X_{Spss} = Mn/(Fe^{2+}+Mn+Mg+Ca)$, $X_{Py} = Mg/(Fe^{2+}+Mn+Mg+Ca)$, $X_{Grs} = Ca/(Fe^{2+}+Mn+Mg+Ca)$, $Mg\# = 100 \times Mg/(Mg + Fe^{2+})$, $x(g) = Fe^{2+}/(Fe^{2+}+ Mg)$, $z(g) = Ca/[Fe^{2+} + Mg + Ca]$, $x(opx) = Fe^{2+}/(Fe^{2+}+ Mg)$; $X_{Ab} = Na/(Ca+Na+K)$, $X_{An} = Ca/(Ca+Na+K)$, $X_{San} = K/(Ca+Na+K)$.

The sample has a moderate- to well-developed gneissic fabric defined by the preferred alignment of Bt and lenses of Qtz and feldspar. The Grt occurs as rounded, subhedral 0.8-2 mm poikiloblasts with inclusion-rich cores (Fig. 4f) which contain lobate Qtz, high Ti Bt (Mg# = 55-61), Zrn, Mnz, and low dihedral angle, polycrystalline inclusions of Bt + Qtz + Pl interpreted to represent former melt inclusions. The Grt poikiloblasts have broad, compositionally unzoned interiors where Mg# = 24-25, XSpss = 0.02 and XGrs = 0.04-0.05, surrounded by 100-200µm wide compositional rims (Table 1b; Fig. 5b). Within the rim domains there is a gradual decrease in Mg# from 24 to 19 from the core to the outer edge of the Grt, where XSpss = 0.02, and XGrs = 0.04-0.06. The garnets have embayed margins where they are rimmed and extensively replaced by high Ti matrix Bt (Mg# = 49) defining the foliation, as well as Pl (XAb = Na/(Ca + Na + K) = 0.70) and Qtz (Fig. 4f; Table 1b). The Bt typically anastomoses around the Grt and is concentrated in the pressure shadows around the poikiloblasts. Coarse-grained, ferrosilite-rich (Mg# = 46) Opx occurs interstitially in the matrix. It also contains high Ti Bt inclusions (Mg# = 50) that are identical in composition to the matrix Bt, in addition to inclusions of Pl (XAb = 0.70), perthitic Kfs (XSan = 0.77), polycrystalline former 'melt' inclusions, and Ap + Py inclusions. The Opx is extensively replaced by fine-grained anthophyllite (Mg# = 73) along cracks and cleavage planes.

Sample Kub23 is a medium to coarse-grained metagraywacke located near the source of the Matsanjeni River (26º49'24.5''S and 31º23'44.5''E). It contains Grt + Bt + Qtz + Pl + minor Kfs, plus accessory phases Zrn, Mnz, Ilm, Aln and Py (Fig. 4g). The rock carries a strong gneissic fabric defined by the preferred alignment of Bt and lenses of Qtz and feldspar. Evidence for in situ melting in this sample includes thin foliation parallel leucosomes or patchy domains of Qtz and feldspar concentrated around aggregates of poikiloblastic, ~1mm Grt grains. As in sample Kub8, the garnets have highly embayed margins where they are extensively retrogressed and replaced by Bt + Pl + Qtz intergrowths (Fig. 4g & h), with strongly foliated matrix Bt concentrating in the pressure shadows around the Grt.

STRUCTURAL FEATURES

Excellent exposure of the migmatites along river pavements allows their local structural features to be observed in detail. At both localities, the earliest discernable fabric in the rocks, S_1, is represented by mm- to cm-wide stromatic leucosomes which alternate with concordant layers of the high-grade host gneiss (Fig. 3d,e & h). The stromatic layering is locally cross-cut by discordant leucosomes (Fig. 3h) or thicker melt sheets, indicating melt extraction and the syn-peak anatectic nature of the early D_1 deformation event.

This S_1 layering is overprinted by a pervasive, high-temperature fabric, S_2, associated with a period of solid-state deformation, D_2. The regionally developed S_2 foliation strikes NE-SW and dips moderately to steeply towards

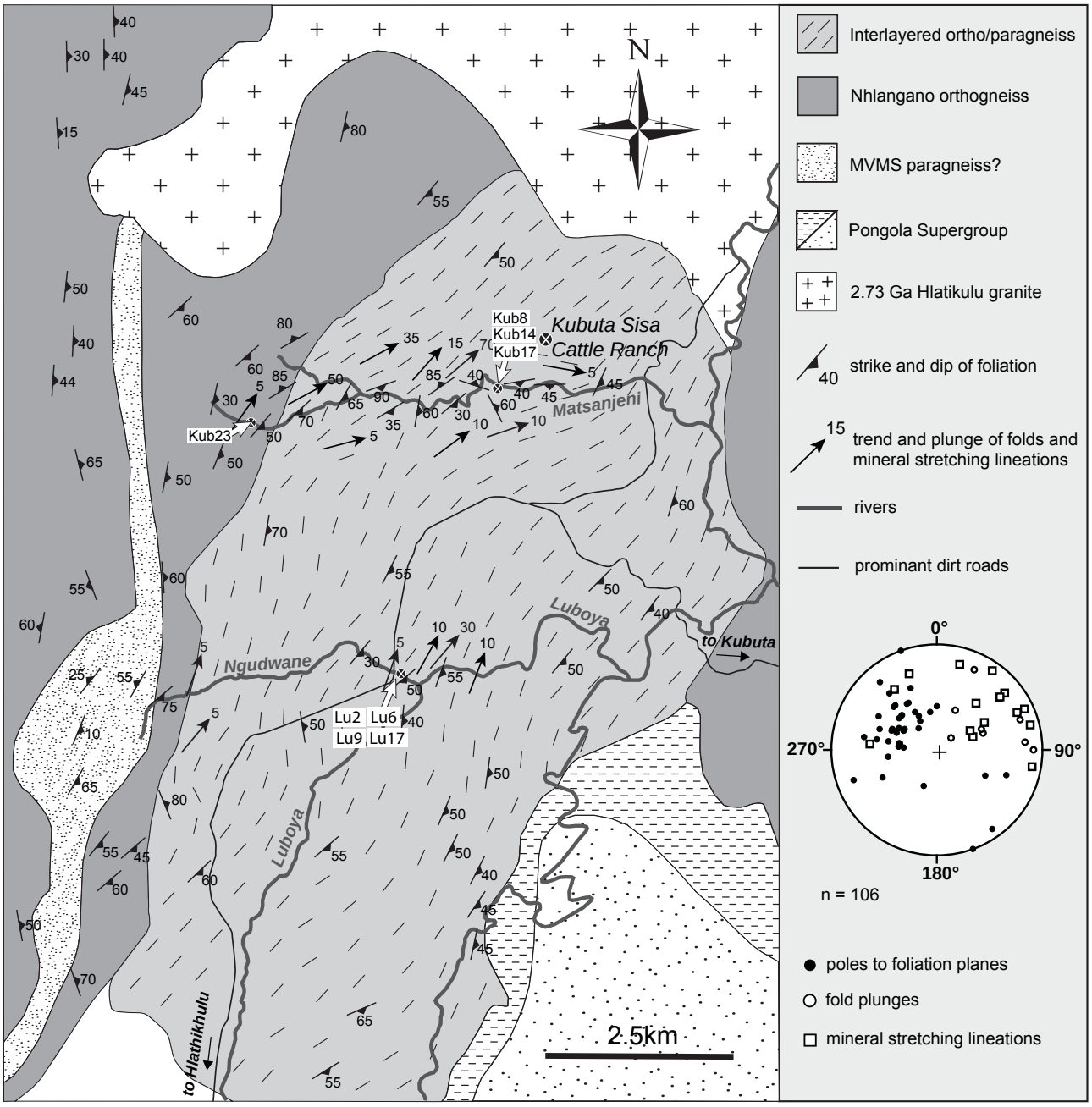

Figure 6. Structural map and sample localities of the Luboya and Kubuta supracrustal gneisses exposed along the Ngudwane-Luboya and Matsanjeni Rivers in south-central Swaziland. Structural data was compiled from this study and the literature (Wilson, 1980, 1982).

the SE (av. dip direction 133º) (Fig. 3d; Fig. 6). The high temperature, yet solid-state nature of the D_2 event is indicated by intense deformation of the leucosomes themselves, e.g. recrystallized feldspar grains in the leucosomes (recrystallization takes place at temperatures > 400-500 ºC, Paschier and Trouw, 1996) and aligned accumulations of peritectic Grt (Fig. 3f & g). In addition, the leucosome margins exhibit cuspate flame structures at the contact with the host gneisses, indicating higher competency of the leucosomes relative to the gneisses at the time of D_2 deformation (Fig. 3f) (e.g. Ramsay and Huber, 1987). Qtz/feldspar rods define the

main L_2 mineral stretching lineation (Fig. 3d). L_2 is oblique, plunging shallowly to moderately towards the NE- to ENE (av. plunge direction 51º) (Fig. 6). In places, anatectic leucosomes form m-scale, subhorizontal prolate rods that plunge parallel to the internal L_2 stretching lineation (Fig. 3c). At several localities it was observed that the S_2 fabric, L_2 stretching lineation and leucosome rods are intimately associated with tight to isoclinal folding of the migmatite layers (Fig. 3d & e). The axial trends of these folds are aligned with the strike of the S_2 foliation, and plunge shallowly to moderately towards the NE- to ENE, therefore parallel to the L_2 stretching lineation (Fig. 6). Many of the tight folds develop an elongate, tube-like geometry (Fig. 3d) that, together with the prolate leucosome rods and L-tectonite fabrics, is suggestive of a strong constrictional stress field with a principal subhorizontal to oblique NE-SW stretching direction.

Kinematic indicators are rare, which is consistent with this type of constrictional deformation. However, some D_2 asymmetric folds, as shown in Fig. 3 (d & e), occur locally at Luboya. The fold asymmetry is linked to a normal-sense of shear (SE-side down, NW-side up) along low angle, parallel shear planes. Similarly, large, rotated Grt porphyroblasts with leucosome mantles occur in metapelites (Fig. 3i) where they indicate a normal component for the shearing. Thus, movement associated with the shearing resulted in the progressive exhumation of structurally deeper layers.

SUMMARY OF LA-ICP-MS U-Pb GEOCHRONOLOGY

A brief presentation of the U-Pb age data generated by LA-ICP-MS dating of zircon and monazite from a variety of Luboya and Kubuta metasedimentary rocks and leucosomes follows. For an in-depth description of the LA-ICP-MS dating method, as well as a detailed interpretation of the samples, the reader is referred to the online Appendix and Supplementary Tables A1, A2, B1, B2 and B3.

Zircons extracted from metagraywacke sample Kub23, metapelite Kub17 and metapsammite Lu17 record complex, yet similar growth histories. Cathodoluminescence (CL) imaging and spot analyses of the zircons grains show that they typically contain euhedral, oscillatory-zoned cores with high Th/U ratios, which are truncated by as many as two, CL-distinct, generally structureless, low Th/U rims (Fig. 7a, b, c, d & e; Table 2). In addition, Lu17 contains round, structureless, low Th/U grains. Low Th/U zircon is a typical feature of zircon from high-grade metamorphic rocks (e.g. Rubatto, 2002) in which zircon has grown in the presence of another mineral that strongly partitions Th with respect to U (e.g. monazite, allanite, titanite). Therefore the oscillatory-zoned, high Th/U cores in the Luboya and Kubuta zircons are viewed as detrital, having been derived from a magmatic source, and low Th/U rims and structureless grains are regarded as having a metamorphic origin. Zircon and monazite

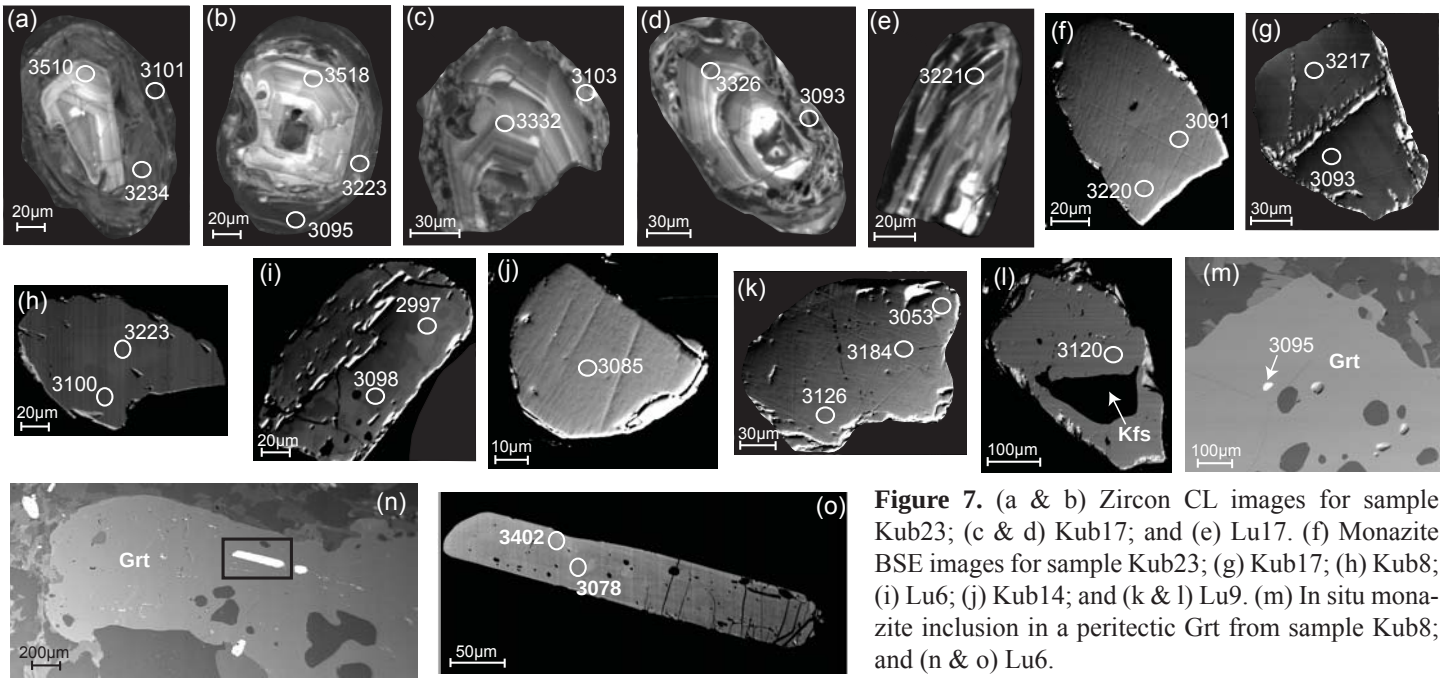

Figure 7. (a & b) Zircon CL images for sample Kub23; (c & d) Kub17; and (e) Lu17. (f) Monazite BSE images for sample Kub23; (g) Kub17; (h) Kub8; (i) Lu6; (j) Kub14; and (k & l) Lu9. (m) In situ monazite inclusion in a peritectic Grt from sample Kub8; and (n & o) Lu6.

U-Pb data used to calculate weighted mean $^{207}Pb/^{206}Pb$ ages for the samples (Table 2) were generally concordant (103-95%); a minority were moderately discordant (as low as 83%). Analyses of detrital cores in the zircons yield weighted mean $^{207}Pb/^{206}Pb$ ages of 3514 ± 12 Ma; 3320.2 ± 7.3 Ma and 3503 ± 31 Ma from samples Kub23, Kub17 and Lu17 respectively (Table 2; Fig. 8a & c, Fig. 9a; Supplementary Table A1). The low Th/U metamorphic rims on zircons yield weighted mean $^{207}Pb/^{206}Pb$ ages of 3222 ± 19 Ma and 3098 ± 18 Ma respectively from sample Kub23; 3092 ± 12 Ma from sample Kub17; and 3225 ± 16 Ma and 3108 ± 16 Ma from sample Lu17 (in this sample, both ages were obtained from zircon rims and round structureless grains) (Table 2; Fig. 8a & c, Fig. 9a; Supplementary Table A1).

Monazite from Kub23, Kub17 and metagraywacke sample Kub8 was also dated. Back-scattered electron (BSE) imaging of the monazite grains shows that they are either internally unzoned, or characterized by irregular, weak, patchy zonation (Fig. 7f, g & h). Analyses from older core domains in monazites from samples Kub23 and Kub17 yield weighted mean $^{207}Pb/^{206}Pb$ ages of 3228.6 ± 7.5 Ma and 3213.8 ± 6.0 Ma respectively (Table 2; Fig. 8b & d; Supplementary Table A2). Analyses from younger unzoned grains, or rim domains in monazite from samples Kub23, Kub17 and Kub8 yield weighted mean $^{207}Pb/^{206}Pb$ ages of 3160 ± 11 Ma and 3080 ± 8.9 Ma; 3161 ± 15 Ma and 3087 ± 15 Ma; and 3091.3 ± 7.1 Ma respectively (Table 2; Fig. 8b, d & e; Supplementary Table A2). Therefore, ignoring the intermediate ca. 3.16 Ga ages for now, monazite age populations at ca. 3.23-3.21 Ga and ca. 3.09-3.08 Ga are consistently within error of the age of metamorphic rims on zircons from the same samples. Monazite from metapelite sample Lu6 display extremely complex, irregular BSE zoning (Fig. 7i), and

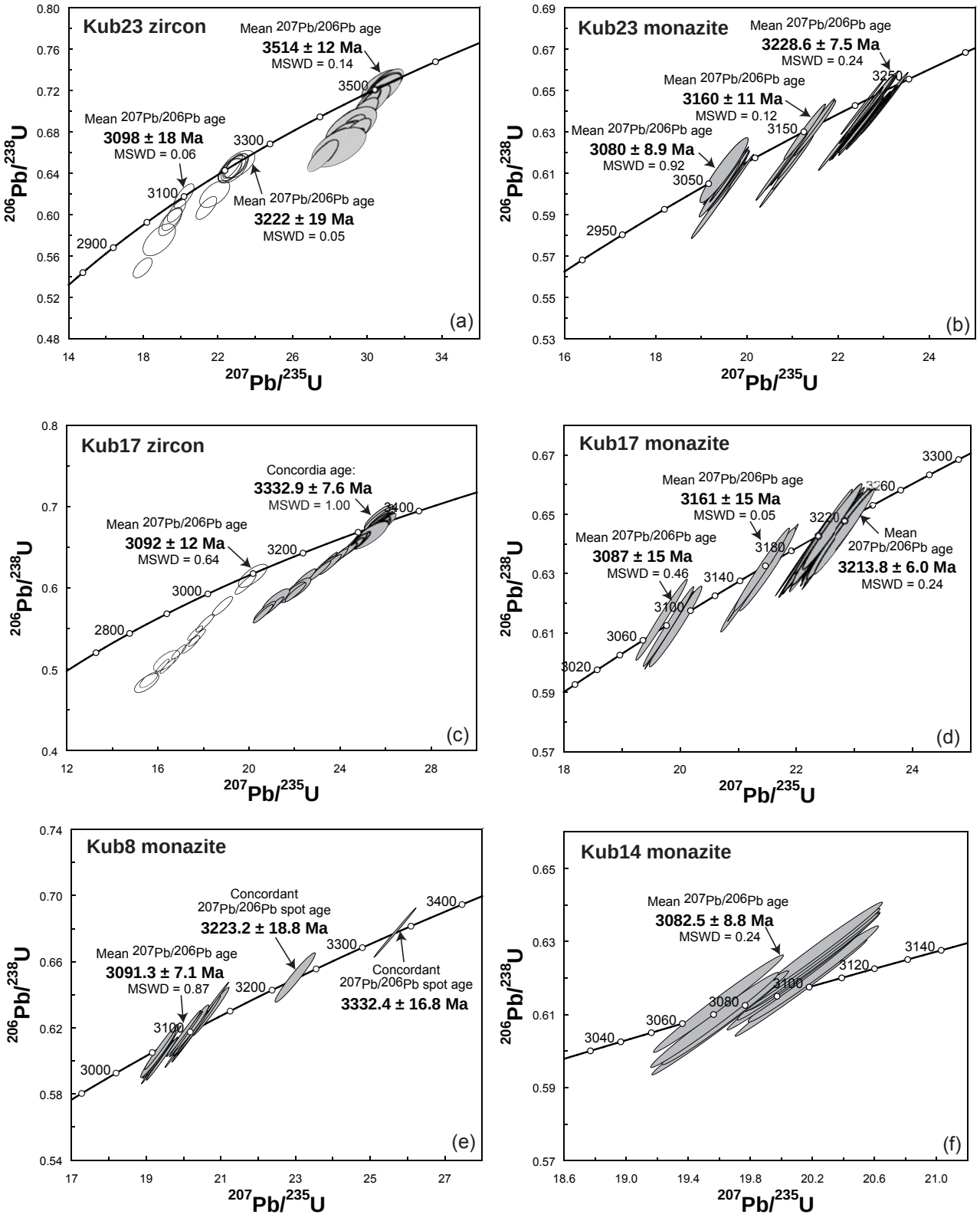

Figure 8. (a-e) U-Pb Concordia diagram plots for zircon and monazite from Kubuta metasedimentary samples; and (f) a Kubuta leucosome.

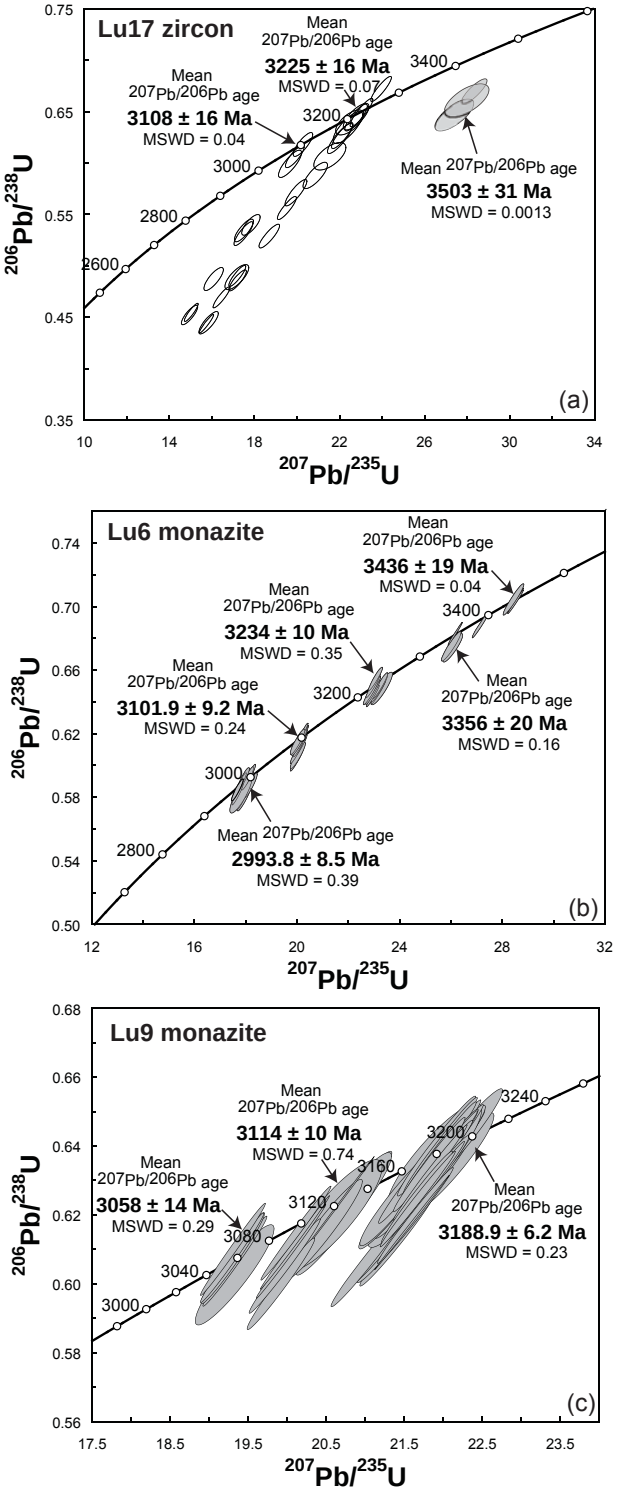

Figure 9. (a & b) U-Pb Concordia diagram plots for zircon and monazite from Luboya metasedimentary samples; and (c) a Luboya leucosome.

analyses of the various domains in the grains define five distinct age populations with weighted mean $^{207}Pb/^{206}Pb$ ages of 3436 ± 19 Ma, 3356 ± 20 Ma, 3234 ± 10 Ma, 3101.9 ± 9.2 Ma and 2993.8 ± 8.5 Ma (Table 2; Fig. 9b; Supplementary Table A2), in addition to a single spot age of 3395 ± 17 Ma. Older ages tended to be derived from BSE-darker core domains, and the three younger ages were obtained from analyzing brighter rim domains in the grains.

An anatectic Kubuta leucosome Kub14 contains BSE unzoned monazite (Fig. 7j). It yields a single weighted mean $^{207}Pb/^{206}Pb$ age of 3082.5 ± 8.8 Ma (Table 2; Fig. 8f; Supplementary Table A2), and is hence within error of the youngest metamorphic zircon and monazite from host gneisses in this area. Monazite from an anatectic Luboya leucosome Lu9 is BSE unzoned or contains weak, patchy zonation (Fig. 7k & l). Analyses of unzoned grains or darker core domains yield a weighted mean $^{207}Pb/^{206}Pb$ age of 3188.9 ± 6.2 Ma (Table 2; Fig. 9c; Supplementary Table A2), which is considerably younger than the oldest ca. 3.22 Ga metamorphic zircon and ca. 3.23 Ga monazite from host gneisses in this area. Analyses of brighter rim domains define two dominant younger age populations with weighted mean $^{207}Pb/^{206}Pb$ ages of 3114 ± 10 Ma and 3058 ± 14 Ma (Table 2; Fig. 9c), which are within error of the youngest metamorphic zircon and monazite from the Kubuta and Luboya areas. Two analyses yield $^{207}Pb/^{206}Pb$ spot ages of e.g. 2973 ± 24 Ma (Table 2).

In addition to dating monazite grain separates,

Table 2 Summary results of zircon and monazite LA-ICP-MS U-Pb age data.

Sample	Grain size and shape	CL/BSE domain	Th/U	n	Weighted mean $^{207}Pb/^{206}Pb$ Age Ma (95% c.l.)	MSWD	% Concordance
Kub23							
zircon	50-400µm, subrounded to oval	oscillatory zoned core	1.14-0.29	24	3514 ± 12	0.14	100-95%
		structureless rim1	0.13-0.01	10	3222 ± 19	0.05	100-96%
		structureless rim2	0.07-0.01	12	3098 ± 18	0.06	100-83%
monazite	80-200µm, amoeboid shaped, subrounded to slightly elongate	core/unzoned grains	21.7-2.8	19	3228.6 ± 7.5	0.24	100-98%
		bright domains	16.4-8.2	10	3160 ± 11	0.12	100-96%
		dark rim domains	17.9-11.7	15	3080 ± 8.9	0.92	103-95%
		in situ inclusions in Grt	10.3-3.4	6	3216 ± 19	0.52	100-96%
		in situ inclusions in Grt	6.3	1	3083 ± 25 (spot age)		100%
Kub17							
zircon	50-400µm, prismatic, subhedral to subrounded	oscillatory zoned core	0.80-0.26	27	3320.2 ± 7.3	0.61	101-95%
		structureless rim	0.03-0.00	14	3092 ± 12	0.64	99-88%
monazite	80-200µm, rounded, oval to subhedral and elongate	bright core domains	28.6-17.1	29	3213.8 ± 6.0	0.24	100-99%
		intermediate to dark domains	28.0-15.6	5	3161 ± 15	0.05	100-99%
		dark rim domains	23.1-19.3	5	3087 ± 15	0.46	100%
Kub8							
monazite	40-180µm, rounded, oval to teardrop-shaped	unzoned grains	49.3-5.4	22	3091.3 ± 7.1	0.87	101-99%
		core	47	1	3332 ± 17 (spot age)		100%
		core	33.8	1	3223 ± 19 (spot age)		100%
		in situ inclusions in Grt	14.6-4.4	7	3110 ± 21	0.42	101-97%
Lu17							
zircon	50-300µm, subhedral prismatic to oval/rounded	core	0.37-0.33	3	3503 ± 31	0.0013	96-94%
		core and rim	0.01-0.07	10	3225 ± 16	0.07	101-95%
		rim	0.02-0.04	9	3108 ± 16	0.04	100-83%

*For a more comprehensive description of the geochronological data, the reader is referred to the online Appendix and Supplementary Tables A1 and A2

Table 2 Continued.

Sample	Grain size and shape	CL/BSE domain	Th/U	n	Weighted mean $^{207}Pb/^{206}Pb$ Age Ma (95% c.l.)	MSWD	% Concordance
Lu6 monazite	100-400µm, grains shapes vary from elongate, subhedral/blocky, to subrounded/oval	dark core domains	35.4-7.4	3	3436 ± 19	0.04	100%
		dark core domains	36.8	1	3395 ± 17 (spot age)		100%
		dark core domains	18.5-14.7	3	3356 ± 20	0.16	100-99%
		bright rim domains	54.1-16.0	11	3234 ± 10	0.35	101-99%
		bright rim domains	31.8-17.6	14	3101.9 ± 9.2	0.24	100-99%
		bright rim domains	31.5-17.7	18	2993.8 ± 8.5	0.39	100-99%
		in situ inclusions in Grt	95.3-28.4	5	3440 ± 28	0.33	100-98%
		in situ inclusions in Grt	107.0-31.5	3	3402 ± 42	0.007	100-99%
		in situ inclusion in Grt	43.6	1	3231 ± 28 Ma (spot age)		100%
		in situ inclusions in Grt	27.8-20.2	3	3072 ± 33	0.16	100%
Kub14 monazite	80-100µm, euhedral to crescent shaped	unzoned grains	21.6-12.0	13	3082.5 ± 8.8	0.24	101-98%
		unzoned grain	14	1	3212 ± 16 (spot age)		100%
Lu9 monazite	80-100µm, subrounded, oval to amoeboid shaped	dark core/unzoned grains	32.6-5.2	33	3188.9 ± 6.2	0.23	100-97%
		bright rim domains	29.0-4.9	13	3114 ± 10	0.74	100-98%
		bright rim domains	23.8-10.7	6	3058 ± 14	0.29	100-99%
		bright rim domains	28.9-16.2	1	2997 ± 17 (spot age)		93%

*For a more comprehensive description of the geochronological data, the reader is referred to the online Appendix and Supplementary Tables A1 and A2

in situ monazite inclusions in Grt were dated so as to provide better constraints on the age of Grt growth in these samples. The youngest monazite inclusions in Grt produced weighted mean $^{207}Pb/^{206}Pb$ ages of 3077 ± 33 Ma, 3110 ± 21 Ma and 3072 ± 33 Ma in samples Kub23, Kub8 and Lu6 respectively (Fig. 7m, n & o; Table 2; Supplementary Table A2) with the relatively large uncertainties reflecting the small number of monazite inclusions found in each case. This constrains peritectic Grt growth, and hence partial melting in the Luboya and Kubuta terrane to at, or post, ca. 3.11-3.07 Ga. In general there was no systematic correlation between the position of the monazite inclusions in the Grt and their age. However in the Luboya metapelite Lu6, of the two monazite grains found included in the core domains of Grt porphyroblasts, ages exclusively older than 3.40 Ga were obtained. Whether this is merely a sampling bias or a real trend requires further investigation. However, the possibility does exist that a component of Grt older than ca. 3.11-3.07 Ga is preserved in the Luboya rocks.

ZIRCON AND MONAZITE TRACE ELEMENT GEOCHEMISTRY

Zircon and monazite U-Pb age data presented above clearly indicate a polymetamorphic history for the Luboya and Kubuta granulites. In the following section we investigate the trace element characteristics of key zircon and monazite age populations, in order to make general conclusions about their conditions of growth and equilibration. For a detailed description of the LA-ICP-MS trace element method, the reader is referred to the online Appendix.

Figure 10 shows the chondrite-normalized REE patterns of zircon and monazite age domains from samples Kub23, Lu6 and Lu9. In general, the ca. 3.22 Ga metamorphic zircon rims from sample Kub23 are characterized by

Table 3 REE compositions of average (a.v.) zircon and monazite age domains from metagraywackes Kub23, metapelite Lu6 and anatectic leucosome Lu9. Values are given in ppm.

	Kub23			Lu6		Lu9		
	av. zircon			av. monazite		av. monazite		
	3.51 Ga	3.22 Ga	3.10 Ga	3.23 Ga	3.10 Ga	3.18 Ga	3.11 Ga	3.05 Ga
Y	1871	1711	1240	8356	5315	7320	12194	9804
La	0.81	3.8	0.46	116780	114278	107563	109799	99502
Ce	15	26	3.4	230469	230469	230469	230469	230469
Pr	0.75	3.0	0.4	26705	26350	27189	27390	28621
Nd	7.1	20	2.6	117464	115024	110734	112704	123545
Sm	9.5	13	2.8	24248	24208	23795	23877	27469
Eu	1.8	3.3	0.57	2403	1796	465	531	304
Gd	48	46	16	19945	17688	16480	18456	20534
Tb	15	14	7.8	1759	1313	1324	1706	1630
Dy	184	172	116	4499	3021	3577	5316	4596
Ho	64	58	43	345	228	303	531	429
Er	287	277	216	326	221	316	651	491
Tm	58	65	52	16	11	17	42	28
Yb	557	732	593	45	29	46	143	80
Lu	92	134	105	3.2	2.5	3.3	12	5.9

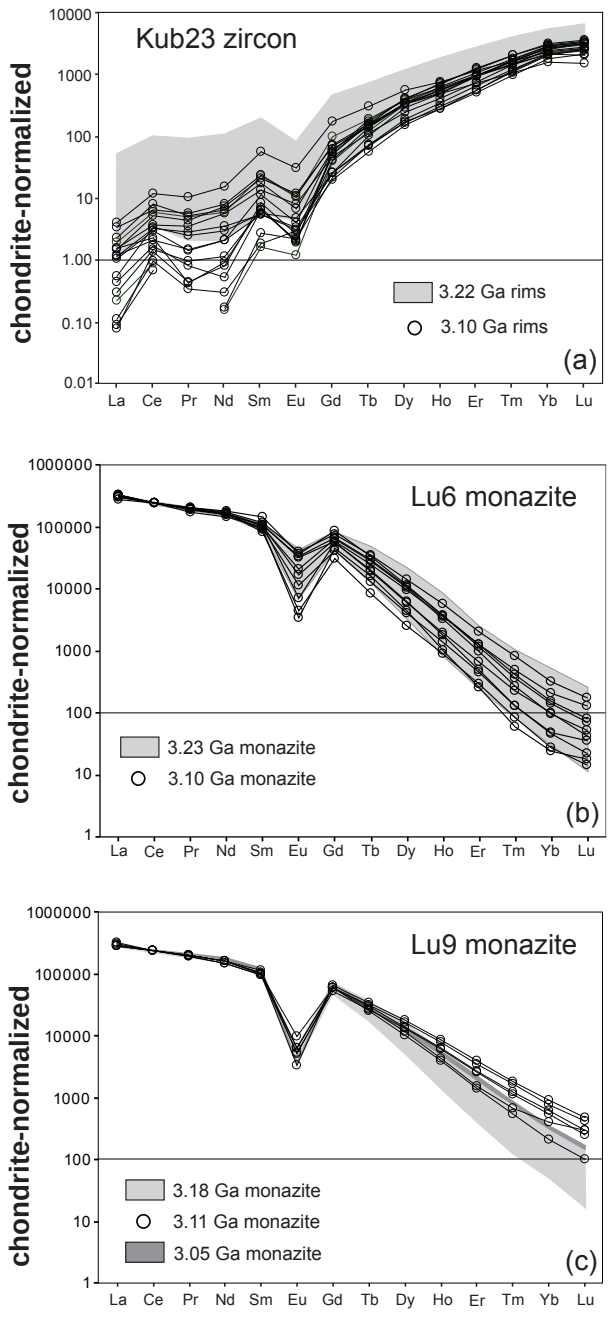

Figure 10. (a) Chondrite-normalized (Taylor and McLennan, 1985) REE patterns of zircon and monazite age domains from samples Kub23; (b)Lu6; and (c) Lu9.

moderately negative Eu anomalies (Eu/Eu* = 0.23-0.52 av. 0.32), and moderately steep HREE patterns (Gd_N/Lu_N = 0.01-0.09 av. 0.04); whilst the ca. 3.10 Ga metamorphic zircon rims typically display large negative Eu anomalies (Eu/Eu* = 0.06-0.30 av. 0.18) and slightly steeper HREE patterns (Gd_N/Lu_N = 0.01-0.07 av. 0.02) (Table 3, Fig. 10a). The ca. 3.23 Ga monazite age domains from sample Lu6 are characterized by moderately negative Eu anomalies (Eu/Eu* = 0.11-0.46 av. 0.31) and moderate to strong HREE depletion (Gd_N/Lu_N = 277-3555 av. 1260); whilst the ca. 3.10 Ga monazite domains display large to moderate negative Eu anomalies (Eu/Eu* = 0.05-0.42 av. 0.24) and similar HREE depletion (Gd_N/Lu_N = 427-2525 av. 1351) compared to ca. 3.10 Ga domains (Table 3, Fig. 10b). All three monazite age domains from leucosome Lu9 have large negative Eu anomalies (Eu/Eu* = 0.07-0.08 av. 0.07 for ca. 3.18 Ga monazite; 0.04-0.12 av. 0.07 for ca. 3.11 Ga monazite), with ca. 3.05 Ga aged monazite displaying the largest negative Eu anomalies (Eu/Eu* = 0.04) (Table 3, Fig. 10c). The ca. 3.18 Ga monazite is the most HREE depleted (Gd_N/Lu_N = 404-2998 av. 817), and the ca. 3.11 Ga monazite (Gd_N/Lu_N = 132-611 av. 251) and ca. 3.05 Ga monazite (Gd_N/Lu_N = 414-461 av. 435) is moderately HREE depleted.

DISCUSSION

CONSTRAINING THE CONDITIONS AND TIMING OF METAMORPHISM

Mineral equilibria modeling

Luboya gneisses

In the Luboya migmatites, large Grt porphyroblasts contained within leucosomes and the inclusion characteristics of both the cores and rims of the garnets, indicate that partial melting in the metapelites involved incongruent, fluid absent melting via the reaction Bt + Sill + Qtz → Grt + Crd + Kfs + Melt. Although there is petrographic evidence for two Grt generations, the textural rims on the garnets are volumetrically subordinate compared to the cores (Grt core-volume to rim-volume ratios are typically > 3:1, e.g. Fig. 4a), and are therefore insufficient to give rise to the large proportion of leucosome observed in the metapelites. In addition, growth of the rims occurred exclusively where the rocks were penetratively deformed. Therefore, we interpret the cores and rims of the porphyroblasts to have grown during a single partial melting episode, the rims being intimately associated with the development of a high-grade fabric in the rocks. Significant replacement of Grt by Crd and Bt during a period of decompression at high temperature, above the blocking temperature for Fe-Mg diffusion in Grt, likely gave rise to the broad diffusionally reset rims on the garnets. We suggest that the water required to rehydrate the assemblage came from crystallizing in situ melt (e.g. Stevens, 1997).

Equilibrium phase diagrams (pseudosections) constraining the stability of the peak metamorphic assemblage in pressure-temperature-compositional (P-T-X) space, were calculated using the whole-rock bulk compositions of the samples (Table 4). For a detailed description of the mineral equilibria modeling method, the reader is referred to the online Appendix. Modeling of the peak assemblage Grt + Bt + Crd + Sil + Kfs + Ilm + Qtz + Melt, using the restitic bulk composition of metapelite Lu2 and a chosen bulk water content of 1.85 molar % H_2O, constrains the stability of the observed assemblage to a narrow field between 800 and 875 ºC at 5.7-7.3 kbar (Fig. 11a). Pressure limits for this assemblage are provided by the Crd-out univariant reaction line up pressure, the Sil-out univariant reaction line down pressure and up temperature, and the solidus down temperature (white stippled line in Fig. 11a). Given that in this sample, Crd enters the assemblage relatively late as a replacement of Grt and Sil, the rock must have evolved from a Crd absent field into the Grt + Bt + Crd + Sil + Kfs + Ilm + Qtz + Melt stability field during a period of decompression at high temperature. Whether decompression was accompanied by increasing or decreasing temperature is difficult to constrain, as the likely positive dP/dT slope on the Bt + Sil melting reaction allows for decompression melting of Bt, even with a small component of concurrent cooling. In order to constrain the retrograde path followed by the rock, Figure 5a was contoured for x(Grt) = $Fe^{2+}/[Fe^{2+} + Mg]$ compositional isopleths

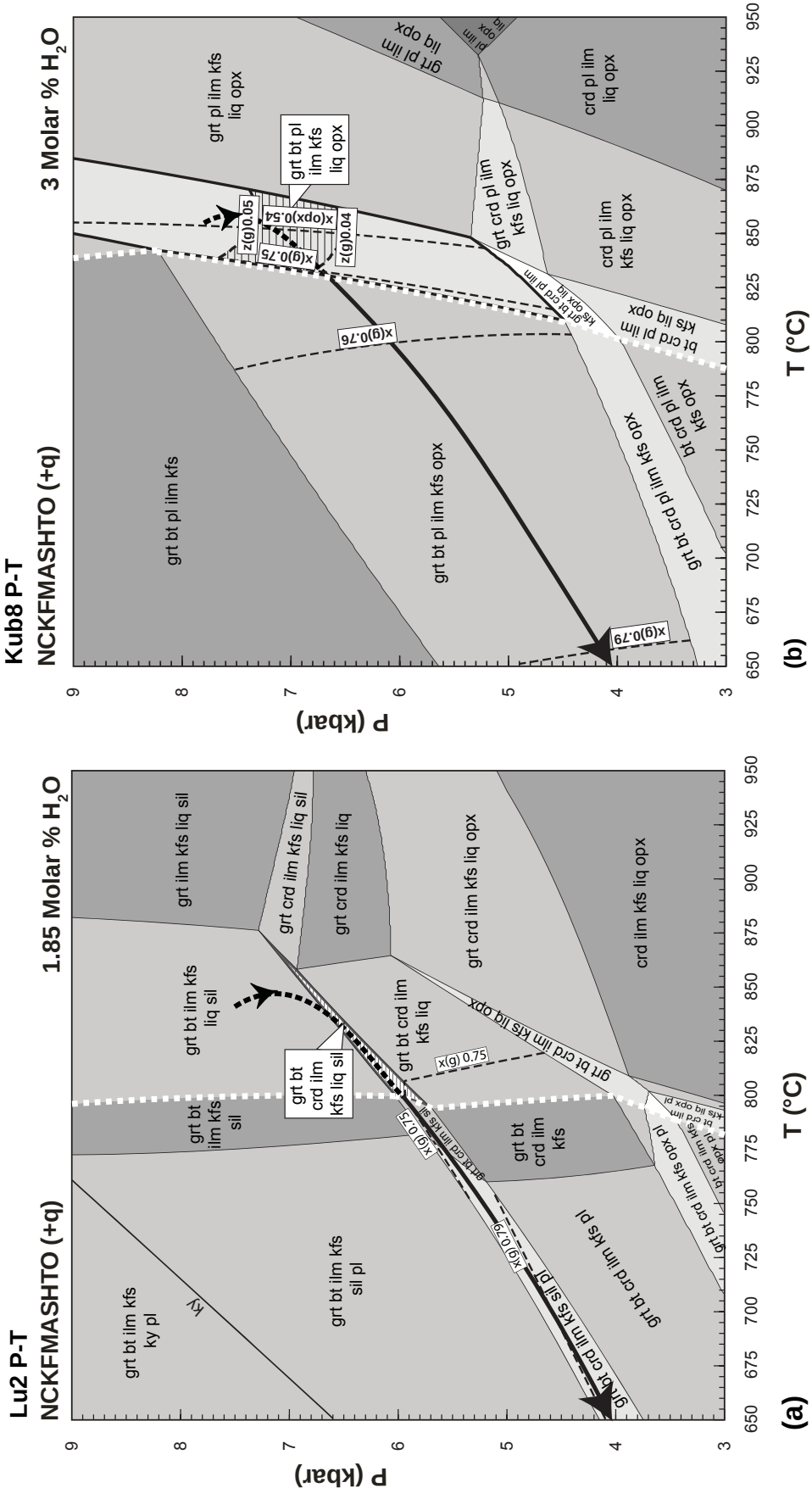

Figure 11. (a) P-T pseudosection calculated for metapelite Lu2, constraining the stability of the preserved peak assemblage to 800-875 °C at 5.7-7.3 kbar (area with horizontal line shading). Measured x(g) = $Fe^{2+}/[Fe^{2+} + Mg]$ Grt core and rim compositional isopleths (stippled black lines) overlap with the fields through which the rock cooled (black arrow) upon crossing the solidus (stippled white line). (b) P-T pseudosection calculated for metagraywacke Kub8. The intersection of measured x(g) core, z(g) = $Ca/[Fe^{2+} + Mg + Ca]$ core, and x(opx) = $Fe^{2+}/[Fe^{2+} + Mg]$ core compositional isopleths (stippled black lines) with the peak assemblage stability field (area with horizontal line shading) constrains the stability of the preserved peak assemblage to 830-870 °C at 6.5-7.6 kbar. Overlap between measured x(g) rim compositional isopleths and the field through which the rock cooled allows a likely cooling path to be depicted (black arrow).

Table 4 Representative bulk-rock compositions of metasediments and anatectic leucosomes from the Luboya and Kubuta granulites, determined via XRF analysis. b.d. = below detection

	Luboya				Kubuta			
Sample	**Lu2**	**Lu6**	**Lu17**	**Lu9**	**Kub8**	**Kub23**	**Kub17**	**Kub14**
Wt% Oxide	**metapelite**	**metapelite**	**metapsammite**	**leucosome**	**metagraywacke**	**metagraywacke**	**metapelite**	**leucosome**
SiO_2	74.27	72.80	67.02	75.11	67.11	73.27	69.66	72.88
TiO_2	0.44	0.45	0.71	0.03	0.59	0.68	0.55	<0.01
Cr_2O_3	<0.002	<0.002	b.d.	<0.002	0.09	b.d.	b.d.	<0.002
Al_2O_3	10.48	9.56	15.93	14.24	10.33	11.40	15.82	13.99
FeO	6.48	7.62	3.97	1.05	11.10	4.32	2.56	1.23
MnO	0.11	0.10	0.06	0.02	0.18	0.04	0.05	0.04
MgO	2.35	3.28	1.20	0.29	4.14	1.39	2.59	0.19
CaO	0.09	0.15	3.57	1.70	0.90	1.39	0.97	0.99
Na_2O	0.59	0.70	3.70	4.63	0.86	3.37	2.19	2.02
K_2O	2.90	3.32	1.46	1.90	2.82	1.68	2.72	7.48
P_2O_5	0.03	0.04	0.18	0.01	0.16	0.07	0.06	0.05
LOI	1.00	0.50	0.61	0.50	0.10	0.72	1.85	0.80
Total	**99.42**	**99.37**	**98.85**	**99.59**	**99.64**	**98.81**	**99.29**	**99.78**
Mg#	**39**	**43**	**35**	**33**	**40**	**36**	**64**	**22**

and compared to measured Grt core x(g) = 0.75, and rim x(g) = 0.79 compositions. Figure 5a shows the x(g) = 0.75 core compositional isopleth intersecting the peak assemblage stability field at ~805 ºC and 5.9 kbar. Because the garnets display flat zonation profiles in their cores, it is assumed that they were diffusionally homogenized at high temperature and that their compositions do not faithfully record peak conditions, hence the intersection of the x(g) core isopleth with the lowest P-T domain of the peak assemblage stability field. The x(g) = 0.79 rim compositional isopleth intersects the appropriate subsolidus field through which the rock must have cooled between 755-650 ºC and 5.1-4.1 kbar.

Thus, the modeled metapelite evolved along a clockwise P-T path with the conditions of peak metamorphism and anatexis constrained to 800-875 ºC at > 5.7 kbar, followed by concurrent decompression and cooling to ~650 ºC and 4.1 kbar.

Kubuta gneisses

Petrographic evidence indicates that the Kubuta metagraywackes underwent high-temperature, fluid-absent partial melting via the reaction Bt + Pl + Qtz → Grt ± Opx + Kfs + Melt. A characteristic feature in the rocks is the extensive replacement of peritectic Grt by Bt + Pl +Qtz. This is a typical feature in rocks which underwent concurrent decompression and cooling, with the water required to retrogress the assemblage derived from crystallizing in situ melts, i.e. crystallization-hydration reactions (Stevens, 1997). As in the Luboya metapelites, decompression at temperatures high enough to allow significant major element diffusion, may explain the broad 100-200µm retrograde rims on the garnets.

Mineral equilibria modeling of the peak assemblage Grt + Bt + Opx + Pl + Kfs + Ilm + Qtz + Melt, using the bulk composition of metagraywacke Kub8 (Table 4) and a chosen bulk-H_2O content of 3 molar % H_2O, indicates that the peak assemblage is stable across a

narrow temperature range, from 810-885 ºC, but that it spans a broad pressure range from 4.5 to ≥ 9.0 kbar (Fig. 11b). Tight temperature constraints are provided by the Bt-out univariant reaction line up temperature and the solidus down temperature (white stippled line in Fig. 11b). However, the intersection of measured x(Grt) = 0.75 core, z(Grt) = Ca/[Fe^{2+} + Mg + Ca] = 0.04-0.05 core and x(Opx) = 0.54 core compositional isopleths with the peak assemblage stability field between 6.5-7.6 kbar provides tighter pressure constraints for this sample (diagonally shaded area, Fig. 11b). As in the Luboya sample, this represents a minimum estimate for peak pressure, if complications surrounding diffusional homogenization of the Grt are considered. Overlap between the measured x(g) = 0.76-0.79 rim compositions and the subsolidus field through which the rock cooled provides less accurate constraints on the retrograde path; however a likely cooling path is depicted in Fig. 11b.

Thus, modeling constrains the conditions for peak metamorphism and partial melting in this sample to 830-870 ºC, ≥ 6.5-7.6 kbar, followed by decompression and cooling along a broadly clockwise P-T path to ~650 ºC and 4.0 kbar.

Zircon and monazite age and trace element constraints

The combined zircon and monazite age data presented in this study indicate two dominant metamorphic age peaks in the Luboya and Kubuta granulites at ca. 3.23-3.21 Ga and at ca. 3.11-3.07 Ga, with important differences in the age spectra of individual samples. Some metasedimentary samples retain evidence of older (ca. 3.43 Ga, ca. 3.40-3.39 Ga, ca. 3.35 Ga and ca. 3.33 Ga) age domains in monazite crystals. Considering the detrital zircon record in the gneisses and the oldest metamorphic overgrowths on zircon, we suggest a depositional age of ca. 3.33-3.23 Ga for the sedimentary precursors of the gneisses; thus, all monazite grains older than 3.23 Ga may also be regarded as detrital. The preservation of detrital monazite through successive granulite-grade metamorphic events is unusual because detrital monazite typically breaks down under lower greenschist-facies conditions to assemblages involving apatite and LREE-rich silicate minerals (e.g. allanite, REE-epidote), and subsequently grows again under mid-amphibolite-facies conditions at the expense of these minerals (e.g. Smith and Barreiro, 1990). The preservation or destruction of detrital monazite appears to be controlled by bulk-rock composition, with preservation being favored by low bulk CaO and/or CaO/Al_2O_3 (e.g. Spear, 2010). Detrital monazite has been recorded in unusually Ca-poor granulite-facies metapelites from Mt. Stafford, Central Australia (Rubatto et al., 2006) and from the upper amphibolite- to lower granulite-facies Mt. Narryer supracrustal belt, Western Australia (Iizuka et al., 2010). Indeed, the two samples in this study that retain evidence of detrital monazite domains are also characterized by the lowest bulk-rock CaO contents (Kub8 = 0.90 wt% CaO and Lu6 = 0.15 wt% CaO). Additional differences in the age spectra are intermediate monazite age populations at ca. 3.18 Ga from a Luboya leucosome and ca. 3.16 Ga from Kubuta metasedimentary rocks,

as well as much younger populations at ca. 2.99 Ga from the same Luboya leucosome and a Luboya metapelite. These intermediate and younger ages may have recorded thermal episodes related to discrete magmatic events in northern Swaziland (Kröner et al., 1989; Schoene and Bowring, 2007; 2010), and during early Pongola Basin development (Hegner et al., 1994). As a last point of difference, the youngest monazite ages from Kubuta samples are typically slightly younger on average than corresponding metamorphic zircon ages from the same samples. We propose that the slight offset in zircon versus monazite ages may be the result of zircon and monazite crystallizing at different stages (i.e. monazite typically crystallizing slightly later than zircon in melt-bearing systems) upon cooling (Kelsey et al., 2008).

In situ dating of monazite included in peritectic Grt makes a convincing case for a granulite-facies partial melting event in the Luboya-Kubuta terrane at ca. 3.11-3.07 Ga, and the P-T estimates obtained from modeling the relevant assemblages constrains the conditions for ca. 3.11-3.07 Ga anatexis to ~830-875 ºC and ≥ 6.5-7.6 kbar. In all of the samples investigated, clear metamorphic/petrographic evidence of older metamorphic events appears to have been entirely reworked by the latter granulite event. This is consistent with the well-homogenized interiors of Grt porphyroblasts of considerable size. Hence the only true insight into the nature of the earlier ca. 3.23-3.18 Ga metamorphic episodes resides in the trace element character of the zircons and monazites of this age. In general, the REE patterns of zircon and monazite are strongly dependent on whether they grew in equilibrium with minerals that preferentially partition these elements. For instance, a large negative Eu anomaly is a common feature of zircon and monazite which grew in the presence of a Pl and Kfs bearing mineral assemblage (e.g. granulite-facies anatectic rocks of metapelitic/quartzofeldspathic composition; Rubatto et al., 2001; Rubatto, 2002; Rubatto et al., 2006; Buick et al., 2010); and pronounced HREE depletion in monazite is generally attributed to growth in equilibrium with Grt, which strongly partitions HREE (e.g. Rubatto, 2002). All ca. 3.23-3.18 Ga metamorphic zircon and monazite age domains are characterized by moderate to large negative Eu anomalies, suggesting growth at P-T conditions at least above the second Sil isograd, at temperatures where Ms breaks down via the reaction Ms + Pl + Qtz → Kfs + Sil + Melt (> ~750 ºC). In addition, most ca. 3.23-3.18 Ga monazite displays pronounced HREE depletion, implying the presence of a significant fraction of Grt in the assemblage. Fluid-absent melting experiments and mineral equilibria modeling of a typical aluminous metapelite composition demonstrates that, at temperatures > 750 ºC, pressures of at least 4-5 kbar are required for > 2-4 volume % Grt to be stable in the assemblage (White et al., 2011 and references therein). The implications of these interpretations are that the rocks either experienced minor melting during the earlier event, or considerable rehydration between successive anatectic events, in order to account for the general lack of preservation of earlier formed Grt (with the possible exception of

some Luboya metapelites) and the fertility of the rocks at 3.11-3.07 Ga.

IMPLICATIONS FOR MESOARCHAEAN CRUSTAL EVOLUTION

Regional setting for metamorphism

Key constraints for the Luboya-Kubuta gneisses, inferred from the metamorphic, structural, and geochronological-geochemical data presented in this study, can be summarized as follows: (1) A depositional age of ca. 3.33-3.23 Ga is indicated for the sedimentary precursors of the gneisses, rendering them tentative age equivalents of the 3.26-3.22 Ga Fig Tree Group of the BGB; (2) The Luboya-Kubuta migmatites were primarily affected by two high-grade metamorphic events at ca. 3.23-3.21 Ga and ca. 3.11-3.07 Ga, with intermediate events recorded at ca. 3.18 Ga and ca. 3.16 Ga.; (3) Metamorphic conditions associated with ca. 3.23-3.18 Ga metamorphism is largely unconstrained, although REE patterns in zircon and monazite suggest temperatures > ~750 ºC and pressures > 4-5 kbar; (4) Peak temperatures of ~830-875 ºC and pressures of ≥ 6.5-7.6 kbar are indicated for the ca. 3.11-3.07 Ga granulite event, translating to a burial depth of 20-25 km and a geothermal gradient of 36-44 ºC/km. The migmatites subsequently evolved along clockwise cooling paths to ~650 ºC accompanied by 3-4 kbar of decompression; (5) Pervasive solid-state deformation occurred immediately after peak partial melting conditions prevailed, and involved combined NW-SE shortening, intense constrictional deformation and NE-SW layer-parallel extension. Low-angle shearing and exhumation of structurally deeper layers, while the rocks remained hot and ductile, is consistent with deformation during uplift and cooling of the terrane. Extensional uplift is bracketed to the interval ca. 3.08-3.05 Ga, which is the inferred crystallization age of anatectic leucosomes.

These constraints allow us to consider the Luboya-Kubuta granulites within the existing regional framework for eastern Kaapvaal Craton evolution. Firstly, high-grade metamorphism in the Luboya-Kubuta terrane at ca. 3.23-3.21 Ga overlapped with subduction-accretion in the adjacent BGB at ca. 3.23-3.22 Ga. An extended period of mid- to lower-crustal melting followed, marked by a transition from typically sodic TTG, Archaean-type magmatism to granitic (senso stricto) magmatism. Recent Sm-Nd and Lu-Hf isotopic studies by Schoene et al. (2009) and Zeh et al. (2011) show that after ca. 3.23 Ga, the eastern Kaapvaal Craton was dominated by intense crustal recycling. This recycling likely began at ca. 3.23-3.21 Ga with granodioritic Usutu magmatism in Swaziland (Schoene and Bowring, 2007, 2010) and in the southern Stolzburg terrane (Dziggel et al., 2005; Schoene et al., 2008; Lana et al., 2010a) (Fig. 12). Discrete pulses of potassic granitic magmatism followed at 3.20 Ga (Lana et al., 2010a), 3.18 Ga (Kröner et al., 1989; Schoene and Bowring, 2010), and 3.14 Ga (Schoene and Bowring, 2007), culminating in the generation of voluminous, sheet-like GMS suite batholiths at ca. 3115-3100 Ma (Fig. 12). As Fig. 12 demonstrates, not only did ca. 3.11-3.07 Ga Luboya-Kubuta mid-crustal anatexis coincide with the final phase of GMS suite

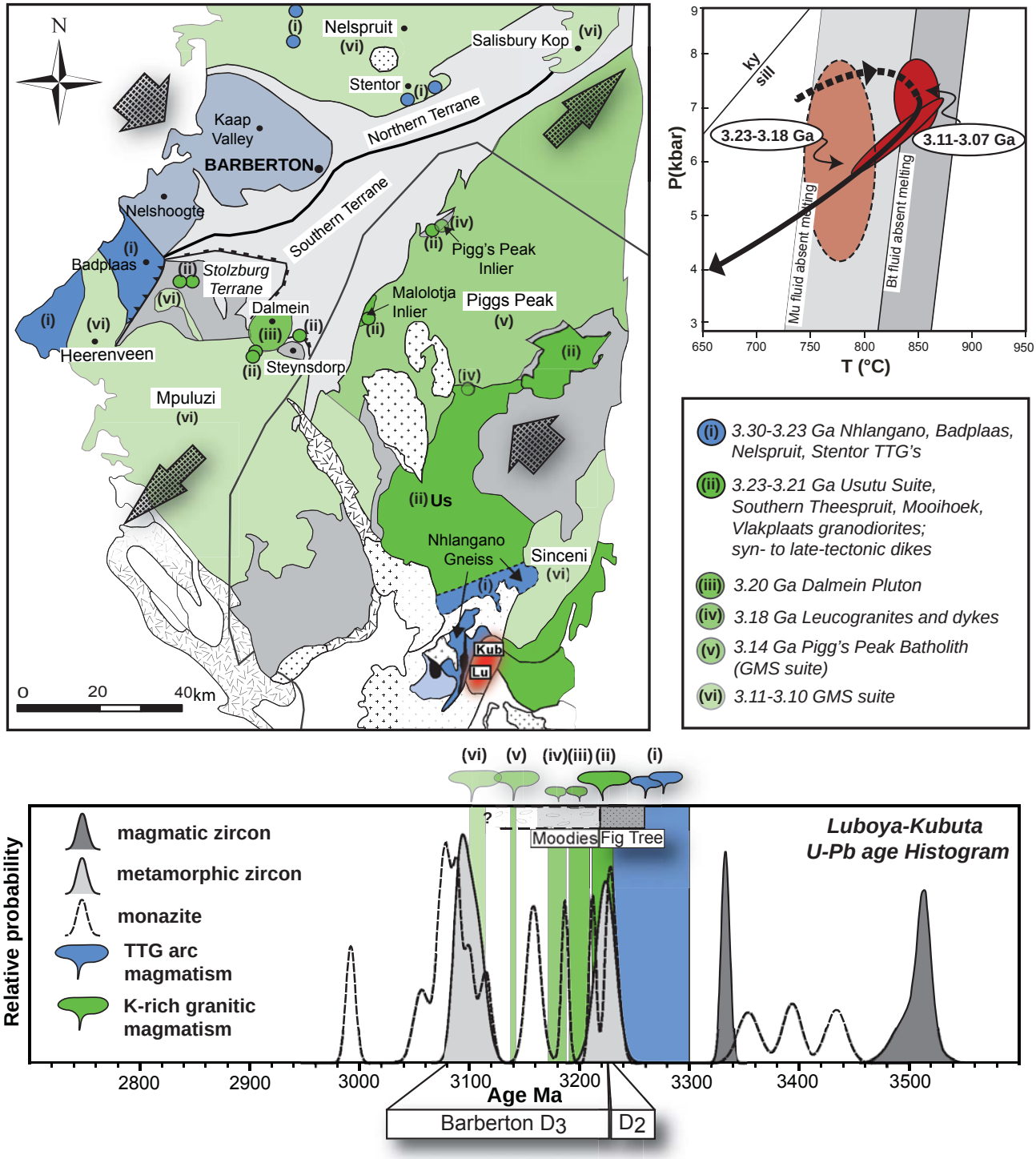

Figure 12. Schematic map of the eastern Kaapvaal Craton and complementary histogram summarizing zircon and monazite ages from this study. The histogram shows dominant metamorphic age peaks for the Luboya and Kubuta gneisses at ca. 3.23-3.21 Ga and at ca. 3.11-3.07 Ga, with intermediate peaks at ca. 3.18 Ga and ca. 3.16 Ga. These metamorphic ages overlap with BGB-D_2 subduction-accretion events, and episodes of crustal differentiation which coincided with early- to late-BGB D_3 deformation. The diagram in the top right-hand corner shows likely (red stippled area) and calculated (solid red areas) P-T conditions in the Luboya-Kubuta terrane during ca. 3.23-3.18 Ga and ca. 3.11-3.07 Ga metamorphism. Symbols match those in Fig. 1.

emplacement at ca. 3.11-3.10 Ga, virtually every pulse of granitic magmatism on the Craton prior to this is immediately preceded, or coincident with a spike in metamorphic ages from the Luboya-Kubuta granulite terrane. This apparent mirroring of thermal pulses indicates protracted, episodic heating of the southeastern Kaapvaal Craton following ca. 3.23 Ga orogeny, and that the Luboya-Kubuta granulites represent the response of the mid-crust to a large-scale anatectic episode towards the end of this heating phase.

In addition, fabric development in the Luboya-Kubuta terrane at ca. 3.11-3.07 Ga leads to a number of important observations. The NE-SW alignment of post peak-metamorphic deformation structures in the migmatites are coaxial with the orientation of magmatic and solid-state compressional fabrics recorded in the 3.28-3.22 Ga Usutu Suite and Nhlangano gneisses in Swaziland (Schoene and Bowring, 2010), as well as the main NE-SW trending structural grain of the BGB which formed in response to orogeny between 3.23 and 3.10 Ga. Strain in the migmatites also mirrors the overall NW-SE, subhorizontal shortening and concomitant NE-SW orogen-parallel extension exhibited by the later ca. 3.14-3.10 Ga GMS suite plutons (Westraat et al., 2005; Belcher and Kisters, 2006a). Thus it agrees strongly with early- to late-D_3 deformation recorded in and around the BGB, i.e. episodes of convergence documented between 3227-3084 Ma (De Ronde and De Wit, 1994). Post-anatectic constriction, orogen-parallel stretching and low angle extensional shearing progressively exhumed the granulites, which we interpret to be consistent with the horizontal flow of soft, partially molten layers in the mid-crust subjected to overthickening and convergence (e.g. Chardon, 2011).

A geodynamic model for Mesoarchaean orogeny along the SE margin of the proto-Kaapvaal Craton

Although Schoene and Bowring (2010) evoke a doubly-vergent subduction zone to account for coeval ca. 3.33-3.23 Ga magmatism and deformation north and south of the BGB, the authors note that this interpretation of the subduction geometry is not unique. Given the geochronological and metamorphic evidence presented here, the following points need to be considered: (1) Deposition of the Luboya-Kubuta sediments is constrained to a period consistent with basin closure, prior to burial and high-temperature metamorphism of the rocks at ca. 3.23-3.18 Ga; demonstrating that the sediments are close analogues to the Fig Tree Group in the BGB. (2) The far-field stresses driving plate convergence at ca. 3.23 Ga persisted long after the main D_2 collisional events recorded in Barberton, with the regional stress-field (NW-SE shortening and NE-SW extension) having remained coaxial on the Craton from 3.23 to 3.07 Ga (e.g. De Ronde and De Wit, 1994; Westraat et al., 2005; Belcher and Kisters, 2006a; this study). (3) Importantly, the Luboya-Kubuta granulites evolved along clockwise P–T paths at ca. 3.11-3.07 Ga, similar to paths documented for metamorphism in modern collisional orogens. Hence, we suggest that the best way of reconciling all of these features with Mesoarchaean terrane

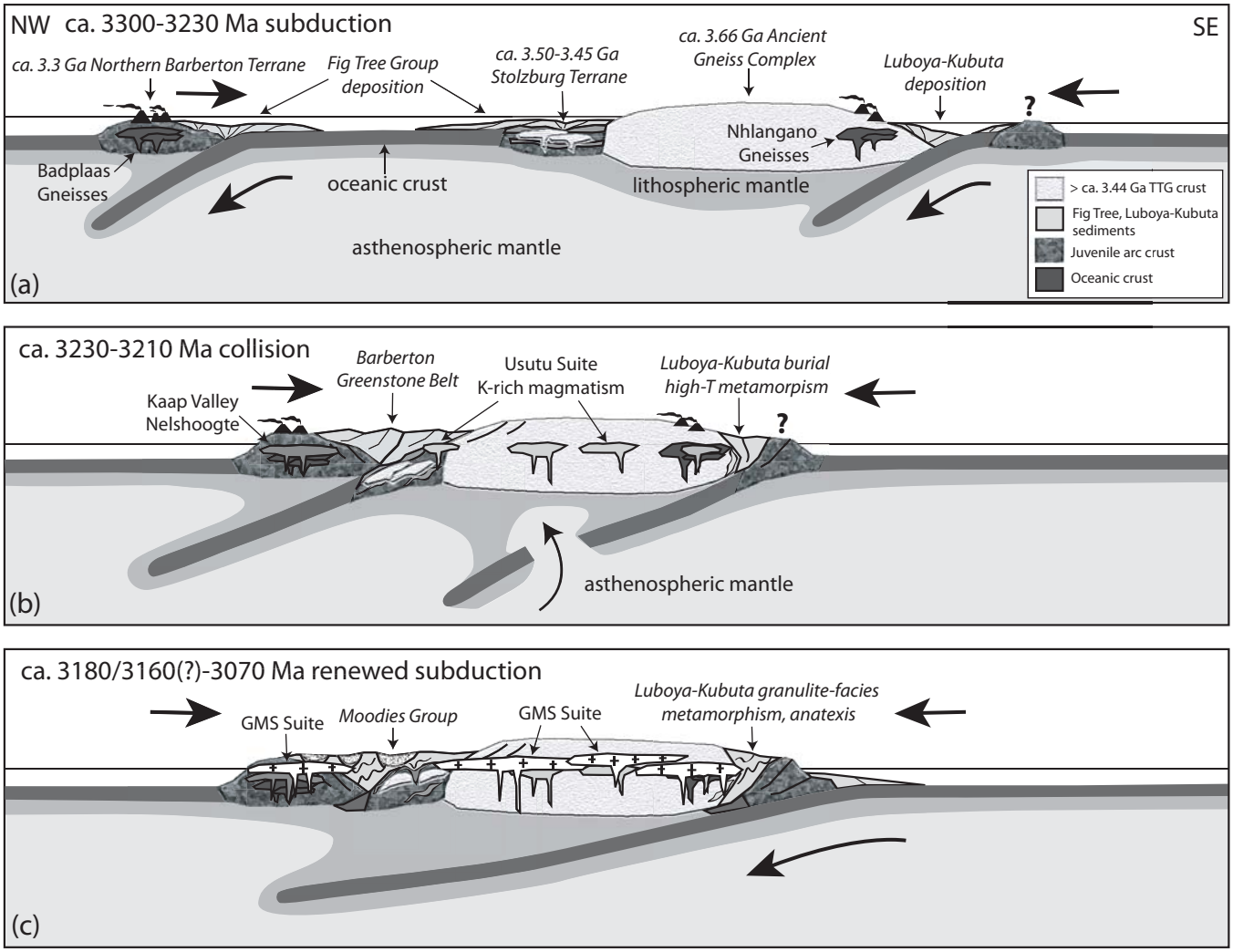

Figure 13. Schematic diagram illustrating the 3.30-3.07 Ga tectonic evolution of the southeastern Kaapvaal Craton. (a) Two northwestward dipping subduction zones at ca. 3.30-3.23 Ga led to ocean basin closure north and south of the AGC, generation of the Badplaas and Nhlangano Gneisses and deposition of the Fig Tree and Luboya-Kubuta sediments. (b) ca. 3.23 Ga tectonic accretion of the respective BGB and AGC terranes, including an exotic terrane from the south, corresponded with high-pressure low-temperature metamorphism in Barberton during partial subduction of the southern Stolzburg Terrane, and burial and high-temperature metamorphism in the Luboya-Kubuta terrane at ca. 3.23-3.21 Ga. (c) After ca. 3.20 Ga (ca. 3.18-3.16 Ga), northwestward subduction beneath the AGC resumed, resulting in renewed NW-SE compression and steepening of regional structures (i.e. BGB-D_3), accompanied by extensive melting of the orogenically thickened crust.

assembly in Barberton would be via a second NW-dipping subduction zone located south of the Luboya-Kubuta and Usutu-Nhlangano gneiss terrane.

In such a model, ca. 3.30-3.23 Ga ocean basin closure and northwestward subduction both north and south of the AGC, resulted in deposition of the Luboya-Kubuta sediments and the Fig Tree Group in a for-arc environment (Fig. 13a). Convergence led to collision of the respective BGB and AGC crustal fragments at ca. 3.23 Ga, including accretion of an exotic terrane from the south that resulted in burial and ca. 3.23-3.21 Ga high-temperature metamorphism of the Luboya-Kubuta migmatites in the vicinity of the Usutu magmatic arc (Fig. 13b). We suggest that shortly after (at 3.18-3.16

Ga?), subduction resumed via migration of the subduction zone outboard, leading to renewed NW-SE convergence and extensive melting of the orogenically thickened crust (Fig. 13c). The deep burial of K-rich sediments and volcanic arc sequences at ca. 3.23 Ga would not only have added the necessary fertility for subsequent differentiation to the deep crust (Clemens et al., 2010), but would also have promoted incubational heating through protracted radiogenic decay. This, combined with advective heating above the mantle wedge, likely gave rise to the major episodes of mid- to lower-crustal melting on the Craton between 3.23 and 3.10 Ga. In this model, granulite-facies metamorphism in the Luboya-Kubuta terrane and convergence documented throughout the Mesoarchaean, took place along an active, proto-continental margin. Thus, the high-grade gneisses from the AGC provide insight into the mid- to lower-crustal response to what appears to have been a protracted, Mid-Archaean accretionary orogenic event. In a somewhat analogous way, modern Phanerozoic orogens rarely entail a simple, single-stage collision, but rather extended periods of convergence punctuated by episodes of collision and accretion involving major lithospheric plates and minor plate fragments and arcs (e.g. the Alpine and Himalayan Orogenies, O'Brien, 2001).

ACKNOWLEDGEMENTS

The authors wish to thank the Geological Survey and Mines Department, and the Surveyor General's Department of Swaziland for their friendly assistance and support of our research in Swaziland. The authors gratefully acknowledge Riana Rossouw at Stellenbosch University for her assistance with the LA-ICP-MS U-Pb geochronology. The Editors and Reviewers are thanked for their constructive comments on an earlier version of the manuscript. This research was supported by South African National Research Foundation (NRF) grant funding to Gary Stevens via the SARChI programme, as well as a PhD bursary to Jeanne Taylor. Ian Buick acknowledges an NRF Blue Skies Research Grant (Grant number BS2008091500007).

REFERENCES

Belcher, R.W., and Kisters, A.F.M., 2006a, Syntectonic emplacement and deformation of the Heerenveen batholith: conjectures on the structural setting of the 3.1 Ga granite magmatism in the Barberton granite-greenstone terrain, South Africa: Geological Society of America, Special Paper, v. 405, p. 211-231

Buick, I.S., Clark, C., Rubatto, D., Hermann, J., Pandit, M., and Hand, M., 2010, Constraints on the Proterozoic evolution of the Aravalli-Delhi Orogenic belt (NW India) from monazite geochronology and mineral trace element geochemistry: Lithos, v. 120, p. 511-520

Chardon, D., 2011, Lateral constrictional flow of hot orogenic crust: Insights from the Neoarchaean of south India, geological and geophysical implications for orogenic plateaux: Geochemistry Geophysics Geosystems, v. 12, p. 1-24

Clemens, J.D., Belcher, R.W., and Kisters, A.F.M., 2010, The Heerenveen batholith, Barberton Mountain Land, South Africa: Mesoarchaean, potassic, felsic magmas formed by melting of an ancient subduction complex: Journal of Petrology, v. 51, p. 1099-1120.

De Ronde, C.E.J., and De Wit, M.J., 1994, Tectonic history of the Barberton greenstone belt, South Africa: 490 million years of Archean crustal

evolution: Tectonics, v. 13, p. 983-1005.

De Ronde, C.E.J., and Kamo, S.L., 2000, An Archean arc-arc collisional event: A short-lived (ca. 3Myr) episode, Weltevreden area, Barberton greenstone belt, South Africa: Journal of African Earth Science, v. 30, p. 219-248

De Ronde, C.E.J., Kamo, S.L., Davis, W.D., De Wit, M.J., and Spooner, E.T.C., 1991, Field, geochemical and U-Pb isotope constraints from hypabyssal felsic intrusions within the Barberton greenstone belt, South Africa: Implications for tectonics and the timing of gold mineralization: Precambrian Research, v. 49, p. 261-280

De Wit, M.J., Roering, C., Hart, R.J., Armstrong, R.A., De Ronde, C.E.J., Green, R.W.E, Tredoux, M., Peberdy, E., and Hart, R.A., 1992, Formation of an Archaean continent: Nature, v. 357, p. 553-562

Diener, J.F.A, Stevens, G., Kisters, A.F.M., and Poujol, M., 2005, Geotectonic evolution of the Tjakastad Schist belt, Barberton greenstone belt, South Africa: a record of mid-Archaean metamorphism and terrain exhumation: Precambrian Research, v. 143, p. 87-112

Dziggel, A., Stevens, G., Poujol, M., Anhaeusser, C.R., and Armstrong, R.A., 2002, Metamorphism of the granite-greenstone terrane south of the Barberton Greenstone Belt, South Africa: An insight into the tectono-thermal evolution of the 'lower' portions of the Onverwacht Group: Precambrian Research, v. 114, p. 221-247

Hegner, E., Kröner, A., and Hunt, P., 1994, A precise U–Pb zircon age for the Archaean Pongola Supergroup volcanics in Swaziland: Journal of African Earth Sciences, v. 18, p. 339–341

Heubeck, C., and Lowe, D.R., 1994, Depositional and tectonic setting of the Archaean Moodies Group, Barberton Greenstone Belt, South Africa: Precambrian Research, v. 68, p. 257-290

Holness, M.B., 2006, Melt-solid dihedral angles of common minerals in natural rocks: Journal of Petrology, v. 47, p. 791-800

Hunter, D.R., 1970, The Ancient Gneiss Complex in Swaziland: Transactions of the Geological Society of South Africa, v. 73, p. 107-150

Iizuka, T., McCulloch, M.T., Komiya, T., Shibuya, T., Ohta, K., Ozawa, H., Sugimura, E., and Collerson, K.D., 2010, Monazite geochronology and geochemistry of meta-sediments in the Narryer Gneiss Complex, Western Australia: constraints on the tectonothermal history and provenance: Contributions to Mineralogy and Petrology, v. 160, p. 803-823

Jackson, M.P.A., 1984, Archaean structural styles in the Ancient Gneiss Complex of Swaziland, southern Africa, in Kröner, A., and Greiling, R., eds., Precambrian Tectonics Illustrated. Stuttgart, Schweizerbart'sche Verlagsbuchhandlung, p. 1-18

Kamo, S.L., and Davis, D.W., 1994, Reassessment of Archaean crustal development in the Barberton Mountain Land, South-Africa, based on U-Pb dating: Tectonics, v. 13, p. 167-192

Kelsey, D.E., Clark, C., and Hand, M., 2008, Thermobarometric modeling of zircon and monazite growth in melt-bearing systems: examples using model metapelitic and metapsammitic granulites: Journal of Metamorphic Geology, v. 26, p. 199-212

Kisters, A.F.M., Belcher, R.W., Poujol, M., and Dziggel, A., 2010, Continental growth and convergence-related arc plutonism in the Mesoarchaean: Evidence from the Barberton granitoid-greenstone terrain, South Africa: Precambrian Research, v. 178, p. 15-26

Kisters, A.F.M., Stevens, G., Dziggel, A., and Armstrong, R.A., 2003, Extensional detachment faulting and core-complex formation in the southern Barberton granite-greenstone terrain, South Africa: evidence for a 3.2 Ga orogenic collapse: Precambrian Research, v. 127, p. 355-378

Kretz, R., 1983, Symbols for rock-forming minerals: American Mineralogist, v. 68, p. 277-279

Kröner, A., Compston, W., and Williams, I.S., 1989, Growth of early Archaean crust in the Ancient Gneiss Complex of Swaziland as revealed by single zircon dating: Tectonophysics, v. 161, p. 271-298

Kröner, A., and Tegtmeyer, A., 1994, Gneiss-greenstone relationships in the Ancient Gneiss Complex of southwestern Swaziland, southern Africa, and implications for early crustal evolution: Precambrian Research, v. 67, p. 109-139

Kröner, A., Wendt, J.I., Milisenda, C.C., Compston, W., and Maphalala, R., 1993, Zircon geochronology and Nd isotopic systematic of the Ancient Gneiss Complex, Swaziland, and implications for crustal evolution, in Kröner, A., ed., The Ancient Gneiss Complex: Overview papers and guidebook for excursion: Swaziland Geological Survey and Mines Department., Bulletin 11, p. 15-37

Lana, C., Buick, I., Stevens, G., Rossouw, R., and De Wet, W., 2011, 3230-3200 Ma post-orogenic extension and mid-crustal magmatism along the southeastern margin of the Barberton Greenstone Belt, South Africa: Journal of Structural Geology, v. 33, p. 844-858

Lana, C., Kisters, A.F.M., and Stevens, G., 2010b, Exhumation of Mesoarchean TTG gneisses from the mid crust: Insights from the Steynsdorp core complex, Barberton granitoid-greenstone terrain, South Africa: Geological Society of American Bulletin, v. 122, p. 183-197

Lana, C., Tohver, E., and Cawood, P., 2010a, Quantifying rates of dome-and-keel formation in the Barberton granitoid-greenstone belt, South Africa: Precambrian Research, v. 177, p. 199-211

Lowe, D.R., 1994, Accretionary history of the Archean Barberton greenstone belt (3.55-3.22 Ga), Southern Africa: Geology, v. 22, p. 1099-1102

Lowe, D.R., and Byerly, G.R., 1999, Geologic evolution of the Barberton Greenstone Belt, South Africa: Geological Society of America, Special Paper, v. 329, p. 37-82

Milisenda, C.C., 1986, Petrographie und geochemie archaischer granulite und gneise des Ancient Gneiss Complex in Swaziland, südliches Afrika. Unpublished Diploma Thesis, p. 137, University of Mainz, Germany.

Moyen, J.F., Stevens, G., and Kisters, A., 2006, Record of mid-Archaean subduction from metamorphism in the Barberton terrain, South Africa: Nature, v. 442, p. 559-562.

O'Brien, P.J., 2001, Subduction followed by collision: Alpine and Himalayan examples: Physics of the Earth and Planetary Interiors, v.127, p. 277-291

Passchier, C., and Trow, R., 1996, Microtectonics: Springer-Verlag, Berlin Heidelberg New York

Ramsay, J. G., and Huber, M. I., 1987, The Techniques of Modern Structural Geology. Volume 2: Folds and Fractures: Academic Press, London, p. 391

Rubatto, D., 2002, Zircon trace element geochemistry: partitioning with garnet and the link between U-Pb ages and metamorphism: Chemical Geology, v. 184, p. 123-138

Rubatto, D., Hermann, J., and Buick, I.S., 2006, Temperature and bulk composition control on the growth of monazite and zircon during low-pressure anatexis (Mount Stafford, central Australia): Journal of Petrology, v. 47, p. 1973-1996

Rubatto, D., Williams, I.S., and Buick, I.S., 2001, Zircon and monazite response to prograde metamorphism in the Reynolds Range, central Australia: Contributions to Mineralogy and Petrology, v. 140, p. 458-468

Schoene, B., and Bowring, S.A., 2007, Determining accurate temperature-time paths in U-Pb thermochronology: An example from the SE Kaapvaal craton, southern Africa: Geochimica et Cosmochimica Acta, v. 71, p. 165-185

Schoene, B., and Bowring, S.A., 2010, Rates and mechanisms of Mesoarchean magmatic arc construction, eastern Kaapvaal craton, Swaziland: Geological Society of American Bulletin, v. 122, p. 408-429

Schoene, B., De Wit, M.J., and Bowring, S.A., 2008, Mesoarchean assembly and stabilization of the eastern Kaapvaal craton: a structural-thermochronological perspective: Tectonics, v. 27, doi:10.1029/2008TC002267, TC5010.

Schoene, B., Dudas, F.O.L., Bowring, S.A., and De Wit, M., 2009, Sm-Nd isotopic mapping of lithospheric growth and stabilization in the eastern Kaapvaal craton: Terra Nova, v. 21, p. 219-228

Smith, H.A., and Barreiro, B., 1990, Monazite U-Pb dating of staurolite grade metamorphism in pelitic schists: Contributions to Mineralogy and Petrology, v. 105, p. 602-615

Spear, F.S., 2010, Monazite-allanite phase relations in metapelite:. Chemical Geology, doi: 10.1016/j.chemgeo.2010.10.004

Stevens, G., 1997, Melting, carbonic fluids and water recycling in the deep crust: an example from the Limpopo Belt, South Africa: Journal of Metamorphic Geology, v. 15, p. 141-154

Taylor, S.R., and McLennan, S.M., 1985, The continental crust: its composition and evolution. Blackwell, Oxford. P. 312

Taylor, J., Stevens, G., Armstrong, R.A., and Kisters, A.F.M., 2010, Granulite facies anatexis in the Ancient Gneiss Complex, Swaziland, at 2.73 Ga: Mid-crustal metamorphic evidence for mantle heating of the Kaapvaal craton during Ventersdorp magmatism: Precambrian Research, v. 177, p. 88-102

Taylor, J., and Stevens, G., 2010, Selective entrainment of peritectic garnet into S-type granitic magmas: Evidence from Archaean mid-crustal anatectites: Lithos, v. 120, p. 277-292

Westraat, J. D., Kisters, A.F.M., Poujol, M., and Stevens, G., 2005, Transcurrent shearing, granite sheeting and the incremental construction of the tabular 3.1 Ga Mpuluzi batholith, Barberton granite-greenstone terrain, South Africa: Journal of the Geological Society, London, v. 162, p. 373-388

White, R.W., Stevens, G., and Johnson, T.E., 2011, Is the Crucible Reproducible? Reconciling Melting Experiments with Thermodynamic Calculations: Elements, v. 7, p. 241-246

Wilson, A.C., 1980, 1:50 000 Geological Map of Swaziland, with explanatory notes. Swaziland Geological Survey and Mines Department, Mbabane.

Wilson, A.C., 1982, 1:250 000 Geological Map of Swaziland, with explanatory notes. Swaziland Geological Survey and Mines Department, Mbabane.

Zeh, A., Gerdes, A., and Millonig, L., 2011, Hafnium isotope record of the Ancient Gneiss Complex, Swaziland, southern Africa: evidence for Archaean crust–mantle formation and crust reworking between 3.66 and 2.73 Ga. Geological Society of London, v.168, p. 953-964

Chapter 5

GENERAL DISCUSSION AND CONCLUSION

In this thesis I have documented the anatectic history of polymetamorphosed, metasedimentary granulites from the Ancient Gneiss Complex (AGC) in Swaziland. The granulites, which record three distinct high-grade metamorphic events, provide resolution on the Meso- to Neoarchaean evolution of the AGC and southeastern Kaapvaal Craton crust. The results and conclusions drawn from this work, presented in Chapter 2 and Chapter 4, can be summarised as follows:

(i) Combined SHRIMP and LA-ICP-MS U-Pb dating of zircon and monazite from metasediments and anatectic leucosomes has proved key to unravelling the polymetamorphic history of the granulites. SHRIMP spot analyses of zircons crystallised from a Mkhondo Valley Metamorphic Suite (MVMS) leucosome produce a precise weighted mean $^{207}Pb/^{206}Pb$ age of 2729.6 ± 4.9 Ma for the peak of metamorphism. This is similar to the zircon evaporation age determined by Condie et al. (1996) for the age of metamorphism in these rocks. The apparent lack of inheritance in the zircon grains, however, prevents the depositional age of the MVMS from being determined. In contrast, zircon and monazite LA-ICP-MS U-Pb age data produced from the Luboya and Kubuta outcrops define a broad spread in metamorphic ages for these rocks. Peaks in metamorphic ages occur at ca. 3.23-3.21 Ga and ca. 3.11-3.07 Ga, with intermediate and younger age peaks at ca. 3.18 Ga, ca. 3.16 Ga and 2.99 Ga. Detrital zircon ages of ca. 3.51 and ca. 3.33 Ga suggest a depositional age of 3.33-3.23 Ga for the sedimentary precursors of the Luboya and Kubuta gneisses. The youngest monazites included in peritectic garnets constrain the most recent granulite-facies partial melting event in the Luboya and Kubuta terrane to ca. 3.11-3.07 Ga.

(ii) The application of pseudosection modelling constrains the conditions for 2.73 Ga metamorphism and anatexis in pelitic gneisses from the MVMS to 830-855 ºC and 4.4-6.4 kbar, followed by near isobaric cooling to 680 °C and ~3.9 kbar. In contrast, ca. 3.11-3.07 Ga peak metamorphism of the Luboya-Kubuta granulites is constrained to 830-875 ºC at ≥ 6.5-7.6 kbar, hence anatexis took place at significantly higher pressures than in the MVMS. Additionally, this was followed by a period of high-temperature decompression and clockwise cooling to ~650 ºC and 4.0 kbar. Post-peak anatectic deformation fabrics and constrictional strains indicate orogen-parallel extrusion of the Luboya-Kubuta migmatites, consistent with exhumation via lateral constriction flow (LCF) of hot, overthickened crust. Clear petrographic evidence of older metamorphic episodes in the Luboya-Kubuta terrane appears to have been entirely reworked by the most recent granulite-facies event. However,

the REE patterns of ca. 3.23-3.18 Ga aged zircon and monazite grains suggests that they grew in the presence of a garnet + K-feldspar bearing mineral assemblage, therefore at temperatures > ~750 ºC and pressures of at least 4-5 kbar in a pelitic bulk-composition of this kind.

(iii) The high-temperature anatectic events recorded by both the MVMS and Luboya-Kubuta granulites were coeval with regional tectono-magmatic events on the Kaapvaal Craton during the Meso- to Neoarchaean. Firstly, sedimentation in the Luboya-Kubuta terrane, followed by burial and high-grade metamorphism at ca. 3.23-3.21 Ga, coincided precisely with D_2 terrane assembly in Barberton. I reconcile these events by suggesting a second NW-dipping subduction zone located south of the Luboya-Kubuta and Usutu-Nhlangano gneiss terrane. In this model, northwestward convergence both north and south of the AGC led to the collision of the respective BGB and AGC crustal fragments at ca. 3.23 Ga, including, perhaps, accretion of an exotic terrane from the south. This resulted in burial and partial melting of the Luboya-Kubuta sediments in the vicinity of the Usutu magmatic arc. Protracted heating of the mid- to lower-crust followed, which manifested as discrete pulses of calc-alkaline granitic magmatism on the Craton between ca. 3.23 and 3.10 Ga, and culminated in granulite-facies anatexis in the Luboya-Kubuta terrane at ca. 3.11-3.07 Ga. I propose that, following collision at ca. 3.23 Ga, subduction along the SE margin of the Craton resumed via migration of the subduction zone outboard, leading to renewed NW-SE convergence and extensive melting of the orogenically thickened crust, through a combination of incubational heating and advective heating by the mantle. Approximately 370 Ma later, mid- to shallow-crustal partial melting of the MVMS sediments immediately preceded the formation of one of Earth's largest continental flood basalt provinces, the ca. 2.71 Ga Ventersdorp LIP (Armstrong et al., 1991), and coincided with widespread intracratonic granitic magmatism at the end of the Neoarchaean. This is interpreted to reflect heating of the Kaapvaal Craton during a possible, global ca. 2.7 Ga mantle plume event (Nelson, 1998; Condie, 1998, 2001a).

A second contribution of this work, presented in Chapter 3, includes a detailed investigation of the partial melting process in the MVMS metapelites, with important implications for S-type granite chemistry on Earth during both Archaean and post-Archaean times. This was done by documenting physical controls on the selective entrainment of peritectic garnet in the magma during incongruent melting of biotite in a typical pelitic source. Key insights into this process are as follows:

(i) Several factors enhance the capacity of peritectic garnet to become selectively entrained in the melt, and to be transported along narrow conduits through the crust to form high-level plutons. Under circumstances where partial melting is particularly rapid (as it appears to have been in the MVMS), tiny (0.1-1.0 mm) poikiloblastic garnets are generated at the sites of biotite breakdown. These garnets are extremely mobile in the melt, as their small grain-size maximises their surface area contact with the melt, and allows them to move through restricted spaces. In addition, their inclusion-rich character (mainly quartz + melt inclusions) lowers the effective density of the garnets, thereby minimizing the potential for gravitational separation from the magma.

(ii) The work documents the textural and chemical evolution of these entrained garnets as they migrate from source layers, to small-scale melt segregation structures (leucosomes), to larger bodies of magma. The peritectic garnets produced in the source are initially out of trace-element equilibrium with the source rock and the melt. Once they become entrained in the magma, the garnets rapidly loose their tell-tale peritectic character by evolving into coarse-grained, euhedral, inclusion-free and hence 'magmatic' appearing grains. This mainly occurs via two related processes. Firstly, garnet crystals brought together by flow in the magma physically 'amalgamate', i.e. compound crystals form as a result of the fusion of several smaller grains. This process is facilitated by dissolution-precipitation driven recrystallisation of the garnet, arising from the relative low solubility of FeO + MgO in the melt. Only once the peritectic garnets have completely recrystallised and evolved in this way, can trace element equilibrium between the garnet and the magma be achieved.

(iii) In conclusion, the 'restite entrainment model' of Chappell and White (1974), which invokes mobilisation of a whole-rock, diatexitic source is not a viable mechanism for S-type magma generation in the MVMS. Instead, the MVMS migmatites emphasise the potential for the selective entrainment of only the solid peritectic products of the incongruent melting reaction, and efficient segregation of peraluminous, more mafic S-type magmas in aluminous sources where metatexitic conditions were maintained.

The primary results of the work conducted during my PhD therefore highlight the complexity in the anatectic history of the granulites from south-central Swaziland. Importantly, the metamorphism overlapped with key events that led to the formation of an early, stable continental nucleus: i.e. terrane assembly at ca. 3.23-3.21 Ga, consolidation of the Craton ca. 3.23-3.10 Ga, and mid-crustal differentiation at ca. 3.11-3.07 Ga and at ca. 2.73 Ga. These results are consistent with Sm-Nd and

Lu-Hf isotope studies of 3.66-2.73 Ga plutonic rocks from the AGC (e.g. Schoene et al., 2009; Zeh et al., 2011), which define crustal evolution trends that indicate an increased importance of crustal recycling with time. The partial melting of sediments, such as those described here, is central to this mechanism of crustal recycling. For melting to take place at realistically attainable temperatures in the Earth's crust (i.e. at < 900 ºC), it is essential that excess H_2O, or more commonly H_2O trapped in hydrous phases like hornblende, biotite or muscovite, is available during melting. Hence, aluminous sediments with a high mica content are regarded as some of the most fertile sources for granitic magma production in the 800-900 ºC temperature range. Orogenic events produce such sources at depth and generate the temperatures needed to drive crustal differentiation. This is seen in modern convergent margin settings, where sediments deposited at surface are readily buried to appropriate depths for anatexis to take place (e.g. the Himalaya, Damara and Caledonian Orogenies).

The present data presented in this thesis demonstrate that the Meso- to Neoarchaean anatectic events were in many ways akin to Phanerozoic scenarios for crustal differentiation. In line with existing magmatic, structural and metamorphic constraints for the BGB and AGC (e.g. De Ronde and De Wit, 1994; Kamo and Davis, 1994; Dziggel et al., 2002; Kisters et al., 2003; Diener et al., 2005; Moyen et al., 2006; Schoene and Bowring, 2010; Lana et al., 2010b), the data is in support of convergent plate-boundary processes to have been the main driver for the deposition, and rapid burial of fore-arc basin sediments to 20-25 km crustal depths, during terrane accretion at ca. 3.23 Ga. Radiogenic heating of the orogenically thickened crust, and continued subduction-driven convergence along an active plate margin, led to protracted heating of these sediments and major mid- to lower crustal differentiation between ca. 3.23 and 3.07 Ga. The long-lived, coaxial nature of the NW-SE shortening, combined with protracted crustal melting and calc-alkaline granitoid magmatism in the southeastern domain of the Craton is, as a first approximation, reminiscent of an Andean-style accretionary margin. In such a setting, extended periods of subduction-convergence are punctuated by short regional orogenic events (terrane accretion), with strain concentrated into zones of mechanical and thermal weakness such as the back-arc and magmatic arc region (i.e. the GMS suite and Luboya-Kubuta migmatite zone). Perhaps due to the early onset of subduction-accretion processes in the eastern domain of the Craton, highly fertile supracrustal material (such as the Theespruit Formation of the Onverwacht Group, the Fig Tree Group and the Luboya-Kubuta metasedimentary successions), and hence the most appropriate sources for subsequent crustal differentiation, were added to the mid- to lower-crust relatively early on in the evolution of the

Craton. This is corroborated by the findings of Clemens et al. (2010) suggesting that the most likely source rocks for the ca. 3.10 Ga Heerenveen Batholith were K-enriched, felsic to intermediate meta-volcanics and/or Al-poor greywackes, a rock association typical of continental arcs. As suggested by these authors, it therefore seems plausible that significant proportions of the mid- to lower crust in the southeastern region of the Craton was comprised of supracrustal, arc-like complexes, buried during the main ca. 3.23 Ga terrane accretion event.

The various stratigraphic, and tectono-metamorphic features associated with the D_2 events in Barberton have alternatively been attributed by some (e.g. Van Kranendonk et al., 2009), to partial convective overturn of the crust at 3.23 Ga, without the need for subduction-accretion processes. This is proposed to have given rise to the 'dome-and-keel' geometry of the belt, common to many Archaean terranes (Hamilton, 1998; Bédard, 2006). However, there is no obvious evidence for a 'dome-and-keel' crustal architecture in the granulite terrane south of Barberton described in this study. Both the 3.23 Ga magmatic rocks from the AGC and the younger GMS suite granites record unidirectional fabric elements and were actively emplaced into the mid- to upper crust, and hence do not represent remobilized lower-crust (Belcher and Kisters, 2006a; Schoene and Bowring, 2010). There is also no evidence for steep, downdip stretching and subvertically lineated deformation fabrics in the Luboya-Kubuta gneisses, either of 3.1 Ga age or older, which would indicate sinking of supracrustal rocks between rising granite domes. Therefore, my data is directly at odds with such a crustal overturn model.

Nearly 400 Ma later, the MVMS (situated at a crustal depth of about 12-15 km at the time) experienced a distinct high-grade anatectic event at ca. 2.73 Ga. This was associated with an elevated geothermal gradient of ~45-65 ºC/km, which necessitates substantial addition of mantle heat to the crust through magmatic intra/underplating. The tholeiitic lavas of the Ventersdorp Supergroup, erupted during flood basalt volcanism on the Craton at ca. 2.71 Ga, offers direct evidence of the existence of a mantle-derived heat source accompanying metamorphism in the Mkhondo terrane. Melting in the mantle may have been related to mantle pluming during one of Earth's first supercontinent cycles. The fact that the MVMS and Luboya-Kubuta granulites display such a contrast in metamorphic ages, yet occur within a < 20 km radius of each other, is somewhat unusual. One plausible explanation may be that the MVMS represents a much younger, 'Pongola-aged' sedimentary succession. This could account for the apparent lack of existence of a major, regional crustal break between the MVMS and Luboya-Kubuta metamorphic terranes, which would

have been required for the large amount of relative vertical displacement during differential burial and exhumation of the two terranes. Assuming that the Luboya-Kubuta migmatites were exhumed to ~4 kbar following peak metamorphism during the Mesoarchaean, the Luboya-Kubuta and MVMS gneisses were likely situated at more-or-less the same crustal level during the Neoarchaean high-grade event. However, the Luboya-Kubuta gneisses would by this time have experienced multiple episodes of granulite-facies metamorphism and partial melting, and would possibly have been left too restitic to act as fertile sources during subsequent anatexis at ca. 2.73 Ga.

References

Armstrong, R.A., Compston, W., Retief, E.A., Williams, I.S., and Welke, H.J., 1991, Zircon Ion Microprobe studies bearing on the age and evolution of the Witwatersrand Triad: Precambrian Research, v. 53, p. 243-266.

Bédard, J.H., 2006, A catalytic delamination-driven model for coupled genesis of Archaean crust and sub-continental lithospheric mantle: Geochimica et Cosmochimica Acta, v. 70, p. 1188-1214

Belcher, R.W., and Kisters, A.F.M., 2006a, Syntectonic emplacement and deformation of the Heerenveen batholith: conjectures on the structural setting of the 3.1 Ga granite magmatism in the Barberton granite-greenstone terrain, South Africa: Geological Society of America, Special Paper, v. 405, p. 211-231.

Chappell, B.W., and White, A.J.R., 1974, Two contrasting granite types: Pacific Geology, v. 8, p. 173-174.

Clemens, J.D., Belcher, R.W., and Kisters, A.F.M., 2010, The Heerenveen batholith, Barberton Mountain Land, South Africa: Mesoarchaean, potassic, felsic magmas formed by melting of an ancient subduction complex: Journal of Petrology, v. 51, p. 1099-1120.

Condie, K.C., 1998, Episodic continental growth and supercontinents: a mantle avalanche connection?: Earth and Planetary Science Letters, v. 163, p. 97-108

Condie, K.C., 2001a, Mantle plumes and their record in Earth history. Cambridge University Press, Cambridge, U.K., p. 305.

Condie, K.C., Kröner, A., and Milisenda, C.C., 1996, Geochemistry and geochronology of the Mkhondo suite, Swaziland: Evidence for passive-margin deposition and granulite-facies metamorphism in the late Archaean of southern Africa: Journal of African Earth Sciences, v. 22, p. 483-506.

De Ronde, C.E.J., and De Wit, M.J., 1994, Tectonic history of the Barberton greenstone belt, South Africa: 490 million years of Archean crustal evolution: Tectonics, v. 13, p. 983-1005.

Hamilton, W.B., 1998, Archaean magmatism and deformation were not products of plate tectonics: Precambrian Research, v. 91, p. 143–179.

Lana, C., Kisters, A.F.M., and Stevens, G., 2010b, Exhumation of Mesoarchean TTG gneisses from the mid-crust: Insights from the Steynsdorp core complex, Barberton granitoid-greenstone terrain, South Africa: Geological Society of American Bulletin, v. 122, p. 183-197.

Nelson, D.R., 1998, Granite-greenstone crust formation on the Archaean Earth: a consequence of two superimposed processes: Earth and Planetary Science Letters, v. 158, p. 109-119.

Schoene, B., and Bowring, S.A., 2010, Rates and mechanisms of Mesoarchean magmatic arc construction, eastern Kaapvaal craton, Swaziland: Geological Society of American Bulletin, v. 122, p. 408-429.

Schoene, B., Dudas, F.O.L., Bowring, S.A., and De Wit, M.J., 2009, Sm-Nd isotopic mapping of lithospheric growth and stabilization in the eastern Kaapvaal craton: Terra Nova, v. 21, p. 219-228.

Zeh, A., Gerdes, A., and Millonig, L., 2011, Hafnium isotope record of the Ancient Gneiss Complex, Swaziland, southern Africa: evidence for Archaean crust–mantle formation and crust reworking between 3.66 and 2.73 Ga. Geological Society of London, v.168, p. 953-964.

APPENDICES

APPENDIX 1: Analytical techniques and detailed geochronological interpretation associated with Chapter 4

APPENDIX 1

1. Analytical techniques

Bulk-rock geochemistry

Samples were crushed to a fine powder using a jaw crusher and tungsten swing mill at the Department of Earth Sciences, Stellenbosch University, South Africa. Whole-rock compositions were determined at Acme Analytical Laboratories in Vancouver, Canada, following a Lithium metaborate/tetraborate fusion and dilute nitric digestion on 0.2g of powdered rock. Major oxide abundances were determined by Inductively Coupled Plasma (ICP)-emission spectrometry. Loss on ignition (LOI) is by weight difference after ignition at 1000°C. For each element analyzed, the reproducibility of replicate analyses and the deviation from the certified values of the secondary standards are less than 5% relative.

Mineral chemistry

Major element mineral compositions were analyzed using a Leo® 1430VP Scanning Electron Microscope at the Department of Earth Sciences, Stellenbosch University, South Africa. Textures were studied in backscattered electron (BSE) mode and mineral compositions quantified by EDX (Energy Dispersive X-ray) analysis using an Oxford Instruments ® 133 KeV ED X-ray detector and Oxford INCA software. Beam conditions during the quantitative analyses were 20 KV accelerating voltage and 1.5 nA probe current, with a working distance of 13mm and a specimen beam current of −4.0 nA. X-ray counts were typically ~7000 cps, and the counting time was 50s live-time. Analyses were quantified using natural mineral standards, and mineral chemical compositions were recalculated to mineral stoichiometries to obtain resultant mineral structural formulae. Comparisons between measured and accepted compositions of control standards within this laboratory, as a reflection of the accuracy of the analytical technique, have been published by Diener et al. (2005) and Moyen et al. (2006).

Zircon and monazite trace element compositions were analyzed via laser ablation-inductively-coupled-mass spectrometry (LA-ICP-MS) using an Agilent 7500ce quadrupole ICP-MS coupled to a 213 nm New Wave laser at the Department of Earth Sciences, Stellenbosch University, South Africa. Ablations occurred in a He carrier gas, and the resulting aerosol was mixed with Ar prior to introduction into the ICP-MS via a signal-smoothing manifold. Zircon and monazite analyses were

performed on mineral separates mounted in epoxy. Zircon was ablated using a 20µm diameter spot size at a fluence of ~7.8 J/cm^2 and a repetition rate of 5Hz. Monazite was ablated using a 12µm diameter spot size at a fluence of ~4.0-4.5 J/cm^2 and a repetition rate of 4Hz. Data was acquired in time resolved mode which allowed potential contamination from mineral inclusions or fractures to be identified and excluded from the analysis. NIST-612 glass (Pearce et al., 1997) was used as the external standard and stoichiometric SiO_2 (zircon), and CeO_2 (monazite) contents were used as internal standards. Accuracy and reproducibility of multiple analyses was established from the analysis of the secondary standards BHVO 2G and BCR-2G (USGS natural basaltic glass standards). Results were better than 5% relative for most elements. Data was processed using the Glitter software package (Van Achterbergh et al., 2001) and absolute values in ppm, as well as chondrite-normalized trace element values, are reported (Taylor and McLennan, 1985).

LA-ICP-MS U-Pb geochronology

Mineral separates were extracted from 2-5kg rock samples using a panning table, a Frantz isodynamic separator and heavy liquids at the Dept of Earth Sciences Stellenbosch University. Zircon and monazite concentrates were subsequently handpicked, mounted in epoxy, and polished to half their thickness. Transmitted and reflected light microphotography, and SEM (scanning electron microscope; LEO 1450VP) cathodoluminescence (CL; zircon) and back-scattered electron (BSE; monazite) imaging were used to investigate internal structures. Zircon and monazite U–Pb dating was performed using the Stellenbosch University LA-ICP-MS (see above). A small volume sample cell was employed (Horstwood et al., 2003). Integration times for U/Pb age determinations were 15 ms for ^{206}Pb, 40 ms for ^{207}Pb, and 10 ms for ^{29}Si (zircon only), ^{140}Ce (monazite only), ^{208}Pb, ^{204}Pb, ^{232}Th and ^{238}U. The respective isotopic ratios were displayed in time-resolved mode. The first 5-10s of each analysis was discarded, and from the remainder of each analysis the integration window was chosen so as to maximize its concordance (Jackson et al., 2004). The data were not corrected for common Pb because of an interference of ^{204}Hg on ^{204}Pb. Instead, ^{204}Pb was measured so as to exclude analyses with abnormal concentrations of common Pb. Initial data reduction was performed by the Glitter software package (Van Achterbergh et al., 2001) to calculate the relevant isotopic ratios (^{207}Pb/^{206}Pb, ^{208}Pb/^{206}Pb, ^{208}Pb/^{232}Th, ^{206}Pb/^{238}U and ^{207}Pb/^{235}U). ^{235}U was calculated from ^{238}U counts via the natural abundance ratio ^{235}U = ^{238}U/137.88 (Jackson et al., 2004). Errors propagated by the software assume a 1% uncertainty on the age of the standard. The U-Pb data were plotted on Concordia diagrams via the software Isoplot (Ludwig, 2000). For

detailed information on the long-term reproducibility of U/Pb ages of zircon secondary standards using the Stellenbosch LA-ICP-MS, the reader is referred to Lana et al. (2011).

Zircon analyses were performed using a 30µm diameter spot size at a fluence of ~10 J/cm^2 and a repetition rate of 10Hz. Instrumental drift was corrected against the primary zircon standard GJ-1 (weighted mean $^{207}Pb/^{206}Pb$ age = 609 ± 0.4 Ma, Jackson et al., 2004) using linear interpolative fits. Ablation depth-dependent elemental fractionation was corrected for by tying the integration window for the unknown zircon to the identical integration window of the standard (Jackson et al., 2004). Calibrations were based on 8 analyses of unknowns bracketed between 2 analyses of the primary standard (GJ-1), 2 analyses of a secondary standard (Plesoviče, weighted mean TIMS $^{206}Pb/^{238}U$ age = 337 ± 0.37 Ma, Sláma et al., 2008), and a trace element standard NIST-612 glass (Pearce et al., 1997). Uncertainties reported for individual analyses (ratios and ages) are at the 1σ level (Supplementary Table A1). Calculated weighted mean, upper intercept, or Concordia ages are reported at the 95% confidence level (Table 3, Fig. 8 & 9). Samples and standards were analyzed over multiple analytical sessions. Over the duration of this study the weighted mean $^{207}Pb/^{206}Pb$ normalization age for the GJ-1 primary standard varied between 608 ± 11 Ma [*n* = 25, 95% c.l., MSWD = 0.27] and 609 ± 9 Ma [*n* = 12, 95% c.l., MSWD = 0.41], while the weighted mean $^{206}Pb/^{238}U$ age of the secondary standard Plesoviče zircon varied between 337.6 ± 1.8 Ma [*n* = 18, 95% c.l., MSWD = 0.46] and 346.2 ± 2.5 Ma [*n* = 7, 95% c.l., MSWD = 0.54] (Supplementary Table B1).

Monazite analyses were performed using a 20µm diameter spot size at a fluence of ~ 2.5-3.9 J/cm^2 and a repetition rate of 4Hz. Instrumental drift was corrected against the primary Thompson Mine monazite standard (ID-TIMS weighted mean $^{207}Pb/^{206}Pb$ age = 1766 Ma , Williams et al., 1996) using linear interpolative fits. Ablation depth-dependent elemental fractionation was corrected, as for zircon (Jackson et al., 2004). Calibrations were based on 8-10 analyses of unknowns bracketed between 2 analyses of the primary Thompson Mine monazite standard, one to two secondary monazite standards (RGL4B, SHRIMP weighted mean $^{207}Pb/^{206}Pb$ age = 1562 ± 4 Ma, Rubatto et al., 2001; monazite 44069, ID-TIMS weighted mean $^{206}Pb/^{238}U$ age = 425 ± 0.4 Ma, Aleinikoff et al., 2006), as well as a trace element standard NIST-612 glass (Pearce et al., 1997). Uncertainties reported for individual analyses (ratios and ages) are at the 1σ level (Supplementary Table A2). Calculated weighted mean ages are reported at the 95% confidence level (Table 3, Fig. 8 & 9). Samples and standards were analyzed over multiple analytical sessions. Over the duration of this

study the weighted mean $^{207}Pb/^{206}Pb$ normalization age for the Thompson Mine primary standard varied between 1758 ± 8 Ma [*n* = 19, 95% c.l., MSWD = 0.42] and 1767 ± 9 Ma [*n* = 18, 95% c.l., MSWD = 0.13]; and the weighted mean $^{207}Pb/^{206}Pb$ age of the secondary monazite standard RGL4B varied between 1532 ± 24 Ma [*n* = 7, 95% c.l., MSWD = 1.2] and 1568 ± 17 Ma [*n* = 7, 95% c.l., MSWD = 0.17] (Supplementary Table B2).

Monazite geochronology via LA-ICP-MS or ionprobe may potentially be subject to matrix effects related to its highly variable REE (and hence Th) content, and potentially additionally due to grain orientation (Stern and Berman, 2000**;** Kohn, 2009**;** Fletcher et al., 2010). Matrix effects related to composition and grain orientation for LA-ICP-MS geochronology appear to be greater for the Th/Pb than the U/Pb system (Kohn, 2009) and, in the latter case, should affect $^{207}Pb/^{235}U$ and $^{206}Pb/^{238}U$ ages but not $^{207}Pb/^{206}Pb$ ages. In this study we used the 1766 Ma Thompson Mine monazite (Williams et al., 1996) as the primary age standard. However, its Th content is highly variable (Th = 7-19 wt%; e.g. Buick et al., 2011), and in general significantly higher than that of monazite from the samples in this study (e.g. for the Luboya and Kubuta migmatites, monazite Th content varied between 1.0-8.3 wt%). In order to test for the significance of matrix-related effects, in each analytical session we analyzed a secondary standard of variable but more comparable Th content to the unknowns, RGL4B (SHRIMP $^{207}Pb/^{206}Pb$ age = 1562 ± 4 Ma, Rubatto et al., 2001). The weighted mean $^{207}Pb/^{206}Pb$ age of RGL4B in the LA-ICP-MS sessions was always within error of its SHRIMP age (Supplementary Table B2). In addition, we analyzed the much lower Th USGS monazite standard 44609 (1.3-5.0 wt%; Aleinikoff et al., 2006; Buick et al., 2011), in addition to Thompson Mine monazite and RGL4B for a couple of the samples. In these cases we calculated the age of the monazite first using Thompson Mine and then USGS monazite 44609 as the primary age standard. Use of the Palaeozoic USGS monazite standard 44609 resulted in calculation of weighted mean $^{207}Pb/^{206}Pb$ ages of the unknowns that were identical within error to those calculated via Thompson Mine monazite as the standard (Supplementary Table B3). The weighted mean $^{207}Pb/^{206}Pb$ age of Thompson Mine calculated using the USGS monazite as the standard was within error of its accepted age; however the data were slightly reversely discordant. Since the preferred age determinations for Mesoproterozoic and older monazite depend primarily on weighted mean $^{207}Pb/^{206}Pb$ ages the use of variable but high-Th Thompson Mine as the primary age standard had no discernable effect on the calculated weighted mean $^{207}Pb/^{206}Pb$ ages for lower-Th monazite from the study area.

2. Detailed zircon and monazite U-Pb age interpretation

Luboya and Kubuta metasediments

Sample Kub23

Zircon - This metagreywacke yielded 50-400µm, subrounded to oval shaped zircons. The grains display complex internal zoning, as indicated via cathodoluminescence (CL) imaging. CL-bright, euhedral, oscillatory zoned cores are enveloped and truncated by two distinct rim generations; an inner structureless domain of intermediate CL response around the cores and an outer, more uniform, CL-dark-grey overgrowth (Fig. 7a,b). Twenty-four spot analyses of the cores show that they have variable, moderate to high Th/U (Th/U = 1.14-0.29) (Table A1). All twenty-four analyses have $^{207}Pb/^{206}Pb$ equal within analytical error, are 100-95% concordant and yield a weighted mean $^{207}Pb/^{206}Pb$ age of 3514 ± 12 Ma [95 % c.l., MSWD = 0.14] (Table A1, Fig. 8a). In contrast, ten spot analyses of the inner, and twelve spot analyses of the outer overgrowths (Fig. 7a,b) show that both rims are characterized by low Th/U ratios (inner rim Th/U = 0.13-0.01; outer rim Th/U = 0.07-0.01) (Table A1). All ten analyses of the inner overgrowths with a brighter CL response have $^{207}Pb/^{206}Pb$ equal within analytical error, are 100-96% concordant and yield a weighted mean $^{207}Pb/^{206}Pb$ age of 3222 ± 19 Ma [95% c.l., MSWD = 0.05] (Table A1, Fig. 8a). The twelve analyses of the outer rims are more variably concordant (100-83%). However, all have $^{207}Pb/^{206}Pb$ within analytical error, and yield a weighted mean $^{207}Pb/^{206}Pb$ age of 3098 ± 18 Ma [95% c.l., MSWD = 0.06]. The relationship between the CL zoning in the zircons and the Th/U ratios of the various CL domains lead us to interpret the cores to be of magmatic, detrital origin and both rim generations to be of metamorphic origin (e.g. Corfu et al., 2003; Williams and Claesson, 1987).

Monazite – Kub23 yielded 80-200µm, amoeboid shaped, subrounded to slightly elongate monazite grains. Back-scattered electron (BSE) imaging shows that they are either internally unzoned, or display patchy zonation patterns where darker BSE domains typically occur around the edges of the grains, and lighter domains are concentrated in the centre of the grains (Fig. 7f). Spot analyses of both unzoned and zoned grains define three distinct, concordant- to near-concordant age populations (Table A2; Fig. 8b). Nineteen analyses of unzoned monazite and brighter BSE domains in the center of the grains have highly variable Th/U (21.7-2.8). However, all have $^{207}Pb/^{206}Pb$ equal within analytical error, are 100-98% concordant and yield a weighted mean $^{207}Pb/^{206}Pb$ age of 3228.6 ± 7.5 Ma [95% c.l., MSWD = 0.24]. Ten analyses of unzoned grains or irregular, BSE-bright domains in the grains have Th/U = 16.4-8.2, have $^{207}Pb/^{206}Pb$ equal within analytical error,

are 100-96% concordant and yield a weighted mean $^{207}Pb/^{206}Pb$ age of 3160 ± 11 Ma [95% c.l., MSWD = 0.12]. Fifteen analyses of unzoned grains or darker BSE domains along the edges of the grains have Th/U = 17.9-11.7, $^{207}Pb/^{206}Pb$ equal within analytical error, are 103-95% concordant and yield a weighted mean $^{207}Pb/^{206}Pb$ age of 3080 ± 8.9 Ma [95% c.l., MSWD = 0.92]. The inferred $^{207}Pb/^{206}Pb$ age of the oldest and youngest monazite age populations from this sample are therefore identical within error to corresponding metamorphic zircon rim ages from the same sample. In addition to dating monazite grain separates, we dated *in situ* monazite inclusions in garnet using polished rock chips mounted in epoxy, so as to provide better constraints on the age of garnet growth in these samples. Six out of eight spot analyses of *in situ* monazite inclusions have $^{207}Pb/^{206}Pb$ equal within analytical error, are 100-96% concordant and yield a weighted mean $^{207}Pb/^{206}Pb$ age of 3216 ± 19 Ma [95% c.l., MSWD = 0.52] (Table A2). The remaining two analyses obtained from a single grain inclusion are 100% concordant and give $^{207}Pb/^{206}Pb$ spot ages of 3083 ± 25 Ma and 3072 ± 22 Ma (Table A2). Therefore, the ages of *in situ* monazite inclusions in garnet are identical within error to the oldest and youngest monazite ages obtained from dating grain separates from this sample. There was no systematic correlation between the position of the monazite inclusion in the garnet and its age.

Sample Kub17

Zircon – This metapelite contains 50-400µm, prismatic, subhedral to subrounded zircon grains with weakly developed apical terminations. CL imaging reveals that the zircons are complexly zoned, with CL-light-grey to -dark, euhedral, oscillatory zoned cores truncated by bright, structureless overgrowths around the cores (Fig. 7c & d). Twenty-seven spot analyses of the oscillatory-zoned cores have variable Th/U (0.80-0.26) (Table A1). All have the same $^{207}Pb/^{206}Pb$ within analytical uncertainty, are 101-95% concordant and yield a weighted mean $^{207}Pb/^{206}Pb$ age of 3320.2 ± 7.3 Ma [95% c.l., MSWD = 0.61] (Table A1). A subset of the fourteen most concordant analyses produce a Concordia age of 3332.9 ± 7.6 Ma [95% c.l., MSWD = 1.00] (Fig. 8c). Thirty-three analyses of the structureless rim overgrowths on the cores were obtained. Of these, fourteen analyses have $^{207}Pb/^{206}Pb$ equal within analytical error, are 99-88% concordant and were combined to form a population. The remaining nineteen analyses gave apparent $^{207}Pb/^{206}Pb$ spot ages ranging between 3150 ± 47 Ma and 2878 ± 29 Ma; however they are highly discordant and it is not apparent whether they lie on a Discordia segment related to the other analyses, hence they were not included in the age calculations. The fourteen 99-88% concordant analyses of the rims have Th/U = 0.03-0.00, and yield a weighted mean $^{207}Pb/^{206}Pb$ age of 3092 ± 12 Ma [95% c.l., MSWD = 0.64] (Table

A1; Fig. 8c). Based on the CL zoning and Th/U content of the core and rim domains, we interpret the cores to be magmatic in origin and hence detrital, and the rims to be of metamorphic origin.

Monazite – Kub17 contains abundant 80-200µm, rounded, oval to subhedral, elongate grains of monazite. They are characterized by weak, patchy zonation in BSE (Fig. 7g). This typically involves a brighter core domain truncated by darker domains along the edges of the grains, but locally this relationship is reversed. As in the metagreywacke sample Kub23, spot analyses of the various BSE domains define three distinct, concordant age populations (Table A2, Fig. 8d). The relationship between the BSE domains and $^{207}Pb/^{206}Pb$ age is not consistent, however there appears to be a general tendency for the BSE bright core domains to be older than the BSE intermediate to darker rims. Twenty-nine analyses from predominantly brighter core domains all have $^{207}Pb/^{206}Pb$ equal within analytical error, are 100-99% concordant, have Th/U = 28.6-17.1 and yield a weighted mean $^{207}Pb/^{206}Pb$ age of 3213.8 ± 6.0 Ma [95% c.l., MSWD = 0.24]. This appears to be the dominant monazite age population from this sample. Five analyses of intermediate to darker monazite domains all have $^{207}Pb/^{206}Pb$ equal within analytical error, are 100-99% concordant, have Th/U = 28.0-15.6 and yield a weighted mean $^{207}Pb/^{206}Pb$ age of 3161 ± 15 Ma [95% c.l., MSWD = 0.05]. Five analyses of darker domains concentrated along the edges of the grains all have $^{207}Pb/^{206}Pb$ equal within analytical error, are concordant, have a narrow range of Th/U (23.1-19.3) and yield a weighted mean $^{207}Pb/^{206}Pb$ age of 3087 ± 15 Ma [MSWD = 0.46]. The inferred $^{207}Pb/^{206}Pb$ age of the oldest and youngest monazite age populations are therefore identical within error to corresponding metamorphic zircon rim ages from this sample, as well as sample Kub23. In addition, the three monazite age populations from this sample are identical within error to the three monazite age populations from Kub23.

Sample Kub8

Monazite – This metagreywacke contains 40-180µm, rounded, oval to teardrop-shaped monazite grains. In BSE images the grains are largely unzoned, with rare brighter, patchy domains in their cores (Fig. 7h). Twenty-two analyses of unzoned monazite have a wide range of Th/U (49.3-5.4), are 101-99% concordant, and have the same $^{207}Pb/^{206}Pb$ within analytical error. They are therefore interpreted to form a single age population, with a weighted mean $^{207}Pb/^{206}Pb$ age of 3091.3 ± 7.1 Ma [95% c.l., MSWD = 0.87] (Table A2; Fig. 8e). The age of this population is equal within error to the youngest monazite from samples Kub23 and Kub17. One additional grain analyzed gave a concordant $^{207}Pb/^{206}Pb$ spot age of 3332 ± 17 Ma, and one bright core domain in another grain gave a concordant $^{207}Pb/^{206}Pb$ spot age of 3223 ± 19 Ma. As in sample Kub23, we dated *in situ* monazite

inclusions in garnet in order to constrain the age of garnet growth in this sample. Seven spot analyses of monazite, included in the poikiloblastic core domains of the garnet and up to 100µm from the rim, all have $^{207}Pb/^{206}Pb$ equal within analytical error, are 101-97% concordant and yield a weighted mean $^{207}Pb/^{206}Pb$ age of 3110 ± 21 Ma [95% c.l., MSWD = 0.42] (Table A2, Fig. 7m). This age is identical within error to the age of the dominant monazite population obtained from grain separates from this sample, and indicates that the garnet grew at, or after ca. 3.10 Ga.

Sample Lu17

Zircon – This Grt-bearing metapsammite contains 50-300µm, subhedral prismatic or oval/rounded zircon grains. Two varieties of zircon can be distinguished based on morphology and CL zoning in the grains. Larger, prismatic zircons contain euhedral cores with moderate to weak CL response, with occasional, faint oscillatory zoning. Cores in these large grains are typically surrounded by euhedral to subhedral, faintly oscillatory-zoned to structureless rims (Fig. 7e). Smaller, well-rounded, structureless zircon grains are also present. Three spot analyses of euhedral, uniformly grey cores in three large grains have $^{207}Pb/^{206}Pb$ equal within analytical error, Th/U = 0.37-0.33, are 96-94% concordant and yield a weighted mean $^{207}Pb/^{206}Pb$ age of 3503 ± 31 Ma [95% c.l., MSWD = 0.0013] (Table A1; Fig. 9a). Ten spot analyses targeting a combination of CL-dark, euhedral zircon cores, euhedral- to subhedral oscillatory-zoned rims around these cores, or patchy domains in small structureless grains have same $^{207}Pb/^{206}Pb$ within analytical uncertainty, low Th/U (0.01-0.07), and are 101-95% concordant. They yield a weighted mean $^{207}Pb/^{206}Pb$ age of 3225 ± 16 Ma [95% c.l., MSWD = 0.07] (Table A1; Fig. 9a). Nine analyses targeting a combination of rims on larger grains with ca. 3.50 Ga or 3.22 Ga cores, as well as domains in small structureless grains have $^{207}Pb/^{206}Pb$ equal within analytical error, low Th/U (0.02-0.04), are 100-83% concordant and yield a weighted mean $^{207}Pb/^{206}Pb$ age of 3108 ± 16 Ma [95% c.l., MSWD = 0.04] (Table A1, Fig. 9a). Based on CL zoning and Th/U ratios we interpret the rare ca. 3.5 Ga cores in larger prismatic grains to be magmatic, and hence detrital in origin. The ca. 3.22 Ga zircon cores, ca. 3.22 Ga and ca. 3.10 Ga rims on the larger grains as well as smaller, structureless grains are interpreted to be metamorphic in origin. Both $^{207}Pb/^{206}Pb$ ages obtained for the metamorphic zircon domains/grains are therefore identical within error to corresponding metamorphic zircon rim ages, and the oldest and youngest monazite age populations from metasediments Kub23, Kub17 and Kub8.

APPENDIX 1

Sample Lu6

Monazite –The metapelite sample Lu6 contains abundant, 100-400µm monazite with a variety of grain shapes that vary from elongate, subhedral/blocky, to subrounded/oval in shape. BSE imaging shows that the zoning in monazite from this sample is extremely complex, with as many as four distinct, irregular and patchy BSE domains observed (Fig. 7i). Fifty spot analyses of the various monazite domains define five concordant age populations (Table A2, Fig. 9b). In general, the older domains in composite grains are BSE dark and tend to occur in grain cores. The BSE brighter domains are younger and typically occur in the rims. Throughout the analytical session where monazite grain separates from sample Lu6 were dated, the trace element standard NIST-612 glass was not analyzed, therefore the Th/U ratios of the individual spot analyses presented in Table A2 are not available. Subsequent trace element work on the same monazites targeting the same age domains in the grains has however allowed the Th/U ratios of the various age populations to be determined (Table 3). Three analyses from older grain domains have $^{207}Pb/^{206}Pb$ equal within analytical error, Th/U = 35.4-7.4, are 100% concordant and yield a weighted mean $^{207}Pb/^{206}Pb$ age of 3436 ± 19 Ma [95% c.l., MSWD = 0.04]. One analysis has Th/U = 36.8 and gives a concordant $^{207}Pb/^{206}Pb$ spot age of 3395 ± 17 Ma. Three analyses have the same $^{207}Pb/^{206}Pb$ within analytical uncertainty, Th/U = 18.5-14.7, are 100-99% concordant and yield a weighted mean $^{207}Pb/^{206}Pb$ age of 3356 ± 20 Ma [95% c.l., MSWD = 0.16]. However, the majority of the U-Pb data from this sample define three younger monazite age populations. One population, comprised of eleven 101-99% concordant analyses, has Th/U = 54.1-16.0 and yields a weighted mean $^{207}Pb/^{206}Pb$ age of 3234 ± 10 Ma [95% c.l., MSWD = 0.35]. A population comprised of fourteen 100-99% concordant analyses has Th/U = 31.8-17.6, and yielded a weighted mean $^{207}Pb/^{206}Pb$ age of 3101.9 ± 9.2 Ma [95% c.l., MSWD = 0.24]. The youngest monazite age population obtained from analysing the brightest rim domains on some of the monazite grains consists of eighteen 100-99% concordant analyses with Th/U = 31.5-17.7, and yields a weighted mean $^{207}Pb/^{206}Pb$ age of 2993.8 ± 8.5 Ma [95% c.l., MSWD = 0.39]. As in samples Kub23 and Kub8, we performed *in situ* dating of monazite included in peritectic garnet, in order to constrain the maximum age of garnet growth in this sample. Five out of twelve spot analyses of *in situ* monazite inclusions in garnet can be grouped to form a 100-98% concordant population with a weighted mean $^{207}Pb/^{206}Pb$ age of 3440 ± 28 Ma [95% c.l., MSWD = 0.33] (Table A2). Three out of twelve spot analyses can be grouped to form a 100-99% concordant population with a weighted mean $^{207}Pb/^{206}Pb$ age of 3402 ± 42 Ma [95% c.l., MSWD = 0.007] (Table A2). The latter two ages are identical within error to the oldest monazite ages obtained from dating grain separates from this sample. These older monazite inclusions are

situated ~1000µm from the garnet margin, in the core domain, and also occur as older domains in younger monazite inclusions situated ~250µm inboard from the garnet margin, in the inclusion-rim of the garnet. One out of twelve spot analyses from a younger domain in a ca. 3.40 Ga aged monazite gave a concordant $^{207}Pb/^{206}Pb$ spot age of 3231 ± 28 Ma. Three out of twelve spot analyses can be grouped to form a 100% concordant population with a weighted mean $^{207}Pb/^{206}Pb$ age of 3072 ± 33 Ma [95% c.l., MSWD = 0.16] (Table A2), identical within error to the ca. 3.10 Ga monazite age obtained from dating grain separates from this sample. The youngest monazites occur in the 100-400µm wide inclusion-rich, peritectic rims of the garnet porphyroblasts. In one particular example a 375µm long monazite was found included in the rim domain of a peritectic garnet, ~250µm from the garnet edge (Fig. 7n & o). The monazite, together with micro-inclusions of zircon and ilmenite, define an internal foliation in the garnet. Dating of a lighter domain in this monazite gave a concordant analysis with a $^{207}Pb/^{206}Pb$ spot age of 3402 ± 28 Ma, while a darker domain gave a concordant analysis with a $^{207}Pb/^{206}Pb$ spot age of 3078 ± 23 Ma (these two spot analyses were included in the calculated weighted mean $^{207}Pb/^{206}Pb$ ca. 3.40 Ga and ca. 3.07 Ga ages described for the *in situ* inclusions above).

Luboya and Kubuta anatectic leucosomes

Sample Kub14

Monazite – This Grt-bearing leucosome contains very few monazite grains. These are 80-100µm in size, euhedral to crescent shaped, and are unzoned in BSE images (Fig. 7j). Fourteen spot analyses were performed on 8 grains. Thirteen out of the fourteen analyses have $^{207}Pb/^{206}Pb$ equal within analytical uncertainty, Th/U = 21.6-12.0, are 101-98% concordant and yield a weighted mean $^{207}Pb/^{206}Pb$ age of 3082.5 ± 8.8 Ma [96% c.l., MSWD = 0.24] (Table A2; Fig. 8f). The remaining analysis has a concordant $^{207}Pb/^{206}Pb$ spot age of 3212 ± 16 Ma (Th/U = 14). Thus we interpret the weighted mean $^{207}Pb/^{206}Pb$ age of 3082.5 ± 8.8 Ma to be the best estimate of the crystallization age of the leucosome. This estimate is identical within error to the age of the youngest monazite populations dated in host gneisses from this area i.e. samples Kub23, Kub17 and Kub8.

Sample Lu9

Monazite – This Grt-bearing leucosome contains abundant 80-100µm, subrounded, oval to amoeboid shaped monazite grains. They are largely unzoned in BSE images or show weak, irregular, patchy zonation (Fig. 7k & l). Thirty-three spot analyses of unzoned monazite or darker

APPENDIX 1

BSE domains in the cores of the grains have the same $^{207}Pb/^{206}Pb$ within analytical uncertainty. They show a wide range of Th/U (32.6-5.2), are 100-97% concordant and yield a weighted mean $^{207}Pb/^{206}Pb$ age of 3188.9 ± 6.2 Ma [95% c.l., MSWD = 0.23] (Table A2; Fig. 9c). Nineteen spot analyses of brighter domains typically concentrated in the rims of the grains define two younger age populations (Table A2; Fig. 9c). Thirteen out of the nineteen analyses are 100-98% concordant, have Th/U = 29.0-4.9 and yield a weighted mean $^{207}Pb/^{206}Pb$ age of 3114 ± 10 Ma [95% c.l., MSWD = 0.74]. The remaining six analyses are 100-99% concordant, have Th/U = 23.8-10.7 and yield a weighted mean $^{207}Pb/^{206}Pb$ age of 3058 ± 14 Ma [95% c.l., MSWD = 0.29]. Two analyses of brighter rim domains have Th/U = 28.9-16.2, are 95-93% concordant and have $^{207}Pb/^{206}Pb$ spot ages of 2997 ± 17 Ma and 2973 ± 24 Ma (Table A2).

Appendix 1 References

Aleinikoff, J. N., Schenk, W. S., Plank, M. O., Srogi, LA, Fanning, C. M., Kamo, S. L., and Bosbyshell, H., 2006, Deciphering igneous and metamorphic events in high-grade rocks of the Wilmington complex, Delaware: Morphology, cathodoluminescence and backscattered electron zoning, and SHRIMP U/Pb geochronology of zircon and monazite: Geological Society of America Bulletin, v. 118, p. 39-64.

Buick, I.S., Lana, C., and Gregory, C., 2011, A LA-ICP-MS and SHRIMP U/Pb age constraint on the timing of REE mineralization associated with Bushveld granites: South African Journal of Geology, *in press*

Corfu, F., Hanchar, J.M., Hoskin, P.W.O., and Kinny, P., 2003, Atlas of zircon textures, *in* Hanchar, J.M., and Hoskin, P.W.O., ed., Zircon, Mineralogical Society of America, v. 53, p. 468-500.

Diener, J.F.A, Stevens, G., Kisters, A.F.M., and Poujol, M., 2005, Geotectonic evolution of the Tjakastad Schist belt, Barberton greenstone belt, South Africa: a record of mid-Archaean metamorphism and terrain exhumation: Precambrian Research, v. 143, p. 87-112.

Fletcher, I.R., McNaughton, N.J., and Davis, W.J., 2010, Matrix effects and calibration limitations in ionprobe U-Pb and Th-Pb dating of monazite: Chemical Geology, v. 270, p. 31-44.

Horstwood, M. S. A., Foster, G. L., Parrish, R. R., Noble, S. R., and Nowell, G. M., 2003, Common-Pb corrected in situ U–Pb accessory mineral geochronology by LA-MC-ICP-MS: Journal of Analytical Atomic Spectrometry, v. 18, p. 837–846.

Jackson, S. E., Pearson, N.J., Griffin, W. L., and Belousova, E. A., 2004, The application of laser ablation-inductively coupled plasma-mass spectrometry to in situ U-Pb zircon geochronology: Chemical Geology, v. 211, p. 47–69.

Kohn, M. J., 2009, Chronologic microanalysis of monazite. V.M. Goldschmidt Conference in Geochemistry, Abstracts Volume, p. A675.

Ludwig, K.R., 2000, Isoplot/Ex: a Geochronological Toolkit for Microsoft Excel. Berkeley, California, *in* Berkeley Geochronology Center, Special Publication, v. 1a, p. 53.

Moyen, J.F., Stevens, G., and Kisters, A., 2006, Record of mid-Archaean subduction from metamorphism in the Barberton terrain, South Africa: Nature, v. 442, p. 559-562.

Pearce, N. J. G., Perkins, W. T., Westgate, J. A., Gorton, M. P., Jackson, S. E., Neal, C. R., and Chenery, S. P., 1997, A compilation of new and published major and trace element data for NIST SRM 610 and NIST SRM 612 glass reference materials: Geostandards Newsletter, v. 21, p. 115-144.

Rubatto, D., Williams, I.S., and Buick, I.S., 2001, Zircon and monazite response to prograde metamorphism in the Reynolds Range, central Australia: Contributions to Mineralogy and Petrology, v. 140, p. 458-468.

Sláma, J., Košler, J., Condon, D.J., Crowley, J.L., Gerdes, A., Hanchar, J.M., Horstwood, M.S. A., Morris, G.A., Nasdala, L., Norberg, N., Schaltegger, U., Schoene, B., Tubrett, M.N., and Whitehouse, M.J., 2008, Plešovice zircon—a new natural reference material for U–Pb and Hf isotopic microanalysis: Chemical Geology, v. 249, p. 1–35.

Stern, R. A., and Berman, R. G., 2000, Monazite U–Pb and Th–Pb geochronology by ion probe, with an application to in situ dating of an Archean metasedimentary rock: Chemical Geology, v. 172, p. 113–130.

Taylor, S.R., and McLennan, S.M., 1985, The continental crust: its composition and evolution. Blackwell, Oxford, p. 312.

Van Achterbergh, E., Ryan, C. G., Jackson, S. E., and Griffin, W., 2001, Data reduction software for LA-ICP-MS, *in* Sylvester, P., ed., Laser ablation-ICPMS in the Earth Science, Mineralogical Association of Canada, v. 29, p. 239-243.

Williams, I. S., Buick, I. S., and Cartwright, I., 1996, An extended episode of early Mesoproterozoic metamorphic fluid flow in the Reynolds Range, central Australia: Journal of Metamorphic Geology, v. 14, p. 29-48.

Williams, I.S., and Claesson, S., 1987, Isotopic evidence for the Precambrian provenance and Caledonian metamorphism of high grade paragneisses from the Seve Nappes, Scandinavian Caledonides: Contributions to Mineralogy and Petrology, v. 97, p. 205–217.

Table A1 Summary of LA-ICP-MS U-Pb zircon age data for metasediments Kub23, Kub17, and Lu17 from south-central Swaziland. Errors are 1-sigma. Data presented in this table are < 5% discordant. magm. = magmatic; met. = metamorphic; Disc. = discordance.

Sample/Spot	^{206}Pb (ppm)	U (ppm)	$^{232}Th/^{238}U$	$^{206}Pb/^{238}U$		$^{207}Pb/^{235}U$		$^{207}Pb/^{206}Pb$		%	$^{206}Pb/^{238}U$		$^{207}Pb/^{235}U$		$^{207}Pb/^{206}Pb$		Rho
				Age (Ma)	1σ	Age (Ma)	1σ	Age (Ma)	1σ	Disc.	ratio	1σ	ratio	1σ	ratio	1σ	
Kub23 magm. cores																	
KUB23-1	271	96	0.29	3520	33	3514	15	3510	23	0	0.72652	0.00870	30.84560	0.46221	0.30789	0.00459	0.80
KUB23-2	740	282	0.46	3515	39	3512	23	3511	36	0	0.72507	0.01036	30.77101	0.73073	0.30800	0.00729	0.60
KUB23-3	292	111	0.32	3512	36	3513	17	3514	25	0	0.72411	0.00954	30.82399	0.51709	0.30868	0.00511	0.79
KUB23-4	133	50	0.32	3512	43	3516	22	3519	34	0	0.72421	0.01145	30.89293	0.68695	0.30953	0.00698	0.71
KUB23-5	614	233	0.37	3509	36	3515	20	3518	31	0	0.72341	0.00962	30.86706	0.62257	0.30950	0.00626	0.66
KUB23-6	179	68	0.45	3495	38	3503	17	3509	27	0	0.71963	0.01024	30.50761	0.53807	0.30764	0.00535	0.81
Kub23 met. rim 1																	
KUB23-7	654	245	0.01	3220	31	3218	15	3217	24	0	0.64792	0.00796	22.77875	0.34550	0.25511	0.00397	0.81
KUB23-8	891	326	0.01	3226	34	3231	24	3235	39	0	0.64936	0.00876	23.10320	0.57212	0.25806	0.00654	0.54
KUB23-9	767	259	0.01	3220	30	3226	18	3230	31	0	0.64801	0.00759	22.98046	0.43051	0.25720	0.00505	0.63
KUB23-10	799	297	0.02	3220	31	3226	17	3231	28	0	0.64799	0.00784	22.97769	0.40578	0.25737	0.00467	0.69
KUB23-11	882	328	0.01	3213	31	3219	19	3223	31	0	0.64615	0.00800	22.81536	0.43317	0.25618	0.00505	0.65
KUB23-12	788	264	0.01	3206	30	3212	18	3216	29	0	0.64422	0.00761	22.64199	0.40833	0.25493	0.00475	0.66
Kub23 met. rim 2																	
KUB23-13	1018	453	0.05	3106	31	3100	17	3095	27	0	0.61905	0.00783	20.16974	0.35071	0.23632	0.00400	0.73
KUB23-14	807	331	0.02	3060	45	3083	36	3099	60	1	0.60752	0.01126	19.81737	0.73362	0.23689	0.00910	0.50
KUB23-15	939	408	0.03	3048	29	3080	16	3102	26	1	0.60457	0.00718	19.77551	0.32808	0.23729	0.00387	0.72
KUB23-16	980	440	0.02	3018	30	3069	18	3103	28	2	0.59697	0.00738	19.53401	0.35450	0.23741	0.00426	0.68
KUB23-17	1118	516	0.02	3006	35	3064	20	3103	33	2	0.59406	0.00861	19.44034	0.40811	0.23747	0.00501	0.69
KUB23-18	485	188	0.01	2936	42	3035	29	3102	49	3	0.57684	0.01024	18.86131	0.57440	0.23725	0.00736	0.58
Kub17 magm. cores																	
KUB17-1	333	126	0.28	3357	37	3338	16	3326	23	-1	0.68332	0.00963	25.77515	0.41621	0.27354	0.00405	0.87
KUB17-2	439	153	0.33	3348	31	3334	12	3325	17	0	0.68096	0.00808	25.66359	0.31606	0.27334	0.00303	0.96
KUB17-3	568	214	0.38	3343	34	3331	14	3324	20	0	0.67964	0.00888	25.59854	0.36470	0.27314	0.00343	0.92
KUB17-4	469	164	0.39	3350	31	3338	12	3332	17	0	0.68135	0.00810	25.78547	0.31929	0.27448	0.00306	0.96
KUB17-5	254	94	0.26	3347	34	3338	14	3333	19	0	0.68064	0.00891	25.77580	0.35748	0.27468	0.00339	0.94
KUB17-6	273	105	0.28	3336	37	3336	16	3336	22	0	0.67791	0.00952	25.71487	0.40712	0.27513	0.00395	0.89
Kub17 met. rim1																	
KUB17-7	711	320	0.01	3093	37	3099	20	3103	32	0	0.61583	0.00938	20.15967	0.41741	0.23751	0.00474	0.74
KUB17-8	1090	464	0.01	3051	32	3084	15	3105	21	1	0.60528	0.00800	19.84580	0.29938	0.23776	0.00320	0.88
KUB17-9	1122	499	0.01	2944	32	3034	15	3093	22	3	0.57886	0.00773	18.83631	0.29246	0.23599	0.00329	0.86
KUB17-10	1143	534	0.00	2859	30	2994	14	3087	20	5	0.55804	0.00726	18.08358	0.25943	0.23510	0.00303	0.91

Table A1 Continued.

Sample/Spot	^{206}Pb (ppm)	U (ppm)	$^{232}Th/^{238}U$	$^{206}Pb/^{238}U$ Age (Ma)	1σ	$^{207}Pb/^{235}U$ Age (Ma)	1σ	$^{207}Pb/^{206}Pb$ Age (Ma)	1σ	% Disc.	$^{206}Pb/^{238}U$ ratio	1σ	$^{207}Pb/^{235}U$ ratio	1σ	$^{207}Pb/^{206}Pb$ ratio	1σ	Rho
Lu17 magm. cores																	
LU17-1	284	109	0.33	3306	31	3430	14	3503	21	4	0.67004	0.00797	28.30416	0.39427	0.30641	0.00415	0.85
LU17-2	335	143	0.36	3273	40	3418	24	3503	37	4	0.66152	0.01039	27.95577	0.69062	0.30633	0.00749	0.64
Lu17 met. rim 1																	
LU17-3	1140	397	0.05	3315	31	3266	13	3236	20	-1	0.67234	0.00803	23.93437	0.31570	0.25827	0.00325	0.91
LU17-4	396	159	0.01	3227	35	3228	15	3229	22	0	0.64975	0.00905	23.02180	0.35695	0.25702	0.00358	0.90
LU17-5	963	636	0.07	3212	33	3217	17	3221	28	0	0.64582	0.00853	22.76728	0.39898	0.25582	0.00461	0.75
LU17-6	1072	415	0.05	3208	33	3217	15	3223	22	0	0.64479	0.00850	22.76540	0.35233	0.25618	0.00364	0.85
LU17-7	889	664	0.03	3189	32	3204	19	3214	29	0	0.64010	0.00813	22.46855	0.43432	0.25458	0.00473	0.66
LU17-8	384	166	0.02	3169	40	3201	20	3221	30	1	0.63502	0.01025	22.38852	0.45717	0.25581	0.00491	0.79
Lu17 met. rim 2																	
LU17-9	931	341	0.02	3105	30	3105	14	3105	23	0	0.61883	0.00758	20.28194	0.30055	0.23774	0.00341	0.83
LU17-10	938	338	0.04	3058	29	3086	14	3104	23	1	0.60703	0.00718	19.88409	0.28221	0.23756	0.00338	0.83
LU17-11	988	362	0.02	3030	36	3075	18	3104	30	1	0.59999	0.00883	19.65449	0.35585	0.23762	0.00444	0.81

Table A2 Summary of LA-ICP-MS U-Pb monazite age data for metasediments Kub23, Kub17, Kub8, and Lu6 and anatectic leucosomes Kub14 and Lu9 from south-central Swaziland. Errors are 1-sigma. Data presented are ≤ 5% discordant. Disc. = discordance. Incl. = inclusion. n.a. = not analysed.

Sample/Spot	^{206}Pb (ppm)	U (ppm)	^{232}Th/^{238}U	^{206}Pb/^{238}U		^{207}Pb/^{235}U		^{207}Pb/^{206}Pb		%	^{206}Pb/^{238}U		^{207}Pb/^{235}U		^{207}Pb/^{206}Pb		Rho
				Age (Ma)	1σ	Age (Ma)	1σ	Age (Ma)	1σ	Disc.	ratio	1σ	ratio	1σ	ratio	1σ	
Kub23																	
KUB23 -1	3993	1630	9.7	3213	35	3220	13	3225	16	0	0.64610	0.00895	22.83972	0.31482	0.25643	0.00259	1.00
KUB23 -2	3477	1425	10.7	3200	35	3207	14	3212	17	0	0.64278	0.00897	22.53890	0.31500	0.25439	0.00268	1.00
KUB23 -3	3084	1224	14.5	3207	36	3217	14	3223	18	0	0.64448	0.00912	22.75401	0.32626	0.25615	0.00287	0.99
KUB23 -4	2133	881	21.7	3204	36	3215	14	3222	18	0	0.64372	0.00920	22.70876	0.32704	0.25591	0.00285	0.99
KUB23 -5	3686	1483	12.5	3201	37	3215	14	3225	18	0	0.64312	0.00936	22.72272	0.33605	0.25636	0.00293	0.98
KUB23 -6	3230	1338	12.8	3203	35	3218	14	3228	16	0	0.64363	0.00897	22.79225	0.31669	0.25688	0.00264	1.00
Incl. in Grt	**7174**	**3390**	**5.1**	**3197**	**38**	**3196**	**17**	**3196**	**24**	**0**	**0.64190**	**0.00973**	**22.27485**	**0.37702**	**0.25174**	**0.00387**	0.90
Incl. in Grt	**7414**	**3416**	**3.4**	**3185**	**38**	**3196**	**16**	**3203**	**24**	**0**	**0.63898**	**0.00976**	**22.27684**	**0.37387**	**0.25287**	**0.00384**	0.91
Incl. in Grt	**3928**	**1878**	**9.6**	**3168**	**37**	**3192**	**16**	**3208**	**23**	**1**	**0.63473**	**0.00945**	**22.19536**	**0.36439**	**0.25362**	**0.00379**	0.91
Incl. in Grt	**4280**	**2101**	**9.4**	**3097**	**39**	**3172**	**18**	**3220**	**27**	**2**	**0.61687**	**0.00973**	**21.73049**	**0.39116**	**0.25563**	**0.00434**	0.88
Incl. in Grt	**4409**	**2165**	**10.3**	**3070**	**36**	**3167**	**16**	**3229**	**23**	**3**	**0.60989**	**0.00902**	**21.61823**	**0.34772**	**0.25712**	**0.00371**	0.92
Incl. in Grt	**4699**	**2335**	**8.3**	**3061**	**38**	**3171**	**17**	**3243**	**26**	**4**	**0.60765**	**0.00950**	**21.71568**	**0.38513**	**0.25937**	**0.00430**	0.88
KUB23 -7	2945	1197	13.2	3160	35	3159	14	3159	17	0	0.63272	0.00896	21.44633	0.30579	0.24591	0.00270	0.99
KUB23 -8	3734	1516	12.6	3151	35	3151	14	3151	18	0	0.63034	0.00885	21.25990	0.30289	0.24466	0.00274	0.99
KUB23 -9	3382	1336	15.5	3158	35	3161	14	3163	18	0	0.63223	0.00881	21.48165	0.30483	0.24651	0.00275	0.98
KUB23 -10	3723	1573	11.5	3113	35	3144	14	3165	17	1	0.62079	0.00870	21.12084	0.29778	0.24684	0.00265	0.99
KUB23 -11	3113	1353	14.8	3102	35	3137	14	3161	17	1	0.61798	0.00882	20.97218	0.29908	0.24619	0.00259	1.00
KUB23 -12	3346	1499	13.5	3094	36	3132	14	3157	17	1	0.61609	0.00893	20.86068	0.30345	0.24561	0.00264	1.00
KUB23 -13	3020	1298	16.7	3078	41	3067	17	3059	25	0	0.61200	0.01032	19.49565	0.34925	0.23097	0.00362	0.94
KUB23 -14	3056	1310	14.5	3071	34	3073	14	3074	17	0	0.61019	0.00848	19.61650	0.27319	0.23321	0.00246	1.00
KUB23 -15	3388	1501	12.1	3062	34	3064	13	3066	16	0	0.60807	0.00845	19.44856	0.26926	0.23202	0.00236	1.00
KUB23 -16	3026	1298	14.4	3068	34	3071	13	3074	17	0	0.60940	0.00843	19.59084	0.27156	0.23321	0.00244	1.00
KUB23 -17	3070	1368	12.9	3064	35	3072	14	3079	18	0	0.60837	0.00877	19.60557	0.28563	0.23387	0.00262	0.99
KUB23 -18	2520	1102	17.9	3062	35	3073	14	3081	17	0	0.60797	0.00861	19.62384	0.28011	0.23417	0.00257	0.99
Incl. in Grt	**5912**	**2980**	**6.3**	**3076**	**38**	**3080**	**17**	**3083**	**25**	**0**	**0.61143**	**0.00958**	**19.76782**	**0.34145**	**0.23443**	**0.00372**	0.91
Incl. in Grt	**6179**	**3112**	**5.5**	**3081**	**36**	**3076**	**15**	**3072**	**22**	**0**	**0.61274**	**0.00895**	**19.67863**	**0.31184**	**0.23287**	**0.00329**	0.92

Table A2 Continued.

Sample/Spot	^{206}Pb (ppm)	U (ppm)	$^{232}Th/^{238}U$	$^{206}Pb/^{238}U$		$^{207}Pb/^{235}U$		$^{207}Pb/^{206}Pb$		%	$^{206}Pb/^{238}U$		$^{207}Pb/^{235}U$		$^{207}Pb/^{206}Pb$		Rho
				Age (Ma)	1σ	Age (Ma)	1σ	Age (Ma)	1σ	Disc.	ratio	1σ	ratio	1σ	ratio	1σ	
Kub17																	
KUB17 -1	3328	1349	17.5	3207	36	3204	14	3203	17	0	0.64455	0.00926	22.46459	0.32514	0.25285	0.00273	0.99
KUB17 -2	3732	1515	20.4	3213	37	3210	15	3209	18	0	0.64613	0.00947	22.60983	0.33819	0.25385	0.00291	0.98
KUB17 -3	3544	1432	20.6	3207	36	3209	14	3211	16	0	0.64469	0.00914	22.58259	0.31719	0.25411	0.00258	1.01
KUB17 -4	3892	1557	17.7	3211	36	3214	14	3216	16	0	0.64554	0.00907	22.68669	0.31576	0.25494	0.00258	1.01
KUB17 -5	3640	1473	17.1	3204	36	3207	14	3210	16	0	0.64386	0.00914	22.54215	0.31995	0.25397	0.00264	1.00
KUB17 -6	3060	1236	28.6	3201	36	3206	14	3209	16	0	0.64294	0.00910	22.50357	0.31490	0.25391	0.00257	1.01
KUB17 -7	2921	1203	19.1	3156	36	3157	14	3158	18	0	0.63168	0.00916	21.39998	0.31492	0.24577	0.00276	0.99
KUB17 -8	3663	1493	15.6	3162	36	3164	14	3166	17	0	0.63307	0.00906	21.55392	0.31008	0.24699	0.00269	0.99
KUB17 -9	3453	1423	17.1	3156	36	3161	15	3165	18	0	0.63165	0.00919	21.49350	0.32069	0.24685	0.00285	0.98
KUB17 -10	3265	1336	20.3	3141	35	3151	14	3158	17	0	0.62776	0.00891	21.26797	0.30186	0.24578	0.00262	1.00
KUB17 -11	6427	2650	28.0	3127	36	3146	14	3159	18	1	0.62425	0.00900	21.16077	0.30807	0.24591	0.00277	0.99
KUB17 -12	3371	1423	23.1	3080	36	3088	15	3093	19	0	0.61253	0.00894	19.92409	0.29844	0.23598	0.00277	0.97
KUB17 -13	4987	2090	19.3	3075	35	3082	14	3087	17	0	0.61131	0.00862	19.81264	0.27957	0.23511	0.00249	1.00
KUB17 -14	2961	1249	20.4	3080	35	3082	14	3083	18	0	0.61252	0.00883	19.79921	0.28848	0.23452	0.00261	0.99
KUB17 -15	3617	1521	20.6	3089	36	3076	14	3068	18	0	0.61480	0.00897	19.68100	0.29099	0.23227	0.00266	0.99
KUB17 -16	3213	1368	19.7	3090	35	3095	14	3099	16	0	0.61492	0.00877	20.08112	0.28459	0.23690	0.00243	1.01
Kub8																	
KUB8 -1	2049	834	47.0	3336	38	3333	14	3332	17	0	0.67786	0.00975	25.65411	0.36954	0.27458	0.00296	1.00
KUB8 -2	5067	2143	33.8	3232	38	3226	15	3223	19	0	0.65090	0.00977	22.98342	0.35807	0.25616	0.00306	0.96
KUB8 -3	10608	4815	9.0	3099	37	3100	15	3101	18	0	0.61714	0.00928	20.17183	0.31182	0.23709	0.00273	0.97
KUB8 -4	15185	6756	5.4	3102	35	3101	14	3100	16	0	0.61807	0.00870	20.19663	0.28210	0.23707	0.00240	1.01
KUB8 -5	5872	2663	16.3	3070	35	3088	14	3100	17	1	0.60987	0.00870	19.92789	0.28505	0.23706	0.00250	1.00
KUB8 -6	8925	4104	9.5	3099	35	3099	14	3099	16	0	0.61718	0.00882	20.15356	0.28613	0.23689	0.00242	1.01
KUB8 -7	12447	5431	6.8	3113	36	3102	15	3095	18	0	0.62067	0.00905	20.21284	0.30437	0.23633	0.00270	0.97
KUB8 -8	5573	2499	16.2	3097	36	3095	14	3093	17	0	0.61683	0.00904	20.06639	0.29518	0.23600	0.00249	1.00
Incl. in Grt	**6813**	**3027**	**14.6**	**3082**	**59**	**3076**	**27**	**3073**	**45**	**0**	**0.61304**	**0.01472**	**19.67976**	**0.55482**	**0.23297**	**0.00669**	0.85
Incl. in Grt	**15480**	**7090**	**6.0**	**3081**	**37**	**3089**	**16**	**3095**	**24**	**0**	**0.61266**	**0.00920**	**19.94456**	**0.33866**	**0.23627**	**0.00359**	0.88
Incl. in Grt	**7514**	**3620**	**4.4**	**3028**	**39**	**3069**	**18**	**3096**	**28**	**1**	**0.59945**	**0.00958**	**19.54238**	**0.36498**	**0.23645**	**0.00416**	0.86
Incl. in Grt	**13547**	**5841**	**6.0**	**3053**	**76**	**3096**	**36**	**3125**	**60**	**1**	**0.60580**	**0.01892**	**20.09174**	**0.74435**	**0.24075**	**0.00932**	0.84
Incl. in Grt	**4871**	**2317**	**8.3**	**3021**	**41**	**3072**	**20**	**3106**	**31**	**2**	**0.59790**	**0.01023**	**19.60406**	**0.39724**	**0.23784**	**0.00469**	0.84
Incl. in Grt	**9308**	**4568**	**10.1**	**3000**	**37**	**3076**	**17**	**3126**	**25**	**3**	**0.59261**	**0.00904**	**19.67588**	**0.34146**	**0.24097**	**0.00384**	0.88

Table A2 Continued.

Sample/Spot	^{206}Pb (ppm)	U (ppm)	$^{232}Th/^{238}U$	$^{206}Pb/^{238}U$		$^{207}Pb/^{235}U$		$^{207}Pb/^{206}Pb$		%	$^{206}Pb/^{238}U$		$^{207}Pb/^{235}U$		$^{207}Pb/^{206}Pb$		Rho
				Age (Ma)	1σ	Age (Ma)	1σ	Age (Ma)	1σ	Disc.	ratio	1σ	ratio	1σ	ratio	1σ	
Kub14																	
KUB14 -1	11253	4448	14.7	3213	35	3213	14	3212	16	0	0.64622	0.00902	22.66031	0.31613	0.25440	0.00265	1.00
KUB14 -2	10066	4202	16.3	3132	36	3101	14	3081	17	-1	0.62559	0.00897	20.19914	0.28778	0.23426	0.00245	1.01
KUB14 -3	9897	4166	19.8	3129	35	3101	14	3084	16	-1	0.62481	0.00881	20.20820	0.28158	0.23461	0.00238	1.01
KUB14 -4	10604	4245	17.7	3128	35	3101	14	3084	16	-1	0.62445	0.00883	20.19504	0.28415	0.23462	0.00242	1.00
KUB14 -5	11786	4839	13.5	3118	35	3098	13	3085	16	-1	0.62197	0.00871	20.13762	0.27961	0.23484	0.00238	1.01
KUB14 -6	7663	3121	21.6	3115	34	3101	13	3093	16	0	0.62130	0.00863	20.20462	0.27734	0.23590	0.00237	1.01
KUB14 -7	11214	4563	13.0	3106	34	3095	13	3087	16	0	0.61903	0.00857	20.06492	0.27557	0.23515	0.00239	1.01
Lu9																	
LU9 -1	2868	1211	8.7	3160	36	3175	14	3185	18	0	0.63265	0.00905	21.81109	0.31875	0.25008	0.00289	0.98
LU9 -2	8574	3778	5.2	3170	38	3188	16	3200	21	1	0.63518	0.00965	22.09495	0.36031	0.25239	0.00336	0.93
LU9 -3	2565	1050	9.6	3156	37	3178	15	3192	20	1	0.63150	0.00926	21.86766	0.33650	0.25116	0.00324	0.95
LU9 -4	3586	1544	22.8	3131	37	3158	15	3176	20	1	0.62532	0.00922	21.43085	0.33112	0.24865	0.00315	0.95
LU9 -5	3879	1613	17.1	3139	36	3166	15	3184	19	1	0.62724	0.00905	21.60863	0.32374	0.24989	0.00307	0.96
LU9 -6	2081	848	16.6	3129	38	3158	15	3178	21	1	0.62475	0.00944	21.42786	0.33715	0.24890	0.00336	0.96
LU9 -7	3333	1438	17.3	3124	39	3130	16	3133	23	0	0.62363	0.00969	20.80492	0.34823	0.24201	0.00349	0.93
LU9 -8	1946	857	13.2	3111	42	3120	19	3126	28	0	0.62032	0.01051	20.60447	0.40323	0.24094	0.00435	0.87
LU9 -9	3239	1497	20.6	3052	36	3090	15	3114	19	1	0.60552	0.00897	19.96334	0.29927	0.23910	0.00284	0.99
LU9 -10	2017	907	29.0	3069	36	3094	14	3110	18	1	0.60980	0.00896	20.04966	0.29369	0.23855	0.00266	1.00
LU9 -11	3403	1525	14.4	3079	36	3096	14	3107	18	1	0.61233	0.00890	20.09500	0.29286	0.23798	0.00268	1.00
LU9 -12	3121	1356	17.1	3090	36	3097	14	3101	18	0	0.61506	0.00896	20.10796	0.29497	0.23714	0.00273	0.99
LU9 -13	4765	1994	20.3	3039	34	3059	14	3073	17	1	0.60223	0.00855	19.34075	0.27531	0.23298	0.00250	1.00
LU9 -14	6863	3080	10.7	3042	39	3058	17	3069	23	1	0.60298	0.00957	19.32298	0.33392	0.23243	0.00333	0.92
LU9 -15	4130	1827	23.8	3058	35	3058	14	3059	17	0	0.60690	0.00861	19.32843	0.27101	0.23100	0.00241	1.01
LU9 -16	3801	1750	22.2	3061	35	3057	14	3055	16	0	0.60782	0.00869	19.29897	0.26967	0.23039	0.00234	1.02
LU9 -17	3836	1684	23.2	3062	35	3057	14	3053	17	0	0.60798	0.00860	19.29290	0.26987	0.23017	0.00239	1.01
LU9 -18	3550	1616	22.7	3072	35	3057	14	3047	17	0	0.61036	0.00875	19.29940	0.27449	0.22932	0.00248	1.01
LU9 -20	2657	1437	16.2	2736	38	2873	17	2973	24	5	0.52878	0.00888	15.93479	0.28270	0.21895	0.00333	0.95

Table A2 Continued.

Sample/Spot	^{206}Pb (ppm)	U (ppm)	$^{232}Th/^{238}U$	$^{206}Pb/^{238}U$		$^{207}Pb/^{235}U$		$^{207}Pb/^{206}Pb$		%	$^{206}Pb/^{238}U$		$^{207}Pb/^{235}U$		$^{207}Pb/^{206}Pb$		Rho
				Age (Ma)	1σ	Age (Ma)	1σ	Age (Ma)	1σ	Disc.	ratio	1σ	ratio	1σ	ratio	1σ	
Lu6																	
LU6 -1	n.a	n.a	n.a	3438	24	3434	9	3432	19	0	0.70466	0.00641	28.41883	0.26983	0.29263	0.00362	0.96
LU6 -2	n.a	n.a	n.a	3435	19	3436	7	3437	16	0	0.70391	0.00509	28.48871	0.20609	0.29370	0.00308	1.00
LU6 -3	n.a	n.a	n.a	3433	18	3436	7	3438	16	0	0.70329	0.00483	28.49596	0.19804	0.29391	0.00299	0.99
Incl. in Grt	**492**	**189**	**93.6**	**3437**	**85**	**3430**	**34**	**3427**	**54**	**0**	**0.70440**	**0.02246**	**28.30665**	**0.98577**	**0.29171**	**0.01032**	0.92
Incl. in Grt	**3221**	**1177**	**28.4**	**3429**	**40**	**3436**	**16**	**3441**	**21**	**0**	**0.70214**	**0.01062**	**28.49237**	**0.45268**	**0.29441**	**0.00392**	0.95
Incl. in Grt	**551**	**203**	**91.6**	**3389**	**71**	**3404**	**29**	**3412**	**44**	**0**	**0.69168**	**0.01850**	**27.56913**	**0.80045**	**0.28900**	**0.00837**	0.92
Incl. in Grt	**2230**	**816**	**30.2**	**3349**	**53**	**3424**	**22**	**3467**	**32**	**2**	**0.68128**	**0.01382**	**28.15033**	**0.61735**	**0.29940**	**0.00619**	0.92
Incl. in Grt	**571**	**222**	**95.5**	**3294**	**63**	**3376**	**26**	**3426**	**40**	**2**	**0.66699**	**0.01630**	**26.79878**	**0.70927**	**0.29150**	**0.00767**	0.92
LU6 -4	n.a	n.a	n.a	3378	20	3388	8	3395	17	0	0.68874	0.00533	27.13668	0.21384	0.28588	0.00315	0.98
Incl. in Grt	**2226**	**815**	**31.5**	**3413**	**71**	**3408**	**30**	**3398**	**47**	**0**	**0.69805**	**0.01877**	**27.66969**	**0.83933**	**0.28633**	**0.00874**	0.89
Incl. in Grt	**512**	**187**	**87.9**	**3374**	**71**	**3394**	**29**	**3406**	**45**	**1**	**0.68778**	**0.01870**	**27.27931**	**0.80271**	**0.28775**	**0.00848**	0.92
Incl. in Grt	**642**	**232**	**107.0**	**3400**	**50**	**3401**	**19**	**3402**	**28**	**0**	**0.69442**	**0.01306**	**27.47865**	**0.54534**	**0.28713**	**0.00522**	0.95
LU6 -5	n.a	n.a	n.a	3357	18	3352	7	3350	16	0	0.68318	0.00469	26.14818	0.18068	0.27769	0.00282	0.99
LU6 -6	n.a	n.a	n.a	3326	23	3346	9	3358	19	1	0.67528	0.00609	25.99640	0.25041	0.27910	0.00342	0.94
LU6 -7	n.a	n.a	n.a	3323	23	3349	9	3364	19	1	0.67449	0.00589	26.06789	0.25148	0.28016	0.00342	0.91
LU6 -8	n.a	n.a	n.a	3248	19	3229	8	3218	17	-1	0.65498	0.00478	23.04609	0.17655	0.25530	0.00275	0.95
LU6 -9	n.a	n.a	n.a	3232	20	3225	8	3222	18	0	0.65096	0.00509	22.95712	0.18787	0.25592	0.00287	0.96
LU6 -10	n.a	n.a	n.a	3224	19	3225	8	3227	17	0	0.64904	0.00486	22.96233	0.17992	0.25671	0.00281	0.96
LU6 -11	n.a	n.a	n.a	3231	21	3236	9	3241	18	0	0.65070	0.00538	23.22359	0.20333	0.25899	0.00303	0.94
LU6 -12	n.a	n.a	n.a	3229	18	3236	7	3241	16	0	0.65028	0.00461	23.21352	0.16725	0.25903	0.00269	0.98
LU6 -13	n.a	n.a	n.a	3214	20	3221	8	3226	18	0	0.64639	0.00505	22.86635	0.18852	0.25663	0.00287	0.95
Incl. in Grt	**1724**	**681**	**43.6**	**3235**	**45**	**3232**	**19**	**3231**	**28**	**0**	**0.65166**	**0.01155**	**23.11090**	**0.45388**	**0.25736**	**0.00467**	0.90
LU6 -14	n.a	n.a	n.a	3092	21	3093	9	3093	19	0	0.61556	0.00523	20.02355	0.18383	0.23593	0.00282	0.93
LU6 -15	n.a	n.a	n.a	3095	22	3096	10	3098	20	0	0.61619	0.00553	20.10208	0.19750	0.23671	0.00303	0.91
LU6 -16	n.a	n.a	n.a	3092	17	3095	7	3097	17	0	0.61541	0.00433	20.06414	0.14900	0.23653	0.00253	0.95
LU6 -17	n.a	n.a	n.a	3091	21	3095	9	3097	19	0	0.61522	0.00525	20.06877	0.18507	0.23652	0.00281	0.93
LU6 -18	n.a	n.a	n.a	3081	18	3096	7	3106	17	0	0.61285	0.00446	20.10041	0.15185	0.23788	0.00251	0.96
LU6 -19	n.a	n.a	n.a	3083	18	3098	7	3109	17	1	0.61323	0.00441	20.14555	0.15176	0.23832	0.00255	0.95
Incl. in Grt	**2317**	**971**	**24.9**	**3072**	**38**	**3075**	**16**	**3078**	**23**	**0**	**0.61054**	**0.00944**	**19.67321**	**0.32459**	**0.23378**	**0.00333**	0.94
Incl. in Grt	**4251**	**1623**	**27.8**	**3075**	**45**	**3075**	**20**	**3073**	**30**	**0**	**0.61133**	**0.01115**	**19.66544**	**0.40565**	**0.23300**	**0.00444**	0.88
Incl. in Grt	**2820**	**1241**	**20.2**	**3056**	**57**	**3053**	**26**	**3051**	**43**	**0**	**0.60649**	**0.01415**	**19.22272**	**0.52237**	**0.22979**	**0.00624**	0.86

Table A2 Continued.

Sample/Spot	^{206}Pb (ppm)	U (ppm)	$^{232}Th/^{238}U$	$^{206}Pb/^{238}U$		$^{207}Pb/^{235}U$		$^{207}Pb/^{206}Pb$		% Disc.	$^{206}Pb/^{238}U$		$^{207}Pb/^{235}U$		$^{207}Pb/^{206}Pb$		Rho
				Age (Ma)	1σ	Age (Ma)	1σ	Age (Ma)	1σ		ratio	1σ	ratio	1σ	ratio	1σ	
LU6 -20	n.a	n.a	n.a	2976	21	2986	9	2993	20	0	0.58670	0.00509	17.92025	0.17143	0.22170	0.00275	0.91
LU6 -21	n.a	n.a	n.a	2982	17	2992	7	3001	17	0	0.58821	0.00420	18.04852	0.13274	0.22273	0.00236	0.97
LU6 -22	n.a	n.a	n.a	2982	16	2994	7	3003	16	0	0.58826	0.00394	18.07720	0.12138	0.22302	0.00226	1.00
LU6 -23	n.a	n.a	n.a	2960	18	2973	8	2982	18	0	0.58284	0.00450	17.68571	0.14330	0.22020	0.00245	0.95
LU6 -24	n.a	n.a	n.a	2975	16	2988	6	2998	16	0	0.58655	0.00385	17.97111	0.11884	0.22233	0.00226	0.99
LU6 -25	n.a	n.a	n.a	2973	17	2987	7	2998	17	0	0.58601	0.00407	17.95087	0.12583	0.22235	0.00229	0.99

Table B1 The performance of the secondary zircon standard Plesoviče, analyzed over multiple analytical sessions during the study.

Sample	$^{206}Pb/^{238}U$		$^{207}Pb/^{235}U$		$^{207}Pb/^{206}Pb$		$^{206}Pb/^{238}U$		$^{207}Pb/^{235}U$		$^{207}Pb/^{206}Pb$	
Kub17 (3 sessions)	***Age (Ma)***	***1σ***	***Age (Ma)***	***1σ***	***Age (Ma)***	***1σ***	***Ratio***	***1σ***	***Ratio***	***1σ***	***Ratio***	***1σ***
PLES-1	340.9	3.7	349.9	3.7	409	26	0.05431	0.00061	0.41139	0.00514	0.05493	0.00065
PLES-2	338.0	3.9	343.6	4.1	382	30	0.05383	0.00063	0.40271	0.00564	0.05426	0.00073
PLES-3	338.1	3.8	343.3	3.7	379	27	0.05385	0.00062	0.40234	0.00513	0.05419	0.00065
PLES-4	338.9	3.8	342.6	3.9	368	29	0.05397	0.00061	0.40134	0.00539	0.05393	0.00070
PLES-5	341.3	3.7	341.9	3.6	346	26	0.05437	0.00061	0.40038	0.00497	0.05340	0.00063
PLES-6	336.4	3.8	341.8	4.0	378	30	0.05357	0.00062	0.40016	0.00555	0.05418	0.00073
PLES-7	339.0	3.7	340.7	3.6	352	27	0.05400	0.00061	0.39870	0.00498	0.05355	0.00064
PLES-8	339.4	3.7	340.7	3.8	349	29	0.05406	0.00061	0.39868	0.00529	0.05349	0.00069
PLES-9	336.4	3.7	340.0	3.6	365	26	0.05356	0.00061	0.39770	0.00497	0.05385	0.00063
PLES-10	340.0	3.8	339.9	3.6	339	27	0.05416	0.00061	0.39759	0.00500	0.05324	0.00063
PLES-11	338.2	3.7	339.3	3.6	347	27	0.05386	0.00061	0.39677	0.00499	0.05342	0.00064
PLES-12	338.5	3.8	339.2	3.9	344	30	0.05391	0.00061	0.39660	0.00541	0.05335	0.00071
PLES-13	338.3	3.7	338.1	3.6	337	27	0.05389	0.00060	0.39515	0.00500	0.05318	0.00064
PLES-14	339.5	3.7	337.5	3.6	324	27	0.05407	0.00061	0.39435	0.00492	0.05289	0.00063
PLES-15	333.8	3.7	336.8	4.0	357	31	0.05315	0.00060	0.39335	0.00552	0.05368	0.00075
PLES-16	336.8	3.7	336.3	3.6	332	27	0.05364	0.00060	0.39259	0.00499	0.05308	0.00065
PLES-17	333.8	3.6	335.4	3.6	347	27	0.05314	0.00059	0.39146	0.00497	0.05342	0.00066
PLES-18	330.1	3.7	332.6	4.1	350	32	0.05255	0.00061	0.38762	0.00560	0.05350	0.00076
PLES-19	340.3	3.7	340.7	3.9	344	30	0.05421	0.00060	0.39875	0.00540	0.05335	0.00072
PLES-20	339.3	3.7	341.0	3.9	353	30	0.05404	0.00060	0.39913	0.00542	0.05357	0.00073
PLES-21	339.3	3.6	339.3	3.6	339	27	0.05404	0.00058	0.39675	0.00488	0.05325	0.00065
PLES-22	339.9	3.6	345.5	3.7	383	28	0.05414	0.00058	0.40532	0.00510	0.05430	0.00069
PLES-23	337.5	3.5	338.2	3.6	343	28	0.05374	0.00057	0.39526	0.00490	0.05334	0.00067
Kub23 (6 sessions)												
PLES-1	342.0	3.4	343.0	3.6	349	29	0.05449	0.00055	0.40187	0.00499	0.05349	0.00069
PLES-2	336.3	3.3	339.7	3.7	363	30	0.05356	0.00054	0.39729	0.00510	0.05380	0.00072
PLES-3	336.5	3.3	339.1	3.6	357	29	0.05359	0.00053	0.39651	0.00498	0.05366	0.00071
PLES-4	338.8	3.4	345.3	4.0	389	31	0.05396	0.00055	0.40507	0.00547	0.05444	0.00076
PLES-5	341.8	3.3	342.2	3.8	345	30	0.05446	0.00055	0.40075	0.00522	0.05337	0.00072
PLES-6	342.7	3.5	347.5	4.3	380	33	0.05460	0.00057	0.40812	0.00590	0.05422	0.00081
PLES-7	336.1	3.6	340.3	5.4	369	43	0.05353	0.00059	0.39819	0.00747	0.05396	0.00105
PLES-8	329.7	3.3	333.4	3.6	359	29	0.05248	0.00053	0.38865	0.00494	0.05372	0.00070
PLES-9	330.8	3.3	343.8	3.7	432	29	0.05265	0.00054	0.40295	0.00513	0.05551	0.00073

Table B1 Continued.

Sample	$^{206}Pb/^{238}U$		$^{207}Pb/^{235}U$		$^{207}Pb/^{206}Pb$		$^{206}Pb/^{238}U$		$^{207}Pb/^{235}U$		$^{207}Pb/^{206}Pb$	
Kub23 (continued)	*Age (Ma)*	*1σ*	*Age (Ma)*	*1σ*	*Age (Ma)*	*1σ*	*Ratio*	*1σ*	*Ratio*	*1σ*	*Ratio*	*1σ*
PLES-10	330.8	3.3	328.5	3.5	312	29	0.05266	0.00054	0.38193	0.00481	0.05260	0.00068
PLES-11	333.2	3.4	336.1	3.8	356	31	0.05304	0.00055	0.39234	0.00523	0.05365	0.00073
PLES-12	329.3	3.3	337.4	3.7	394	29	0.05241	0.00054	0.39418	0.00512	0.05455	0.00073
PLES-13	329.5	3.4	333.2	4.1	359	33	0.05244	0.00056	0.38834	0.00564	0.05372	0.00080
PLES-14	327.8	3.4	330.7	4.1	352	33	0.05216	0.00055	0.38503	0.00558	0.05354	0.00079
PLES-15	336.9	3.2	346.1	3.6	409	29	0.05365	0.00053	0.40618	0.00501	0.05491	0.00072
PLES-16	341.3	3.3	341.6	3.6	344	29	0.05437	0.00054	0.39992	0.00499	0.05336	0.00070
PLES-17	337.3	3.3	353.0	3.7	458	29	0.05371	0.00053	0.41572	0.00521	0.05614	0.00074
PLES-18	343.5	3.3	344.3	3.6	350	29	0.05473	0.00055	0.40369	0.00498	0.05350	0.00069
PLES-19	343.0	3.3	347.1	3.7	375	29	0.05464	0.00054	0.40754	0.00509	0.05409	0.00071
PLES-20	342.5	3.3	352.4	3.6	418	28	0.05457	0.00054	0.41486	0.00495	0.05513	0.00069
PLES-21	342.5	3.3	343.4	3.9	350	31	0.05456	0.00054	0.40239	0.00532	0.05349	0.00074
PLES-22	338.9	3.3	342.9	3.8	370	30	0.05398	0.00053	0.40174	0.00526	0.05398	0.00074
PLES-23	340.4	3.3	337.4	3.9	317	32	0.05423	0.00055	0.39422	0.00539	0.05272	0.00074
PLES-24	341.0	3.4	340.2	4.0	335	32	0.05431	0.00055	0.39805	0.00554	0.05315	0.00076
PLES-25	339.9	3.4	340.3	4.1	343	32	0.05415	0.00055	0.39816	0.00560	0.05333	0.00077
PLES-26	336.1	3.3	336.2	4.2	336	34	0.05352	0.00054	0.39245	0.00576	0.05318	0.00081
PLES-27	337.7	3.3	338.9	4.3	347	34	0.05378	0.00055	0.39618	0.00591	0.05343	0.00082
PLES-28	344.3	3.5	343.6	3.7	339	29	0.05486	0.00058	0.40265	0.00516	0.05323	0.00070
PLES-29	344.1	3.5	341.2	3.7	322	30	0.05482	0.00058	0.39943	0.00515	0.05285	0.00070
PLES-30	342.2	3.5	343.4	4.0	351	32	0.05452	0.00057	0.40243	0.00553	0.05353	0.00077
PLES-31	340.0	3.5	342.6	4.5	360	37	0.05416	0.00057	0.40127	0.00617	0.05374	0.00088
PLES-32	333.4	3.5	337.3	4.6	364	38	0.05308	0.00057	0.39407	0.00634	0.05384	0.00092
PLES-33	339.9	3.6	342.3	4.3	358	35	0.05415	0.00060	0.40091	0.00598	0.05369	0.00083
PLES-34	333.9	3.6	333.0	4.2	327	33	0.05317	0.00059	0.38816	0.00569	0.05295	0.00079
PLES-35	336.7	3.7	336.2	4.2	332	33	0.05362	0.00061	0.39248	0.00581	0.05308	0.00079
PLES-36	336.7	3.8	340.9	4.0	370	30	0.05362	0.00062	0.39902	0.00556	0.05397	0.00074
PLES-37	336.0	3.8	334.4	4.2	323	33	0.05351	0.00062	0.39006	0.00573	0.05287	0.00077
PLES-38	338.1	3.8	336.0	4.2	321	33	0.05385	0.00062	0.39218	0.00577	0.05282	0.00077
PLES-39	342.4	3.9	341.0	4.5	331	34	0.05455	0.00064	0.39905	0.00616	0.05306	0.00081
PLES-40	342.3	3.9	335.8	4.2	291	32	0.05454	0.00064	0.39198	0.00575	0.05213	0.00075
PLES-41	331.7	3.7	335.5	3.9	361	30	0.05281	0.00060	0.39150	0.00540	0.05377	0.00073
PLES-42	335.5	3.7	339.3	4.0	365	31	0.05342	0.00061	0.39675	0.00551	0.05386	0.00073

Table B1 Continued.

Sample	$^{206}Pb/^{238}U$		$^{207}Pb/^{235}U$		$^{207}Pb/^{206}Pb$		$^{206}Pb/^{238}U$		$^{207}Pb/^{235}U$		$^{207}Pb/^{206}Pb$	
Kub23 (continued)	***Age (Ma)***	***1σ***	***Age (Ma)***	***1σ***	***Age (Ma)***	***1σ***	***Ratio***	***1σ***	***Ratio***	***1σ***	***Ratio***	***1σ***
PLES-43	334.2	3.7	336.3	3.9	351	30	0.05321	0.00060	0.39270	0.00539	0.05352	0.00072
PLES-44	345.8	5.5	385.0	8.0	628	52	0.05511	0.00090	0.46112	0.01152	0.06068	0.00148
PLES-45	339.9	3.8	341.8	4.0	354	30	0.05415	0.00061	0.40022	0.00545	0.05361	0.00071
PLES-46	340.1	3.8	342.4	3.9	357	30	0.05418	0.00061	0.40099	0.00542	0.05368	0.00071
PLES-47	346.8	3.9	347.5	4.2	352	31	0.05528	0.00063	0.40808	0.00579	0.05354	0.00075
PLES-48	341.6	3.8	339.1	4.1	322	31	0.05442	0.00062	0.39644	0.00561	0.05284	0.00073
Lu17 (4 sessions)												
PLES-1	350.6	3.3	350.6	3.6	351	29	0.05589	0.00054	0.41236	0.00504	0.05352	0.00069
PLES-2	347.3	3.3	345.3	3.7	332	30	0.05536	0.00054	0.40504	0.00507	0.05307	0.00070
PLES-3	346.3	3.3	345.6	3.6	341	29	0.05518	0.00054	0.40548	0.00493	0.05330	0.00069
PLES-4	344.9	3.4	339.6	3.8	303	30	0.05496	0.00056	0.39712	0.00517	0.05241	0.00071
PLES-5	346.0	3.3	343.4	3.6	326	29	0.05514	0.00054	0.40248	0.00499	0.05294	0.00069
PLES-6	345.6	3.4	344.7	4.0	338	32	0.05508	0.00056	0.40415	0.00555	0.05322	0.00076
PLES-7	342.3	3.6	340.0	4.5	324	35	0.05453	0.00059	0.39766	0.00612	0.05289	0.00083
PLES-8	341.2	3.5	342.3	3.9	350	30	0.05435	0.00057	0.40085	0.00532	0.05349	0.00073
PLES-9	349.1	3.5	348.3	3.9	343	30	0.05565	0.00058	0.40915	0.00544	0.05333	0.00073
PLES-10	349.7	3.5	343.6	3.9	303	31	0.05574	0.00058	0.40269	0.00536	0.05240	0.00072
PLES-11	339.2	3.5	341.7	4.0	359	31	0.05402	0.00056	0.40007	0.00544	0.05371	0.00075
PLES-12	347.7	3.5	345.4	4.0	330	32	0.05541	0.00058	0.40513	0.00559	0.05303	0.00075
PLES-13	339.8	3.5	341.9	4.1	356	33	0.05412	0.00057	0.40029	0.00568	0.05365	0.00078
PLES-14	342.1	3.5	342.4	4.1	344	33	0.05450	0.00057	0.40101	0.00570	0.05337	0.00078
PLES-15	341.0	3.5	341.4	3.9	345	32	0.05432	0.00057	0.39972	0.00537	0.05338	0.00077
PLES-16	341.0	3.4	339.2	3.5	328	30	0.05432	0.00055	0.39669	0.00487	0.05298	0.00070
PLES-17	341.2	3.2	341.2	3.2	341	27	0.05436	0.00053	0.39935	0.00440	0.05329	0.00064
PLES-18	336.6	3.3	343.2	3.5	388	28	0.05361	0.00054	0.40210	0.00480	0.05440	0.00070
PLES-19	337.3	3.4	340.9	3.6	366	30	0.05372	0.00056	0.39900	0.00501	0.05387	0.00072
PLES-20	347.7	3.6	345.5	3.7	331	30	0.05542	0.00058	0.40533	0.00511	0.05305	0.00070
PLES-21	341.6	3.5	345.4	3.7	371	30	0.05442	0.00057	0.40512	0.00518	0.05399	0.00073
PLES-22	341.7	3.8	340.5	4.0	332	30	0.05444	0.00063	0.39846	0.00544	0.05309	0.00070
PLES-23	326.6	3.6	327.9	3.6	338	28	0.05197	0.00059	0.38121	0.00496	0.05321	0.00067
PLES-24	337.7	3.8	341.0	3.8	364	28	0.05378	0.00062	0.39913	0.00527	0.05383	0.00068
PLES-25	337.7	3.8	340.7	3.9	361	29	0.05378	0.00062	0.39863	0.00541	0.05376	0.00070
PLES-26	342.2	3.8	342.7	3.8	346	28	0.05452	0.00062	0.40143	0.00524	0.05340	0.00067

Table B1 Continued.

Sample	$^{206}Pb/^{238}U$		$^{207}Pb/^{235}U$		$^{207}Pb/^{206}Pb$		$^{206}Pb/^{238}U$		$^{207}Pb/^{235}U$		$^{207}Pb/^{206}Pb$	
Lu17 (continued)	***Age (Ma)***	***1σ***	***Age (Ma)***	***1σ***	***Age (Ma)***	***1σ***	***Ratio***	***1σ***	***Ratio***	***1σ***	***Ratio***	***1σ***
PLES-27	340.9	3.8	343.3	3.8	360	28	0.05430	0.00062	0.40227	0.00523	0.05373	0.00067
PLES-28	342.9	3.8	343.9	3.8	351	28	0.05463	0.00062	0.40316	0.00528	0.05353	0.00068
PLES-29	339.7	3.8	338.8	3.9	333	28	0.05410	0.00063	0.39601	0.00530	0.05309	0.00067
PLES-30	337.3	3.7	338.9	3.8	351	28	0.05371	0.00061	0.39626	0.00519	0.05351	0.00068
PLES-31	336.6	3.8	335.7	3.8	330	28	0.05360	0.00061	0.39186	0.00518	0.05302	0.00067
PLES-32	334.8	3.9	336.6	4.1	350	31	0.05330	0.00064	0.39309	0.00567	0.05349	0.00073
PLES-33	335.9	3.8	358.2	4.6	505	34	0.05349	0.00061	0.42297	0.00647	0.05735	0.00089
PLES-34	339.5	3.9	338.1	4.0	328	30	0.05408	0.00064	0.39514	0.00555	0.05299	0.00071
PLES-35	343.6	4.0	348.4	4.4	380	32	0.05475	0.00066	0.40937	0.00610	0.05423	0.00077
PLES-36	359.4	4.3	355.6	5.1	330	38	0.05734	0.00070	0.41934	0.00715	0.05304	0.00090
PLES-37	340.4	3.8	345.0	3.9	376	29	0.05422	0.00062	0.40460	0.00539	0.05412	0.00069

Table B2 The performance of the secondary monazite standard RGL4B, analyzed over multiple analytical sessions during the study.

Sample	$^{206}Pb/^{238}U$		$^{207}Pb/^{235}U$		$^{207}Pb/^{206}Pb$		$^{206}Pb/^{238}U$		$^{207}Pb/^{235}U$		$^{207}Pb/^{206}Pb$	
Kub8 (1 session)	***Age (Ma)***	***1σ***	***Age (Ma)***	***1σ***	***Age (Ma)***	***1σ***	***Ratio***	***1σ***	***Ratio***	***1σ***	***Ratio***	***1σ***
RGL4B-1	1573	21	1571	12	1570	22	0.27629	0.00406	3.69998	0.05717	0.09714	0.00117
RGL4B-2	1535	20	1547	12	1563	21	0.26876	0.00392	3.58620	0.05336	0.09679	0.00107
RGL4B-3	1512	19	1536	12	1568	21	0.26435	0.00382	3.53755	0.05248	0.09706	0.00109
RGL4B-4	1565	21	1573	12	1585	22	0.27469	0.00406	3.70761	0.05703	0.09791	0.00115
RGL4B-5	1558	20	1562	12	1568	20	0.27343	0.00396	3.65770	0.05365	0.09703	0.00104
RGL4B-6	1575	22	1565	15	1552	29	0.27674	0.00442	3.67006	0.06733	0.09621	0.00150
RGL4B-7	1570	21	1567	13	1563	25	0.27566	0.00416	3.67873	0.06074	0.09680	0.00130
Kub14 (1 session)												
RGL4B-1	1521	19	1535	11	1554	20	0.26614	0.00370	3.53320	0.04946	0.09631	0.00101
RGL4B-2	1554	19	1552	11	1550	20	0.27255	0.00378	3.61038	0.05052	0.09610	0.00102
RGL4B-3	1526	19	1539	11	1558	20	0.26702	0.00372	3.55245	0.04972	0.09651	0.00102
RGL4B-4	1537	19	1537	12	1537	21	0.26918	0.00381	3.54139	0.05165	0.09543	0.00108
RGL4B-5	1537	19	1539	11	1541	21	0.26926	0.00381	3.55022	0.05132	0.09563	0.00107
RGL4B-6	1518	19	1526	12	1538	22	0.26544	0.00382	3.49548	0.05260	0.09550	0.00114
RGL4B-7	1562	20	1547	11	1527	20	0.27421	0.00386	3.58867	0.05050	0.09494	0.00100
RGL4B-8	1544	20	1541	12	1538	21	0.27056	0.00387	3.56154	0.05187	0.09551	0.00108
RGL4B-9	1550	20	1535	12	1516	23	0.27186	0.00397	3.53614	0.05456	0.09439	0.00117
RGL4B-10	1524	19	1536	11	1554	20	0.26669	0.00371	3.54021	0.04973	0.09630	0.00102
RGL4B-11	1500	19	1525	11	1561	20	0.26194	0.00366	3.49149	0.04952	0.09670	0.00104
RGL4B-12	1517	19	1542	11	1578	20	0.26529	0.00369	3.56689	0.05016	0.09754	0.00104
RGL4B-13	1518	19	1535	11	1560	20	0.26541	0.00370	3.53547	0.04988	0.09664	0.00103
RGL4B-14	1508	19	1534	11	1570	20	0.26348	0.00366	3.52800	0.04955	0.09714	0.00103
RGL4B-15	1504	19	1527	11	1559	20	0.26270	0.00365	3.49749	0.04887	0.09659	0.00102
RGL4B-16	1540	19	1546	11	1556	20	0.26983	0.00377	3.58584	0.05093	0.09641	0.00104
Kub17 (1 session)												
RGL4B-1	1513	19	1531	11	1556	20	0.26456	0.00375	3.51580	0.05049	0.09640	0.00104
RGL4B-2	1531	19	1545	12	1563	21	0.26813	0.00383	3.57792	0.05251	0.09680	0.00108
RGL4B-3	1504	19	1521	11	1545	19	0.26284	0.00371	3.47386	0.04901	0.09588	0.00098
RGL4B-4	1578	20	1570	12	1559	21	0.27742	0.00398	3.69331	0.05475	0.09658	0.00109
RGL4B-5	1564	20	1561	12	1557	21	0.27462	0.00396	3.65292	0.05461	0.09649	0.00110
RGL4B-6	1518	19	1539	12	1567	21	0.26555	0.00378	3.55098	0.05192	0.09700	0.00109
RGL4B-7	1514	19	1531	12	1556	21	0.26475	0.00378	3.51816	0.05189	0.09639	0.00110
RGL4B-8	1541	19	1550	11	1563	20	0.27012	0.00384	3.60408	0.05181	0.09679	0.00104

Table B2 Continued.

Sample	$^{206}Pb/^{238}U$		$^{207}Pb/^{235}U$		$^{207}Pb/^{206}Pb$		$^{206}Pb/^{238}U$		$^{207}Pb/^{235}U$		$^{207}Pb/^{206}Pb$	
Kub17 (Continued)	***Age (Ma)***	***1σ***	***Age (Ma)***	***1σ***	***Age (Ma)***	***1σ***	***Ratio***	***1σ***	***Ratio***	***1σ***	***Ratio***	***1σ***
RGL4B-9	1513	19	1534	12	1564	21	0.26458	0.00377	3.53202	0.05187	0.09684	0.00111
RGL4B-10	1523	19	1533	11	1548	20	0.26643	0.00375	3.52683	0.04976	0.09603	0.00100
RGL4B-11	1506	19	1531	11	1565	21	0.26312	0.00373	3.51482	0.05100	0.09690	0.00108
RGL4B-12	1523	19	1539	12	1562	21	0.26640	0.00381	3.55299	0.05219	0.09675	0.00109
RGL4B-13	1531	19	1548	12	1571	21	0.26815	0.00383	3.59315	0.05300	0.09721	0.00111
Kub23 (1 session)												
RGL4B-1	1491	18	1525	11	1574	20	0.26025	0.00361	3.49176	0.04893	0.09734	0.00103
RGL4B-2	1543	19	1551	12	1562	21	0.27033	0.00377	3.60518	0.05215	0.09675	0.00110
RGL4B-3	1504	18	1533	11	1574	20	0.26277	0.00361	3.52643	0.04932	0.09736	0.00104
RGL4B-4	1523	19	1537	11	1556	20	0.26652	0.00367	3.54275	0.04920	0.09643	0.00101
RGL4B-5	1493	18	1532	11	1587	20	0.26066	0.00359	3.52125	0.04945	0.09800	0.00105
RGL4B-6	1519	19	1542	11	1574	21	0.26566	0.00367	3.56567	0.05112	0.09737	0.00110
RGL4B-7	1534	19	1543	11	1557	19	0.26865	0.00370	3.57240	0.04957	0.09647	0.00101
RGL4B-8	1502	19	1533	11	1577	20	0.26244	0.00368	3.52652	0.05079	0.09748	0.00107
RGL4B-9	1528	19	1541	11	1558	20	0.26756	0.00373	3.56031	0.05081	0.09653	0.00105
RGL4B-10	1523	19	1536	11	1553	20	0.26659	0.00371	3.53774	0.05008	0.09627	0.00104
RGL4B-11	1537	19	1551	11	1571	20	0.26927	0.00377	3.60777	0.05167	0.09720	0.00106
RGL4B-12	1524	19	1542	11	1567	19	0.26671	0.00370	3.56515	0.04962	0.09697	0.00100
RGL4B-13	1530	19	1551	11	1580	20	0.26787	0.00369	3.60661	0.05025	0.09767	0.00103
Lu9 (1 session)												
RGL4B-1	1510	19	1531	12	1560	22	0.26392	0.00382	3.51579	0.05324	0.09664	0.00116
RGL4B-2	1527	20	1523	12	1519	23	0.26721	0.00386	3.48181	0.05271	0.09452	0.00114
RGL4B-3	1549	20	1545	12	1539	21	0.27167	0.00388	3.57833	0.05197	0.09555	0.00106
RGL4B-4	1515	20	1518	12	1522	22	0.26498	0.00394	3.45887	0.05357	0.09470	0.00113
RGL4B-5	1557	27	1587	22	1627	48	0.27326	0.00536	3.77358	0.10161	0.10014	0.00263
RGL4B-6	1538	20	1527	12	1512	20	0.26945	0.00388	3.49841	0.05097	0.09419	0.00103
RGL4B-7	1568	20	1547	12	1519	23	0.27545	0.00403	3.59030	0.05547	0.09457	0.00117

Table B3 The effect on the calculated U-Pb monazite ages for sample Kub23 when the lower Th, USGS monazite 44609 is used as the primary monazite standard.

Sample	**$^{206}Pb/^{238}U$**		**$^{207}Pb/^{235}U$**		**$^{207}Pb/^{206}Pb$**		**$^{206}Pb/^{238}U$**		**$^{207}Pb/^{235}U$**		**$^{207}Pb/^{206}Pb$**	
Kub23	***Age (Ma)***	***1σ***	***Age (Ma)***	***1σ***	***Age (Ma)***	***1σ***	***Ratio***	***1σ***	***Ratio***	***1σ***	***Ratio***	***1σ***
KUB23-1	3334	39	3284	15	3254	19	0.67732	0.01004	24.39117	0.38230	0.26118	0.00309
KUB23-2	3278	37	3252	15	3236	18	0.66266	0.00960	23.59017	0.35720	0.25816	0.00301
KUB23-3	3209	36	3225	16	3232	23	0.64506	0.00921	22.96135	0.38659	0.25751	0.00386
KUB23-4	3238	36	3230	15	3225	18	0.65249	0.00924	23.07277	0.34450	0.25639	0.00302
KUB23-5	3253	39	3235	18	3224	25	0.65631	0.00992	23.19112	0.42158	0.25631	0.00403
KUB23-6	3224	38	3224	18	3224	24	0.64890	0.00983	22.92506	0.41501	0.25629	0.00400
KUB23-7	3236	40	3228	19	3224	27	0.65207	0.01026	23.02566	0.45234	0.25623	0.00444
KUB23-8	3232	36	3226	15	3222	19	0.65109	0.00929	22.98383	0.34841	0.25601	0.00308
KUB23-9	3202	38	3214	18	3222	24	0.64340	0.00981	22.70069	0.41315	0.25595	0.00399
KUB23-10	3259	37	3236	15	3221	19	0.65787	0.00941	23.20435	0.35116	0.25581	0.00305
KUB23-11	3243	38	3229	17	3221	24	0.65380	0.00968	23.05594	0.41174	0.25572	0.00400
KUB23-12	3260	38	3232	17	3215	24	0.65824	0.00988	23.12343	0.41158	0.25485	0.00393
KUB23-13	3300	37	3245	15	3212	18	0.66846	0.00959	23.43914	0.34972	0.25427	0.00291
KUB23-14	3257	37	3228	15	3210	19	0.65740	0.00958	23.02374	0.36098	0.25402	0.00315
KUB23-15	3274	40	3234	19	3210	28	0.66182	0.01035	23.16927	0.45797	0.25401	0.00447
KUB23-16	3264	36	3232	15	3209	21	0.65921	0.00925	23.11286	0.35959	0.25379	0.00333
KUB23-17	3277	38	3231	16	3203	22	0.66254	0.00970	23.09499	0.38337	0.25288	0.00352
KUB23-18	3258	36	3222	15	3199	20	0.65754	0.00922	22.88475	0.34952	0.25222	0.00319
KUB23-19	3134	36	3164	15	3182	20	0.62600	0.00906	21.54692	0.33831	0.24963	0.00317
KUB23-20	3226	38	3190	16	3167	20	0.64941	0.00972	22.13250	0.35591	0.24721	0.00309
KUB23-21	3159	36	3164	15	3166	19	0.63237	0.00901	21.54703	0.32805	0.24711	0.00301
KUB23-22	3153	36	3156	15	3158	18	0.63073	0.00905	21.37978	0.32031	0.24582	0.00284
KUB23-23	3247	40	3190	17	3155	22	0.65469	0.01030	22.14196	0.39262	0.24530	0.00349
KUB23-24	3244	41	3188	22	3152	34	0.65392	0.01061	22.08847	0.50256	0.24494	0.00528
KUB23-25	3172	36	3159	14	3150	18	0.63558	0.00909	21.43475	0.31855	0.24455	0.00277
KUB23-26	3166	37	3145	15	3132	19	0.63402	0.00939	21.13894	0.33367	0.24185	0.00297
KUB23-27	3122	37	3127	18	3130	25	0.62301	0.00937	20.73940	0.37508	0.24153	0.00385

Table B3 Continued.

Sample	$^{206}Pb/^{238}U$		$^{207}Pb/^{235}U$		$^{207}Pb/^{206}Pb$		$^{206}Pb/^{238}U$		$^{207}Pb/^{235}U$		$^{207}Pb/^{206}Pb$	
Kub23	***Age (Ma)***	***1σ***	***Age (Ma)***	***1σ***	***Age (Ma)***	***1σ***	***Ratio***	***1σ***	***Ratio***	***1σ***	***Ratio***	***1σ***
KUB23-28	3179	39	3138	19	3112	29	0.63755	0.00978	20.99273	0.42119	0.23879	0.00445
KUB23-29	3393	40	3216	17	3108	23	0.69267	0.01048	22.74178	0.39167	0.23818	0.00340
KUB23-30	3196	42	3140	20	3105	29	0.64173	0.01079	21.02652	0.44300	0.23772	0.00439
KUB23-31	3115	36	3099	15	3088	18	0.62138	0.00894	20.15868	0.30214	0.23527	0.00272
KUB23-32	3128	38	3101	18	3083	25	0.62461	0.00954	20.19501	0.36688	0.23453	0.00364
KUB23-33	3065	35	3074	15	3079	20	0.60882	0.00871	19.63639	0.30413	0.23392	0.00296
KUB23-34	3077	35	3078	15	3078	18	0.61170	0.00885	19.71626	0.29638	0.23374	0.00267
KUB23-35	3086	42	3083	24	3075	39	0.61401	0.01047	19.82773	0.50188	0.23328	0.00584
KUB23-36	3052	35	3066	16	3074	24	0.60552	0.00860	19.48484	0.32573	0.23312	0.00346
KUB23-37	3077	36	3075	16	3074	22	0.61183	0.00901	19.66054	0.32828	0.23310	0.00327
KUB23-38	2653	32	2902	21	3073	36	0.50908	0.00750	16.42951	0.36412	0.23302	0.00538
KUB23-39	3108	38	3084	18	3069	25	0.61959	0.00964	19.85728	0.36387	0.23243	0.00361
KUB23-40	3354	46	3175	26	3064	40	0.68251	0.01206	21.80980	0.57456	0.23174	0.00590
KUB23-41	3103	37	3079	15	3064	20	0.61825	0.00922	19.74787	0.31562	0.23168	0.00287
KUB23-42	3071	35	3067	15	3064	19	0.61028	0.00884	19.49631	0.29527	0.23166	0.00270
KUB23-43	3108	38	3078	17	3059	22	0.61960	0.00957	19.73256	0.33929	0.23106	0.00324
KUB23-44	3065	35	3061	14	3059	19	0.60871	0.00868	19.38594	0.29100	0.23094	0.00272
KUB23-45	3088	35	3070	15	3058	19	0.61444	0.00882	19.56070	0.29410	0.23087	0.00269
KUB23-46	3065	35	3060	15	3056	20	0.60884	0.00865	19.35753	0.30019	0.23057	0.00295
KUB23-47	3247	42	3127	19	3051	27	0.65490	0.01088	20.74809	0.41624	0.22979	0.00395
KUB23-48	3101	35	3067	15	3042	21	0.61764	0.00875	19.49715	0.30351	0.22862	0.00296

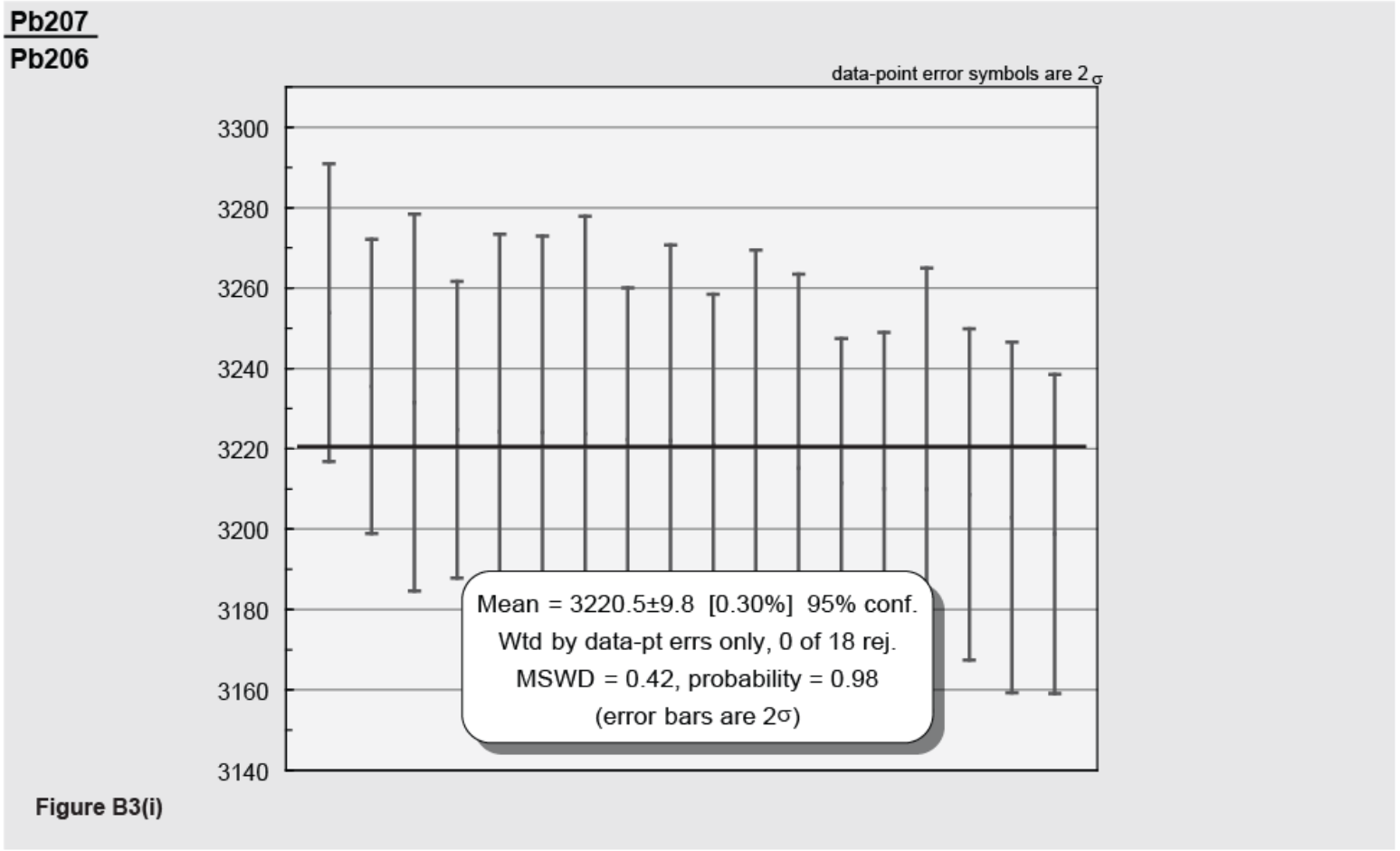
Pb207
Pb206
data-point error symbols are 2σ
3300
3280
3260
3240
3220
3200
3180
3160
3140
Mean = 3220.5±9.8 [0.30%] 95% conf.
Wtd by data-pt errs only, 0 of 18 rej.
MSWD = 0.42, probability = 0.98
(error bars are 2σ)

Figure B3(i)

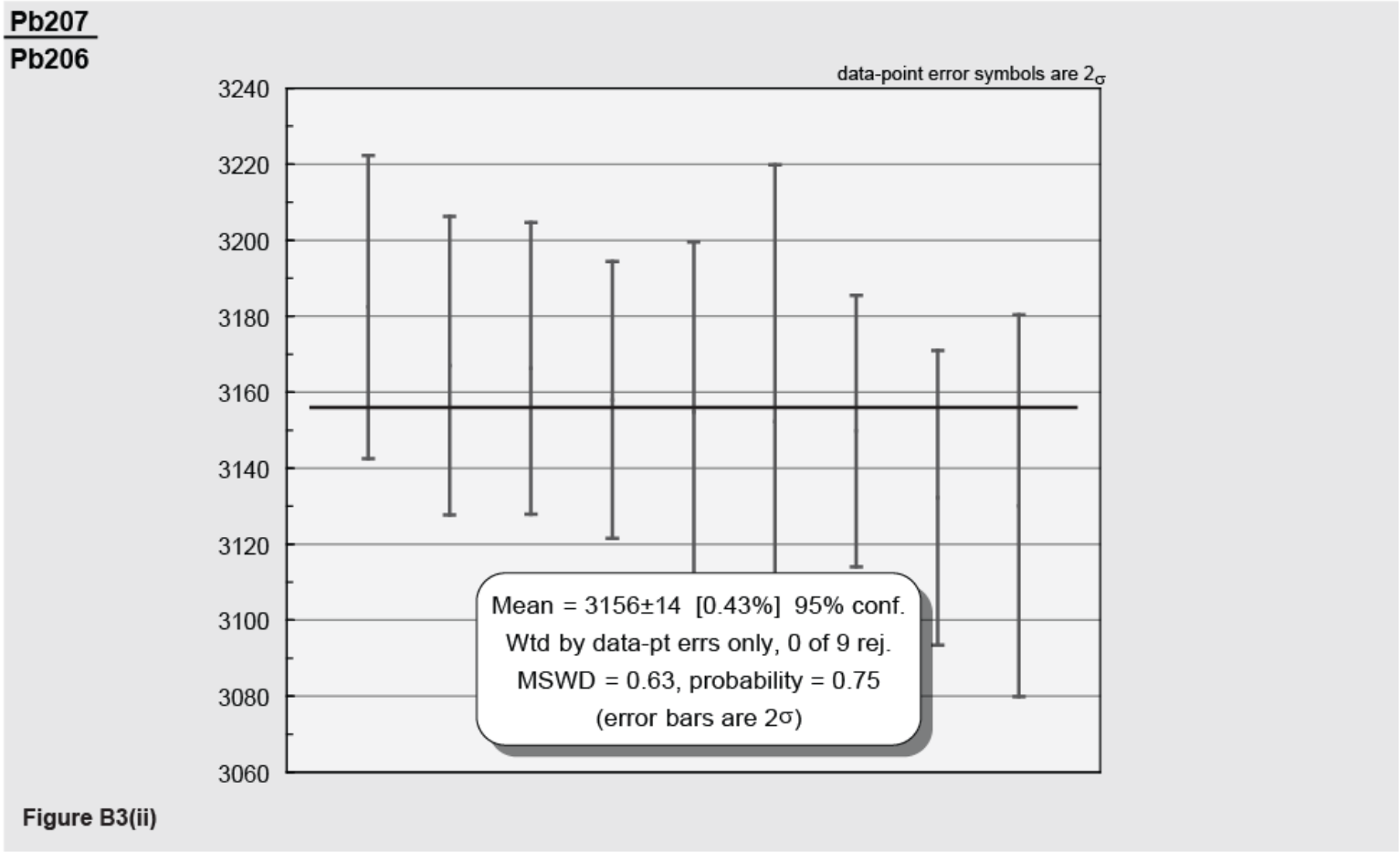
Pb207
Pb206
data-point error symbols are 2σ
3240
3220
3200
3180
3160
3140
3120
3100
3080
3060
Mean = 3156±14 [0.43%] 95% conf.
Wtd by data-pt errs only, 0 of 9 rej.
MSWD = 0.63, probability = 0.75
(error bars are 2σ)

Figure B3(ii)

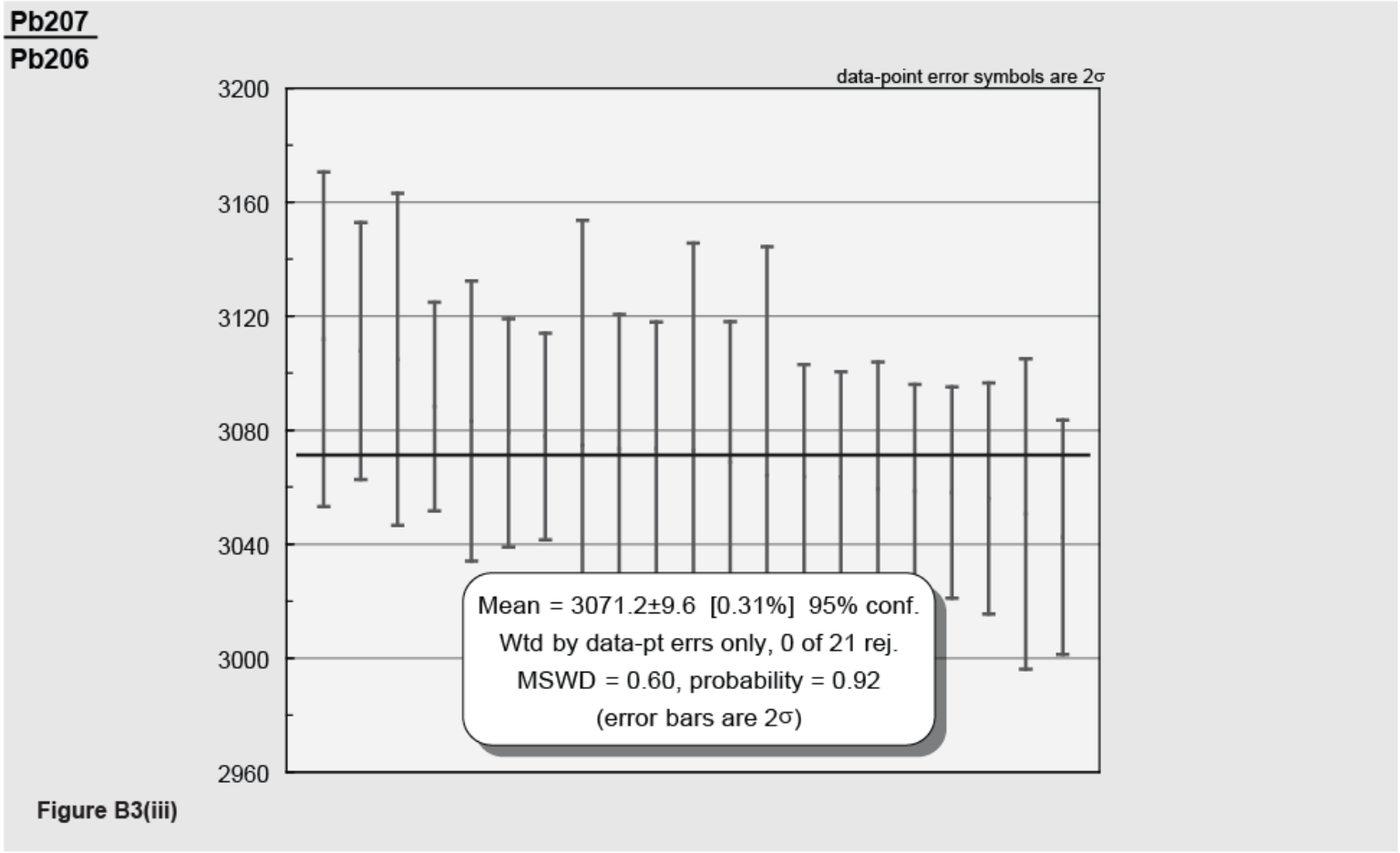

Figure B3 (i, ii & iii) The effect on the weighted mean $^{207}Pb/^{206}Pb$ monazite ages for sample Kub23 when USGS monazite 44609 is used as the primary monazite standard.

APPENDIX 2: Sample information.

APPENDIX 2

Table C1 Location and description of all MVMS, Luboya, and Kubuta gneiss and leucosome samples discussed in the thesis.

Sample	Location	GPS coordinates	Rock type	Grain-size	Major minerals	Accessory minerals
Mk2-1	MVMS	26º 53.058' S and 31º 17.773' E	metapelite	fine-medium	Grt + Crd + Bt + Pl + Qtz ± Kfs	Ap, Zrn, Mnz, Py, Ilm, Mag
Mk2-2a	MVMS	26º 53.058' S and 31º 17.773' E	metapelite	fine-medium		
Mk2-2b	MVMS	26º 53.058' S and 31º 17.773' E	metapelite	fine-medium		
Mk4	MVMS	26º 53.005' S and 31º 17.734' E	metapelite	fine-medium		
Mk5	MVMS	26º 52.971' S and 31º 17.728' E	metapelite	fine-medium		
Mk3	MVMS	26º 53.094' S and 31º 17.744' E	leucosome	coarse	Qtz + Pl + Grt ± Kfs ± Bt	Ap, Zrn, Mnz
Mk10	MVMS	26º 52.969' S and 31º 17.714' E	leucosome	coarse		
Mk11	MVMS	26º 52.969' S and 31º 17.714' E	poorly-segregated leucosome	medium-coarse		
Mk28	MVMS	26º 52.904' S and 31º 17.662' E	anatectic granite	coarse		
Mk29	MVMS	26º 52.904' S and 31º 17.662' E	leucosome	coarse		
Mk32b	MVMS	26º 52.905' S and 31º 17.675' E	granite sheet	coarse		
Lu2	Luboya	26º 51.744' S and 31º 24.518' E	metapelite	fine-medium	Grt + Bt + Crd + Sil + Kfs + Qtz + Ms	Ap, Zrn, Mnz, Ilm, Py, minor Aln
Lu6	Luboya	26º 51.764' S and 31º 24.538' E	metapelite	fine-medium	Grt + Bt + Crd + Sil + Kfs + Qtz + Pl + Spl + Ms	Ap, Zrn, Mnz, Ilm, Py
Lu9	Luboya	26º 51.764' S and 31º 24.538' E	leucosome	coarse	Grt + Qtz + Kfs + Pl	Ap, Zrn, Mnz, Py
Lu17	Luboya	26º 51.718' S and 31º 24.488" E	metapsammite	fine	Grt + Bt + Pl + Qtz + minor Kfs	Ap, Zrn, Ilm, Aln
Kub8	Kubuta	26º 49.214' S and 31º 25.608' E	metagreywacke	medium	Grt + Bt + Opx + Pl + Kfs + Qtz + Ath	Ap, Zrn, Mnz, Ilm, Py
Kub14	Kubuta	26º 49.193' S and 31º 25.478' E	leucosome	coarse	Grt + Qtz + Pl + Kfs + Chl	Zrn, Mnz, Py
Kub17	Kubuta	26º 49.148' S and 31º 25.375' E	metapelite	fine-medium	Crd + Bt + Sil + Kfs + Pl + Mu + Qtz	Ap, Zrn, Mnz, Rt, Sp
Kub23	Kubuta	26º 49.408' S and 31º 23.742' E	metagreywacke	medium-coarse	Grt + Bt + Qtz + Pl + minor Kfs	Zrn, Mnz, Ilm, Aln, Py

APPENDIX 3: Mineral compositional data.

Table D1 Major element compositions and structural formulae of representative mineral compositions from a Luboya metapsammite, sample **Lu3**. The composition of Perthite was determined via bulk area analysis on the SEM. Fsp = feldspar; T = temperature.

	Garnet			**Biotite**				**Plagioclase**		**High T Fsp**
	core	rim		matrix	incl. Grt	rimming Grt		matrix		incl. Grt
SiO_2	37.22	36.02	SiO_2	35.53	35.65	35.51	SiO_2	61.66	SiO_2	61.37
Al_2O_3	19.79	20.13	TiO_2	5.31	5.44	4.17	Al_2O_3	23.79	Al_2O_3	22.84
Fe_2O_3	5.70	1.09	Al_2O_3	17.11	16.65	17.19	FeO	0.00	FeO	0.69
FeO	27.18	32.83	FeO	22.62	17.70	21.84	CaO	5.45	CaO	2.72
MnO	1.35	1.54	MnO	0.00	0.00	0.00	Na_2O	8.39	Na_2O	8.49
MgO	4.11	3.84	MgO	7.82	11.72	8.97	K_2O	0.44	K_2O	1.98
CaO	2.28	1.43	Na_2O	0.28	0.56	0.31	BaO	0.00	BaO	0.00
Totals	**97.63**	**96.89**	K_2O	9.98	9.55	9.87	**Totals**	**99.73**	**Totals**	**98.09**
Si	2.99	2.98	**Totals**	**98.64**	**97.26**	**97.85**	Si	2.75	Si	2.79
^{IV}Al	0.01	0.02	Si	5.34	5.31	5.35	Al	1.25	Al	1.22
^{VI}Al	1.86	1.95	Ti	0.60	0.61	0.47	Fe^{2+}	0.00	Fe^{2+}	0.03
Fe^{3+}	0.34	0.07	^{IV}Al	2.66	2.69	2.65	Ca	0.26	Ca	0.13
$\sum 3^+$	2.20	2.02	^{VI}Al	0.36	0.23	0.41	Na	0.72	Na	0.75
Fe^{2+}	1.82	2.27	Fe^{2+}	2.84	2.20	2.75	K	0.02	K	0.11
Mn	0.09	0.11	Mn	0.00	0.00	0.00	Ba	0.00	Ba	0.00
Mg	0.49	0.47	Mg	1.75	2.60	2.01	**Totals**	**5.00**	**Totals**	**5.03**
Ca	0.20	0.13	Na	0.08	0.16	0.09	X_{Ab}	0.72	X_{Ab}	0.75
$\sum 2^+$	2.60	2.98	K	1.91	1.81	1.90	X_{An}	0.26	X_{An}	0.13
Totals	**7.81**	**8.00**	**Totals**	**15.55**	**15.61**	**15.64**	X_{San}	0.02	X_{San}	0.12
X_{Alm}	0.70	0.76	**Mg#**	**38**	**54**	**42**				
X_{Spss}	0.04	0.04								
X_{Py}	0.19	0.16								
X_{Grs}	0.08	0.04								
Mg#	**21**	**17**								

Number of ions calculated on the basis of 12 oxygens for garnet, 22 oxygens for biotite, and 8 oxygens for feldspar. $X_{Alm} = Fe^{2+}/(Fe^{2+}+Mn+Mg+Ca)$, $X_{Spss} = Mn/(Fe^{2+}+Mn+Mg+Ca)$, $X_{Py} = Mg/(Fe^{2+}+Mn+Mg+Ca)$, $X_{Grs} = Ca/(Fe^{2+}+Mn+Mg+Ca)$, $Mg\# = 100 \times Mg/(Mg + Fe^{2+})$, $X_{Ab} = Na/(Ca+Na+K)$, $X_{An} = Ca/(Ca+Na+K)$, $X_{San} = K/(Ca+Na+K)$.

Table D2 Major element compositions and structural formulae of representative mineral compositions from a Luboya metapelite, sample **Lu6**. The composition of Perthite was determined via bulk area analysis on the SEM.

	Garnet			**Biotite**				**Plagioclase**		**Perthite**		**Muscovite**		**Spinel**
	core	rim		matrix	incl. Grt	rimming Grt		matrix		matrix		rimming Grt		incl. Grt
SiO_2	37.10	36.92	SiO_2	36.76	37.31	37.81	SiO_2	64.83	SiO_2	66.52	SiO_2	50.40	SiO_2	0.43
Al_2O_3	20.82	20.96	TiO_2	2.42	2.75	0.60	Al_2O_3	22.17	Al_2O_3	18.92	TiO_2	0.00	Al_2O_3	56.77
Fe_2O_3	1.19	1.06	Al_2O_3	17.49	17.60	17.73	FeO	0.17	FeO	0.34	Al_2O_3	33.37	Fe_2O_3	2.76
FeO	31.11	32.23	FeO	17.81	10.17	13.44	CaO	3.29	CaO	0.20	FeO	0.83	FeO	13.47
MnO	0.69	0.71	MnO	0.00	0.00	0.00	Na_2O	9.77	Na_2O	4.41	MnO	0.00	MnO	0.00
MgO	6.57	5.86	MgO	12.54	17.46	16.14	K_2O	0.13	K_2O	10.52	MgO	1.55	MgO	5.35
CaO	0.65	0.59	Na_2O	0.40	0.68	0.41	BaO	0.00	BaO	0.09	Na_2O	0.29	CaO	0.00
Totals	**98.13**	**98.33**	K_2O	9.68	9.45	9.86	**Totals**	**100.37**	**Totals**	**101.00**	K_2O	10.84	ZnO	21.89
Si	2.98	2.97	**Totals**	**97.10**	**95.42**	**95.97**	Si	2.85	Si	2.99	BaO	0.00	**Totals**	**100.67**
^{IV}Al	0.02	0.03	Si	5.46	5.43	5.55	Al	1.15	Al	1.00	**Totals**	**97.28**	Si	0.01
^{VI}Al	1.95	1.96	Ti	0.27	0.30	0.07	Fe^{2+}	0.01	Fe^{2+}	0.01	Si	6.52	Al	1.92
Fe^{3+}	0.07	0.06	^{IV}Al	2.54	2.57	2.45	Ca	0.16	Ca	0.01	Ti	0.00	Fe^{3+}	0.06
$\sum 3^+$	2.02	2.03	^{VI}Al	0.52	0.45	0.62	Na	0.83	Na	0.38	^{IV}Al	1.48	Fe^{2+}	0.32
Fe^{2+}	2.09	2.17	Fe^{2+}	2.21	1.24	1.65	K	0.01	K	0.60	^{VI}Al	3.61	Mn	0.00
Mn	0.05	0.05	Mn	0.00	0.00	0.00	Ba	0.00	Ba	0.00	Fe^{2+}	0.09	Mg	0.23
Mg	0.79	0.70	Mg	2.77	3.79	3.53	**Totals**	**5.00**	**Totals**	**5.00**	Mn	0.00	Ca	0.00
Ca	0.06	0.05	Na	0.11	0.19	0.12	X_{Ab}	0.84	X_{Ab}	0.39	Mg	0.30	Zn	0.46
$\sum 2^+$	2.98	2.97	K	1.83	1.75	1.85	X_{An}	0.16	X_{An}	0.01	Na	0.07	**Totals**	**3.00**
Totals	**8.00**	**8.00**	**Totals**	**15.72**	**15.73**	**15.83**	X_{San}	0.01	X_{San}	0.60	K	1.79	**Mg#**	**41**
X_{Alm}	0.70	0.73	**Mg#**	**56**	**75**	**68**					Ba	0.00		
X_{Spss}	0.02	0.02									**Totals**	**13.86**		
X_{Py}	0.26	0.24									**Mg#**	**77**		
X_{Grs}	0.02	0.02												
Mg#	**27**	**24**												

Number of ions calculated on the basis of 12 oxygens for garnet, 22 oxygens for biotite and muscovite, 4 oxygens for spinel, and 8 oxygens for feldspar.
$X_{Alm} = Fe^{2+}/(Fe^{2+}+Mn+Mg+Ca)$, $X_{Spss} = Mn/(Fe^{2+}+Mn+Mg+Ca)$, $X_{Py} = Mg/(Fe^{2+}+Mn+Mg+Ca)$, $X_{Grs} = Ca/(Fe^{2+}+Mn+Mg+Ca)$, $Mg\# = 100 \times Mg/(Mg + Fe^{2+})$,
$X_{Ab} = Na/(Ca+Na+K)$, $X_{An} = Ca/(Ca+Na+K)$, $X_{San} = K/(Ca+Na+K)$.

Table D3 Major element compositions and structural formulae of representative mineral compositions from a Luboya metapsammite, sample **Lu7**. The composition of Perthite was determined via bulk area analysis on the SEM. Fsp = feldspar; T = temperature.

	Garnet			**Biotite**				**Plagioclase**		**High T Fsp**
	core	rim		matrix	incl. Grt	rimming Grt		matrix		incl. Grt
SiO_2	36.17	36.30	SiO_2	36.12	36.64	36.01	SiO_2	62.22	SiO_2	62.00
Al_2O_3	20.33	20.32	TiO_2	5.89	5.09	4.42	Al_2O_3	23.61	Al_2O_3	22.89
Fe_2O_3	1.13	0.89	Al_2O_3	17.25	17.12	17.50	FeO	0.00	FeO	0.15
FeO	32.82	34.92	FeO	22.29	16.99	21.64	CaO	5.19	CaO	3.99
MnO	1.10	1.30	MnO	0.00	0.00	0.00	Na_2O	8.45	Na_2O	8.99
MgO	4.37	3.19	MgO	8.15	12.50	9.33	K_2O	0.43	K_2O	0.83
CaO	1.20	1.17	Na_2O	0.08	0.56	0.07	BaO	0.00	BaO	0.00
Totals	**97.10**	**98.07**	K_2O	10.14	9.47	9.73	**Totals**	**99.89**	**Totals**	**98.86**
Si	2.98	2.99	**Totals**	**99.92**	**98.38**	**98.71**	Si	2.76	Si	2.78
^{IV}Al	0.02	0.01	Si	5.33	5.35	5.36	Al	1.24	Al	1.21
^{VI}Al	1.95	1.96	Ti	0.65	0.56	0.49	Fe^{2+}	0.00	Fe^{2+}	0.01
Fe^{3+}	0.07	0.06	^{IV}Al	2.67	2.65	2.64	Ca	0.25	Ca	0.19
$\sum 3^+$	2.02	2.01	^{VI}Al	0.34	0.30	0.42	Na	0.73	Na	0.78
Fe^{2+}	2.26	2.40	Fe^{2+}	2.75	2.08	2.69	K	0.02	K	0.05
Mn	0.08	0.09	Mn	0.00	0.00	0.00	Ba	0.00	Ba	0.00
Mg	0.54	0.39	Mg	1.79	2.72	2.07	**Totals**	**5.00**	**Totals**	**5.02**
Ca	0.11	0.10	Na	0.02	0.16	0.02	X_{Ab}	0.73	X_{Ab}	0.77
$\sum 2^+$	2.98	2.99	K	1.91	1.76	1.85	X_{An}	0.25	X_{An}	0.19
Totals	**8.00**	**8.00**	**Totals**	**15.48**	**15.58**	**15.55**	X_{San}	0.02	X_{San}	0.05
X_{Alm}	0.76	0.80	**Mg#**	**39**	**57**	**43**				
X_{Spss}	0.03	0.03								
X_{Py}	0.18	0.13								
X_{Grs}	0.04	0.03								
Mg#	**19**	**14**								

Number of ions calculated on the basis of 12 oxygens for garnet, 22 oxygens for biotite, and 8 oxygens for feldspar. $X_{Alm} = Fe^{2+}/(Fe^{2+}+Mn+Mg+Ca)$, $X_{Spss} = Mn/(Fe^{2+}+Mn+Mg+Ca)$, $X_{Py} = Mg/(Fe^{2+}+Mn+Mg+Ca)$, $X_{Grs} = Ca/(Fe^{2+}+Mn+Mg+Ca)$, $Mg\# = 100 \times Mg/(Mg + Fe^{2+})$, $X_{Ab} = Na/(Ca+Na+K)$, $X_{An} = Ca/(Ca+Na+K)$, $X_{San} = K/(Ca+Na+K)$.

Table D4 Major element compositions and structural formulae of representative mineral compositions from a Luboya metapelite, sample **Lu10**. The composition of Perthite was determined via bulk area analysis on the SEM.

	Garnet			**Biotite**				**Plagioclase**		**Perthite**		**Muscovite**		**Spinel**
	core	rim		matrix	incl. Grt	rimming Grt		matrix & rimming Grt		matrix		matrix		matrix
SiO_2	36.44	36.26	SiO_2	36.27	37.00	36.66	SiO_2	65.24	SiO_2	65.79	SiO_2	46.49	SiO_2	0.14
Al_2O_3	20.59	20.45	TiO_2	3.00	3.63	0.64	Al_2O_3	21.63	Al_2O_3	18.77	TiO_2	0.20	Al_2O_3	56.55
Fe_2O_3	1.43	1.56	Al_2O_3	17.58	17.56	19.02	FeO	0.63	FeO	0.00	Al_2O_3	31.07	Fe_2O_3	3.06
FeO	32.42	34.76	FeO	19.68	11.66	14.04	CaO	2.80	CaO	0.00	FeO	4.91	FeO	17.85
MnO	0.48	0.76	MnO	0.00	0.00	0.00	Na_2O	9.86	Na_2O	3.19	MnO	0.00	MnO	0.00
MgO	5.59	4.04	MgO	10.96	15.62	15.28	K_2O	0.00	K_2O	12.64	MgO	3.70	MgO	3.12
CaO	0.56	0.49	Na_2O	0.30	0.65	0.33	BaO	0.00	BaO	0.00	Na_2O	0.24	CaO	0.00
Totals	**97.50**	**98.31**	K_2O	9.90	8.84	9.22	**Totals**	**100.17**	**Totals**	**100.39**	K_2O	9.20	ZnO	20.61
Si	2.97	2.97	**Totals**	**97.70**	**94.95**	**95.20**	Si	2.87	Si	2.99	BaO	0.00	**Totals**	**101.33**
^{IV}Al	0.03	0.03	Si	5.41	5.43	5.43	Al	1.12	Al	1.01	**Totals**	**95.80**	Si	0.00
^{VI}Al	1.94	1.94	Ti	0.34	0.40	0.07	Fe^{2+}	0.02	Fe^{2+}	0.00	Si	6.24	Al	1.92
Fe^{3+}	0.09	0.10	^{IV}Al	2.59	2.57	2.57	Ca	0.13	Ca	0.00	Ti	0.02	Fe^{3+}	0.07
$\sum 3^+$	2.03	2.03	^{VI}Al	0.50	0.47	0.75	Na	0.84	Na	0.28	^{IV}Al	1.76	Fe^{2+}	0.43
Fe^{2+}	2.21	2.38	Fe^{2+}	2.45	1.43	1.74	K	0.00	K	0.73	^{VI}Al	3.15	Mn	0.00
Mn	0.03	0.05	Mn	0.00	0.00	0.00	Ba	0.00	Ba	0.00	Fe^{2+}	0.55	Mg	0.13
Mg	0.68	0.49	Mg	2.44	3.42	3.37	**Totals**	**4.99**	**Totals**	**5.01**	Mn	0.00	Ca	0.00
Ca	0.05	0.04	Na	0.09	0.19	0.09	X_{Ab}	0.86	X_{Ab}	0.28	Mg	0.74	Zn	0.44
$\sum 2^+$	2.97	2.97	K	1.88	1.66	1.74	X_{An}	0.14	X_{An}	0.00	Na	0.06	**Totals**	**3.00**
Totals	**8.00**	**8.00**	**Totals**	**15.70**	**15.57**	**15.76**	X_{San}	0.00	X_{San}	0.72	K	1.57	**Mg#**	**24**
X_{Alm}	0.74	0.80	**Mg#**	**50**	**70**	**66**					Ba	0.00		
X_{Spss}	0.01	0.02									**Totals**	**14.10**		
X_{Py}	0.23	0.17									**Mg#**	**57**		
X_{Grs}	0.02	0.01												
Mg#	**23**	**17**												

Number of ions calculated on the basis of 12 oxygens for garnet, 22 oxygens for biotite and muscovite, 4 oxygens for spinel, and 8 oxygens for feldspar.
$X_{Alm} = Fe^{2+}/(Fe^{2+}+Mn+Mg+Ca)$, $X_{Spss} = Mn/(Fe^{2+}+Mn+Mg+Ca)$, $X_{Py} = Mg/(Fe^{2+}+Mn+Mg+Ca)$, $X_{Grs} = Ca/(Fe^{2+}+Mn+Mg+Ca)$, $Mg\# = 100 \times Mg/(Mg + Fe^{2+})$,
$X_{Ab} = Na/(Ca+Na+K)$, $X_{An} = Ca/(Ca+Na+K)$, $X_{San} = K/(Ca+Na+K)$.

Table D5 Major element compositions and structural formulae of representative mineral compositions from a Kubuta metagraywacke, sample **Kub12**. The composition of Perthite was determined via bulk area analysis on the SEM.

	Garnet			**Biotite**				**Orthopyroxene**		**Perthite**	**Plagioclase**	
	core	rim		matrix; rimming Grt & Opx	incl. Grt	incl. Opx		matrix & rimming Grt		matrix	matrix	rimming Grt
SiO_2	36.77	36.33	SiO_2	35.85	36.96	34.79	SiO_2	48.75	SiO_2	64.74	59.07	67.61
Al_2O_3	20.37	20.23	TiO_2	4.21	4.38	4.37	Al_2O_3	1.40	Al_2O_3	18.47	25.62	20.04
Fe_2O_3	1.50	1.57	Al_2O_3	15.59	15.92	15.09	Fe_2O_3	2.21	FeO	0.30	0.25	0.24
FeO	32.67	33.48	Cr_2O_3	0.24	0.20	0.23	FeO	34.40	CaO	0.00	7.43	0.97
MnO	0.66	0.70	FeO	22.69	19.51	23.53	MnO	0.26	Na_2O	2.23	7.42	11.46
MgO	4.25	3.47	MnO	0.00	0.00	0.00	MgO	13.09	K_2O	13.73	0.21	0.14
CaO	2.39	2.39	MgO	8.97	12.01	9.15	CaO	0.25	BaO	0.71	0.00	0.00
Totals	**98.61**	**98.17**	Na_2O	0.19	0.49	0.35	**Totals**	**100.35**	**Totals**	**100.16**	**99.98**	**100.46**
Si	2.98	2.97	K_2O	9.90	9.34	9.34	Si	1.93	Si	2.98	2.64	2.95
^{IV}Al	0.02	0.03	**Totals**	**97.62**	**98.81**	**96.84**	^{IV}Al	0.07	Al	1.00	1.35	1.03
^{VI}Al	1.93	1.93	Si	5.45	5.44	5.36	^{VI}Al	0.00	Fe^{2+}	0.01	0.01	0.01
Fe^{3+}	0.09	0.10	Ti	0.48	0.49	0.51	Fe^{3+}	0.07	Ca	0.00	0.36	0.05
$\sum 3^+$	2.02	2.02	^{IV}Al	2.55	2.56	2.64	Fe^{2+}	1.14	Na	0.20	0.64	0.97
Fe^{2+}	2.22	2.29	^{VI}Al	0.24	0.20	0.10	Mn	0.01	K	0.81	0.01	0.01
Mn	0.05	0.05	Cr	0.03	0.02	0.03	Mg	0.77	Ba	0.01	0.00	0.00
Mg	0.51	0.42	Fe^{2+}	2.88	2.40	3.03	Ca	0.01	**Totals**	**5.02**	**5.01**	**5.02**
Ca	0.21	0.21	Mn	0.00	0.00	0.00	**Totals**	**4.00**	X_{Ab}	0.20	0.64	0.95
$\sum 2^+$	2.98	2.98	Mg	2.03	2.63	2.10	**Mg#**	**40**	X_{An}	0.00	0.35	0.04
Totals	**8.00**	**8.00**	Na	0.06	0.14	0.10			X_{San}	0.80	0.01	0.01
X_{Alm}	0.74	0.77	K	1.92	1.75	1.84						
X_{Spss}	0.02	0.02	**Totals**	**15.65**	**15.63**	**15.72**						
X_{Py}	0.17	0.14	**Mg#**	**41**	**52**	**41**						
X_{Grs}	0.07	0.07										
Mg#	**19**	**16**										

Number of ions calculated on the basis of 12 oxygens for garnet, 22 oxygens for biotite, 6 oxygens for pyroxene, and 8 oxygens for feldspar.
$X_{Alm} = Fe^{2+}/(Fe^{2+}+Mn+Mg+Ca)$, $X_{Spss} = Mn/(Fe^{2+}+Mn+Mg+Ca)$, $X_{Py} = Mg/(Fe^{2+}+Mn+Mg+Ca)$, $X_{Grs} = Ca/(Fe^{2+}+Mn+Mg+Ca)$,
$Mg\# = 100 \times Mg/(Mg + Fe^{2+})$, $X_{Ab} = Na/(Ca+Na+K)$, $X_{An} = Ca/(Ca+Na+K)$, $X_{San} = K/(Ca+Na+K)$.

Table D6 Major element compositions and structural formulae of representative mineral compositions from a Kubuta metapelite, sample **Kub17**. The composition of Perthite was determined via bulk area analysis on the SEM.

	Cordierite			**Biotite**				**Plagioclase**	**Perthite**		**Muscovite**	
	core	rim		matrix	incl. Crd	rimming Crd		matrix	matrix		matrix	incl. Crd
SiO_2	50.72	50.22	SiO_2	37.80	37.01	37.17	SiO_2	64.22	66.52	SiO_2	46.97	47.73
Al_2O_3	28.41	28.34	TiO_2	4.32	3.92	2.94	Al_2O_3	23.76	18.88	TiO_2	0.24	0.00
FeO	6.74	5.34	Al_2O_3	18.92	18.76	19.51	FeO	0.00	0.00	Al_2O_3	36.41	30.77
MnO	0.21	0.13	FeO	16.06	16.59	15.03	CaO	4.66	0.00	FeO	1.02	1.13
MgO	9.86	8.14	MnO	0.05	0.00	0.00	Na_2O	9.40	3.07	MnO	0.00	0.00
CaO	0.00	0.00	MgO	11.69	10.84	11.82	K_2O	0.25	12.43	MgO	0.94	0.76
Na_2O	0.09	0.76	Na_2O	0.28	0.27	0.28	BaO	0.00	0.00	Na_2O	0.39	0.64
K_2O	0.00	2.28	K_2O	10.12	9.80	9.82	**Totals**	**102.30**	**100.90**	K_2O	10.98	10.80
Totals	**96.04**	**95.20**	**Totals**	**99.24**	**97.19**	**96.57**	Si	2.78	3.00	**Totals**	**96.95**	**91.83**
Si	5.30	5.33	Si	5.43	5.44	5.45	Al	1.21	1.00	Si	6.14	6.59
Al	3.50	3.55	Ti	0.47	0.43	0.32	Fe^{2+}	0.00	0.00	Ti	0.02	0.00
Fe^{2+}	0.59	0.47	^{IV}Al	2.57	2.56	2.55	Ca	0.22	0.00	^{IV}Al	1.86	1.41
Mn	0.02	0.01	^{VI}Al	0.63	0.69	0.83	Na	0.79	0.27	^{VI}Al	3.75	3.59
Mg	1.53	1.29	Fe^{2+}	1.93	2.04	1.84	K	0.01	0.72	Fe^{2+}	0.11	0.13
Ca	0.00	0.00	Mn	0.01	0.00	0.00	Ba	0.00	0.00	Mn	0.00	0.00
Na	0.02	0.16	Mg	2.50	2.38	2.58	**Totals**	**5.01**	**4.99**	Mg	0.18	0.16
K	0.00	0.31	Na	0.08	0.08	0.08	X_{Ab}	0.77	0.27	Na	0.10	0.17
Totals	**10.96**	**11.12**	K	1.85	1.84	1.84	X_{An}	0.21	0.00	K	1.83	1.90
Mg#	**72**	**73**	**Totals**	**15.47**	**15.46**	**15.50**	X_{San}	0.01	0.73	**Totals**	**14.00**	**13.95**
			Mg#	**56**	**54**	**58**				**Mg#**	**62**	**55**

Number of ions calculated on the basis of 22 oxygens for biotite and muscovite, 8 oxygens for feldspar, and 18 oxygens for cordierite.
Mg# = 100 x Mg/(Mg + Fe^{2+}), X_{Ab} = Na/(Ca+Na+K), X_{An} = Ca/(Ca+Na+K), X_{San} = K/(Ca+Na+K).

Table D7 Major element compositions and structural formulae of representative mineral compositions from a Kubuta metagreywacke, sample **Kub23**. The composition of Perthite was determined via bulk area analysis on the SEM.

	Garnet			**Biotite**				**Perthite**	**Plagioclase**
	core	rim		matrix	incl. Grt	rimming Grt		matrix	matrix
SiO_2	37.10	37.38	SiO_2	35.66	36.73	36.16	SiO_2	65.31	64.69
Al_2O_3	20.69	20.82	TiO_2	4.33	2.58	2.61	Al_2O_3	18.15	22.19
Fe_2O_3	1.66	1.28	Al_2O_3	15.53	16.12	16.18	FeO	0.38	0.55
FeO	34.53	35.27	Cr_2O_3	0.00	0.00	0.00	CaO	0.00	3.41
MnO	1.11	1.40	FeO	24.28	18.04	23.78	Na_2O	0.22	9.83
MgO	4.11	3.62	MnO	0.00	0.00	0.00	K_2O	17.02	0.00
CaO	1.08	1.22	MgO	8.46	13.43	9.88	BaO	0.00	0.00
Totals	**100.28**	**100.99**	Na_2O	0.26	0.58	0.32	**Totals**	**101.08**	**100.66**
Si	2.97	2.98	K_2O	10.02	9.23	9.89	Si	3.00	2.84
^{IV}Al	0.03	0.02	**Totals**	**98.53**	**96.72**	**98.83**	Al	0.98	1.15
^{VI}Al	1.93	1.94	Si	5.42	5.48	5.45	Fe^{2+}	0.01	0.02
Fe^{3+}	0.10	0.08	Ti	0.49	0.29	0.30	Ca	0.00	0.16
$\sum 3^+$	2.03	2.02	^{IV}Al	2.58	2.52	2.55	Na	0.02	0.84
Fe^{2+}	2.31	2.35	^{VI}Al	0.20	0.32	0.32	K	1.00	0.00
Mn	0.08	0.09	Cr	0.00	0.00	0.00	Ba	0.00	0.00
Mg	0.49	0.43	Fe^{2+}	3.08	2.25	2.99	**Totals**	**5.02**	**5.00**
Ca	0.09	0.10	Mn	0.00	0.00	0.00	X_{Ab}	0.02	0.84
$\sum 2^+$	2.97	2.98	Mg	1.92	2.99	2.22	X_{An}	0.00	0.16
Totals	**8.00**	**8.00**	Na	0.08	0.17	0.09	X_{San}	0.98	0.00
X_{Alm}	0.78	0.79	K	1.94	1.76	1.90			
X_{Spss}	0.03	0.03	**Totals**	**15.71**	**15.77**	**15.82**			
X_{Py}	0.17	0.14	**Mg#**	**38**	**57**	**43**			
X_{Grs}	0.03	0.03							
Mg#	**18**	**15**							

Number of ions calculated on the basis of 12 oxygens for garnet, 22 oxygens for biotite, and 8 oxygens for feldspar. $X_{Alm} = Fe^{2+}/(Fe^{2+}+Mn+Mg+Ca)$, $X_{Spss} = Mn/(Fe^{2+}+Mn+Mg+Ca)$, $X_{Py} = Mg/(Fe^{2+}+Mn+Mg+Ca)$, $X_{Grs} = Ca/(Fe^{2+}+Mn+Mg+Ca)$, $Mg\# = 100 \times Mg/(Mg + Fe^{2+})$, $X_{Ab} = Na/(Ca+Na+K)$, $X_{An} = Ca/(Ca+Na+K)$, $X_{San} = K/(Ca+Na+K)$.